Geometric Variances in Hip Osteoarthritis and Tribology of the Natural Hip

Dawn Groves

Submitted in accordance with the requirements for the degree of

Doctor of Philosophy

The University of Leeds

School of Mechanical Engineering

June 2015

The candidate confirms that the work submitted is her own and that appropriate credit has been given where reference has been made to the work of others.

Acknowledgements

This PhD has been funded by an EPSRC case studentship, kindly supported by DePuy Synthes and Imorphics Ltd. I was supervised by Dr Sophie Williams (primary supervisor), Professor John Fisher, Dr Mike Bowes and Professor David Beverland.

The creation of active shape models, application of the Sammon mapping algorithm, and sphere fitting in Chapter 2 was carried out by Dr Mike Bowes, Imorphics Ltd. (Manchester, UK), using their custom algorithm and EndPoint software.

Firstly, and most importantly, I would like to express my sincere gratitude to my primary supervisor Dr Sophie Williams for the continuous support and mentorship of my PhD study. Your expert knowledge, advice, patience, and at times pastoral care, have guided and motivated me thorough the whole process, and for this I am truly grateful. I must also say a special thank you to Dr Mike Bowes, who has patiently guided me through the once mysterious world of medical imaging with his specialist skills and knowledge. I would also like to thank my other supervisors, Professor John Fisher and Professor David Beverland, who have always been there to help and offer additional advice and expertise.

During the time I have spent studying for my PhD I have had the privilege of working with some amazing people, both in the Institute of Medical and Biological Engineering (iMBE), and through collaborations with Imorphics Ltd., the Leeds Musculoskeletal Biomedical Research Unit (LMBRU) at Chapel Allerton hospital (CAH), and the arthroplasty outcomes unit at Musgrave Park hospital in Belfast. You have been inspirational to me and I have learnt so much from you all.

I would like to thank the iMBE technicians led by Phil Wood. The support of all the iMBE technical staff has been excellent and I have really appreciated the help and advice that I have received from you.

During my studies I spent many hours in the LMBRU and orthopaedic outpatient department at CAH, and I would thank everyone there for their help and for always making me feel welcome. I have to say a special thank you to Carole Burnett, who would go out of her way to offer advice about my MRI work, and to Dr Richard Hodgson (consultant radiologist), who I started this project with, and to Dr Phil Robinson (also a consultant radiologist), who has offered great advice, teaching and guidance, and who

also checked the accuracy of my medical imaging work. Thank you also to Rob Evens, radiographer, who scanned most of the participants in the MRI study, and Tracy Hulland, who ensured that the patient administration and paperwork was always in order. I must also thank all of the staff in the orthopaedic pre-operative assessment clinic at CAH, orthopaedic outpatient sister Caroline Cooper, and orthopaedic consultants Mr Martin Stone, Mr David MacDonald, Mr Peter Bobak, and Mr Joseph Aderinto, all of whom assisted me with the recruitment of hip osteoarthritis patients for my study.

I would also like to thank all my friends and colleagues in iMBE who have supported me in numerous different ways over the years such as Claire, Jia, Mazen, Simon, and more recently Seb for his IT assistance, to name just a few. I hope that in the years to come I am able to offer the same help and support to students and colleagues that you have given me. I must also say a big thank you to the iMBE administrative support staff, especially Debra Baldwin and Cheryl Harris, who have provided help and support, and kept me on the right track administratively over the years.

Lastly I would like to thank my partner Martyn, who has constantly offered love, support and encouragement throughout this journey. I would like to dedicate this thesis to my father, who will never be forgotten and from whom I inherited my sense of humour from. This has undoubtedly kept me sane over the last few months…if not years...and will hopefully continue to do so for many more years to come.

In loving memory of my father

Abstract

Osteoarthritis (OA) of the hip joint is a common form of arthritis that often requires surgical intervention using total hip replacement (THR), as treatment using early interventional techniques is still poorly understood. It is hoped that gaining a better understanding of hip geometry, and that using this information in future *in vitro* simulations, will contribute to the evidence base regarding the aetiology of OA and the use of early surgical interventions to prevent or delay the onset of hip OA.

This thesis aimed to investigate geometric variations in patients with known hip OA and compare them to asymptomatic participants of the same age. The thesis also aimed to develop a novel *in vitro* simulation model for the tribological testing of complete natural hip joints.

Twenty nine participants were recruited into the study (n = 15 control and n = 14 hip OA), and the geometry of their hip joints was explored and compared using high resolution (3.0 T) MRI and 3D shape matching software (EndPoint), which in the main, had previously been used for investigating the knee joint. In the study group, obvious shape differences such as superior flattening of the femoral head, differences in the sphericity of the head and acetabulum, and a significantly smaller degree of acetabular anteversion were observed when compared to the asymptomatic group.

Experimental work began by validating a new pendulum friction simulator (Mk B) using THR bearings and hemiarthroplasties. One major modification and several minor modifications were required before the simulator could be used to develop the novel complete natural hip joint *in vitro* simulation model, which was done successfully using porcine tissue. This model and the novel sample potting methodology developed alongside it can be used in future *in vitro* tribological studies of the natural hip joint, and information gained from the MRI study can be used as geometric parameters for future *in vitro* simulations.

Contents

List of Figures

List of Tables

Nomenclature and Abbreviations

ω	Angular velocity
A_d	Deformation area of profilometry trace (mm^2)
B_o	Magnetic field in the MRI scanner
$\overline{D_d}$	Mean depth of wear scar (mm)
E, E'	Young's Modulus, Equivalent Young's Modulus
$\emptyset$	Diameter
u	Entraining velocity
f	Friction factor
f_a	Mean post-test friction factor (porcine tissue studies)
f_b	Mean pre-test friction factor (porcine tissue studies)
f_d	Dynamic mean friction factor (porcine tissue studies)
f_n	Normalised friction factor (porcine tissue studies)
f_o	Mean frictional offset (porcine tissue studies)
G_t	Size of gap between profilometry traces (mm)
h_{min}	Minimum film thickness
η	Fluid viscosity (dynamic) in Pa s (Pascal-second)
λ	Lambda ratio
L	Length of a tube (Equation 4.3), L_A & L_B for simulators A & Mk B
L_t	Length of profilometry trace
µm	Microns
H_o	Null hypothesis
H_1	Alternative hypothesis
ν	Poisson's Ratio
ΔP	Pressure difference
Q	Volumetric flow rate
r	Radius
R	Equivalent radius of the bearing
R	Internal radius of a tube (Equation 4.3), R_A & R_B for simulators A & Mk B
R_a	Roughness average (surface profilometry)
R_{ac}	Combined average surface roughness
r_h	Radius of femoral head
T	Frictional torque
$T_{frictional}$	Total frictional torque
$T_{misalignment}$	Torque due to any misalignment/offset
T_t	True frictional torque
T_F	Frictional torque – forward measurement
T_R	Frictional torque – reverse measurement
V_d	Surface deformation volume (mm^3)
v/v	Volume-to-volume
W	Load (in Newtons)
AI	Acetabular index, or Tönnis angle
AP	Anteroposterior
APP	Anterior pelvic plane
ASM	Active shape model

AV	Acetabular version
BMI	Body mass index
CAD	Computer aided drawing
CAH	Chapel Allerton hospital
CI/CL	Confidence interval/limit
COR	Centre of rotation
CoC	Ceramic-on-ceramic
CoCr	Cobalt chrome
CMM	Coordinate measuring machine
DDH	Developmental dysplasia of the hip
DICOM	Digital Imaging and Communications in Medicine
DOF	Degrees of freedom
DTI	Dial test indicator
ECM	Extra cellular matrix
FAI	Femoroacetabular impingement
FE	Flexion-extension
FFS	Feet first supine
FHEI	Femoral head extrusion index
FNSA	Femoral neck shaft angle
FoV	Field of view
GAG	Glycosaminoglycan
Hz	Hertz
HR	Higher resolution
IRAS	Integrated research application system
ISO	International Organization for Standardisation
JSN	Joint space narrowing
kN	Kilonewton
K/L	Kellgren and Lawrence
LMBRU	Leeds Musculoskeletal Biomedical Research Unit
m	Meter
MoP	Metal-on-polyethylene
MRI	Magnetic resonance imaging
mg/ml	Milligrams per millilitre
ms	Millisecond
N	Newton
Nm	Newton per meter
n	Number
OHS	Oxford hip score
Pa s	Pascal-second
PAO	Periacetabular osteotomy
PC	Personal computer
PG	Proteoglycan
PID	Proportional-integral-derivative controller
PD	Proton density
PG	Proteoglycans
psi	Pounds per square inch

RDA	Rapidly destructive arthrosis
REC	Research Ethics Committee
RF	Radiofrequency
ROI	Region of interest
SD	Standard deviation
SimSol	Simulation Solutions Ltd.
SLR	Single-lens reflex
SNR	Signal to noise ratio
SPACE	Sampling Perfection with Application optimised Contrasts using different flip angle Evolution
SOP	Standard operating procedure
SPL	Swing phase load
SUFE/SCFE	Slipped upper (or capital) femoral epiphysis
TAL	Transverse acetabular ligament
T	Tesla (e.g. 3.0 T)
TE	Echo time
THR	Total hip replacement
TR	Repetition time
TSE	Turbo spin echo
UHMWPE	Ultra-high molecular weight polyethylene

Chapter 1 Literature Review

1.1 Introduction

Osteoarthritis (OA) is the most common form of arthritis and the percentage of individuals seeking treatment for OA generally increases with age (Arden and Nevitt, 2006). The economic burden of OA from both indirect (e.g. loss of productivity, wages) and direct healthcare costs is increasing and it is expected to continue doing so (Bitton, 2009) because it has been estimated that by 2030, approximately 33% of the UK population will be aged 60 years or more (Croft, 2005). The most recent published report by the National Joint Registry (NJR) for England, Wales and Northern Ireland recorded a total of 80,194 primary total hip replacements (THRs) and 9,751 revision hip procedures in 2013 (NJR, 2014), with the average age being approximately 69 and 71 years respectively. In Scotland a further 7,609 primary THAs and 953 revision procedures were performed in 2013 (NHS Scotland, 2014).

Revision THR is a more complex and costly procedure than primary THR (Crowe *et al.*, 2003), and it is considered to be less favourable in terms of functional outcome and patient satisfaction (Saleh *et al.*, 2003; Lubbeke *et al.*, 2007). This highlights the need for continued research to not only increase the longevity of implanted hip prostheses, therefore reducing the need for revision surgery at a later date, but also to develop effective early interventions that prevent or slow the progression of OA and delay the need for primary THR.

This review has been undertaken in order to assist the author with research pertaining to the effect of natural hip geometry on tribology and hip OA. It will illustrate and critically discuss the current body of knowledge and highlight any gaps or flaws in the current evidence base. The main topics covered include an overview of acetabular and proximal femoral morphology, biomechanics and tribology of the hip joint, OA of the hip, joint-preserving surgery and acetabular cup placement in THR.

1.2 The Natural Hip Joint

1.2.1 Gross Anatomy and Osteokinematics

The hip joint (also known as the coxofemoral joint) is a diarthrodial ball-and-socket joint formed by the articulation of the femoral head of the femur and the acetabulum of the

pelvis (also known as the innominate or os coxa bone). It connects the lower limb to the trunk and has a primarily weight-bearing function, however its large range of motion with three degrees of freedom (Table 1.1) and circumduction motion, also enable a wide range of locomotor activities. In a study of 55 healthy subjects Dujardin *et al*. (1997) found that during walking the mean value for flexion-extension was ∼31°, whilst abduction−adduction was ∼7° and rotation ∼13°. Movement occurs around the centre of the femoral head (centre of rotation) where the three axes intersect (Moore and Dalley, 1999). There are 21 muscles crossing the hip joint and these are contained in six functional muscle groups relating to the direction of movement (e.g. flexors, extensors, abductors, adductors, internal rotators and external rotators). In addition to moving the joint, the hip and pelvic musculature also contributes to the stability of the joint (Ranawat and Kelly, 2005).

Table 1.1: Average maximum range of movement in a normal adult hip and the range of movement required at the hip for normal gait on level ground (Palastanga *et al.*, 2002).

Direction of Movement	Range of Movement (ROM)	ROM Required for Normal Gait
Flexion	120° to 140° (90° if knee extended)	30°
Extension	-10° to -30° (less if knee flexed)	-10°
Abduction	30° to 50°	5°
Adduction	10° to 30°	5°
Medial Rotation	45°	5°
Lateral Rotation	45°	5°

The articulating surfaces are covered with hyaline cartilage and the joint is surrounded by a strong capsule, which also makes a substantial contribution to the stability of the hip joint. The capsule is reinforced by three ligaments, two on the anterior aspect of the joint (iliofemoral and pubofemoral), and one on the posterior aspect (ischiofemoral). These ligaments work synergistically with the joint capsule and surrounding musculature to limit the magnitude of joint distraction and translation, even in the presence of strong forces acting on the joint (Levangie and Norkin, 2001). Branches of the lumbar and sacral plexuses provide the nerve supply to the hip joint and the main blood supply is provided by branches of the circumflex femoral arteries (Moore and Dalley, 1999).

The acetabulum forms the proximal articular surface of the hip joint but normally only the horse-shoe-shaped periphery of the acetabulum (lunate surface) articulates with the head of the femur. The acetabular bone is comprised of three component parts: the pubis, the ilium and the ischium (Figure 1.1), which join at the Y-shaped triradiate cartilage. These three bones fuse together and ossification is normally complete around the age of puberty (i.e. 15 to 16 years of age). A fibroelastic fat pad lies within the acetabular fossa and inferiorly there is a deficiency in the acetabulum called the acetabular notch. This is bridged by the transverse acetabular ligament (TAL) thus creating a tunnel through which blood vessels can pass into the acetabular fossa, which is the deepest and non-articular part of the acetabulum (Levangie and Norkin, 2001). The anatomy and orientation of the acetabulum, together with some of its associated structures will be discussed in more detail in Section 1.3.

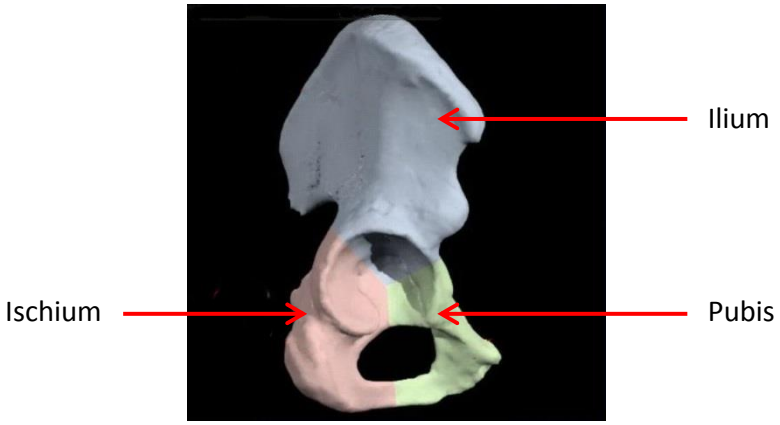

Figure 1.1: Diagram illustrating the three parts of the innominate bone viewed from the medial side (Primal Pictures, 2006b).

The distal articular surface is the femoral head and this is described as being conchoid in shape (Hossain and Andrew, 2008), however, it appears to be almost spherical as the mean squared deviation between the osseous femoral head and a fitted sphere has been measured as 0.035 mm (range 0.014 mm to 0.072 mm) (Menschik, 1997). The fovea capitis, which is a small, roughened area on the medial surface of the head, is not covered with hyaline cartilage and is the point of attachment for the ligament of the head of femur (ligamentum teres). The femoral head is attached to the shaft of the femur via the femoral neck. In a normal adult the angle of inclination (femoral offset), which is on average 125°, and the femoral neck anteversion or angle of torsion, which has an average of 10°, causes the femoral head to face medially, superiorly and

anteriorly (Figure 1.2 a) (Palastanga *et al.*, 2002; Sariali *et al.*, 2008). A schematic diagram of the hip joint is shown in Figure 1.2 b.

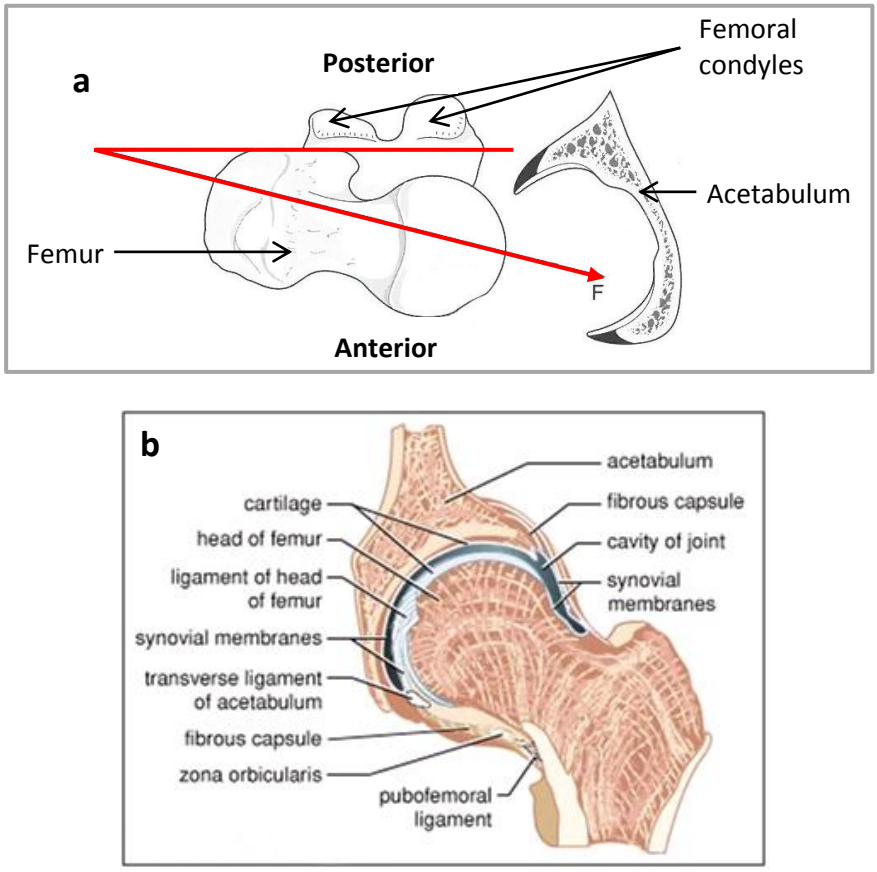

Figure 1.2: (a) Femoral anteversion: the angle between a line parallel to the femoral condyles and a line along the femoral neck axis (F) (Palastanga *et al.*, 2002) and (b) Schematic diagram of the hip joint (Merriam-Webster Inc., 2006).

The hip is a relatively congruent joint but the rounded articulating surface of the spheroidal (i.e. slightly flattened superiorly) femoral head is not as spherical as the shallower, hemispherical arched acetabulum. Under low loading conditions more than half of the head fits within the acetabulum, and with increased loading in a weight-bearing position the congruency of the joint is improved and the articular contact surface area has been reported to increase from 2470 mm^2 to 2830 mm^2 (Palastanga *et al.*, 2002).

1.3 The Acetabulum

The acetabulum is located on the outer surface of the innominate bone and a considerable amount of literature has been published relating to its morphology and

the existence of intra- and inter-individual differences. A detailed diagram of the acetabulum showing features that are discussed in this section is shown in Figure 1.3.

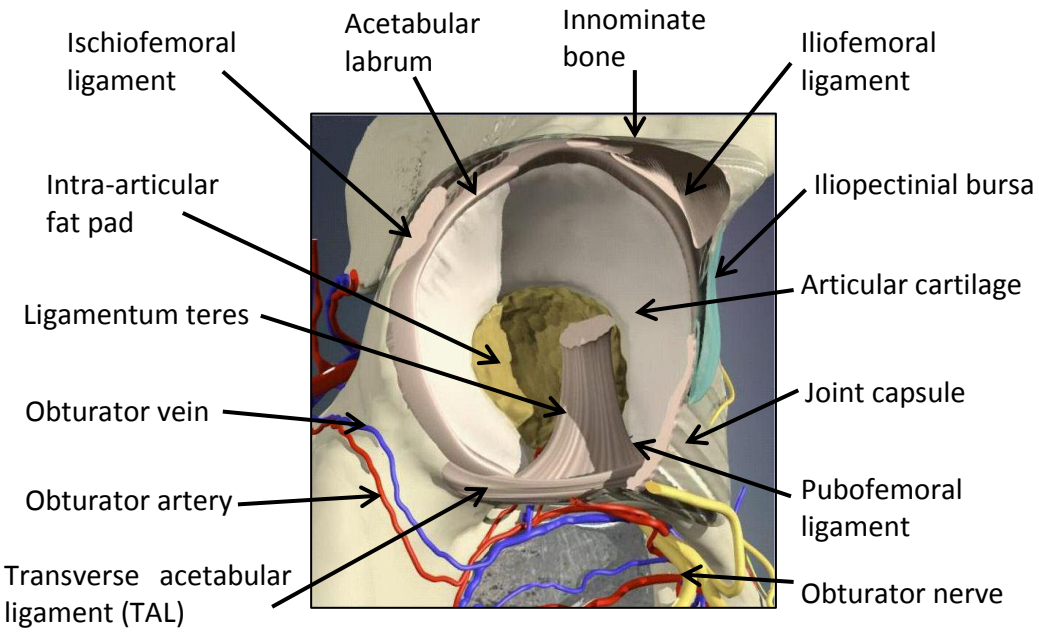

Figure 1.3: Detailed diagram of the human acetabulum and its associated structures (Primal Pictures, 2006a).

1.3.1 Acetabular Depth and Diameter

The depth and diameter of the acetabular bone have been investigated by a number of researchers in order to establish the existence of any variations with respect to gender. With the exception of Murtha *et al*. (2008) and Vandenbussche *et al*. (2007; 2008), all of the studies reported in this section have been conducted on skeletal specimens and digital callipers have been used to take the measurements.

Krebs *et al*. (2009) created a topographical map of the bone surfaces in relation to the acetabular cavity on 50 healthy pelves (25 male and 25 female). As part of this work, they measured the diameter of the acetabulum in two directions, which they named height and depth (Figure 1.4).

They reported the mean height as being 53.7 ± 3.47 mm standard deviation (SD) in males and 47.0 ± 2.47 mm (SD) in females, and the mean width reported as being 52.4 ± 3.44 mm (SD) in males and 45.5 ± 2.47 mm (SD) in females. The researchers concluded that the width, but not the height was significantly smaller in females than in

males (p = 0.01). Kohnlein *et al*. (2009) studied bone morphology using 66 skeletal acetabula, also concluding that the female acetabula specimens had significantly smaller diameters than the male specimens did (p < 0.00001). In their study, the mean diameter was reported as 47.5 ± 2.7 mm (SD) in females (n = 33) and 54.0 ± 2.8 mm (SD) in males (n = 33). Unfortunately, it is difficult to make direct comparisons of these results with those of other studies, as they have not presented the reader with information on how the measurements were obtained or what landmarks were used.

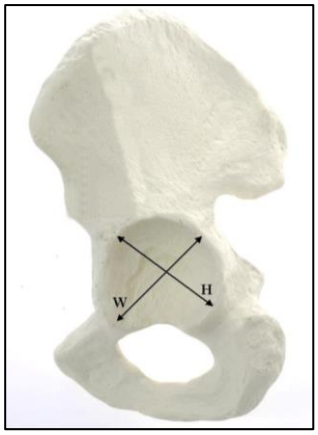

Figure 1.4: Pelvic specimen showing the height (H), which was taken from the rim of the ischium to the anterior superior iliac spine, and the width (W), which was taken from the acetabular rim at the pubic ramus to the sciatic notch (Krebs *et al.*, 2009).

Vandenbussche *et al*. (2008) used 3D bone reconstructions of CT scans to investigate the bony morphology of the acetabulum, and they compared intra-individual differences as well as variations between genders. The acetabular rim was digitised with a minimum of 80 points, and the coordinates of these points were used to calculate the diameter, however it is not clear at what location on the acetabula this was done. The mean diameter of 100 healthy female acetabula (in 50 subjects) was 45.1 ± 2.1 mm (SD), compared to 51.9 ± 3.1 mm (SD) in an equal number of male subjects, which was a statistically significant difference of 6.8 mm (p < 0.0001). This study also reported mean intra-individual differences of 1.14 ± 1.0 mm (SD), 17% of which had a significant difference of 2 mm or more (p < 0.0001). Previous research conducted by Vandenbussche *et al.* (2007) also concluded that the mean diameter of the female acetabulum is significantly smaller than the males' (46.5 mm to 52.8 mm respectively; p < 0.01), however this was a much smaller study (n = 34) and cadaveric specimens were used.

Murtha *et al.* (2008) also used volumetric CT data from the scans of 42 subjects (20 male and 22 female acetabula) undergoing THR to investigate variations in acetabular anatomy. In this study, 3D surface models containing a triangulated mesh were created from the vertices of segmented volumetric CT data. The diameter was calculated by measuring the radius of a sphere that had been electronically fitted to an average of 310 vertices used to define the lunate surface of each acetabulum. They reported a mean diameter of 53.4 mm (range 49.0 mm to 57.4 mm) in males and a mean diameter of 50.0 mm (range 43.4 mm to 60.6 mm) in females, which was described as being significantly smaller ($p = 0.003$). The results of this study are consistent with those of other studies suggesting that the female pelvis has a smaller diameter than that of the male. However, it should be noted that measurements taken by Murtha *et al.* (2008) included the cartilage, whereas measurements reported in the other studies included in this literature review were based on only the osseous parts of the acetabulum. Murtha *et al*. (2008) also investigated acetabular depth by measuring the distance from the deepest point in the centre of the acetabulum relative to a plane that had been fitted to 84 vertices around the acetabular rim. Following normalisation of the depth to account for male and female size differences, the mean depth in females was reported to be 19.5 mm (range 15.7 mm to 24.2 mm) and in males it was 22.7 mm (17.5 mm to 28.0 mm), suggesting that the acetabulum is shallower in females.

The lunate surface is the articulating surface of the acetabulum. It is semilunar in shape and is covered in articular (hyaline) cartilage (Figure 1.3), which in a normal hip is described as being thickest anterosuperiorly (Hossain and Andrew, 2008). Salamon *et al*. (2004) reported the mean lunate surface area of 30 macerated human pelvic specimens as being 2,294 ± 329 mm^2 (SD), which was said to be proportional to both radius and depth.

1.3.2 Acetabular Rim Profile

In recent years, more information has become available regarding the profile of the acetabular rim, which appears to be asymmetrical with differently shaped configurations anteriorly and posteriorly.

Maruyama *et al.* (2001) studied the acetabular rim profile of 50 male and 50 female normal skeletal specimens (n = 200 acetabula). The assessment of the rim shape was done visually by one author to maintain consistency. They recorded the existence of a

simple hemispherical or straight posterior rim, and the shape distribution for the anterior acetabula rims was as follows: 60.5 % curved, 25.5 % angular, 9.5 % irregular, and 4.5 % straight. Examples of acetabular rim profiles that have been described in the literature are shown in Figure 1.5.

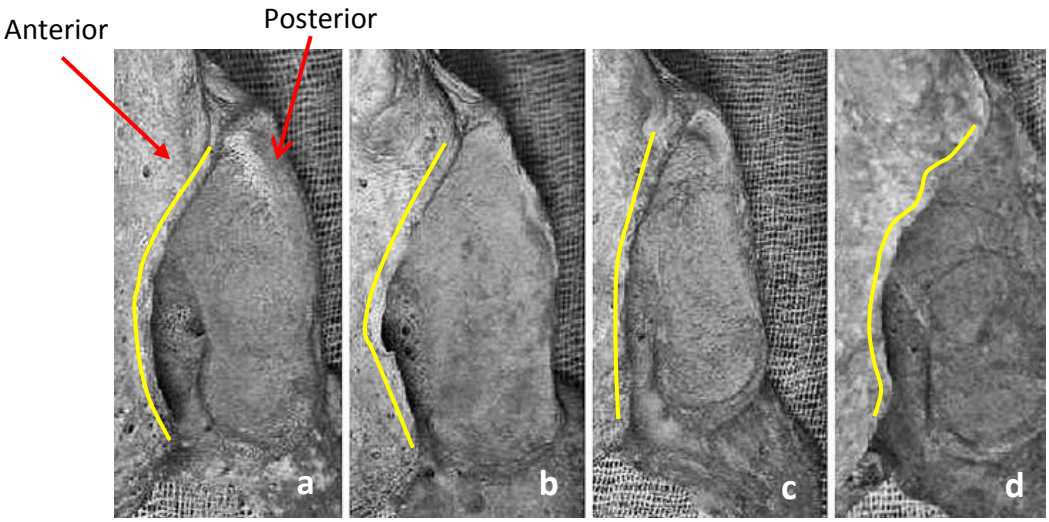

Figure 1.5: Cadaveric acetabula illustrating the anterior rim profile descriptions used in the literature: (a) curved, (b) angular, (c) straight and (d) irregular (Govsa *et al.*, 2005).

Govsa *et al.* (2005) reported a similar distribution of anterior rim profiles in their study of 113 normal skeletal pelves (n = 226 acetabula): 43.36 % curved, 28.33 % angular, 16.47 % irregular, 11.94 % straight. The researchers in both studies concluded that these results are clinically significant, particularly with reference to positioning the acetabular cup relative to anteversion during THR.

The CT-based study by Vandenbussche *et al.* (2008) discussed above used digitised acetabular rim coordinates to investigate the shape of the posterosuperior depression and the anterior acetabular depression, which the researchers referred to as the psoas valley. They described the rim as being a succession of three peaks (prominences) and three troughs, with the troughs being said to correspond with the points of fusion of the ilium, ischium and pubis (Figure 1.1). The rim configurations were reported to have the following distribution of shapes; posteriorly: 57 % curved, 28 % irregular, 15 % straight, and anteriorly: 79 % curved, 11 % angular, 10 % irregular, 0 % straight. This study also measured the depth of the psoas valley and reported the average as 5 mm (range 2 mm to 10 mm), concluding that the depth is proportional to the diameter of the acetabulum. These results mirror those of an earlier study by Vandenbussche *et al.*

(2007) where digitised measurements were taken from cadaveric specimens in order to investigate the acetabular rim. In this study they reported a significantly deeper anterior (or psoas) depression in males (4.7 mm) than in females (3.2 mm) ($p < 0.01$). The data was not normalised to the diameter, however, the presence of possible gender-related differences was investigated using regression analysis, and a weak correlation between diameter and the psoas depression ($R = 0.26$, $p > 0.01$) was reported. The study by Kohnlein *et al*. (2009), also discussed above, supports the findings of both of these studies in that they described the rim profile as being asymmetrical with the anterior depression never being straight. In contrast to the two Vandenbussche studies however, they described the rim as being a succession of three prominences but only two depressions.

The heterogeneity of the studies could provide a possible explanation for the inconsistent findings in the above studies regarding the description and distribution of shapes, particularly of the anterior acetabular rim. These studies do however agree that the profile of the rim is asymmetrical and that the shape differs between individuals. It should also be noted that the measurement of acetabular anteversion could be affected by the point on the anterior rim from which the reading is taken, which could affect acetabular cup placement during THR.

1.3.3 Acetabular Orientation

Orientation is normally described in terms of its anatomical version and inclination (or abduction), and a normal acetabulum is described as being anteverted (Kim *et al.*, 2006a). The anterior pelvic plane (APP) (Figure 1.6) is frequently used as a reference point when measuring the orientation of the acetabulum, however inconsistent positioning of the subject can cause measurement inaccuracies. An example of this is the presence of either anterior or posterior pelvic tilt, which is defined as the rotation around the horizontal axis of the pelvis (Zhu *et al.*, 2010).

Murray (1993) defined anatomical anteversion and inclination (Figure 1.7) using the transverse plane. These definitions are commonly used when measuring the orientation of the natural acetabulum however, operative and radiographic definitions, using the sagittal and anterior pelvic planes respectively, have also been defined. These definitions are normally used for measuring the orientation of acetabular prostheses intra- and postoperatively.

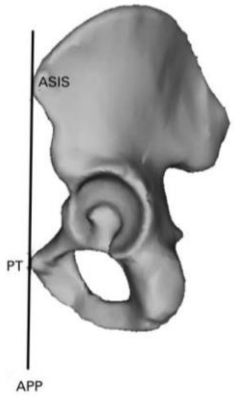

Figure 1.6: Hemi-pelvis indicating the left-hand side landmarks for the anterior pelvic plane (APP), which is defined by four anatomical landmarks on the pelvis. The left and right anterior superior iliac spines (ASIS) and the left and right pubic tubercles (PT) (Murtha *et al.*, 2008).

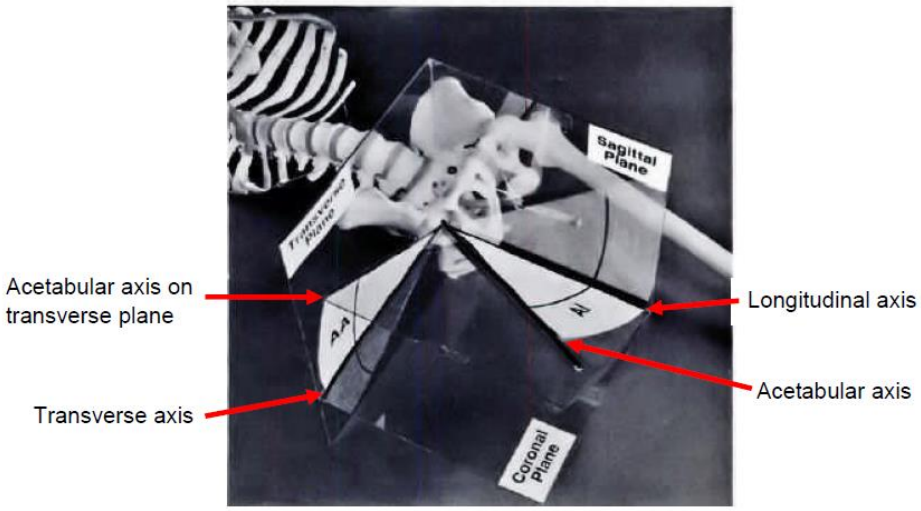

Figure 1.7: Anatomical Anteversion (AA) – angle between the transverse axis and the acetabular axis (when it is projected onto the transverse plane). Anatomical Inclination (AI) – the angle between the acetabular and longitudinal axes (Murray, 1993).

A considerable amount of literature has been published on the orientation of the acetabulum and some of these will be discussed in this section. In order to make it easier to compare the results, the mean anatomical inclination and/or anteversion angles (± SD where available) for each of these studies has been summarised in Table 1.2. Measurements generated using computational methods from two or three-dimensional CT images should be considered as being less subjective than skeletal measurements taken from reconstructed pelves using manual measurement techniques such as goniometry. There is also a risk of measurement error from studies

using skeletal models if the bones are not positioned accurately during the pelvic reconstruction.

Studies conducted by Stem *et al*. (2006), Vandenbussche *et al.* (2007) and Kohnlein *et al.* (2009) reported statistically significantly larger degrees of anteversion in female subjects compared to males ($p = 0.01$, $p < 0.01$, and $p = 0.013$ respectively for the three studies). In addition, slightly larger degrees of inclination that were not significantly different were also reported. Stem *et al*. (2006) measured these angles on topographic images derived from CT scans (n = 200 acetabula), with each measurement being repeated three times by the same observer to increase the reliability of the results.

Table 1.2: Summary of mean anteversion and inclination values ± SD (where available) for males (M), females (F) and both sexes (B), reported in the literature presented in this section. All values are in degrees and n = study group size.

Study	n	Anteversion (°) ± SD			Inclination (°) ± SD			Method
		M	F	B	M	F	B	
Bargar (2010)	46			15.1 ± 6.7			N/A	CT
Kohnlein (2009)	58	16.9 ± 4.8	21.0 ± 6.7	18.3 ± 5.5	48.1 ± 4.4	49.8 ± 4.1	48.9 ± 4.1	Skeletal
Krebs (2009)	100			20.7			39.8	Skeletal
Maruyama (2001)	100	21.3 ± 7.1	18.5 ± 5.8	19.9 ± 6.6	37.8	38.9	38.3	Skeletal
Murtha (2008)	42	19.3 3.4	24.1 10.3	21.7 6.8	55.5 61.8	57.1 62.9	56.3 62.3	CT – Full CT - 2/3
Stem (2006)	100	22.0 ± 6.0	24.0 ± 5.0	23.0 ± 5.0	38.0 ± 4.5	39.5 ± 4.0	39.0 ± 4.0	CT
Vandenbussch (2007)	34	15.7 ± 8.8	24.1 ± 7.8	19.9 ± 9.1	41.0 ± 4.8	40.5 ± 4.3	40.7 ± 4.4	Skeletal

Kohnlein *et al.* (2009) used goniometry to measure the angle between the parasagittal plane and a chord, which was fitted along the anterior and posterior acetabular rim, on 42 male and 16 female skeletal specimens. Again all measurements were taken by one observer but it has to be noted that the group sizes were very unequal, which could affect the validity of the results. Vandenbussche *et al.* (2007) calculated the orientation of 68 acetabula using a plane that had been fitted to 60-70 digitised points around the acetabular rim. Interestingly this was the only study included in this review that

reported slightly larger angles of inclination in male subjects, however, the researchers have acknowledged that fitting a plane to the irregular-shaped acetabular rim could have been a source of error. The study by Maruyama *et al.* (2001) is largely in agreement with these two studies but they also reported the mean angle of inclination as being significantly higher in their female skeletal specimens. The degree of significance however was marginal ($p = 0.038$) and as with Vandenbussche *et al.* (2007), the researchers have identified that variations in acetabular rim topography could be a possible source of error in their measurements. Krebs *et al.* (2009) used a similar technique to that of Maruyama *et al.* (2001) for preparing the skeletal specimens, which involved assembling the pelves from skeletal bones using rubber bands. It is possible that using this technique introduced a degree of design bias and could potentially reduce the reliability of these results.

As stated in the previous section, Murtha *et al.* (2008) used data from CT scans to investigate acetabular anatomy, which was done through the use of 3D surface models. Version and inclination was measured, relative to the APP, using planes that were fitted to the acetabular rim in two ways. Digitised points around the whole rim where initially used and these results were then compared to data collected by only picking points on the superior and posterior portions of the rim. The researchers reported a relatively small difference in inclination angle but a larger difference in version angle when comparing the two measurement methods (Table 1.2: CT – Full, CT – 2/3). The researchers concluded that the fitting of a plane, and consequently any morphological values calculated using this method, is greatly affected by the choice of points around the acetabular rim due to the irregular profile created by the fusion of the three pelvic bones.

A more recent study by Bargar *et al.* (2010) reported a mean value for acetabular anteversion of $15.1 \pm 6.7°$ (SD) which, other than the study by Murtha *et al.* (2008) discussed in the previous paragraph, is a lower value than that of the other studies included in this review. The study group consisted of subjects who were undergoing THR for hip OA, and a small number of subjects with known abnormal hip morphology such as mild dysplasia, traumatic arthritis, ankylosing spondylitis and avascular necrosis were also included. This may be a spurious result and could be explained in part by the heterogeneous aetiology of the subjects, as those with a history of trauma or surgery,

and subjects with abnormal hip morphology were excluded from the other studies included in this review.

Tönnis and Heinecke (1999) implemented a grading system for acetabula with reduced and increased anteversion (Table 1.3), which was based on the assumption that the normal orientation is 15° to 20° of anteversion.

Table 1.3: Grading system for acetabular version (Tonnis and Heinecke, 1999).

Grade	Range (degrees)	Description of Version
-3	< 10	Severely decreased
-2	10 – 14	Moderately decreased
1	15 – 20	Assumed normal range
+2	21 – 25	Moderately increased
+3	> 25	Severely increased

Hips with decreased anteversion are often described as being retroverted, and the cross-over sign (i.e. the anterior wall of the superior aspect of the acetabulum projects lateral to the posterior wall of the superior aspect of the acetabulum), is normally present on plain radiographs (Dandachli *et al.*, 2009). Acetabular retroversion has been associated with the development of hip OA and its aetiology can be idiopathic due to a congenital deformity or premature closure of the triradiate cartilage. It can however also exist alongside other conditions such as acetabular dysplasia, slipped capital femoral epiphysis or a deep acetabulum (Giori *et al.*, 2003; Ezoe *et al.*, 2006; Kim *et al.*, 2006a).

Research findings with respect to acetabular orientation are inconsistent (Table 1.2) and it has been noted that a wide range of skeletal and radiographic methods have been used to measure acetabular orientation, which could account for the poor homogeneity of the results. In recent years, researchers have fitted planes to the bony aspects of the acetabulum in an attempt to make morphological measurements, particularly orientation, more accurate. The methodology used to do this also varies considerably but despite these discrepancies, most of the above studies agree that the female acetabulum is more inclined and anteverted than that of the male, with the gender difference in anteversion being reported as significantly different in most cases.

1.4 The Proximal Femur

The proximal end of the femur (Figure 1.8) comprises of the femoral head, femoral neck, and greater and lesser trochanters, which are connected by the intertrochanteric line anteriorly and intertrochanteric crest posteriorly. The head, with the exception of the fovea capitis, is covered with articular cartilage. The fovea capitis, which is described as an ovoid depression, is located slightly inferiorly to the most medial point of the femoral head, and is the point of attachment for the ligamentum teres (or head of femur ligament, (Figure 1.2), which extends between the head and the acetabula fossa (Figure 1.3). The neck connects the head to the shaft of femur and varies in length, but in general is reported to be ~50 mm long (Gray, 2000). It has also been reported that the femoral neck is slightly shorter in women (Traina *et al.*, 2009).

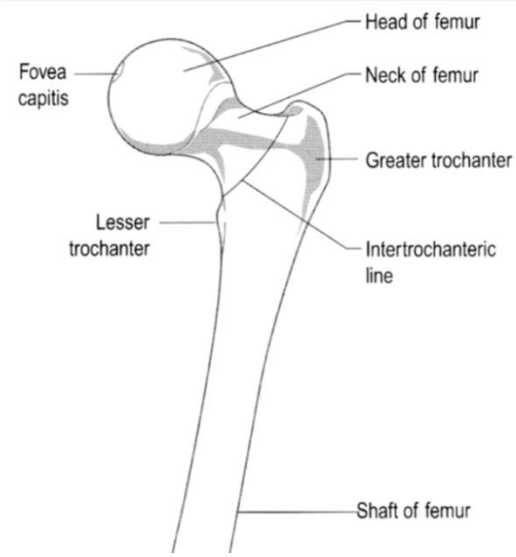

Figure 1.8: Schematic diagram of the proximal femur, anterior view (Palastanga *et al.*, 2002).

The trochanters are bony prominences to which muscles, mainly those that rotate the hip, attach to, providing them with some leverage. The greater trochanter is a large prominence and generally quadrilateral in shape, and the lesser trochanter is described as having a more conical morphology with greater variability in size than the greater trochanter (Gray, 2000).

The head and neck make two angulations, the femoral neck shaft angle (FNSA), which is the angle formed between an axis going through the head and neck and an axis through the femoral shaft, and the angle of torsion. The FNSA is in the frontal plane, with a mean angle of ~125° in an adult. The angle of torsion, or anteversion angle, occurs in

the transverse plane and is the angle between an axis through the femoral head and neck, and an axis through the femoral condyles on the distal aspect of the femur. The mean range of this angle is reported to be 10° to 15° (Levangie and Norkin, 2001). A pathological decrease in FNSA (< 120°) is described as coxa vara and a pathological increase in FNSA (> 135°) is called coxa valga (Palastanga *et al.*, 2002).

The FNSA was measured on radiographs taken from n = 70 normal cadaveric femora and n = 120 normal clinical radiographs by Clark *et al.* (1987), who reported FNSA angles in the range of ∼109° to ∼144° (mean 123 ± 6.8° SD) for the cadaveric femora and ∼109° to ∼155° (mean 128.7 ± 7.2° SD) for the clinical radiographs. The wide range of values could be related to the heterogeneous sample group, which had an age range of 42-94 years (cadaveric) and 15-87 years (clinical), as FNSA is known to reduce from childhood to adulthood, and reduce further in older adults (Palastanga *et al.*, 2002). A study by Wright *et al.* (2011) used CT scans and an established anatomical landmark-based method to measure FNSA in two dimensions (2D) and 3D on a smaller group of participants (n = 28, mean age 69 years). They reported no differences between male and female FNSA measurements, however, they reported a significant difference ($p < 0.001$) in the 2D and 3D results, which were 107.9° and 140.0° respectively. The authors reported that small differences in surface geometry when using 2D compared to 3D anatomical landmarks can cause the variations in geometric measurements observed in this study, which could have important clinical implications when measuring this parameter from either a 2D image or a 3D surface model. This could also be an important finding to consider when comparing the results from different studies. The findings of a study of FNSA by Unnanuntana *et al.* (2010) using digital images of femora taken from a human osteologic collection (n = 200, ≤ 40 years old at the time of death), also found no significant differences between males and females, and their reported mean measurement was 132.69 ± 5.91° (SD).

1.5 Radiography of the Hip Joint

Radiography is frequently used for orthopaedic investigations including the diagnosis, treatment planning, and monitoring of diseases such as OA, with different modalities being utilised depending on the clinical application required (Grenier and Wessely, 2006). Plain film radiography, normally anteroposterior (AP) radiographs, are routinely used for basic orthopaedic investigations to highlight bone morphology and pathology,

as well as the cartilaginous aspects of the hip joint by measuring joint space (Karachalios *et al.*, 2007). This modality is also routinely used in the clinical setting as a postoperative assessment tool following procedures such as THR and joint preserving surgery (Kim *et al.*, 2006b; Beckmann *et al.*, 2009).

Magnetic resonance imaging (MRI) is regarded as an excellent diagnostic imaging tool for investigating musculoskeletal pathology because when compared to CT, it provides better contrast and visualisation of the soft tissues, and can produce multidimensional images in any plane (Watanabe *et al.*, 2007; Mamisch *et al.*, 2009). MRI can also be used in conjunction with an intra-articular contrast medium to provide a more detailed image of the intra-capsular structures such as the acetabular labrum and articular cartilage (Hong *et al.*, 2008). MR images are produced by applying a powerful external magnetic field to the area to be scanned whilst simultaneously subjecting the area to a sequence of radiofrequency pulses, which causes a temporary misalignment of the hydrogen atoms as they absorb the energy. The hydrogen atoms realign when the signal stops and a small amount of energy (in the form of a magnetic resonance signals) is emitted and detected by a receiver coil before being directed to the scanners computer to produce a 3D image. The unit of measurement for the strength of the magnet is the Tesla (T), and stronger magnets produce a higher quality and more detailed image (McKie and Brittenden, 2005). A 1.5 T scanner is generally regarded as being acceptable for clinical orthopaedic work, however, the introduction of higher resolution 3.0 T scanners has enabled reproducible morphological measurements of cartilage morphology to be undertaken as well as accurate, reproducible assessments of the labrum, cartilage and synovial fluid, all without the use of contrast agents (Eckstein *et al.*, 2008; Potter and Schachar, 2010).

Exact positioning of a subject during radiographic examinations can be very difficult and variations such as differences in pelvic positioning, or taking radiographs in a weight bearing or non-weight bearing position, can lead to inaccuracies when interpreting the images. This is particularly evident when measurements such as acetabular orientation or other radiographic parameters of the hip and pelvis are being calculated (Tannast *et al.*, 2005; Fuchs-Winkelmann *et al.*, 2008), and this can be a source of error in both the clinical and research environment.

1.6 Tribology of the Natural Hip Joint

1.6.1 Articular Cartilage

Articular or hyaline cartilage is a thin layer of deformable connective tissue covering the ends of diarthrodial joints. Its primary functions are to deform and distribute loads, therefore decreasing joint stresses, and to allow movement with minimal friction by contributing to joint lubrication (Setton *et al.*, 1999). Articular cartilage comprises of the extra cellular matrix (ECM) (95 %) and specialised cells called chondrocytes (5 %). The ECM contains water (65-85 %), collagen (mainly Type II) (10-20 %), which gives the cartilage its tensile strength, and proteoglycans (10-20 %). Proteoglycans (PG) maintain fluid and electrolyte balance, and they are negatively charged protein polysaccharide molecules consisting of a protein core with one or more glycosaminoglycan (GAG) molecule chains attached to them. The ECM also contains small amounts of enzymes, which are required for cartilage metabolism. Chondrocytes control the balance of the ECM by producing and maintaining the PG, collagen and enzymes. Articular cartilage is avascular, aneural and alymphatic therefore it receives its nutrition is via diffusion from the synovial fluid, relying primarily on anaerobic metabolism to do this (Bhosale and Richardson, 2008; Getgood *et al.*, 2009).

Morphologically, articular cartilage is arranged into zones (Figure 1.9). Densely packed collagen fibres, which are orientated parallel to the articular surface in the superficial zone, protect the deeper layers from shear stresses. The middle zone contains large amounts of PG and this region provides the initial resistance to compressive forces, partly due the negatively charged PGs repelling each other. The deep zone provides the greatest amount of resistance to compressive forces due to it containing the largest concentration of PG and lowest water content, and its large diameter collagen fibres are arranged perpendicular to the articular surface. The tidemark is the transition layer between the deep zone and the calcified cartilage. Collagen fibres within the deep layer are attached vertically into the tidemark, and the calcified layer is considered to play an essential role in securing the cartilage to the subchondral bone. The calcified cartilage layer contains Type X collagen fibres, which provide structural integrity to the cartilage (Neville *et al.*, 2007; Fox *et al.*, 2009).

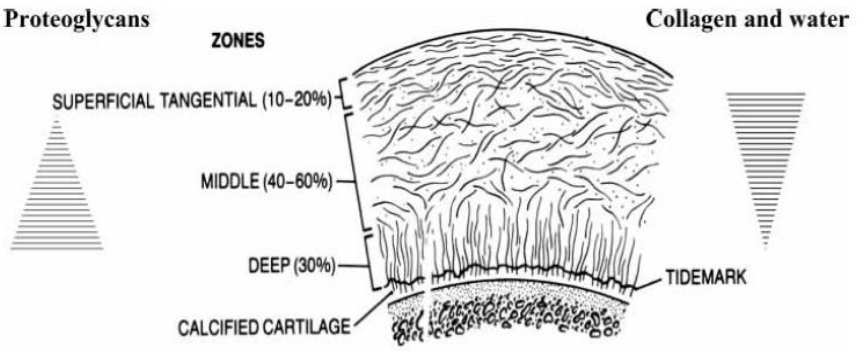

Figure 1.9: Schematic diagram of articular cartilage showing the approximate percentage of cartilage volume (in brackets) and structural variations of the zones (Neville *et al.*, 2007).

1.6.2 Synovial Fluid

The articular surfaces and inner surface of the hip joint capsule are covered with a film of synovial fluid, which is a clear, or sometimes slightly yellowish viscous liquid. The fluid, which is secreted into the joint cavity in order to maintain nourishment, lubrication and reduce friction, has a similar composition to that of blood plasma but contains hyaluronate (an extended GAG chain), and lubricin (a glycoprotein that contributes to boundary lubrication) (Ludwig *et al.*, 2012). Synovial fluid also contains hyaluronic acid, which is a macromolecule that gives the synovial fluid its viscoelastic properties (Swann *et al.*, 1974). The fluid exhibits non-Newtonian, or thixotropic properties, as the viscosity of the fluid exhibits a shear thinning effect when the joint is moving quickly (Mow and Huiskes, 2005; Neville *et al.*, 2007).

1.6.3 Lubrication

The presence of a lubricant affects the wear, friction and interfacial temperature of the samples due to its interaction between the two contacting surfaces. A number of factors, such as the load, sliding speed, lubricant properties (e.g. viscoelasticity), material properties, geometry and surface roughness of the bearings can affect the mode of lubrication. A number of different lubrication theories exist, which are described briefly in the following section, with theoretical tribological theory and equations presented in Section 1.6.4.

1.6.3.1 Boundary Lubrication

If the fluid film thickness becomes smaller than the average surface roughness then contact can occur between the two surfaces. In synovial joints it is suggested that large molecules in the synovial fluid, which are absorbed by the cartilage (e.g. lubricin), help prevent direct contact between the two surfaces, therefore reducing surface wear (Katta *et al.*, 2008).

1.6.3.2 Fluid Film Lubrication

Complete separation of the two articulating/bearing surfaces enables a fluid film lubrication regime to operate, which can be hydro or elastic-hydrodynamic, squeeze film, boosted, or weeping (Levangie and Norkin, 2001). A schematic diagram of the four main fluid film lubricating regimes is shown in Figure 1.10.

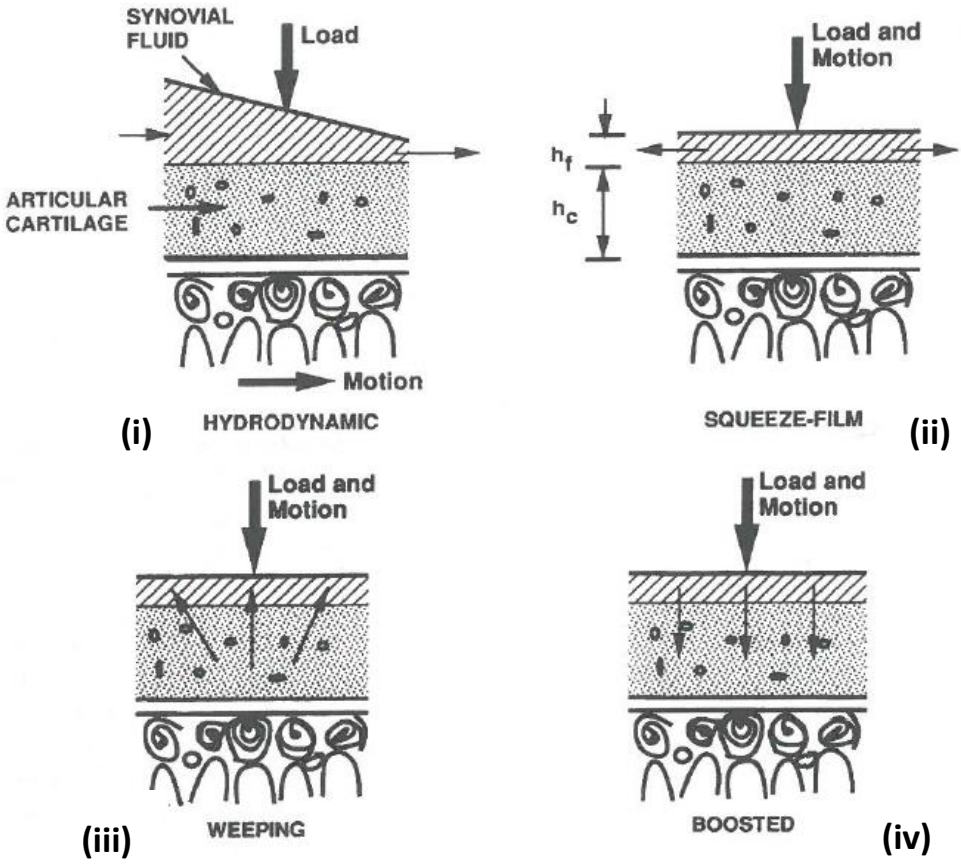

Figure 1.10: Schematic diagrams of fluid film lubricating regimes where the small arrows represent the direction of fluid flow. Subchondral bone is schematically represented beneath the articular cartilage layer. (i) hydrodynamic lubrication, (ii) squeeze film lubrication (where hf = height of fluid film and hc = cartilage height), (iii) weeping lubrication and (iv) boosted lubrication.

In **hydrodynamic lubrication** (Figure 1.10 i), non-parallel opposing surfaces slide over each other which, providing the fluid is viscous enough, creates a wedge of fluid that lifts the two surfaces. Elastic-hydrodynamic lubrication is similar to hydrodynamic lubrication, however the fluid film thickness is maintained by the elastic deformation of the two surfaces (Mow and Huiskes, 2005). In **squeeze film lubrication** (Figure 1.10 ii), movement of the surfaces towards each other, usually quickly, creates an internal pressure in the fluid film as the lubricant becomes trapped between the deforming surfaces. This causes the fluid to flow out of the gap tangentially (Higginson, 1978). **Weeping lubrication** (Figure 1.10 iii), or self-pressurised hydrostatic lubrication, occurs when the fluid film is maintained between the two surfaces by pressurised fluid being expelled from the cartilage matrix when loaded. **Boosted lubrication** (Figure 1.10 iv) occurs when the load forces small molecules (e.g. water) out of the joint leaving a more viscous fluid with a greater concentration of hyaluronate (Macirowski *et al.*, 1994).

1.6.3.3 Biphasic Lubrication

Biphasic lubrication was based on the theory that cartilage is made up of immiscible and incompressible fluid and solid phases. Under load, the fluid flow in the solid matrix is restricted by the permeability of the tissue causing pressurisation. This interstitial fluid pressure is then able to support some of the load, therefore producing a low friction environment (Ateshian and Wang, 1995).

1.6.3.4 Mixed Lubrication

Mixed lubrication occurs when a combination of boundary and fluid film lubricating regimes exist, and the load is distributed between the fluid film and the absorbed layer of fluid film lubrication. Higher friction and wear than fluid film lubrication, and lower friction and wear than boundary lubrication is normally observed with this lubricating regime (Nordin and Frankel, 2012).

1.6.4 Lubrication Theory

The hip joint *in vivo* is subjected to variable velocity and loading conditions, with the natural hip also undergoing elastic deformation of the cartilage surfaces. In contrast to this, the *in vitro* simulations reported throughout this thesis were conducted using pendulum friction simulators that applied known cyclic loads and angular displacements to the samples, aiding the theoretical analysis of predicted lubricating

regimes. A theoretical prediction of the lubricating regime can be determined by calculating the minimum lubrication film thickness (h_{min}) and lambda ratio (λ) using Equations 1.1 to 1.6 (Hamrock and Dowson, 1978; Jin *et al.*, 1997).

The lambda ratio is a dimensionless parameter of the ratio of film thickness to the combined average surface roughness (R_{ac}) of the two bearing surfaces (R_{a1}; femoral head and R_{a2}; acetabular cup), which is calculated using Equation 1.1.

$$R_{ac} = \sqrt{{R_{a1}}^2 + {R_{a2}}^2} \qquad \textbf{Equation 1.1}$$

The equivalent radius of the bearing (R) is calculated using Equation 1.2, where R_1 is the radius of the head and R_2 is the radius of the cup:

$$R = \frac{R_1 R_2}{R_2 - R_1} \qquad \textbf{Equation 1.2}$$

and E', which is the equivalent Young's Modulus (or material stiffness), is calculated using Equation 1.3, where E_1 and E_2 are the Young's Moduli for the femoral (E_1) and (E_2) acetabular bearing surfaces, with ν_1 and ν_2 being their respective Poisson's Ratios:

$$E' = \frac{2}{\left(\frac{1-{\nu_1}^2}{E_1} + \frac{1-{\nu_2}^2}{E_2}\right)} \qquad \textbf{Equation 1.3}$$

The entraining velocity (u) is calculated from the angular velocity (ω) of the femoral head using Equation 1.4:

$$u = \frac{\omega R_1}{2} \qquad \textbf{Equation 1.4}$$

The minimum lubricating film thickness is then calculated using the Hamrock and Dowson equation (Equation 1.5), where η is the viscosity of the lubricant and *W* is the load:

$$h_{min} = 2.8\,R\left(\frac{\eta u}{E'R}\right)^{0.65} \times \left(\frac{W}{E'R^2}\right)^{-0.21} \qquad \textbf{Equation 1.5}$$

The minimum film thickness and Equation 1.6 is used to calculate the lambda ratio (λ):

$$\lambda = \frac{h_{min}}{R_{ac}} \qquad \textbf{Equation 1.6}$$

A Stribeck curve (Figure 1.11), which gives the relationship between friction and fluid film thickness can then be used to interpret the lambda ratio values for hemispherical bearings such as total hip replacements, where values < 1 indicate boundary lubrication, values > 1 but < 3 indicate a mixed lubrication mode, and a value > 3 suggests the presence of a fluid film lubrication regime (Stewart, 2010).

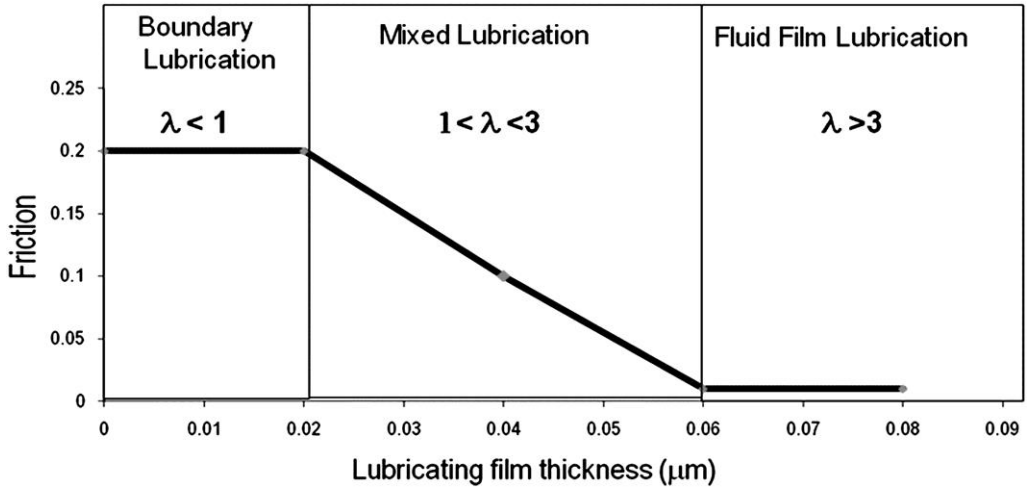

Figure 1.11: Stribeck curve illustrating the relationship between lubricating film thickness and friction (Stewart, 2010).

1.6.5 Wear of Articular Cartilage

Wear causes degradation and progressive loss of substance from the bearing surface. Two types of mechanical wear have been described, interfacial wear and fatigue wear. Biochemical degradation has also been reported, however, this wear mechanism is currently less well understood and reported. Interfacial wear can be further divided into adhesion and abrasion. Abrasive wear occurs when a soft surface is damaged by a harder surface (e.g. in hemiarthroplasty), or by a loose body between the joint surfaces. Adhesive wear occurs when two asperities from opposing surfaces adhere to each other. Fatigue wear arises from microscopic damage of the bearing surfaces due to repetitive stresses, and is not related to contact between the two bearing surfaces. This can may occur from the application of high loads over a short period of time or low loads over a longer period of time. Two mechanisms exist for fatigue wear, the first being cumulative damage due to disruption of the collagen-proteoglycan solid matrix through repetitive straining. The second mechanism is degradation and loss of proteoglycan with eventual “washout” of the PG from the matrix into the joint cavity.

Articular cartilage is avascular, which is a contributing factor to the progression of degenerative joint diseases such as OA (Mow and Huiskes, 2005; Nordin and Frankel, 2012).

1.7 Osteoarthritis of the Hip Joint

Osteoarthritis (OA) causes pathological degenerative changes that affect the whole joint including the bone, cartilage, ligaments, tendons, synovium/synovial fluid, and joint capsule (Nuki, 1999). Clinically these changes can result in loss of function due to symptoms such as pain, decreased range of movement, instability, crepitus and stiffness following a period of inactivity (Bijlsma and Knahr, 2007; Felson, 2009). Radiographic findings can include joint space narrowing (JSN), subchondral sclerosis, subchondral cyst formation, and the formation of osteophytes (Karachalios *et al.*, 2007). The underlying pathological processes behind these findings are both destructive and productive (i.e. osteophyte formation), and a combination of these processes will result in either a progressive or a non-progressive disease, the latter of which can sometimes be asymptomatic. Secondary inflammatory processes in OA also contribute to the destructive changes within the joint (Hutton, 1989). Many people over the age of 65 who are asymptomatic have been found to have radiological evidence of hip OA (Cobb *et al.*, 1957; Lanyon *et al.*, 2003; Lane *et al.*, 2004), and conversely some individuals with clinical symptoms such as joint pain display no evidence of degenerative changes on x-ray (Bijlsma and Knahr, 2007).

OA has traditionally been classified as either idiopathic (i.e. primary), where the cause is unknown, or secondary where the cause is known. Examples of possible aetiologies pertaining to secondary OA of the hip are described in Table 1.4. Over the last few years, the existence of a purely idiopathic aetiology has been questioned and it is now generally accepted that the cause or origin of hip OA is multifactoral (Solomon, 1976; Ganz *et al.*, 2008). In addition to being classified as idiopathic or secondary, OA of the hip can be further defined according to the type of bone response. Individuals that have the tendency to develop large osteophytes are regarded as having hypertrophic OA (Felson *et al.*, 2000a), and those with no or very few osteophytes are described as having atrophic OA (Lane *et al.*, 2004).

Table 1.4: Possible aetiologies of secondary osteoarthritis of the hip (Nuki, 2005; Arden and Nevitt, 2006; Karachalios *et al.*, 2007; Leunig *et al.*, 2009b).

Subgroup	Examples
Trauma	Major joint trauma or chronic injury Fracture (especially through the joint) Labral tear/pathology Avascular necrosis (can also have insidious onset) Joint surgery
Congenital/Developmental	Acetabular dysplasia Congenital dislocation of the hip Slipped capital femoral epiphysis Femoroacetabular impingement Legg-Calve-Perthes disease Protrusio acetabuli Hypermobility syndrome
Inflammatory	Septic arthritis
Miscellaneous	Paget's disease Genetic factors Acromegaly Haemochromatosis Calcium crystals deposition

The choice of intervention depends on the severity of the symptoms but this can include conservative treatments such as pharmacological therapy, walking aids and physiotherapeutic modalities (e.g. heat, joint specific exercises, electrotherapy etc.), or more invasive techniques such as soft-tissue repair, osteotomy, arthrodesis and ultimately joint arthroplasty (Felson *et al.*, 2000b; Bijlsma and Knahr, 2007).

1.7.1 Diagnosis of Hip Osteoarthritis

A diagnosis of hip OA may be based solely on clinical assessment and patient history (i.e. pain, stiffness and loss of function), but these findings are normally combined with the results of radiographic investigations before making a firm diagnosis (Lane, 2007). Symptoms include a history of pain with an insidious onset made worse by certain movements and/or weight bearing, and stiffness on waking or after periods of inactivity. In more advanced hip OA, patients may also complain of difficulty bending, making it hard to put on shoes and socks, get in and out of a car, or stand from a low

chair. Clinically patients may present with an antalgic gait, reduced hip flexion and internal rotation, and/or shortening of the affected leg. There may also be evidence of weakness with possible wasting of the gluteal and/or quadriceps muscles (Doherty *et al.*, 2005). The presence of osteophytes, cysts, sclerosis and JSN on plain radiographs is generally used to diagnose and monitor the progression of hip OA, and the severity of the disease can be assessed using various radiographic grading systems (Karachalios *et al.*, 2007).

Grading systems based upon radiographic findings are frequently used to evaluate the severity of hip OA in both clinical practice and research. Reijman *et al.* (2004) compared the reliability and validity of the Kellgren and Lawrence (K/L), and Croft grading systems, concluding that the Kellgren and Lawrence system demonstrated substantial inter-rater reliability and showed comparable associations with clinical symptoms. Croft's grading system however had only moderate inter-rater reliability and demonstrated weak associations with clinical symptoms. The Tönnis grading system is also sometimes used to assess the presence or severity of hip OA (Bardakos and Villar, 2009).

A minimal joint space of ≤ 2.5 mm is often used to define hip OA (Nevitt, 1996), however, in a study of 1,806 subjects undergoing intravenous urography, Lanyon *et al.* (2003) found that hip joint space was on average 0.3 mm smaller in females than in males. This caused them to question the validity of this definition but they agreed that the measurement of JSN is a reliable and reproducible indicator of hip OA, and that the definition could be modified to accommodate these possible gender differences. These findings were corroborated in a radiographic study by Lequesne *et al.* (2004), who examined joint space variations amongst 127 women and 96 men. They also concluded that women had a significantly smaller joint space compared to men (range $p = 0.02$ to $p = 0.001$), with the mean difference being 0.35 mm. The degree of significance and difference in measurements were dependent on location as they reported large inter-individual variability, but a narrower joint space on the superomedial aspect of the hip and a wider joint space on the superolateral region were consistently present in the majority of subjects (75.8 %). Radiographic examples of JSN, an acetabular osteophyte and an acetabular cyst are illustrated in Figure 1.12 a and Figure 1.12 b.

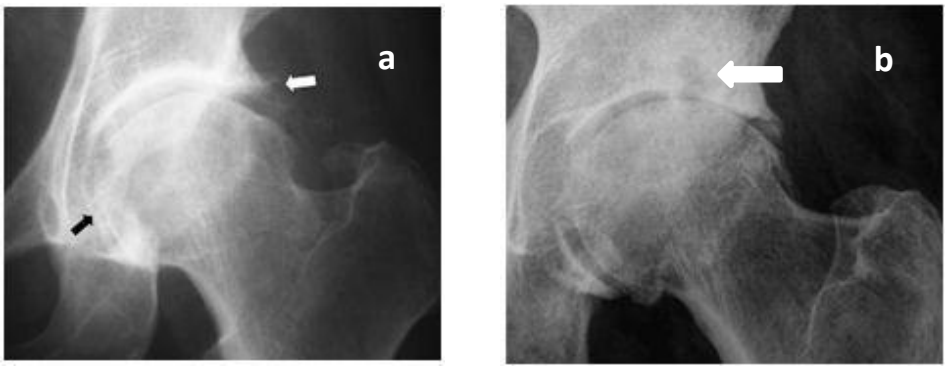

Figure 1.12: (a) A 62-year-old patient with medial OA demonstrated with joint space narrowing (black arrow) and osteophyte formation (white arrow) (Karachalios *et al.*, 2007). (b) Superior acetabular subchondral cyst (large white arrow) (Altman and Gold, 2007).

1.7.2 Pathophysiology of Osteoarthritis

Cartilage loss and/or wear on the articulating surfaces of the hip can arise from trauma or primary/secondary degenerative processes. A number of different mechanical and biological factors can contribute to cartilage degradation (some examples are shown in Table 1.4), by causing a defective cartilage matrix and ultimately, possible structural failure of the joint (Katta *et al.*, 2008). The development of OA appears to arise from an imbalance between the breakdown and synthesis of articular cartilage, and in an effort to repair the damage, there is an increase in cellular activity with large quantities of abnormal PG and collagen being produced, which leads to cell hypertrophy and thickening of the articular cartilage (Hutton, 1989). The abnormal cells break down faster than the new ones are synthesised causing a homeostatic imbalance, the net result of which is a loss of the ECM and damage to the chondrocytes in the superficial zone of the articular cartilage. Calcium crystal deposition within the joint and the release of cartilage-degrading enzymes and inflammatory mediators (i.e. cytokines) may exacerbate this process. Damage to the chondrocytes slows the production and maintenance of the cartilaginous matrix (i.e. collagen and PG), and this in turn leads to cartilage fibrillation (i.e. fine roughening of the surface), fissuring (small cracks), JSN, and erosion, with possible changes to the shape and/or congruity of the articulating surfaces (Getgood *et al.*, 2009). Once the articular cartilage has been sufficiently damaged, these pathological changes extend to the underlying subchondral bone resulting in eburnation and sclerosis. As the bone stiffens, hardens, and increases its bone mineral density, it then becomes susceptible to microfractures and areas of infarction (Karachalios *et al.*, 2007).

Cysts are often present in the bone beneath the load-bearing areas of articular cartilage defects (Figure 1.12 b), and these are formed when synovial fluid enters the cavities in the subchondral bone via the microfractures and/or small areas of necrosis in the cancellous bone (Milgram, 1983). In areas where the cartilage is still intact, patients with a hypertrophic bone response to OA will develop osteophytes as a result of endochondral ossification (Aspden, 2008). Osteophytes, which are cartilage covered bony spurs that develop along diarthrodial joint margins, are normally present on the superior or sometimes inferior aspects of the acetabulum (Figure 1.12 a), and they can also be found on the femoral head (Altman and Gold, 2007). Fibrosis and stiffening of the hip joint capsule has been reported in OA and it has been suggested that this may contribute to joint failure (Aspden, 2008). Sensorimotor dysfunction and muscle weakness have also been reported as possible contributing factors to the development of OA, however, the majority of studies reporting this investigated OA of the knee and therefore their role in the pathogenesis of hip OA is still unclear (Hurley, 2003; Aspden, 2008).

1.7.3 Aetiology and Risk Factors

As discussed earlier, a number of possible risk factors and causes of secondary hip OA have been identified and some of these, specifically those pertaining to abnormal hip/acetabular morphology, will be discussed in more detail in Section 1.8. Idiopathic OA is poorly understood and many researchers now agree that initial cartilage failure may not be the best explanation for the pathological changes that are observed in primary OA of the hip. It is now widely believed that this concept should be replaced with the idea that the aetiology of idiopathic hip OA is largely associated with subtle developmental abnormalities and subclinical hip deformity, which causes increased vulnerability of the joint to damage (Harris, 1986; Wedge *et al.*, 1991; Felson, 2004; Ecker *et al.*, 2007; Aspden, 2008).

Barros *et al.* (2010) reported statistically significantly higher alpha angles (i.e. the angle formed by the axis of the femoral neck and a line connecting the centre of the start of asphericity of the femoral head) ($p < 0.001$) in a group of 50 subjects with idiopathic OA (K/L grades 3 and 4), when compared to an age-matched group of subjects with no radiographic evidence of OA. Despite the relatively small group sizes, the researchers were able to conclude that subclinical abnormalities of the femoral head-neck junction

could be associated with an increased risk of developing hip OA. Lane *et al.* (2000) concluded that subclinical acetabular dysplasia is a risk factor associated with the development of idiopathic hip OA in their study of 176 white females of mean age 70.3 years. This was a prospective study with a follow-up period of eight years, after which 58 of the subjects showed radiographic evidence of hip OA. The subjects in this group had significantly shallower acetabula than the group of subjects that had no radiographic evidence of OA ($p < 0.05$).

Risk factors for idiopathic hip OA can be divided into two categories; systemic and local mechanical factors. Systemic risk factors that have been investigated include age, gender, race, nutrition, smoking, alcohol, genetic influence and sex hormones/bone mineral density. Mechanical factors include obesity, trauma, repetitive joint loading (i.e. during sport and leisure activities), and occupations that may require repetitive carrying of heavy loads (Juhakoski *et al.*, 2009). Some of the above that have been identified as potential risk factors for hip OA will be briefly discussed in the following two sections.

1.7.4 Systemic Risk Factors

Increasing age has been considered a risk factor for some time with one possible explanation for this being a lower regenerative capacity of the articular cartilage, together with reduced resilience to damage due to a decreased number of chondrocytes and thinning of the cartilage plate. Increased joint laxity due to muscle weakness and/or impaired proprioception has also been proposed as a possible reason for the association between age and increased articular cartilage damage (Arden and Nevitt, 2006; Anderson and Loeser, 2010). Unidentified genetic factors, increased bone mineral density and white ethnic origin have also been identified as possible risk factors, although the association between these variables and the risk of developing hip OA is complex and less well defined (Felson *et al.*, 2000a; Doherty *et al.*, 2005; Arden and Nevitt, 2006). A prospective longitudinal study by Vossinakis *et al.* (2008) of 95 subjects with unilateral hip OA demonstrated that those with idiopathic OA in one hip had a statistically significantly higher risk of developing OA in the contralateral hip ($p < 0.001$). In the absence of abnormal hip morphology, the researchers proposed systemic biological factors, such as a genetic predisposition for developing the disease, as a possible explanation for their findings.

1.7.5 Mechanical Risk Factors

There is conflicting evidence regarding links between obesity/high body mass index (BMI) and hip OA, with some studies concluding that it is a strong predictor and risk factor for hip OA and others concluding that it is not. Whilst many researchers believe that there may be a relationship between these two variables, most agree that it is considerably weaker than that for obesity and knee OA (Arden and Nevitt, 2006; Aspden, 2008; Juhakoski *et al.*, 2009). Felson *et al.* (2000a) has suggested that overloading of the hip with subsequent ligament failure or weakness and breakdown of articular cartilage could provide a possible explanation for any associations between obesity and hip OA.

Juhakoski *et al.* (2009) conducted a population-based study with a 22-year follow-up in Finland to identify risk factors that were independent predictors of developing hip OA. They concluded that subjects that had been exposed to heavy physical workloads (i.e. farmers), or major musculoskeletal injury affecting the hip joint, had an increased risk of developing clinically diagnosed OA of the hip. Reviews by Felson *et al.* (2000a), Arden and Nevitt (2006), and a report by Doherty *et al.* (2005), concur with the findings of Juhakoski *et al.* (2009) that farmers, or subjects whose occupation involves repetitive heavy lifting, have a high risk of developing hip OA. However, the association between hip OA and acute hip trauma appears to be less clear.

1.8 Hip Joint Pathology

As described in Table 1.4, a number of mechanical, developmental and congenital hip abnormalities have been associated with secondary OA of the hip, some of which will be discussed in more detail in this section. These abnormalities have been widely researched with a view to initiating early diagnosis and intervention in an attempt to restore normal anatomy, thus preventing or delaying onset, and/or halting or slowing down disease progression (Millis and Kim, 2002).

1.8.1 Acetabular Dysplasia

Hip dysplasia is an abnormality of the hip characterised by a shallow acetabulum resulting in reduced coverage of the femoral head and diminished congruency, occasionally with coexisting joint laxity. The most common cause of this is developmental dysplasia of the hip (DDH), occasionally referred to as congenital hip

dislocation, where the acetabulum fails to develop normally (Salter, 1968). The severity of hip dysplasia ranges from subclinical abnormalities that can go into adulthood undetected, to subluxation, instability or complete dislocation of the joint (Dezateux and Rosendahl, 2007). Schematic diagrams highlighting the different clinical presentations of hip dysplasia are shown in Figure 1.13. Patients with untreated dysplasia together with either subluxation or dislocation (Figure 1.13 C & D), will often present with either no recognisable acetabulum or a proximally created false, or pseudoacetabulum, neither of which are able to withstand prolonged use.

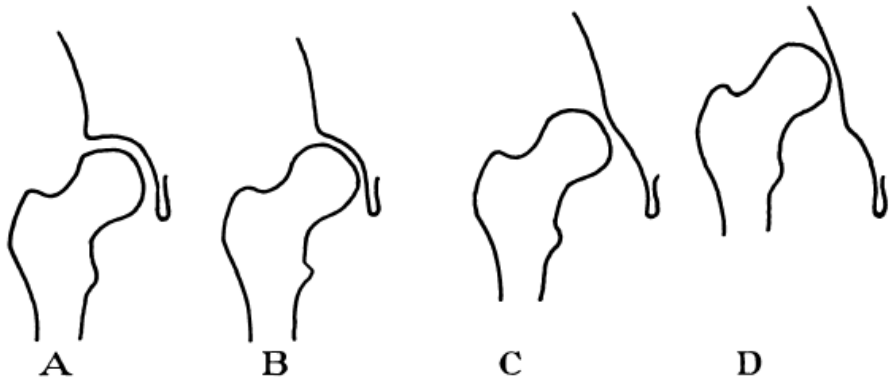

Figure 1.13: Acetabular Dysplasia. (A) Normal acetabulum, (B) Dysplastic acetabulum without subluxation, (C) Dysplastic acetabulum with subluxation, (D) Dislocation (Wiberg, 1953).

Marked limb shortening is often present and surgical treatment with THA remains challenging due to the absence of a properly formed acetabulum and/or its proximal location in the pelvis (Holroyd and Wedge, 2009). A number of radiographic parameters are used to help diagnose DDH, the most common ones being acetabular head index (AHI) < 75° (i.e. the portion of the femoral head covered by the acetabular roof divided by the width of the head expressed as a percentage), Sharp's (acetabular) angle (i.e. the angle between a line passing from the superior to the inferior acetabular rim and the horizontal plane) > 40° (Karachalios *et al.*, 2007), and an acetabular depth of < 9 mm (Yoshimura *et al.*, 1998; Lane *et al.*, 2000). Additionally, the centre-edge (CE) angle (i.e. the angle between a vertical line and a line from the centre of the femoral head to the most lateral part of the acetabulum) is frequently used to assess the severity of dysplasia both clinically and for research purposes. Wiberg (1953) defined a CE angle of > 25° as being normal, angles of between 25° and 20° as being borderline, and acetabula with an angle of < 20° as being pathologically dysplastic.

Developmental dysplasia of the hip appears to be more common in females than males (5:1) leading to suggestions of a hormonal aetiology, and in 20 % of cases the disease is bilateral. Ethnic variations have also been identified with higher rates of dysplasia being reported in American Indians (estimated at 1 in 20), and also in Turkish and Japanese populations (Lavy *et al.*, 2003; Dezateux and Rosendahl, 2007). Ethnicity should be taken into consideration when interpreting study results, as this could introduce as a sampling bias, however, it appears to be generally accepted that there is a higher incidence of hip dysplasia in oriental, especially Japanese, populations (Lau *et al.*, 1996; Lavy *et al.*, 2003).

Incongruous articulation of the femoral head on a deficient acetabular roof, thereby causing localised stress concentrations on a reduced load-bearing area, has been identified as a possible contributory factor to the development of secondary OA in dysplastic hips (Holroyd and Wedge, 2009). Jacobsen and Sonne-Holm (2005) investigated individual risk factors for the development of hip OA in a large longitudinal study of 2,232 women and 1,336 men. They reported a prevalence of hip dysplasia in 5.4 % of subjects (defined by a CE angle < 20°), and other than an age of > 60 years, dysplasia was reported to be the only other significant independent risk factor associated with the development of hip OA ($p < 0.001$). Studies by Murphy *et al.* (1995) and Jessel *et al.* (2009) also investigated dysplasia as a risk factor for developing hip OA, and both concluded that dysplastic hips with a CE angle of approximately 15° would eventually develop secondary OA of the hip. The mean coverage of the femoral head in 36 normal and 39 dysplastic hips was investigated by Dandachli *et al.* (2008) using a CT-based method of producing topographical imaging. They reported a coverage of 73 % in the normal hips compared to 51 % in the dysplastic hips, which was calculated as being significantly higher ($p < 0.001$). A retroverted acetabulum causing deficient coverage posteriorly in dysplastic hips was associated with an earlier onset of pain and OA in a study conducted by Fujii *et al.* (2010). The prevalence of retroversion in dysplastic hips, defined as being a deficiency of the posterior aspect of the acetabulum, has been reported as being slightly higher compared to non-dysplastic hips (Ezoe *et al.*, 2006; Dandachli *et al.*, 2008; Fujii *et al.*, 2010).

1.8.2 Femoroacetabular Impingement

Abnormal contact between the acetabular rim and the proximal femur, specifically the anterosuperior femoral head-neck junction, is referred to as femoroacetabular impingement (FAI). Two types of FAI have been described in the literature:

- Pincer-type impingement, which is more commonly observed in older or middle-aged females (Figure 1.14 B)
- Cam-type impingement, which is observed most frequently in young athletic males (Figure 1.14 C)

Although these two types of impingement can exist in isolation, it is also quite common to find a combination of the two (Figure 1.14 D) (Lavigne *et al.*, 2004).

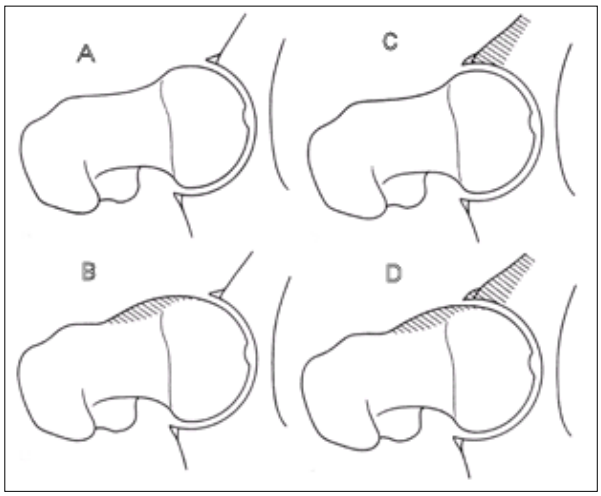

Figure 1.14: Femoroacetabular impingement disease patterns. (A) Normal clearance of the hip, (B) reduced femoral head and neck offset (cam impingement), (C) excessive over coverage of the femoral head by the acetabulum (pincer impingement), (D) combination of reduced head and neck offset and excessive anterior over coverage (combined impingement) (Lavigne *et al*., 2004).

Pincer impingement is characterised by lesions in the acetabular rim caused by the abutment of a relatively normal femoral neck against an acetabulum with abnormal morphology. A number of causes of the acetabular abnormalities have been identified (e.g. acetabular retroversion, coxa profunda, post-traumatic deformity), but the net result is either increased acetabular depth or over-coverage of the femoral head (Leunig *et al.*, 2009a). Another cause of pincer impingement is protrusio acetabuli, where deepening of the acetabulum causes abnormal protrusion of the femoral head

into the centre of the pelvis. This causes increased load transmission through the medial part of the joint and premature onset of secondary hip OA with medial, but initially no superior JSN (Leunig *et al.*, 2009b).

In pure cam FAI the morphology of the acetabulum is normal, and the impingement occurs when either a flattened or convex femoral head-neck junction (i.e. pistol-grip deformity), or an aspherical femoral head jam against the acetabulum during forceful motion, particularly hip flexion (Kassarjian *et al.*, 2007). In addition to the presence of a non-spherical femoral head, other possible causes of cam impingement include coxa vara, a malunited femoral neck fracture, and childhood hip diseases such as Legg-Calvé-Perthes and slipped upper femoral epiphysis (SUFE) (Harris, 1986; Montgomery, 2009). The alpha angle is frequently used to quantify the sphericity of the femoral head and the femoral head-neck offset is normally used to measure the abnormal offset of the femoral head-neck junction (Ganz *et al.*, 2003; Kang *et al.*, 2010). Slipped upper femoral epiphysis, also known as slipped capital femoral epiphysis (SCFE), was investigated by Abraham *et al.* (2007) in a prospective study of femoral head/neck wear in subjects undergoing THR. The researchers concluded that SUFE was associated with cam FAI, and that this is a risk factor for the early development of OA. Research conducted by Leunig *et al.* (2000) in a study of younger subjects with SUFE supports these findings. Abraham *et al.* (2007) also reported extensive involvement of the superior femoral neck on the SUFE hips, whereas neck involvement on the primary OA hips was minimal with the majority of the wear being observed on the anterosuperior and posterosuperior regions of the femoral head.

1.8.3 Labral Pathology

Labral tears are becoming more frequently diagnosed in patients with hip and/or groin pain due to recent advances in both arthroscopic techniques and radiographic imaging modalities such as MRI. Cadaveric investigations and studies using magnetic resonance arthrography have estimated that the prevalence of abnormal labral pathology, such as tears or fraying, in individuals with hip or groin pain is between 22 % and 55 % (McCarthy *et al.*, 2001b; Narvani *et al.*, 2003). Seldes *et al*. (2001) identified two histological types of tear, those that occur within the substance of the labrum, and those that cause detachment of the labrum from the articular cartilage at the transition zone. A number of studies, mainly cadaveric, have reported a large number of labral

lesions in older, asymptomatic subjects, and these have been attributed to age-related degenerative changes (Lewis and Sahrmann, 2006; Groh and Herrera, 2009).

The association between labral pathology and the development of OA is often explained through the existence of comorbid abnormal morphology such as dysplasia or FAI causing altered biomechanics. Labral lesions have however, also been identified as a possible independent risk factor for the development of OA. A study of cadaveric donor hips by Seldes *et al.* (2001) identified labral tears in 53 out of 55 hips, with adjacent acetabular cartilage lesions being identified in 91 % (n = 50) of those hips with more advanced tears. The presence of OA was also recorded in 85 % (n = 47) of the femoral heads. The mean age of the donor hips was 78 years (range 61-98 years) and there were no obvious signs of any abnormal hip morphology, leading the researchers to conclude that labral tears may be one of the causes of OA. In a larger study, McCarthy *et al.* (2001a) investigated the role of labral lesions in the development of OA using 54 cadaveric pelves, and 436 subjects undergoing arthroscopy for anterior groin pain. Of the subjects undergoing arthroscopy (mean age 37.4 years), 241 were reported to have labral lesions, 154 had labral fraying, and 52 of the 54 cadaveric acetabula (mean age 71 years) had labral lesions. The incidence of adjacent chondral lesions in the arthroscopic subjects was 63 %, despite having no radiographic evidence of OA, whereas all of the cadaveric specimens showed some evidence of cartilage degeneration. This was a more heterogeneous study group than that of Seldes *et al.* (2001) because it had a much wider age range (17-82 years). The mean age of the cadaveric and arthroscopy subjects was very different, and they reported evidence of mild undiagnosed acetabular dysplasia in 67 of the 463 arthroscopic subjects. It is possible that these extraneous factors (i.e. increasing age and dysplasia) could have confounded the results, however, the researchers were still confident that labral pathology could be an independent risk factor for the early development of hip OA.

Osteophytes are sometimes present within labral tears and it has been suggested that this is because a torn labrum may cause the femoral head to migrate towards the labral-chondral junction adjacent to the tear (Seldes *et al.*, 2001). This would result in a continued pulling force or traction at the point of insertion of the labrum on this part of the acetabulum, which may then lead to the formation of a traction spur within the tear (van der Kraan and van den Berg, 2007).

There appears to be a consensus agreeing that a relationship exists between labral pathology and hip dysplasia. It has been suggested that abnormal dysplastic morphology, which causes reduced joint incongruity and a reduction in the articulating surface, causes chronic, abnormal shear stresses within the labrum, which in turn leads to separation or detachment of the labrum from the acetabulum (Figure 1.15) (Klaue *et al.*, 1991). It has been suggested that in hips displaying signs of FAI, particularly the pincer-type, higher forces are exerted on the acetabular rim at extremes of motion, which causes overstressing of the labrum and subsequent fraying and tearing along the articular margin (Beck *et al.*, 2005).

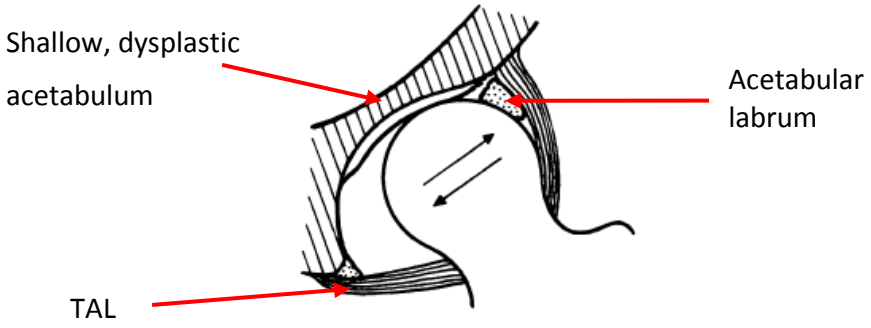

Figure 1.15: Diagram showing how overloading of the labrum in dysplasia could cause it to shear from the acetabular rim (Klaue *et al.*, 1991).

1.8.4 Disease Progression

Hip OA can manifest as a relatively stable chronic disease or it can produce functional loss through either delayed or accelerated progression leading to joint destruction. Identification of prognostic factors associated with disease progression, particularly potentially modifiable ones, could have implications for the treatment and course of the disease by way of early intervention. Progression of hip OA can be assessed either clinically or radiographically, however it has been noted that the majority of studies focus on radiographic progression of hip OA (Reijman *et al.*, 2005; Wright *et al.*, 2009).

Lane *et al.* (2004) monitored 745 women with OA of the hip over a period of eight years and the presence of osteophytes, particularly when located on the femur, was identified as a strong predictor of disease progression. A systematic review conducted by Wright *et al.* (2009) agreed that femoral osteophytes were a strong predictor of rapid progression, but because the presence of acetabular osteophytes was not, they

stated that there was inconclusive evidence regarding progression and overall type of bone response. This is in contrast to a study of hospital referrals conducted by Ledingham *et al.* (1993) who concluded that subjects with an atrophic bone response to hip OA were more susceptible to rapid radiographic progression of the disease. Their study however, had fewer participants (n = 136) and it was conducted over a shorter period of time (range 3-7 months). These factors could potentially affect the validity of the results of this study however, a number of other published studies support these findings. A retrospective longitudinal study of subjects undergoing THR by Conrozier *et al.* (1998), a review of cohort studies by Cheung *et al.* (2010), and a systematic review conducted by Lievense *et al.* (2002), all concluded that an acetabular atrophic bone response is a significant risk factor for a more rapid progression of hip OA.

The above reviews conducted by Wright, Cheung, and Lievense also agreed that there is moderate to strong evidence supporting an association between migration of the femoral head (superiorly or medially) and rapid progression of hip OA, but state that there is conflicting or inconsistent evidence for weight, age at first consultation and gender. All of the authors in this section agree that in order to generate more valid and conclusive evidence regarding the prognostic variables associated with progression, there is a need for further high-quality prospective cohort studies with an adequate follow-up period.

Bardakos and Villa (2009) studied the radiographs of 43 subjects under 55 years of age with FAI and mild or moderate hip OA, in order to investigate the effect of certain radiological parameters on the rate of progression. After 10 years, 28 hips with pincer-type impingement showed evidence of progression and the presence of the posterior wall sign was identified as significant risk factor ($p = 0.02$) for disease progression. They concluded that not all hips with pincer or cam-type impingement will progress rapidly or go on to develop end-stage OA, however, this was a relatively small study and extraneous variables such as BMI and level of physical activity that could confound the results were not controlled.

It has been difficult to draw any firm conclusions regarding the presence of hip dysplasia and the rate of disease progression as the majority of studies investigating risk factors and the progression of OA appears to exclude subjects with dysplasia. Conrozier *et al.* (1998) reported an absence of evidence to suggest that OA in dysplastic hips progresses more rapidly, however, only subjects with mild dysplasia (none of

which had a CE angle of < 25°) were included in the study. Lievense *et al.* (2002) also concluded that there is limited evidence for there being no association between dysplasia and rapid progression of OA in their systematic review, but this was based on only three studies and the methodological quality of two of these was reported to be poor.

Rapidly destructive arthrosis (RDA) of the hip has been described in the literature as being a progressive form of OA culminating in the destruction of the in joint less than two years from initial onset. It is reported to be largely unilateral in presentation and more common in elderly females. It is characterised by an atrophic bone response, uniformly distributed osteolysis, and widespread sclerosis. In addition to rapid destruction of the femoral head, the roof of the acetabulum is also destroyed although involvement of the acetabular floor has also been reported. The aetiology remains uncertain but neuroarthropathy, primary osteonecrosis, calcium crystal deposition, and an abnormal immune reaction are some of the theories that have been suggested (Postel and Kerboull, 1970; Yamamoto *et al.*, 2010).

1.9 Surgical Intervention

1.9.1 Hip Joint Preserving Surgery

Joint preserving surgery is generally carried out on hips with abnormal morphology or intra-articular lesions in order to reduce pain and/or either prevent the early onset of, or halt/slow the progression of OA (Tonnis and Heinecke, 1999; Millis and Kim, 2002). Depending on the nature and extent of the intervention required, hip joint preserving procedures may be performed using open dislocation of the hip or a minimally invasive technique such as hip arthroscopy. The use of arthroscopic surgery is more commonly associated with the diagnosis and treatment of isolated intra-articular lesions and the treatment of soft tissue abnormalities, however it may also be carried out as an adjunct to open procedures (Kim *et al.*, 2006b). The aim of surgical treatment is to correct acetabular and/or femoral deformities that have been shown to contribute to hip OA, whilst also relieving pain and maintaining or improving patient activity and quality of life. This is done using surgical procedures to improve congruency and hip joint contact pressures, and where necessary may include treating joint instability and impingement of the hip joint (Clohisy *et al.*, 2009).

Open surgical treatment such as periacetabular osteotomy (PAO) is frequently used in patients with DDH to normalise joint biomechanics by restoring the centre of rotation, and/or by increasing the load bearing area of the joint, thus allowing a more even distribution of joint contact pressures across the articular cartilage (Mechlenburg *et al.*, 2004; Hasegawa *et al.*, 2007). Numerous different procedures can be incorporated under the term PAO, however they can be broadly subdivided into those that rotate the acetabulum around either the symphysis pubis (i.e. cartilaginous joint between the left and right pubic bones), or the triradiate cartilage. The first method is used to increase femoral head coverage and the second is used to reduce the volume of the joint when joint incongruity is more pronounced (Holroyd and Wedge, 2009). In recent years, there has been an increasing amount of literature reporting the outcome of PAO but a great deal of heterogeneity exists amongst these studies in terms of both the operative procedure and the methodology/subjects (Clohisy *et al.*, 2009). It is difficult to draw conclusions regarding the outcome of specific PAO procedures because of this, but it appears to have favourable outcomes after ten years in the vast majority of cases. Risk factors for less favourable outcomes (i.e. pain or advancing OA requiring revision surgery or THR) are reported to be the presence of advanced OA preoperatively (e.g. K/L grade > 2 or irreversible chondral damage), and severe preoperative joint incongruity (Sharifi *et al.*, 2008; Matheney *et al.*, 2009; Troelsen *et al.*, 2009). Satisfactory results following PAO in some subjects aged 50 years or over have also been reported (Yamaguchi *et al.*, 2009; Teratani *et al.*, 2010), however this appears to be less well supported in the literature. Additionally, procedures such as labral or chondral debridement/repair, the resection of osteophytes, and proximal femoral osteotomy are also sometimes performed on patients with DDH, depending on the presenting complaint and diagnosis (Millis and Kim, 2002; Clohisy *et al.*, 2009).

The main aim of joint preserving surgery for FAI (in addition to pain relief) is to relieve the impingement (i.e. mechanical blockage) at the head-neck junction, which is normally present at the end of ranges of movement (Hossain and Andrew, 2008). Procedures such as acetabular rim resection, intertrochanteric osteotomy and femoral head-neck re-contouring or osteoplasty have been described in the literature to correct these FAI abnormalities (Lavigne *et al.*, 2004; Kim *et al.*, 2006b), and PAO is sometimes used in the presence of a retroverted acetabulum (Zebala *et al.*, 2007), or acetabular over coverage (e.g. protrusio acetabuli) (Leunig *et al.*, 2009b). Corrective surgery for

FAI is known to relieve the mechanical impingement providing good symptomatic relieve, but unlike PAO, normal anatomy is not necessarily restored and the long-term outcome of these procedures does not appear to have been widely investigated. It is generally accepted however, that the presence of advanced secondary OA and chondral damage preoperatively will increase the risk of early failure and contribute to a less favourable outcome (Zebala *et al.*, 2007; Hossain and Andrew, 2008).

1.9.2 Acetabular Component Placement in Total Hip Replacement

Recurrent dislocations and/or an increased dislocation rate associated with improper acetabular cup orientation have been well documented (Kennedy *et al.*, 1998; Kim *et al.*, 2009; Moskal and Capps, 2010). Lewinnek *et al.* (1978) reported a causal relationship between cup orientation and dislocation rate in THR and defined the safe zone for acetabular cup placement as being 15 ± 10° (SD) of radiographic anteversion and 40 ± 10° (SD) of radiographic inclination. A considerable amount of literature has been published regarding the relationship between the intra-operative position of the pelvis and the orientation of the acetabular cup, as many freehand techniques and mechanical alignment/navigation aids rely on visual cues and use the APP (Figure 1.16) as a reference plane. This requires the pelvis to be in a neutral position, which is difficult to achieve and maintain during surgery, particularly when the patient is in the a lateral decubitus position, as pelvic tilt and rolling backwards and/or forwards and can easily occur (Hassan *et al.*, 1998; Lembeck *et al.*, 2005; Kalteis *et al.*, 2009; Legaye, 2009). Factors such as body habitus, which can make locating external bony landmarks and the APP difficult (Zhu *et al.*, 2010), and discrepancies between the orientation of the natural acetabulum and the radiographic safe zone as described by Lewinnek *et al.* (1978) have also been reported to affect cup orientation. Inaccurate measurement and assessment of cup placement has been reported postoperatively due to variations in pelvic positioning/orientation (Beckmann *et al.*, 2009; Hayakawa *et al.*, 2009), but initial studies to evaluate a new method of accurately determining post-operative cup orientation by producing 3D images from 2D standard AP radiographs, have produced favourable results (Steppacher *et al.*, 2009; Zheng *et al.*, 2009).

A preliminary study by Archbold *et al.* (2006) investigated the accuracy of patient specific cup placement in 1000 consecutive primary THRs using the TAL to control

version, and the posterior acetabular labrum as a landmark to help control inclination (Figure 1.16).

Figure 1.16: Correctly orientated acetabular cup. Version was controlled by placing the cup parallel to the TAL and inclination was controlled by placing it flush with the posterior labrum. Height and depth were also determined by the TAL (Archbold *et al.*, 2006).

Conventional and minimally invasive surgical techniques were used and subjects with both idiopathic and secondary OA aetiologies were included in the study. The TAL was easily identifiable in all but 0.3 % of subjects, and after a minimum follow-up period of eight months, only 0.6 % (n = 6) had suffered a dislocation. A further study was conducted in order to define the degree of acetabular version achieved when using the TAL as a landmark on 40 subjects with idiopathic hip OA (Archbold *et al.*, 2009). The acetabular component was again placed flush with the TAL but the degree of inclination was determined using a freehand technique aiming for a conventional 45°. Postoperatively the mean radiographic anteversion was reported to be 19.7 ± 8.1° (SD) and mean radiographic inclination was 48 ± 7.1° (SD). There were no reported dislocations after 12 months. Following these studies, the researchers highlighted the need for patient specific acetabular cup placement due to the natural variations in acetabular morphology, and concluded that the TAL provides a good landmark for controlling version providing there are no major structural abnormalities (e.g. severe dysplasia or trauma).

Similar findings were reported in an *in vivo* study by Kelley and Swank (2009) when they investigated the theory that a plane is created between the TAL and superior labrum. This plane was used to control acetabular cup orientation in 87 subjects undergoing THR and resulted in a mean radiographic anteversion of 20° (range 14° to 36°), and mean inclination angle of 39° (range 26° to 56°). They concluded that anteversion was slightly more successfully controlled than inclination using this technique. A small scale

cadaveric study by Pearce *et al.* (2008) also concluded that placing the acetabular component parallel to the TAL is a reliable and easily reproducible method of determining acetabular cup version during THR.

1.10 Summary of Literature Review

The risk of developing OA is thought to increase with age and because the age of the general population has been estimated to rise over the next few years, it is envisaged that the demand for primary and revision THR procedures will also rise. This highlights the need for continued research to delay the need for primary THR through early intervention, and improve the longevity of implanted hip prostheses.

Studies investigating the geometry of the acetabulum have reported the existence of inter- and intra-individual variations, relating to both the bone (e.g. diameter and depth) and the soft tissues (e.g. labrum). Studies investigating the profile of the acetabular rim, and the shape and height of the labrum agree that both are asymmetrical and that considerable variations exist, however the literature is currently inconsistent regarding the exact nature and location of these variations. The shape and orientation of the acetabulum has been widely investigated and despite the heterogeneous nature of these studies, large degrees of inter-individual variations appear to exist, particularly for anteversion. Studies that are more recent have fitted planes to the bony aspects of the acetabulum in order to measure orientation more accurately, however due to the asymmetrical nature of the rim, this technique requires further work in order to improve its accuracy and consistency. The FNSA is the geometric parameter pertaining to the femur that appears to have the widest reported variation, mainly due to the angle lessening with age, with the method of measurement (i.e. 2D or 3D) also appearing to influence the outcome.

A review of the literature has shown that more variations in acetabula morphology have been reported compared to that of the proximal femur, where there appears to be a general consensus of opinion regarding general shape. This however, could be due to the heterogeneous nature of the studies investigating acetabular morphology, the fact that wider variations in acetabular morphology do exist, or that fewer studies have investigated variations in proximal femoral morphology, particularly in 3D. The lubrication mechanism in natural joints is very complex due to being placed under varying loads and motion. Healthy synovial joints exhibit low levels of friction and wear

and although the process of hip joint lubrication is not fully understood, recent studies have proposed a biphasic mechanism of lubrication, which involves both the interstitial fluid and the solid matrix. Interstitial fluid exudates out of the articular cartilage matrix when placed under load causing deformation of the cartilage, which increases the conformity of the articulating surfaces and distributes the load over a wider surface area. In order for fluid film lubrication to be achieved, the ratio of the theoretical minimum film thickness to the combined average surface roughness of the two bearing surfaces needs to be greater than three (i.e. $\lambda > 3$), with ratios less than one indicating the presence of a boundary lubricating regime. The minimum lubricating thickness is affected by the radius, material properties and surface roughness of the bearing surfaces, as well as the applied load, lubricant viscosity, and entraining velocity.

Abnormal acetabular and/or proximal femoral morphology and increased hip contact stresses, particularly when localised in one area, have been identified as risk factors for cartilage degradation and the subsequent development of secondary hip OA. An increasing body of evidence now also exists to suggest that idiopathic OA is multifactoral, and that subclinical abnormalities or hip joint pathology (e.g. dysplasia, FAI, labral tears) may be causative factors. Studies generally agree that joint preserving surgery such as PAO can slow the onset or progression of OA in some individuals with abnormal morphology such as dysplasia. Evidence regarding the long-term outcome of these procedures however is sparse, and the degree of success appears to be dependent on careful patient selection and preoperative planning. Further studies are required to investigate the long-term outcome of joint preserving surgery as well as the optimum selection criteria, and most effective surgical technique needed to correct the underlying abnormality. Tribological studies using *in vitro* simulations would be of benefit for investigating relationships between hip geometry and degenerative joint diseases such as OA, including the effects of modifying hip joint geometry through early surgical intervention.

A number of techniques relating to accurate acetabular cup placement in THR have been investigated, however most rely on consistent and accurate positioning of the patient and do not account for individual differences in acetabular geometry or body habitus. Patient specific cup positioning using local landmarks (e.g. TAL and labrum), has been investigated and preliminary studies using this technique have produced favourable results.

1.11 Aims and Objectives

1.11.1 Rationale

Primary total hip replacement (THR) surgery is used to alleviate the pain and disability caused by osteoarthritis (OA) of the hip joint, and this is generally accepted as being very successful. However, due to loosening of the prostheses, many younger patients require revision surgery after 15 to 20 years, and patient outcomes following this procedure are not always as favourable. Lubrication is an important mechanism affecting both natural hip joint and THR tribology, as the fluid film thickness between the articulating surfaces and predicted lubricating regime have been shown to influence wear. Factors such as lubricant viscosity, sliding velocity, load and the geometry of the bearings can influence the mode of lubrication. Early interventional surgery (e.g. osteotomy) to correct underlying morphological abnormalities and improve the biomechanics and loading forces of the hip joint may help delay the onset and of OA, therefore reducing the incidence of revision surgery. Three-tesla (3.0 T) MRI scanners facilitate the differentiation between soft tissues and bone, and the use of specialist software enables acetabular and femoral geometry to be assessed and any variations mapped and compared.

It is thought that abnormal acetabular geometry causes increased contact stresses on articular cartilage, which can then increase the risk of developing hip OA and/or accelerate the rate of progression. It is therefore hypothesised that there are fundamental differences in geometry in participants with hip OA compared to those without.

1.11.2 Aims

The primary aim of this research was to investigate a null hypothesis stating that there are no differences in hip geometry in participants with hip OA when compared to age-matched asymptomatic participants. This study was conducted in order to gain clinical and tribological information to help clinicians select suitable patients who may benefit from surgical interventions to prevent, or delay onset and/or slow the progression of hip OA. The information gained from this study will also be used in future *in vitro* tribological simulations of the human natural hip joint.

1.11.3 Objectives

- Characterise and compare the geometry of the acetabulum and proximal femur in a group of participants with hip OA and an asymptomatic control group.
- Validate and commission a new pendulum friction simulator for use in natural hip joint tribological studies.
- Develop a novel *in vitro* simulation model for the tribological testing of complete natural hip joints.
- Use the clinical and tribological knowledge gained to make recommendations regarding the future treatment of hip OA.

1.12 Summary Of Thesis

In summary, this study compared the geometry of the acetabulum and proximal femur in a group of OA patients with a group of asymptomatic participants using 2D analysis of 3T MRI scans, and an analysis of 3D shape models, which were created by segmenting the MR images. In addition to comparing 3D asymptomatic and OA hip joint active shape models, other novel aspects of this part of the study included an investigation of the sphericity and diameter of the femoral heads and acetabula in the cohorts, and determining the clinical importance of using 3D rather than 2D imaging for characterising hip morphology. The potential use of para-sagittal MR imaging for pre-operative planning relating to prosthetic cup placement in THR was also ascertained.

Following the validation of a new pendulum friction simulator, a novel *in vitro* simulation model for the tribological testing of complete natural hip joints was successfully developed, and this was used to compare hip hemiarthroplasty with complete natural hip joint tribology. This novel simulation model will also enable variations in acetabular and/or proximal femoral geometry, for example in OA patients, to be replicated in future *in vitro* simulations.

Chapter 2 Study of Human Hip Geometry Methods and Validation

2.1 Introduction

It has been reported that underlying morphometric abnormalities of the hip joint may be associated with the onset, and potentially the progression of hip OA (Harris, 1986; Bardakos and Villar, 2009; Castaño-Betancourt *et al.*, 2013). This study of human hip geometry (SHIG) aimed to compare the geometry of the hip joint in osteoarthritic patients and asymptomatic participants using high-resolution magnetic resonance imaging (MRI), in order to characterise any fundamental differences relating to the acetabulum or proximal femur. The null hypothesis (H_o) for the study was as follows:

H_o There are no differences in hip geometry in participants with hip OA when compared to age-matched asymptomatic participants.

Additionally, there has been interest in using anatomical landmarks to guide component positioning in THR. Archbold *et al.* (2006) introduced a method of determining the correct degree of anteversion, specific to the patient, for acetabular cup placement by aligning it with a plane between the transverse acetabular ligament (TAL) and the acetabular labrum. Studies investigating the use of local bony and/or soft tissue anatomical landmarks, such as the TAL, for cup positioning in THR have so far been favourable and reduced dislocation rates have been reported. However, a better understanding of natural acetabula morphology and inter-individual variations is required to develop this technique as its reliability is still questionable (Sotereanos *et al.*, 2006; Pearce *et al.*, 2008; Archbold *et al.*, 2009; Viste *et al.*, 2011). A secondary aim of this study, therefore, was to investigate the relationship between soft tissues in the hip joint, namely the acetabular labrum and TAL, and the pelvic bones that form the acetabulum.

Morphometric and geometric data collected from this study will be used to inform future *in vitro* tribological simulation studies conducted on complete natural porcine hip joints, and ultimately natural human hip joints, as described in Chapter 7. The results of this study are reported in Chapter 3.

2.2 Ethical Approval

The imaging of participants for the study was conducted on NHS premises at Chapel Allerton hospital (CAH) in Leeds, and as the study group included NHS patients, NHS ethical approval was therefore required prior to commencing the study. The proposed methodology and study protocol was submitted and reviewed by the Leeds West Research Ethics Committee (REC) via the integrated research application system (IRAS), and ethical approval was subsequently obtained (reference number 09/H1307/105). Approval from the local NHS Research and Development Directorate at the Leeds Teaching Hospitals NHS Trust, including site-specific permission to conduct the research at CAH, was also required and obtained (reference number UI10/9223).

The candidate held a research passport, which gave permission to access and conduct research through the Leeds Teaching Hospitals NHS Trust.

Annual progress reports detailing the recruitment of participants were submitted to the REC throughout the duration of the study and an end of study declaration was submitted once the recruitment of participants had ceased.

2.3 Recruitment of Participants

Participants were recruited into either the asymptomatic group (Section 2.3.2), which provided the control data, or the osteoarthritic study group (Section 2.3.3). At the start of the study the recruitment target was n = 60 (n = 30 in each group), however due to the recruitment process being unpredictably slow, an amendment to the study ethics reducing the target number of participants to n = 15 in each group was submitted to, and supported by the REC.

Anyone expressing an interest in joining the study was given an information sheet, which outlined the purpose of the research, what they would be required to do, any potential risks, information about their right to withdraw at any stage, and contact details of both the study co-ordinator (the candidate) and the chief investigator (Dr S. Williams). On receipt of the participant information sheet, a minimum period of 48 hours to consider their involvement in the study was given before an appointment to have the MRI scan was made. Informed, written consent was obtained by the candidate from each participant prior to being scanned, giving participants further

opportunity to ask any questions. No incentives for participation in the study were offered, however, reasonable travel costs were reimbursed.

2.3.1 Exclusion Criteria

The exclusion criteria for both the control and study groups were as follows:

- younger than 50 years old
- unable to remain stationary for 50 minutes

Potential participants with any of the following exclusion criteria for MRI were also unable to participate due to the potential risk of harm to the participant:

  - a cardiac pacemaker fitted or recent cardiac bypass surgery
  - any aneurysm clips *in situ*
  - history of metal fragments in eyes, head or body
  - implanted medical devices (e.g. stents)
  - surgery up to six weeks before the scan
  - claustrophobia

2.3.2 Asymptomatic (Control) Group

Asymptomatic participants forming the control group were recruited through advertisements placed in the University of Leeds media, posters in staff common rooms, and by word of mouth. All recruitment materials directed any interested subjects to contact the study co-ordinator (i.e. candidate), who discussed the study with them and assessed their eligibility for inclusion.

The inclusion criteria for the control group were as follows:

- aged 50 years or over
- no history of hip pain or hip injury on either side
- no ongoing knee and/or back pain
- able to remain stationary in a supine position for approximately 50 minutes

2.3.3 Hip Osteoarthritis (Study) Group

The study group consisted of symptomatic patients seen in orthopaedic clinics at CAH presenting with pain and evidence of hip OA, which had been diagnosed by orthopaedic surgeons on AP radiographs as part of their normal outpatient care. Patients eligible

for inclusion in the study were referred to the study co-ordinator, who attended the outpatient clinics, by the orthopaedic team.

The inclusion criteria for the study group were as follows:

- aged 50 years or over
- on the waiting list at CAH for a THR due to OA
- able to remain stationary in a supine position for approximately 50 minutes

2.4 Acquisition of MR Images and Study Data

Non-contrast images were taken using a clinical MR scanner located in the Leeds Musculoskeletal Biomedical Research Unit (LMBRU) at CAH. Scanning without intra-articular contrast was performed due to it being a non-invasive procedure, therefore having a lower risk of complications (e.g. infection, anaphylactic reaction) and causing less discomfort to the participants (Potter and Schachar, 2010). The scanner used in the study was a Siemans Verio with a magnetic field strength of 3.0 Tesla (3.0 T), and a Siemans body matrix coil was used to receive the radiofrequency (RF) pulses, or waves (Section 2.4.1). The total time each participant remained in the MRI scanner during the acquisition of the images was approximately 50 minutes.

2.4.1 Positioning of Participants

All participants were positioned by an experienced research radiographer and scanned in a feet first, supine (FFS) position, with the ankles loosely tied together to maintain consistency and reduce leg movement. Each participant's pelvis was placed centrally on the scanner bed with the body matrix RF receiver coil placed over the pelvis. During the scan, the hip joints were positioned as close as possible to the magnetic isocenter (i.e. the centre of the magnet in the x, y and z direction). The homogeneity of the magnetic field reduces when scanning further away from the isocenter, therefore, it was important to use the femoral heads as the central landmark to maintain high signal uniformity and minimise the magnitude of any associated geometrical distortions (Chang and Fitzpatrick, 1992; Moser *et al.*, 2009). To reduce the risk of movement artefact, participants were asked to remain stationary once positioned in the MRI scanner.

2.4.2 Imaging Protocol

The MR imaging protocol, which was developed collaboratively with Dr R. Hodgson (consultant musculoskeletal radiologist, LMBRU) and Dr M. Bowes (external PhD supervisor, Imorphics Ltd.), included a 3D isotropic sequence of the whole pelvis down to the mid shaft of the femurs, so that the bony landmarks of the APP (Figure 1.6) could be used during the analysis phase to register the images. Additionally, one hip was scanned in more detail using five higher resolution (HR) "detailed" sequences and a smaller field of view (FoV) to aid identification of the soft tissues. The detailed scans were done on the affected hip in the OA study group, and the side for the control group was matched with these. A small slice thickness of 1-2 mm increased the likelihood of detecting any small variations in anatomy. The parameters used for the image sequences taken in this study are listed in Table 2.1.

Table 2.1: Details of MR sequences and parameters used for the study of hip geometry. TSE SPACE scans image the whole pelvis. The "detailed" scans are of one hip.

(SPACE = Sampling Perfection with Application optimised Contrasts using different flip angle Evolution; TSE = turbo spin echo; HR = higher resolution; PD = proton density; TR = repetition time; TE = echo time; ms = millisecond; FoV = field of view).

	TSE SPACE	**TSE (HR) Detailed**	**TSE (HR) Detailed**	**TSE (HR) Detailed**	**TSE (HR) Detailed**	**TSE (HR) Detailed**
Acquisition Type / Plane	3D Coronal	2D Coronal	2D Axial	2D Sagittal	2D Para-axial	2D Para-axial
Image Contrast	PD	PD	PD	PD	PD	PD
Fat Suppression	Yes	Yes	Yes	Yes	No	No
TR (ms)	1300	4320	4320	4320	2500	2500
TE (ms)	4.2	9.8	9.8	9.8	27	27
FoV (mm)	361 x 380	190 x 190	190 x 190	190 x 190	159 x 159	159 x 159
Thickness of Slices (mm)	1	2	2	2	1.5	1.5
Number of Slices	192	29	29	29	35	35

The rationale for choosing the combination of sequences detailed in Table 2.1 was as follows. Turbo spin echo (TSE) pulse sequences are known to produce better quality images than gradient echo sequences (Farjoodi *et al.*, 2010). The use of fat suppression, which eliminates the contribution of the fat signal, can improve the visualisation of small anatomical details, however, this can also increase the imaging time (Delfaut *et al.*, 1999). Good contrast between articular cartilage and fluid (Gold *et al.*, 2004), and articular cartilage, labrum and cortical bone (Mintz *et al.*, 2005) has been demonstrated with 3.0 T proton density (PD) weighted images, which are characterised by tissues with a high proton density (e.g. water) being bright and areas with low proton density (e.g. cortical bone) being dark. The Siemen's SPACE (sampling perfection with application optimised contrasts using different flip angle evolution) sequence enabled high resolution 3D images of the whole pelvis to be collected at rapid speeds whilst maintaining low specific absorption rates (SAR), which is known to cause heating of the tissues. This 3D isotropic data set allowed the images to be retrospectively reformatted so that it could be viewed in multiple orientations (Scott and Schmeets, 2005), and this was used to analyse the bone.

Participants were scanned using three orthogonal planes so that the anterior, posterior and superior areas of the hip joint could be visualised. Large FoV coronal images (e.g. the SPACE sequence) allow both hips to be viewed simultaneously, whilst imaging in the axial and sagittal planes are reported as being the optimal views for evaluating the anterior and posterior structures of the hip joint (e.g. rim/labrum), and superior regions respectively (Grenier and Wessely, 2006). Para-axial images were obtained to provide cross-sectional images of the anterior and posterior aspects of the acetabular labrum, and para-sagittal images provided cross-sectional imaging of the TAL.

2.4.3 Patient-reported Assessment of Disability

A patient-reported questionnaire was included in the study so that a subjective assessment of each OA participants' perceived disability could be quantified and compared with the radiographic changes. The Oxford hip score (OHS), which is widely used in clinical practice to subjectively assess the outcome of THR, was chosen as it is a validated outcome measure, has good test-retest reliability, and is simple to use (Murray *et al.*, 2007). Originally developed for use in randomised, controlled trials, the OHS contains 12 questions relating to activities of daily living (Appendix A) in order to

assess pain and function in patients with hip OA (Dawson *et al.*, 1996). Participants in the OA study group completed the questionnaire prior to undergoing their MRI scan. Control group participants, who all confirmed that they did not have hip pain before being scanned, did not complete an OHS questionnaire.

As recommended by the authors who developed the OHS, the new scoring system was used to analyse the results (Murray *et al.*, 2007). Participants allocated a score of 0 to 4 to each of the 12 questions to produce an overall score ranging from 0 to 48, with the lowest scores denoting the most severe pain and disability. This differs from the scoring system originally devised, where a score of 1 to 5 was allocated to each question giving a total score of between 12 and 60. A licence and permission to use the OHS for this study was obtained from Isis Outcomes, Isis Innovation Ltd, at the University of Oxford.

2.4.4 Radiographic Classification of Osteoarthritis

Kellgren and Lawrence (K/L) grades (Table 2.2) were assigned to each participant in the study group in order to provide an objective assessment of the radiographic features associated with OA. This was done using pre-operative AP radiographs by an experienced consultant musculoskeletal radiologist, Dr P. Robinson, at CAH.

Table 2.2: The Kellgren and Lawrence grading system used for the radiographic classification of hip OA in the study group. Hips graded ≥ 2 are defined as having OA (Kellgren and Lawrence, 1957; Reijman *et al.*, 2004).

Grade	Description
0 No OA	No radiographic features of osteoarthritis
1 Doubtful	Possible narrowing of joint space medially and possible osteophytes around the femoral head; or osteophytes alone
2 Minimal	Definite narrowing of joint space inferiorly, definite osteophytes, and slight sclerosis
3 Moderate	Marked narrowing of joint space, definite osteophytes, some sclerosis and cyst formation, and deformity of the femoral head and acetabulum
4 Severe	Gross loss of joint space with sclerosis and cysts, marked deformity of femoral head and acetabulum and large osteophytes

The K/L grading system was chosen as it is the most widely used tool for the quantifiable assessment of hip OA, and it has been shown to have good intra-rater and inter-rater reliability (Günther and Sun, 1999; Terjesen and Gunderson, 2012; Damen *et al.*, 2014). Kellgren and Lawrence grades were not assigned to the control group.

2.4.5 Research Data

Participants recruited into the study were allocated a study identification (ID) code so that their involvement could be kept confidential. Participants in the control and study groups were allocated numerical ID codes, starting at one, with the prefix C and S respectively (e.g. C.01 and S.01). All MR images were anonymised by the hospital using the allocated ID code before being transferred to the University of Leeds server in DICOM (Digital Imaging and Communications in Medicine) format, which is the standard format for handling, transmitting and storing medical imaging information and data (National Electrical Manufacturers Association, 2015). Where applicable, the same study ID code was used for the K/L Grading and OHS. Once each participant had been scanned, all personally identifiable information (e.g. name, date of birth and contact details), which had been collected and held solely for recruitment purposes, was destroyed leaving only coded data to be used in the study.

2.5 Image Segmentation

The MR images were viewed and segmented with EndPoint software (version 1.2, Imorphics Ltd., Manchester, UK) using a process developed in association with Dr M. Bowes, an experienced segmentation supervisor. Segmenting an object of interest from the background image, using a process called surface extraction, enables a solid model of the object to be created and analysed. An extensive period of training and supervision using a practice set of hip MR images, provided by Dr M. Bowes, was completed prior to starting the study that ensured that methodological consistency was achieved before commencing the analysis of the SHIG data set. Additionally, ongoing advice and training relating to interpreting the MR scans was provided by Dr P. Robinson.

The segmentation process enabled 3D morphometric analyses of the DICOM data to be conducted by subdividing the images into regions with similar properties (e.g. proton density/grey scale). The process involved identifying the boundary of the structure to

be analysed and drawing a line around it on each slice of the image sequence using the mouse. The width and window level of the images were adjusted to optimise the contrast levels and brightness, aiding identification of the tissue boundaries for the segmentation process. A combination of manual, which consists of tracing around the region of interest by hand, and the automatic edge detection tool "Live-wire" were used to segment the images. Live-wire is an adaptive edge detection algorithm that computes and selects the optimal boundary of an object. The Live-wire boundary wraps around the object to be segmented when the user moves the mouse in close proximity to the edge, having first manually specified the start point on the edge of the object. Segmentation using Live-wire was used where possible as this is considered a relatively accurate and repeatable method of edge detection (Mortensen *et al.*, 1992; Mortensen and Barrett, 1998); however, poorly delineated areas required manual segmentation due to Live-wire being unable to accurately identify the boundaries of the structures.

The software automatically extracted the segmentations from the background, sequentially stacking them to construct a 3D wire model of the structure(s) to be analysed. In areas where a partial volume effect was present, characterised by low spatial resolution due to the averaging of individual signal intensities (Erasmus *et al.*, 2004), the tissue was categorised according to the majority of volume inside that particular voxel. For example, a voxel traversing the osseolabral or chondrolabral junctions was categorised as acetabular bone if the signal appeared to be predominantly low and from osseous tissue. A methodical approach was adopted whenever a partial volume artefact was observed in order to maintain a consistent approach to the segmentation process for the whole data set.

To improve the accuracy of the segmentation process, the image undergoing segmentation was viewed whilst quickly moving backwards and forwards through the image stacks, simultaneously viewing the segmented image in the other two orthogonal planes. The perpendicular cross hairs were used to determine the exact location of the segmented structure in the other planes (Figure 2.1). This enabled any inconsistent lines on the axial image or stray segmentation points to be identified, located, and then adjusted accordingly. Furthermore, the accuracy of the segmentation was strengthened by visualising the boundaries of the segmented structures using the 3D viewer (Figure 2.1 d), where again, any clearly misaligned points or areas of concern

could be re-assessed and if necessary modified. Additionally, segmentations were checked for accuracy during and after the study by Drs M. Bowes and P. Robinson (consultant radiologist). The segmentation process was a subjective analysis of the MRI data, and the additional assessment of accuracy was conducted to ensure that all parties were in agreement as to where the boundaries of the structures being segmented were located on the scans.

Once the segmentation of the structure to be analysed was complete and believed to be accurate, using the visual inspection methods described above, EndPoint was used to create a solid surface (consisting of a triangulated mesh) from the 3D wire model. The 3D surfaces were then exported into appropriate software for analysis in either .stl (stereolithography), .wrl (plain VRML [virtual reality modeling language]), or .pts (3D points file) format.

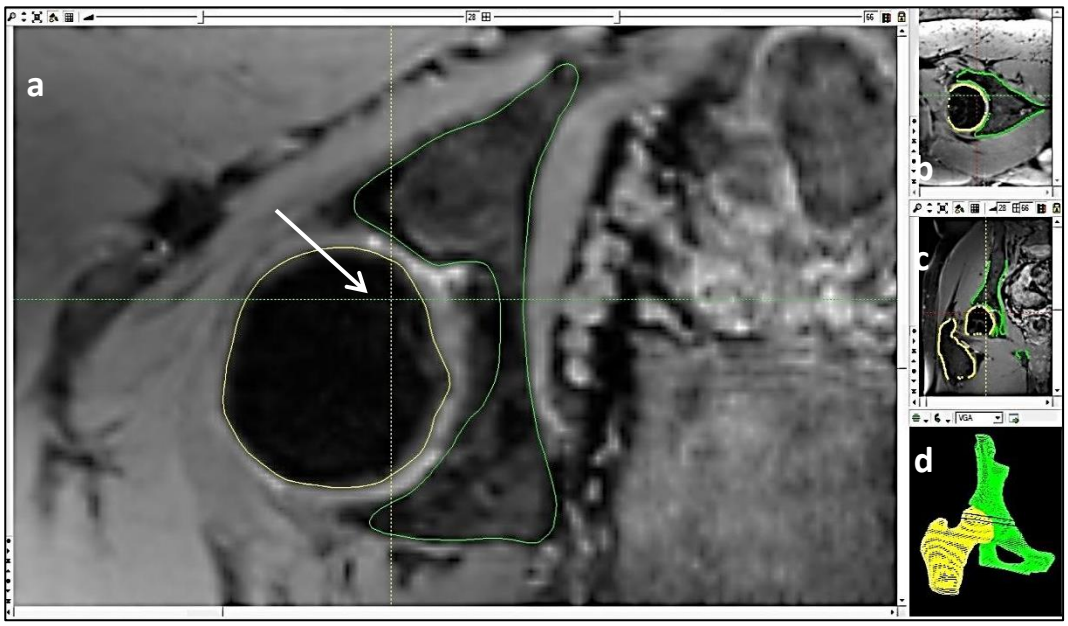

Figure 2.1: Bone segmentation of the right hip joint on an MRI scan using EndPoint software. Screenshot shows segmentation of the femur (yellow) and innominate bone (green) in the axial plane (a) with orthogonal sagittal (b) and coronal (c) views, together with the 3D wire model (d). Arrow indicates location of cross hairs on axial view.

2.5.1 SHIG Data Set Segmentation

The SHIG data set was segmented after the accuracy of the scanner had been established (Section 2.6) and the construct validity and reliability of the segmentation process had been assessed (Section 2.7).

Bony aspects of the hip (i.e. proximal femur and innominate bone) were the first structures in the SHIG data set to be segmented, and this was done in the axial plane using the 3D isotropic sequence. An example of this is shown in Figure 2.1.

On completion of the bone segmentation process, attempts were made to identify and segment the soft tissues (acetabular labrum and TAL) on the same 3D isotropic SPACE sequence. However, after reviewing all the 3D isotropic images in the data set it became apparent that for the majority of subjects, it would not be possible to do this from a single image sequence or plane.

2.6 Accuracy of the MRI Scanner

Checking the accuracy of the scanner reduced the risk of introducing a systematic error into the study by ensuring that as far as possible, the MR images were a true representation of the tissue being scanned. This section was completed following the development of the segmentation process, before the SHIG images were segmented.

2.6.1 Quality Assurance

A rolling quality assurance programme is conducted by medical physicists to assess the signal to noise ratios (SNR) received by the imaging coils in the MRI scanner used in this study. Geometrical testing is conducted twice a year on the scanner using a head coil and the ACR (American College of Radiology) accreditation phantom. In addition to geometric accuracy, the phantom is also used to test spatial resolution and the accuracy of slice thickness and slice position in all three planes (American College of Radiology, 2005).

2.6.2 Three-dimensional Distortion Correction

Distortion is an artefact causing geometrical differences between the MR image and true shape, affecting the spatial positioning of anatomy on a 3D volumetric MRI scan. The manufacturer's two-dimensional (2D) distortion correction algorithm is routinely applied to MR images before being interpreted by a radiologist; however, as this study involved the analysis of 3D models, the use of the manufacturer's 3D distortion correction algorithm was explored. This was done by segmenting the bone of the pelvis and proximal femur on a test scan that had been post-processed with a) no distortion correction, b) 2D distortion correction, and c) 3D distortion correction. The images

were acquired using the same 3D isotropic SPACE sequence that was used in the study, and they were segmented in the coronal plane.

The segmented images were exported as .wrl files and compared using ParaView (version 4.1.0, Kitware Inc., New York, US), which is a software designed for the visualisation and analysis of datasets that are defined in 2D or 3D space. The same image sequence was used for the three segmentations and therefore, the surface models created from them were aligned in the same coordinate frame and did not need to be registered. This meant that by assigning a different colour to each of the three surface models and overlaying them, the models could be compared and any differences visually assessed, with a predominance of any one colour signifying a difference in morphology. Axis aligned cube axes were fitted around the pelves and femurs of each surface to provide a quantitative assessment (data cube) of the overall outer dimensions of the models on the x, y, and z axes (Figure 2.2).

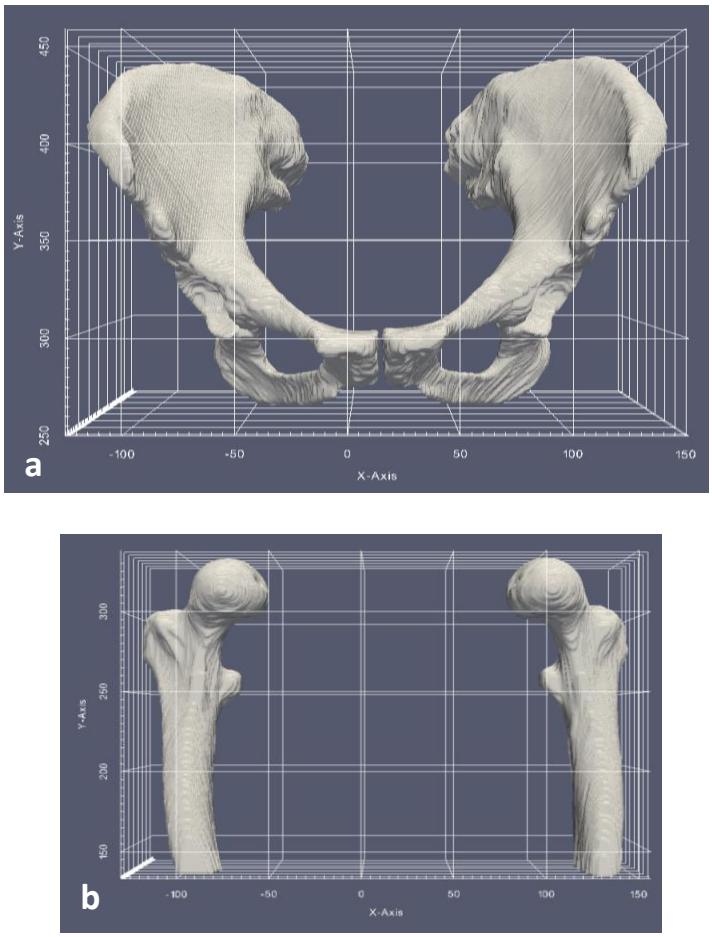

Figure 2.2: ParaView cube axes (data cubes) fitted to the 2D distortion corrected solid surface model of the pelvis (a) and femurs (b) with the x axis running mediolaterally, y axis running superoinferiorly (reversed), and the z axis (not labelled) running anteroposteriorly.

The high resolution SPACE sequences used throughout the study had a slice thickness of 1 mm (Table 2.1), and were regarded as being accurate to a value of ± 1 mm. The volumetric data obtained from these scans was isotropic with a voxel size (i.e. volume element in 3D space) of 1 mm^3, which was uniform in the axial, coronal and sagittal planes (i.e. x, y and z directions). The use of isotropic voxels is important for producing good quality 3D models. Slice thickness, and therefore corresponding voxel size, was kept to a minimum to facilitate the collection of repeatable measurements as clinically, a small voxel size increases the resolution of a scan and reduces the occurrence of partial volume effects, aiding interpretation of the scans and medical diagnosis. (Liney, 2010; Abel *et al.*, 2013). The cube axis parameters were evaluated using SPSS predictive analytics software (version 19, IBM, New York, US), where $p < 0.05$.

2.7 Assessment of the Segmentation Process

In addition to the methods described in Section 2.6 used to determine the accuracy of the MRI scan data, the following two additional studies were undertaken to assess the construct validity and consistency of the segmentation process. This section was completed once the accuracy of the distortion correction technique had been established (Section 2.6.2), before the SHIG images were segmented.

2.7.1 Porcine Tissue Substitute Model

A porcine hip of known geometry was used to assess the imaging and segmentation process by comparing the morphometry of the 3D surface model to the morphometry of the tissue being scanned. A porcine right hind leg of approximately 6 months old at the time of slaughter was obtained from a local abattoir, and scanned at the LMBRU using the same 3.0 T MRI scanner and imaging protocol that had been developed for the study of hip geometry (Section 2.4.2). An application requesting permission to access the MRI scanner for this purpose was submitted to and approved by the imaging team at the LMBRU (reference number 11/06), and the university's standard operating procedure (SOP) for transporting food grade animal tissue to the LMBRU (SOP. 09.9, Issue 1) was followed.

The hip joint geometry of the scanned tissue substitute was measured using ImageJ (version 1.45, National Institutes of Health, Maryland, US), which is an image processing and analysis program. This was done by harvesting the hemi-pelvis and femur from the

scanned porcine leg and photographing the tissue in different positions using a Canon digital SLR (single-lens reflex) camera. All photographic images were calibrated using ImageJ before taking measurements, which were obtained by visually choosing two linear, planar points on various locations around the pelvis (n = 4) and femur (n = 2). Anatomical landmarks visible on both the photographs and 3D surface models were used to maintain consistency when placing the points (Figure 2.3). To reduce the error that could arise from measuring the geometry of 3D objects using 2D images, no measurements were taken from curved surfaces. Five repeats of each measurement were completed on different days, with the candidate blinded to the previous results.

The bone of the hemi-pelvis and femur were segmented using EndPoint from the isotropic SPACE sequence in the coronal plane, and the extracted surface models were uploaded into ParaView. The skeletal immaturity of the animal meant that the acetabular labrum was very poorly delineated; therefore, it was only possible to segment the bone. The ruler function on ParaView was used to replicate the geometric measurements taken from the tissue sample, again with five repeats of each performed on different days. The 3D volumetric MR images obtained from the scanned porcine leg contained more detailed geometrical information than the 2D photographic images taken of the surfaces of the harvested tissue using the SLR camera. This meant that measurements obtained from the photographic data were used as a rough check of the accuracy of the 3D segmented model when compared to the tissue sample, rather than to validate the MR imaging and segmentation process.

Measurements taken from the tissue sample (ImageJ) and segmented MRI scan (ParaView), were not normally distributed, and therefore compared using a Mann-Whitney *U* test with a statistical level of significance of $p < 0.05$. The 95 % limits of agreement (mean difference +/- 1.96 standard deviations) between the two groups of measurements, was assessed using the Bland-Altman method.

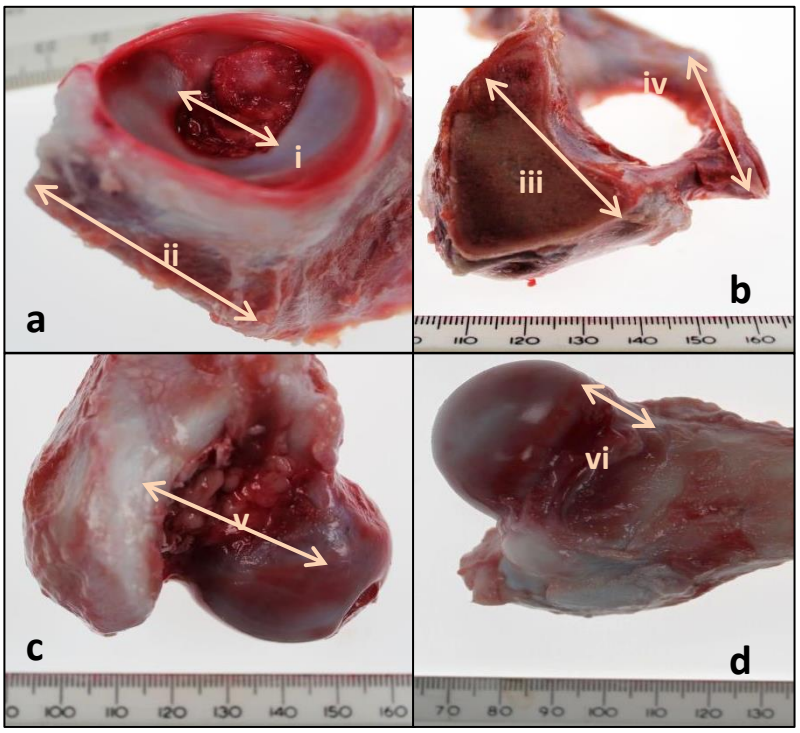

Figure 2.3: Location of measurements taken from the pelvis (a & b, n = 5 [i = Acetabular fossa, ii = dorsal to ventral cut surface of ilium, iii = medial cut surface of ilium, iv = ischium to pubis]) and the femoral head (c & d, n = 2 [v = posterior greater trochanter to centre of femoral head, vi = anteromedial femoral neck]) to compare the hip geometry of the tissue sample with the surface models created from the MRI scan.

2.7.2 Intra-rater Reliability of Segmentation

The consistency and repeatability of the segmentation process by the candidate was assessed by re-examining one acetabulum and one femur from the cohort. Two participants, one from the control group and one from the study group, were randomly chosen using the "randbetween" function in Microsoft Excel, and the SPACE sequence for each of the chosen participants was re-segmented with the candidate blinded to the original segmentations. The MR scan from the control group participant (C.14) was used to assess the repeatability of the pelvic segmentation process, and the scan from the randomly chosen OA study group participant (S.04), was used to assess the repeatability of the proximal femoral segmentation process. This was due to the greatest variation in femoral head shape having been observed in the study group.

The original and re-segmented 3D surface models created using EndPoint were uploaded into ParaView and compared. The surface models had an anatomically

consistent reference due having been created from the same images, and were therefore analysed using the methods described in Section 2.6.2.

2.8 Two-dimensional Evaluation of Hip Morphology

In addition to the 3D analysis of hip morphology (Section 2.9), the following 2D morphometric hip parameters were measured on the distortion corrected MR images using OsiriX image processing application (version 5.5.2, Pixmeo, Geneva, Switzerland). This analysis was performed in order to gain additional information about the geometry of the hip joints scanned in the study:

1. Femoral neck-shaft angle (FNSA), or caput-collum-diaphyseal angle
2. Acetabular index (AI), or Tönnis angle
3. Femoral head extrusion index (FHEI)
4. Acetabular version (AV)

The radiographic parameters listed above were included in the study to determine the presence of any underlying abnormal geometry, for example DDH or FAI. All of the above have been accurately measured using standard coronal and axial MR images in the literature (Tonnis and Heinecke, 1999; Beall *et al.*, 2008; Muhamad *et al.*, 2012; Stelzeneder *et al.*, 2012; Aly *et al.*, 2013). Three non-consecutive repeats of each measurement were completed.

Measurements taken in the coronal plane (FNSA, AI, FHEI) were completed at the level of the femoral head centre on the SPACE scan. The centre of the femoral head was located using a circle of best fit (Stelzeneder *et al.*, 2012) and verified by cross-referencing the coronal image slices with the axial and sagittal views using cross hairs. Cross-referencing was required due to difficulties in ascertaining a circle of best fit on some of the study group participants with more advanced OA affecting femoral head sphericity. Screenshots of the geometric measurements taken from the coronal image slices using OsiriX are shown in Figure 2.4.

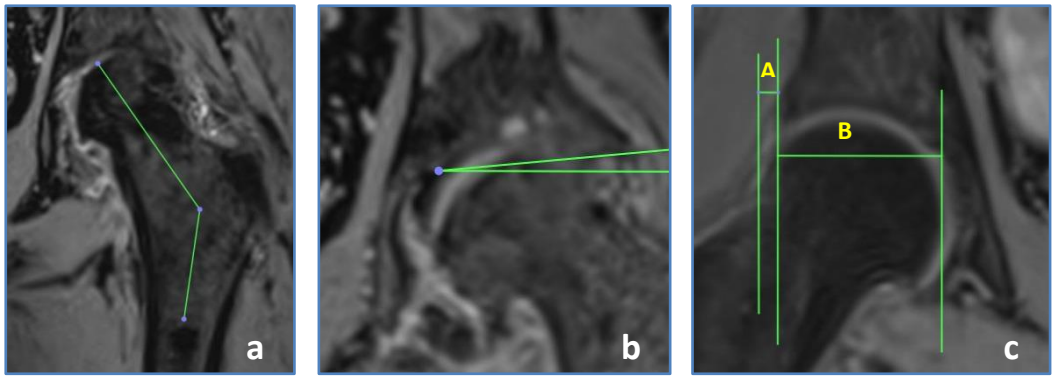

Figure 2.4: 2D measurements taken at the level of the femoral head centre on the MRI SPACE sequence in the coronal plane using OsiriX. (a) femoral neck-shaft angle (FNSA); (b) acetabular index (AI); (c) femoral head extrusion index (FHEI).

The FNSA (Figure 2.4 a) was the internal angle between a line intersecting the femoral neck axis (i.e. passing through the centre of the femoral head and neck), and a line drawn down the proximal femoral diaphyseal axis (i.e. midsection of the shaft) (Beall *et al.*, 2008; Aly *et al.*, 2013). The AI (Figure 2.4 b) was the angle between a horizontal line extending from the medial point of the hard, thickened bone of the acetabulum (sclerotic zone), and the superior osseous margin of the acetabulum (Beall *et al.*, 2008; Stelzeneder *et al.*, 2012). The FHEI (Figure 2.4 c), which is the percentage of femoral head covered by the acetabular roof, was calculated using Equation 2.1 (Murphy *et al.*, 1995), where B was the horizontal width of the femoral head (Figure 2.4 c [B]) and A was the distance measured between the lateral edges of the acetabulum and femur (Figure 2.4 c [A]) (Stelzeneder *et al.*, 2012).

$$\text{FHEI (\%)} = \frac{B}{A+B} \times 100 \qquad \textbf{Equation 2.1}$$

Acetabular version (AV) was measured on the 2D axial scan at the level of the femoral head centre, which was located using the crosshairs on the coronal and axial images. The AV angle (Figure 2.5) was measured by drawing two intersecting lines, one that was perpendicular in the anteroposterior direction on the scan (i.e. corresponding to the sagittal plane), and a second one connecting the anterior and posterior osseous margins of the acetabulum (Tonnis and Heinecke, 1999).

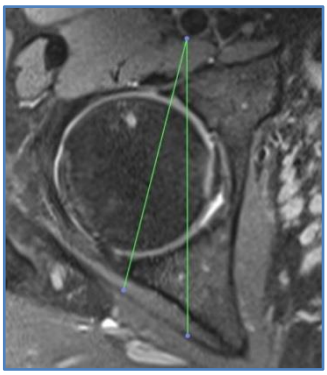

Figure 2.5: Acetabular version (AV) measured at the level of the centre of the femoral head on the 2D axial MRI scan using OsiriX.

Measurements were compared and analysed using SPSS in order to establish the presence of any significant differences (*t*-test; $p < 0.05$) between the control group and the study group. Gender differences were also investigated due to the relatively even numbers in the data set, however, male (n = 12) and female (n = 17) participants from the control and study groups were analysed together due to the small sample size.

2.9 Active Shape Models

The segmented pelvic and femoral bone from the SPACE MR images were initially processed by Imorphics Ltd., who produced active shape models (ASMs) for each femur (n = 29) and pelvis (n = 29) in the data set, using their custom software for statistical shape models. Active shape models are a form of statistical shape model that learn the variation in shape and grey scale from a training set in order to actively find the best fit for the model points (Cootes *et al.*, 1995; Cootes *et al.*, 2001). An overview of the process undertaken to produce the ASMs is provided in Figure 2.6, and this is followed by a brief explanation.

The data from the extracted 2D segmented contours from each slice of the MRI scan (as explained in Section 2.5), was converted to a 3D model using the Marching Cubes algorithm, and then the surfaces were smoothed by applying a series of quadratic patches of diminishing size. The Marching Cubes algorithm was first created by Lorensen and Cline (1987) for the visualisation of volumetric medical imaging data, and works by constructing surface models of constant density with a triangulated mesh and inter-slice points of connectivity. At this stage in the process, left-sided data was

mirrored so that all of the models could be collectively assessed as right-sided hip joints.

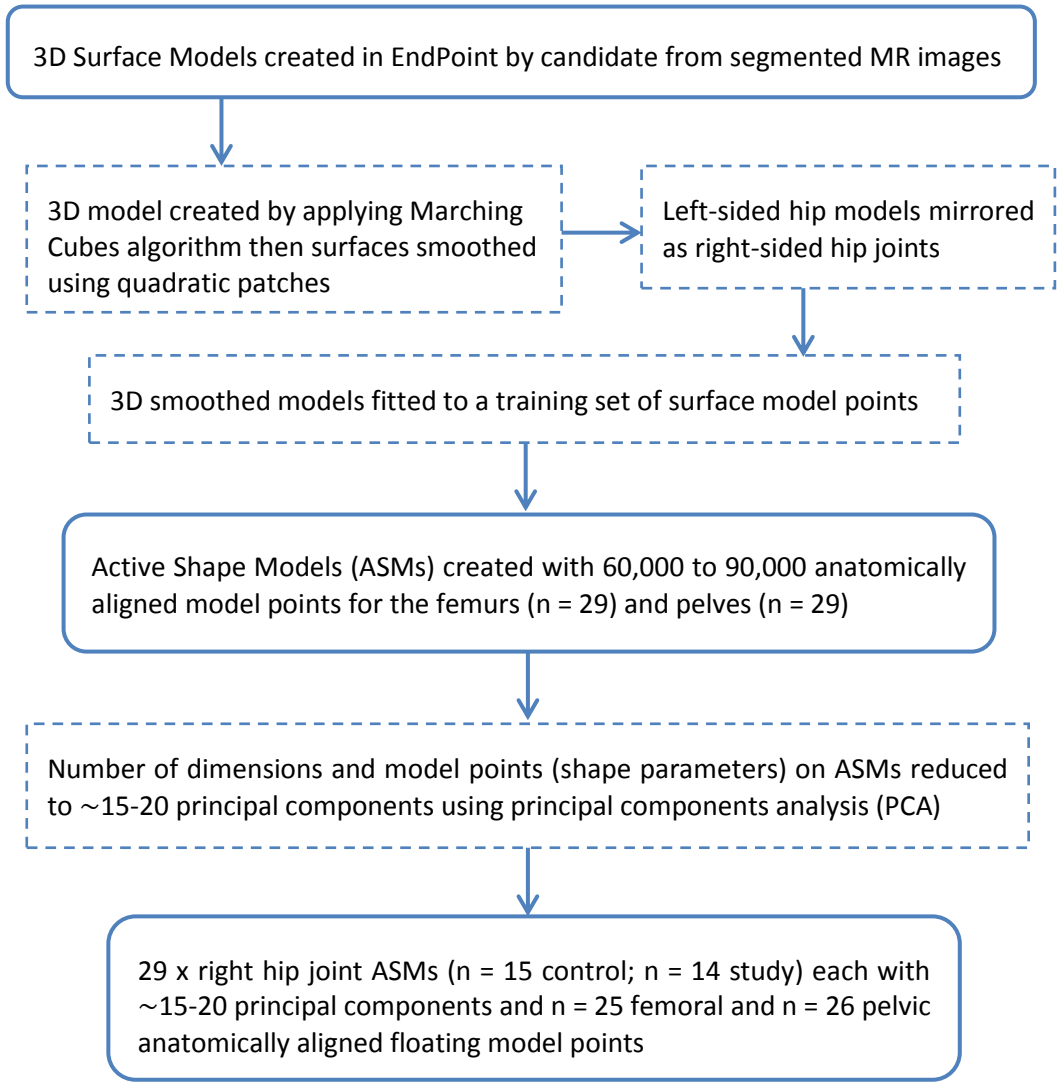

Figure 2.6: Flow chart of the process undertaken by Imorphics Ltd. to convert the segmented MR images into active shape models (ASMs).

The ASMs were then constructed by using training sets of anatomically corresponding models to project and fit model points to the smoothed data from the control and study groups. Optimisation was used to find the best location for the projected model points on the smoothed data in order to align surface landmarks, whilst creating the most compact 3D models. This process resulted in each 3D smoothed surface in the data set being fitted with approximately 60,000 to 90,000 anatomically corresponding model points. To reduce the shape dimensionality and number of model points (reducing computational processing time), principal components analysis (PCA) was

used to reduce the triangulated mesh of 60,000 to 90,000 points to ~25/26 floating points, with ~15-20 orthogonal principal components (shape parameters) for each femur and pelvis. The number of principal components computed using PCA described ~98 % of the variance in shape across the models. The accuracy of using this method of creating anatomically corresponding models has been validated previously in similar work on knee OA (Williams *et al.*, 2010). The final 29 x right hip joint ASMs (n = 15 control; n = 14 study) contained the same number of model points, each with anatomically aligned x, y and z values, meaning that each femoral ASM and each pelvic ASM was registered within the same reference frame and were therefore directly comparable during the analysis.

2.10 Three-dimensional Evaluation of Hip Morphology

The 3D ASMs of the femurs and pelves (n = 29 of each) were viewed as points and connectivity in .pts format using EndPoint Surface ROI (version 1.10, Imorphics Ltd., Manchester, UK), and in .stl format using ParaView visual analysis software. EndPoint Surface ROI provided a visual platform for overlaying, and moving quickly through, the femoral and pelvic models to compare the shapes in the same spatial orientation. ParaView provided an additional platform for viewing and comparing the models, where models could be assigned different colours in order to highlight any obvious shape differences between them. Femoral and pelvic models from the control (n = 15) and study group (n = 14) were quantitatively analysed in their respective groups so that any differences in 3D morphology between the two groups could be identified.

2.10.1 Shape Distributions

Femoral and pelvic shape distributions were explored using Sammon plots, which is a method used to reduce the dimensionality of multivariate data to a lower-dimensional (i.e. 2D) space whilst preserving the geometric relationships between data points (Sammon, 1969). A nonlinear mapping algorithm was applied to the principal components by Imorphics Ltd., which produced x and y coordinates for each ASM. The data points calculated by the Sammon mapping algorithm for the x and y coordinates have no real value, however, the algorithm preserves the inherent structure of the original data so that the distance between the points in 2D space corresponds to the distance between the same points in a higher-dimension (i.e. as described by the principal components). This means that if there is a large distance between two points

in the 2D Sammon plot (with each point representing an ASM), then the variation in shape between the two models will be large. Sammon maps showing the shape distributions for control versus study group participants were created in Microsoft Excel using the 2D data points (i.e. x and y values) that had been computed using the Sammon mapping algorithm. Additionally, due to the relatively even number of male (n = 12) and female (n = 17) participants in the data set, gender differences were also assessed.

2.10.2 Assessment of Shape Parameters

A discriminant function analysis was performed using SPSS to assess how well the shape parameters (i.e. principal components), described variations in shape between the control and study group femurs and pelves. The method used was Fisher's linear discriminant analysis (LDA), as this does not assume a normal distribution or equal variances (Fisher, 1936). The data was also cross-validated to assess how well the shape parameters were able to classify a model into the correct group. The cross-validation process was performed in SPSS using the leave-one-out function, where all cases in the dataset are missed out of the classification in turn and treated as test data. The remaining data is then re-classified into the two groups using the data from all cases other than the one that has been left out, providing an estimate of the predictive accuracy of the discriminant variables (i.e. principal components) (Field, 2009).

2.10.3 Assessment of Hip Joint Sphericity

Imorphics Ltd. fitted a sphere to each femoral head and acetabular lunate surface in the data set (see examples in Figure 2.7), using their custom software and linear least squares fit method. The spheres were fitted to the projected points on the ASMs, and the fit of each sphere was checked as part of their standard quality assurance procedure before the analysis. The residual distance (i.e. error) in mm between the surface of the ASM and the fitted sphere along the z, y and z coordinates was recorded for each model, as were the radii of the fitted spheres.

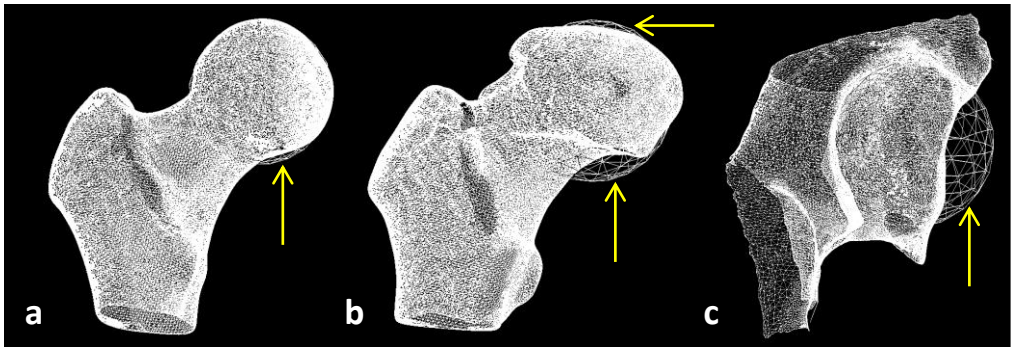

Figure 2.7: Wire frame models, viewed in EndPoint ROI, showing spheres fitted to a femoral head model from the control group (a) and study group (b), and to an acetabulum from the study group (c). Yellow arrows indicate where parts of the spheres lie outside the models.

The Bland-Altman method was used to compare the radius (r) of the sphere fitted to the femoral heads with the radius of the sphere fitted to the lunate surfaces of the acetabula. The data was analysed by comparing intra-group (control and study) and inter-group (control versus study) differences between the mean femoral head and mean acetabula sphere radii. The residual errors (i.e. sum of the deviations of each model from the corresponding sphere), were uploaded and evaluated in Cortona3D Viewer (Version 7.0, Cortona3D, Ireland) as .wrl files. This VRML standard file format enabled the residual errors to be viewed as 3D vector graphics. The residuals were scaled from -1 mm to +1 mm, where any part of the 3D surface inside lying inside the fitted sphere was indicated by a blue shaded area, and parts of the 3D surface model lying outside the sphere were coloured red. Areas of the models that were a good spherical fit were shaded with lighter shades of blue or red, and areas of the models that were a poor fit and more aspherical were identified by darker shades of blue (-1 mm) and red (+1 mm).

2.11 Summary

The main aim of the study described in this chapter (and results in Chapter 3), was to use 3.0 T MRI scans and shape matching software to characterise the geometry of the human hip. This was completed by comparing the hip geometry of subjects with hip OA aged 50 and over awaiting THR, with an age matched asymptomatic group.

The following is a summary of the methods used in the study.

- Ethical approval (ref. no. 09/H1307/105) was obtained from Leeds West REC.

- Asymptomatic participants were recruited through advertisement materials in and around the University of Leeds, and hip OA (i.e. study) participants with a K/L grading ≥ 2 were recruited via the orthopaedic outpatient department at CAH.
- An imaging protocol was developed that included an MRI sequence of the whole pelvis and more detailed images of one hip for visualising soft tissues.
- Study group participants completed a self-reported questionnaire about their perceived disability. A consultant musculoskeletal radiologist provided K/L grades.
- An accurate image segmentation process was developed using EndPoint software, which included a number of techniques to maintain the accuracy of the process.
- The effect of applying different MRI distortion correction algorithms was assessed.
- The accuracy and repeatability of the segmentation process was assessed by scanning and segmenting a porcine tissue substitute model, and re-segmenting two of the human scans.
- A number of 2D morphometric hip parameters were measured to determine the presence of any underling abnormal geometry.
- Active shape models for the control and study group participants were created from the segmented pelvic and femoral bone, and then visually compared.
- The ASMs were used to assess shape distributions of the pelvis and proximal femur across the two groups, and additionally between male and female participants.
- An assessment was made of how well the ASM shape parameters described the variations in shape between the control and study group pelves and femurs.
- Hip joint sphericity was assessed by fitting spheres to the femoral heads and acetabula, and then comparing the radii of the spheres and the residual errors.

Chapter 3 Study of Human Hip Geometry Results and Discussion

3.1 Introduction

The study of hip geometry (SHIG), as described in Chapter 2, aimed to address a null hypothesis stating that there were no differences in hip geometry when comparing subjects with hip OA aged 50 and over awaiting THA, with an age-matched asymptomatic group with no reported hip, knee or low back pain. The results and findings of the SHIG study are presented and discussed in this chapter.

Fifteen participants (n = 7 male; n = 8 female) were recruited into the control group, and 14 participants (n = 5 male; n = 9 female) with osteoarthritis of the hip joint were recruited into the study group. Control group participants were 50–73 years old (mean age 61.13 years), and the study group participants were 57–82 years old (mean age 68.20 years). All participants recruited into the study of hip geometry (SHIG) underwent 3.0 T MR imaging at the LMBRU, however, one study group participant only had SPACE sequence images taken due to hip pain preventing any further imaging.

3.1.1 Recruitment Rate

Twenty-six potential participants responded to the advertisements and enquired about entry into the control group, and 108 hip OA patients were referred to the candidate from the orthopaedic team for possible inclusion in the study group. The recruitment of participants was completed over a five-year period with a success rate of ∼58 % for the control group and only ∼13 % for the OA study group. A small number of potential participants withdrew from the study before consent was obtained (n = 3 control; n = 11 study), and a larger number of volunteers were found to be unsuitable for inclusion during the preliminary screening process (n = 8 control group; n = 47 study group). The main reason for withdrawal from the study in the OA study group was the date of surgery being brought forward leaving insufficient time to be scanned. Potential participants in both groups were found to be unsuitable for MRI scanning due to factors in their past medical history and the potential risk of harm (Section 2.4). Additionally, 55 % (n = 26) of hip OA patients referred for inclusion were excluded due to concerns about needing to lie still in a supine position for any length of time. Relatively equal numbers of male (n = 19) and female (n = 17) OA hip patients declined entry into the

study. The number of potential participants successfully, and unsuccessfully recruited into the study has been summarised in Table 3.1.

Table 3.1: Number of potential SHIG participants in the control and study groups who withdrew (W), were unsuitable (U), or declined (D) participation. Also shown is the number of participants who were recruited into the study.

	Control Group (C)		Total (C)	Study Group (S)		Total (S)
	Male	Female		Male	Female	
Withdrew (W)	2	1	3	6	5	11
Unsuitable (U)	7	1	8	22	25	47
Declined (D)	N/A	N/A	0	19	17	36
Total (W, U, D)	9	2	**11**	47	47	**94**
Recruited	7	8	**15**	5	9	**14**

3.2 Study Group Subjective and Objective Assessment

The results from the patient-reported questionnaire (OHS) and the radiographic classification of hip OA (K/L grade), as described in Section 2.4.3 and Section 2.4.4 respectively, are presented in Table 3.2. All radiographs were classified with a K/L grade ≥ 2, indicating the presence of hip OA, and all study group participants reported an OHS < 29, indicative of moderate to severe symptomatic hip OA (Murray *et al.*, 2007).

Objective radiographic markers and subjective measures of hip OA were generally well matched, with K/L grades 3 and 4 being associated with moderate to severe patient-reported symptoms (i.e. OHS 0 to 29). Interestingly, one of the study group participants (S.05) reported moderate pain and loss of function (OHS 24) but with minimal radiographic evidence of hip OA being reported (K/L grade 2).

Table 3.2: Oxford Hip Scores (0-48, where 0 is most symptomatic) and Kellgren and Lawrence Grades (0-4, where 4 indicates severe radiographic hip OA) for the study group.

ID Code	Oxford Hip Score (OHS)	Kellgren and Lawrence Grade (K/L grade)
S.01	11	4
S.02	11	4
S.03	12	4
S.04	25	4
S.05	24	2
S.06	12	4
S.07	22	4
S.08	20	4
S.09	8	3
S.10	24	4
S.11	13	4
S.12	24	3
S.13	24	3
S.14	22	4
	Average score = 18	Average grade = 4

3.3 Three-dimensional Distortion Correction

Two-dimensional distortion correction to account for any non-linearity or distortion of the image shape from the true shape of the tissue being scanned is routinely applied to MR images before being reported by the radiologist. However, as the SHIG study involved comparing 3D surface models created from the MRI scans, it was thought appropriate to explore the effects of applying different types of distortion correction algorithms. Full 3D distortion correction algorithms, which can be applied to restore the true shape of the images, are checked by imaging a phantom of known dimensions containing a Perspex grid insert with aqueous-filled holes, placed at specific intervals. Measurements taken between these holes on the corrected MR images are used to quantify the distortion as part of the quality assurance measure (Section 2.6.1).

A test scan covering the pelvis and femurs was post-processed on the MRI scanner to give three different sets of images, one with no distortion correction, one with 2D distortion correction, and one with 3D distortion correction. The images were then

segmented to produce 3D models of the bone, which were compared by overlaying the images using ParaView and by fitting cube axes to measure the maximum outer dimensions (Section 2.6.2). Cube axes, fitted to the input data for the 3D pelvic and femoral surfaces, created a spatial grid (or 3D data cube) around the surface model by fitting x, y, and z-axes to the outer corners of the model (Figure 2.2).

The outer dimensions (x, y, z) of the data cubes fitted to the three sets of segmented images (i.e. no distortion correction, 2D and 3D distortion correction) are presented in Figure 3.1 for the pelvic models and Figure 3.2 for the femoral models.

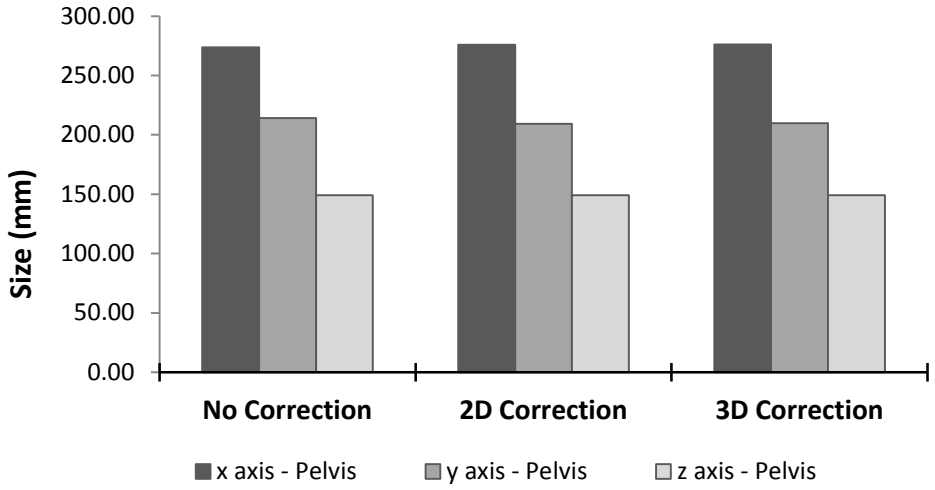

Figure 3.1: Dimensions of the 3D data cubes fitted to the surface models of the pelves created from MR images with no correction, 2D correction , and 3D distortion correction applied to them. All n = 1.

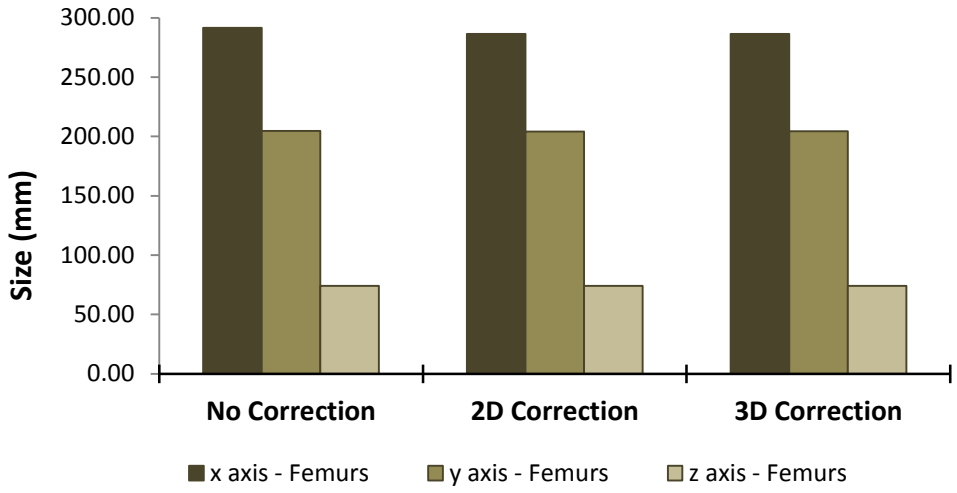

Figure 3.2: Dimensions of the 3D data cubes fitted to the surface models of the femurs created from MR images with no correction, 2D correction, and 3D distortion correction applied to them. All n = 1.

The mean outer dimensions (± SD) of the pelvic data cube (n = 3) along the x, y, and z-axes were 275.27 mm ± 1.37 mm, 210.98 mm ± 2.70 mm, and 149.00 mm ± 0.00 mm respectively. The mean outer dimensions (± SD) of the femoral data cube (n = 3) along the x, y, and z-axes were 288.13 mm ± 2.98 mm, 204.39 mm ± 0.20 mm, and 74.00 mm ± 0.00 mm respectively. The length of the cube anteroposteriorly, i.e. along the z axis, was the same for all three distortion corrected pelvic models and all three femoral models. The largest variations in grid size for each set of distortion corrected models were observed superoinferiorly in the pelves (y axis) and mediolaterally in the femora (x axis).

The overall dimensions of the data cubes fitted to the pelvic and femoral 3D surface models created from the MR images, post-processed with three types of distortion correction (Figure 3.1 and Figure 3.2), were not statistically significantly different on the x, y or z-axes (ANOVA, $p > 0.05$).

Although the maximum outer dimensions of the models did not differ significantly, obvious shape differences were highlighted by overlaying the three surfaces in ParaView (Figure 3.3). The blanket of colour observed distally, with respect to the hip joint, showed that the differences were predominantly sited around the iliac fossa, iliac crest, and shaft of the femur. A marked narrowing or inward curvature was observed in these area on the surface model created from MR images with no distortion correction.

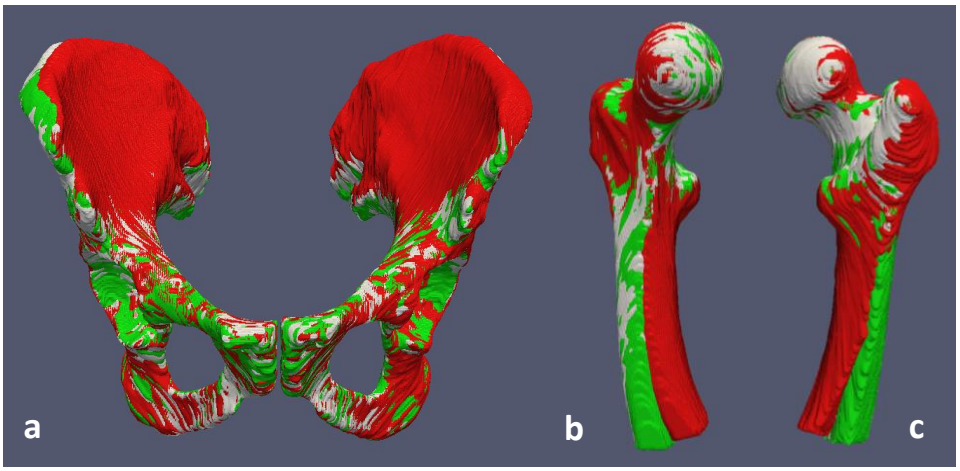

Figure 3.3: Surface models showing the anterior pelvis (a) and the anterior (b) and posterior (c) right femur with no distortion correction (red), 2D distortion correction (neutral), and 3D distortion correction (green) overlaid in ParaView to produce a colour map highlighting the shape differences.

Clinically, 2D correction is routinely applied to MR images before being reported; therefore, the model with no distortion correction was then discounted and the data was re-evaluated using the right innominate bone and femur from just the 2D and 3D distortion corrected surface models (Figure 3.4). Systematic differences between the two shape models were again more notable distally, the shaft of the femur on the 3D corrected model appeared to be straighter than the 2D model, and the pelvis of the 3D model appeared to be slightly wider superiorly.

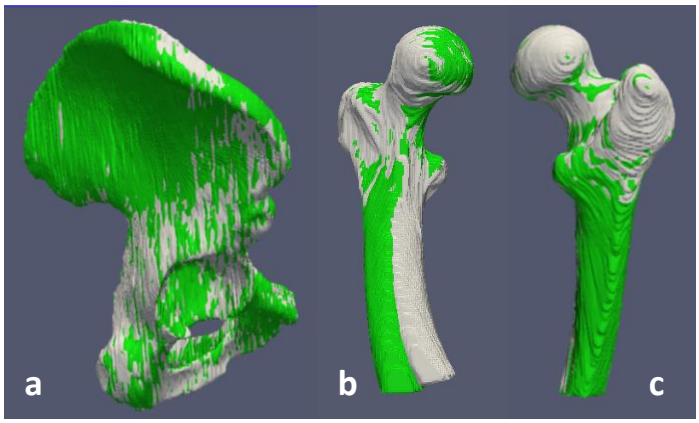

Figure 3.4: Surface models of the right innominate bone (a) and right anterior (b) and posterior (c) femur with 2D distortion correction (neutral) and 3D distortion correction (green) overlaid in ParaView to produce a colour map highlighting the shape differences.

There were no obvious systematic differences affecting the geometry of the acetabulum or femoral head of the hip joint when the 2D and 3D corrected models were compared, as both neutral (2D) and green (3D) areas of the surface models were visible (Figure 3.4). However, due to the differences observed distally, which could potentially affect the bony landmarks of the APP and the registration of the images, 3D distortion correction was applied to all MR images acquired for the study of hip geometry.

3.4 Assessment of Segmentation Technique

The results in this section assessed the accuracy of the geometric measurements taken from a tissue substitute model compared to the geometry of the scanned tissue (Section 2.7.1), and the consistency of the segmentation process (Section 2.7.2).

3.4.1 Porcine Tissue Substitute Model

Visual inspection of the extracted surface models and harvested tissue samples revealed that both the hemi-pelvis and femur were generally comparable in terms of overall shape (Figure 3.5 and Figure 3.6). There were, however, some notable differences in the appearance of the acetabulum due to being unable to segment the soft tissues in and around it (e.g. ligamentum teres, fat pad, labrum, TAL). This meant that the slightly triangulated underlying acetabular bone illustrated by the surface model (Figure 3.6 b) was not mirrored in the tissue sample (Figure 3.6 a). Exposure and visual inspection of the acetabular bone confirmed a triangular shape that was deepened by the labrum, which also gave the acetabulum its rounded appearance.

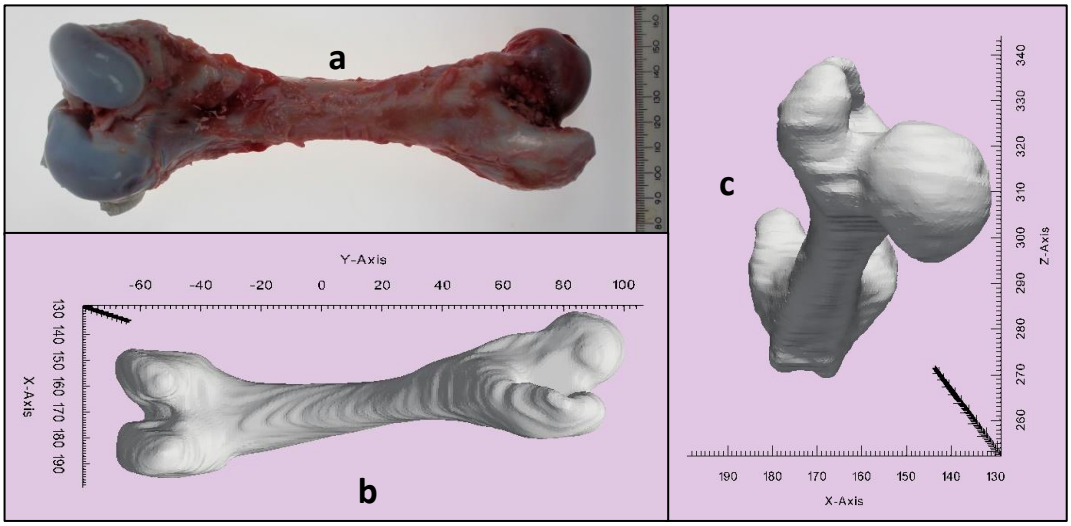

Figure 3.5: Posterior view of harvested porcine femur (a) and 3D surface models extracted from the segmented MRI scan of the porcine tissue substitute viewed (b) posteriorly and (c) superiorly in ParaView.

There were no significant differences (Mann-Whitney *U*; $p > 0.05$) in the length of the pelvic or femoral measurements specified in Figure 2.3, when taken from the harvested tissue sample using ImageJ and from the surface model using ParaView. The largest variation between the two methods was observed in measurements taken across the acetabular fossa (Figure 3.7 i), with mean lengths of 20.4 ± 0.2 mm (ImageJ) and 19.9 ± 0.4 mm (ParaView) being recorded.

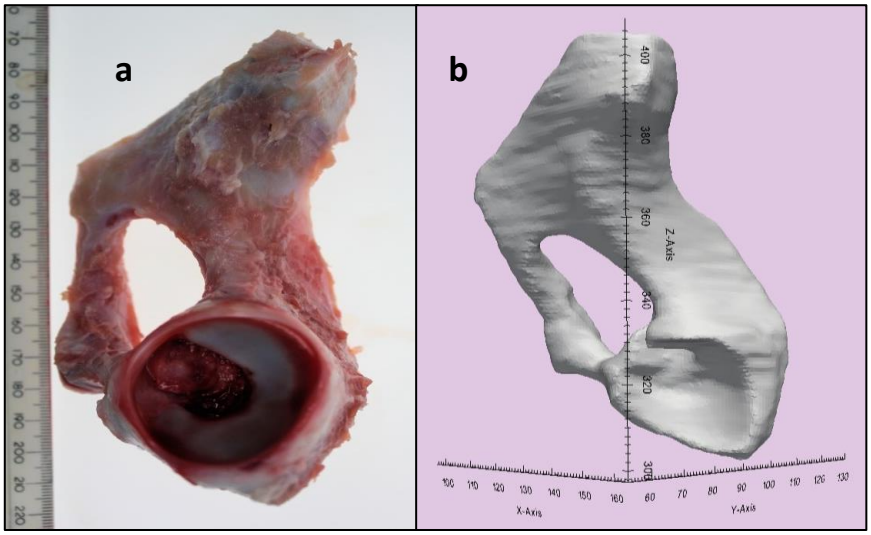

Figure 3.6: Porcine hemi-pelvis showing acetabulum from (a) the harvested tissue substitute and (b) the 3D surface model extracted from the segmented MRI scan viewed in ParaView.

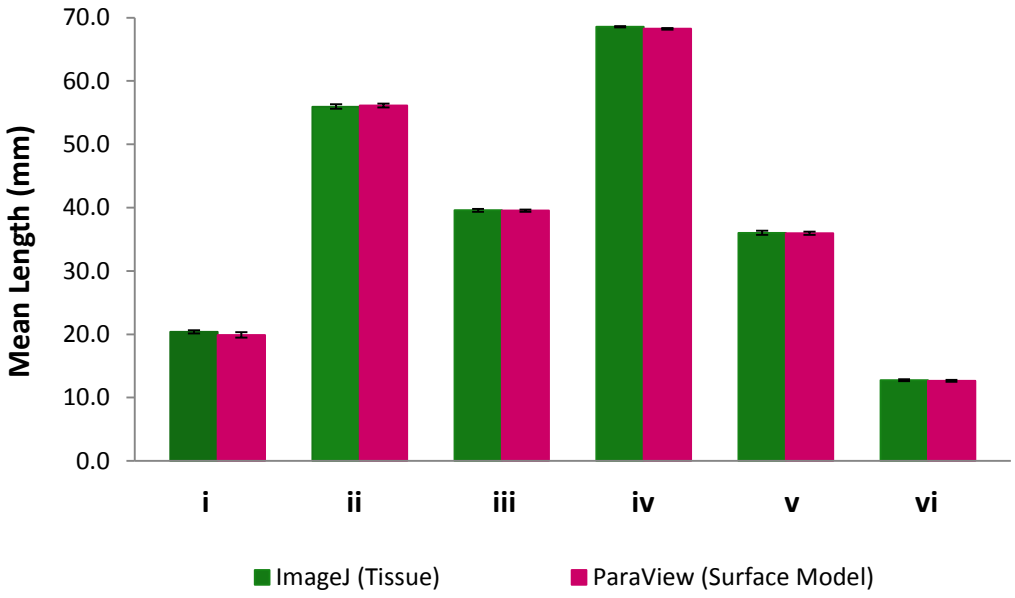

Figure 3.7: Mean length ± 95 % confidence limits (CL) of linear measurements taken from the pelvis (i to iv; 5 repeats of each) and femur (v & vi; 5 repeats of each) of the harvested porcine tissue sample and 3D surface model created from an MRI scan of the same porcine tissue.

(i = Acetabular fossa, ii = dorsal to ventral cut surface of ilium, iii = medial cut surface of ilium, iv = ischium to pubis, v = posterior greater trochanter to centre of femoral head, vi = anteromedial femoral neck [as indicated in Figure 2.3]).

The differences between the two methods of measuring the geometry of the porcine tissue substitute was calculated (Tissue – Surface Model), the results of which were found to be normally distributed, and not significantly different with no fixed bias (one-sample *t*-test; $p > 0.05$). This data supported the use of the Bland-Altman method to assess the level of agreement between the measurements taken from the tissue sample and measurements taken from the 3D surface model (Bland and Altman, 2003). The Bland-Altman plot (Figure 3.8) had an estimated bias (i.e. mean difference in length measurement) of 0.14 mm, and upper and lower 95 % confidence limits of agreement of 0.88 mm and -0.60 mm respectively. The outlier on the plot is a measurement taken from the acetabular fossa. The results appeared to show no obvious proportional bias towards either measurement method as the data plots were evenly dispersed above and below the mean difference (bias) line. This was confirmed by linear regression analysis of the mean difference in length ($p > 0.05$), inferring that there is a level of agreement between the measurements taken from the tissue sample and those taken from the 3D surface model, which had been created from segmented MR images of the same tissue.

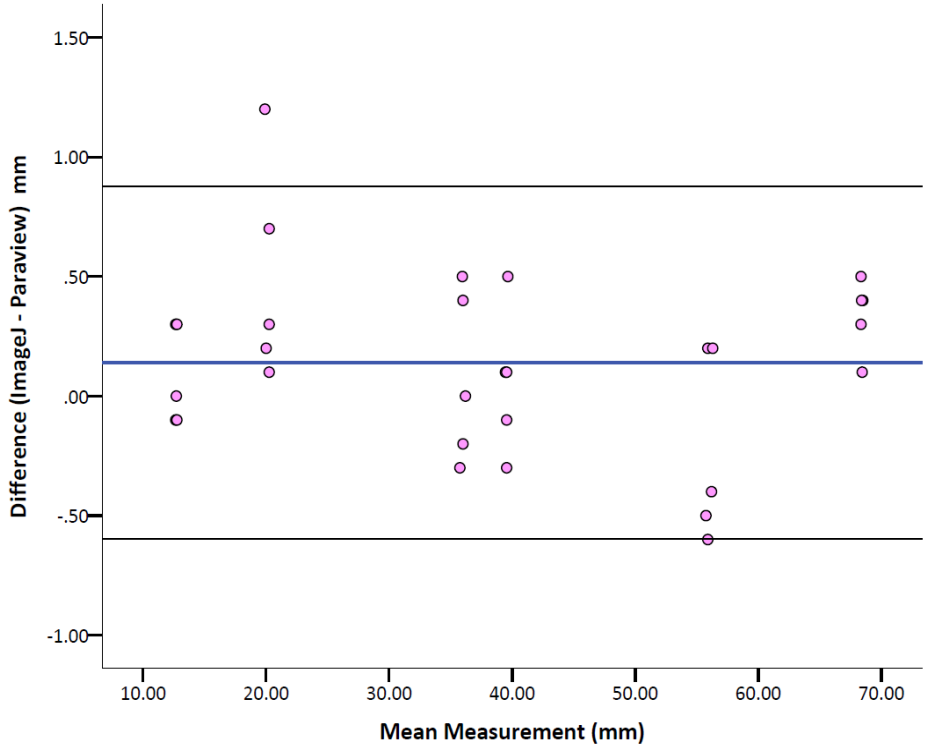

Figure 3.8: Bland-Altman plot of the difference in length (Tissue – Surface Model) against mean length ([Tissue + Surface Model] / 2) for each measurement (n = 30) taken from the porcine tissue sample (ImageJ) and 3D surface model (ParaView). Mean difference (blue line) and 95 % confidence limits of agreement (black lines) of the difference in the methods are shown.

3.4.2 Intra-rater Reliability of Segmentation

The dimensions of the x, y and z data cubes fitted to the initial 3D surface model (Figure 3.9 a and c) were not significantly different (paired *t*-test; $p > 0.05$) to the dimensions of the data cubes fitted to the 3D surface model created from the re-segmented MR images (Figure 3.9 b and d). This finding was observed for both the innominate bone (participant C.14) and proximal femur (participant S.04). The mean dimensions of the grids when comparing the two models in the x, y and z-axes were 106.23 ± 0.07 mm, 135.77 ± 0.45 mm and 128.25 ± 0.00 mm for the innominate bone, and 92.78 ± 0.03 mm, 67.76 ± 0.02 mm and 96.19 ± 0.00 mm for the proximal femur. The combined models of the initial and re-segmented extracted surfaces, which had been overlaid in ParaView, revealed no obvious shape differences (Figure 3.10). This was deduced from there being no predominance of any one colour anywhere on either model, indicating that the segmentation process was consistent and repeatable when performed by the candidate.

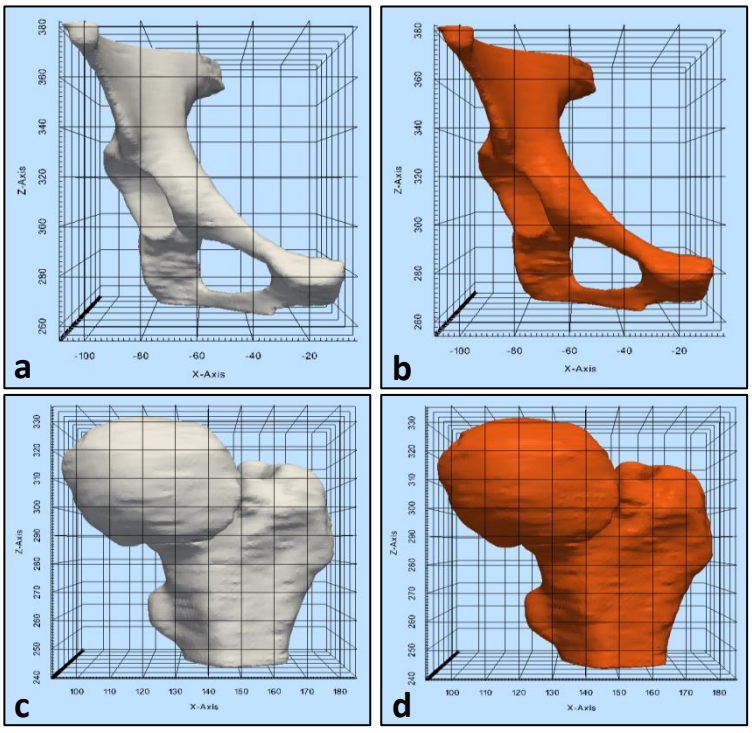

Figure 3.9: Cube axes (data cubes) fitted to the 3D surface models of the right innominate bone (C.14; a & b) and left proximal femur (S.04; c & d) created from the initial (neutral) and re-segmented (dark orange) MR scan images. All models are viewed anteriorly in ParaView.

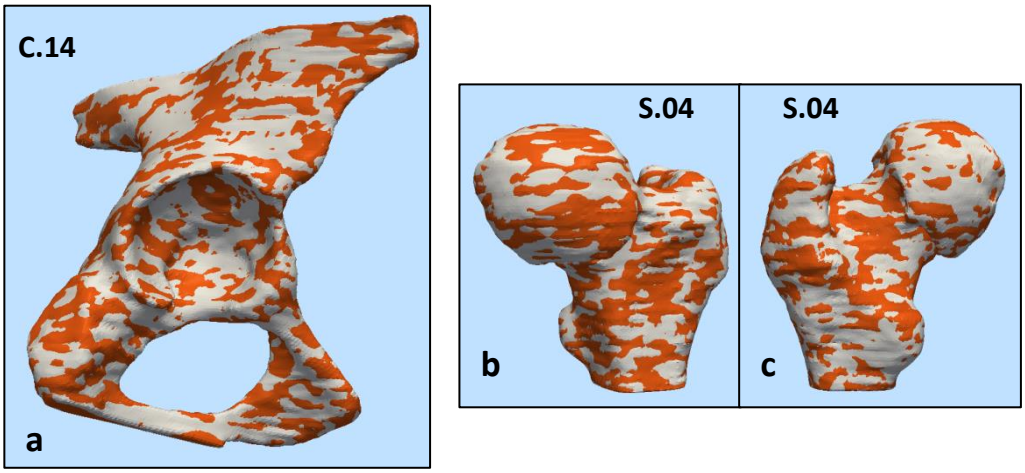

Figure 3.10: Initial (neutral) and re-segmented (dark orange) surface models of the right innominate bone of participant C.14, and the left anterior (b) and posterior (c) proximal femur of participant S.04, overlaid in ParaView to highlight any shape differences.

3.5 Two-dimensional Hip Morphology

The four geometric parameters explained in Section 2.8 (i.e. femoral neck-shaft angle [FNSA], acetabular index [AI], femoral head extrusion index [FHEI] and acetabular version [AV]) were explored by performing control (n = 15) versus study group (n = 14), and male (n = 12) versus female (n = 17) comparisons. One female in the study group did not have a 2D axial sequence due to pain (Section 3.1), hence AV measurements were completed on one less study participant. Mean results ± 95 % confidence limits (CL) have been reported. As the group sizes, particularly gender, were slightly uneven, the results of Levene's test for equality of variances was used to decide if independent *t*-tests assuming equal or unequal variances was used. The variances of the control versus study group measurements for AV, and male versus female FNSA were highlighted as being heterogeneous, and therefore the equal variances not assumed *t*-test result was used for this analysis. All other independent *t*-test results were interpreted with equal variances assumed (Field, 2009).

Mean FNSA, AI and AV angles were all slightly larger in the control group compared to the study group (Figure 3.11). Participants in both groups had anteverted acetabula, with no retroversion (i.e. AV < 0°) being observed. A marginally significant difference in AV was detected between the control and study groups ($p = 0.04$).

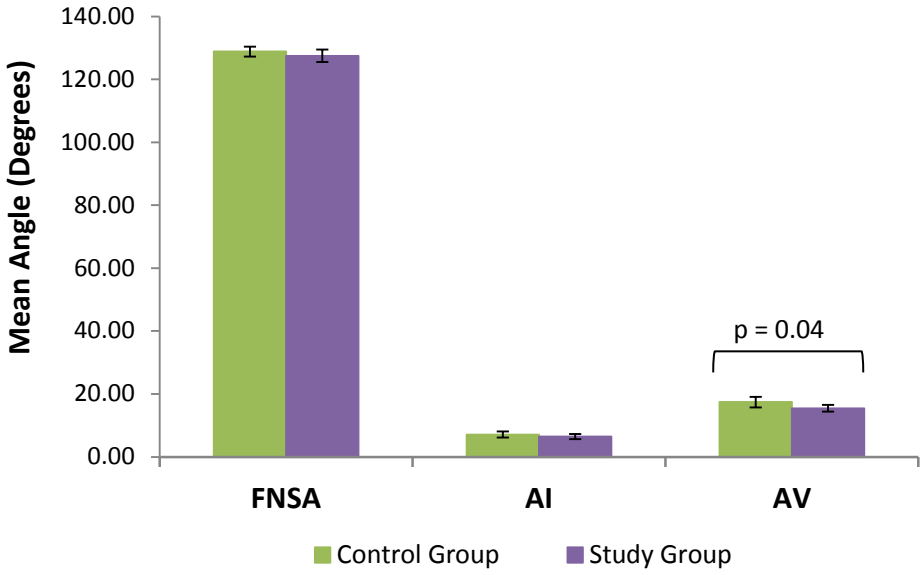

Figure 3.11: Mean angle ± 95 % CL for the femoral neck-shaft angle (FNSA), acetabular index (AI) and acetabular version (AV) for the control group (n = 15) and study group (n = 14 for FNSA & AI; n = 13 for AV).

Mean AV angles were slightly larger in females (n = 16) than males (n = 12), when comparing participants from both the control and study groups. The FNSA and AI were slightly larger in males compared to females, and the AV angle was larger in females (Figure 3.12). The differences observed between the male and female participants for FNSA, AI, and AV angles were not statistically significantly different ($p > 0.05$).

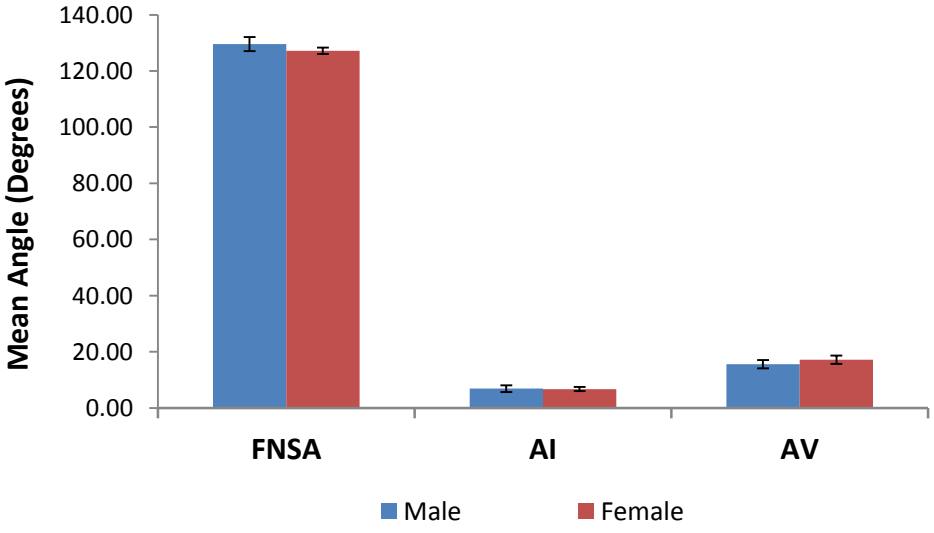

Figure 3.12: Mean angle ± 95 % CL for the femoral neck-shaft angle (FNSA), acetabular index (AI) and acetabular version (AV) for male (n = 12) and female (n = 17 for FNSA & AI; n = 16 for AV) participants.

The FHEI was significantly greater ($p < 0.05$) in the control group (n = 15) compared to the study group (n = 14), with values of ~88 % (± ~3 %) and ~81 % (± ~4 %) respectively, meaning that more of the femoral head was uncovered in the study group. There was a non-significant difference ($p > 0.05$) in the male FHEI values (n = 12; ~87 % [± ~3 %]) when compared to female values (n = 17; ~83 % [± ~4 %]) (Figure 3.13).

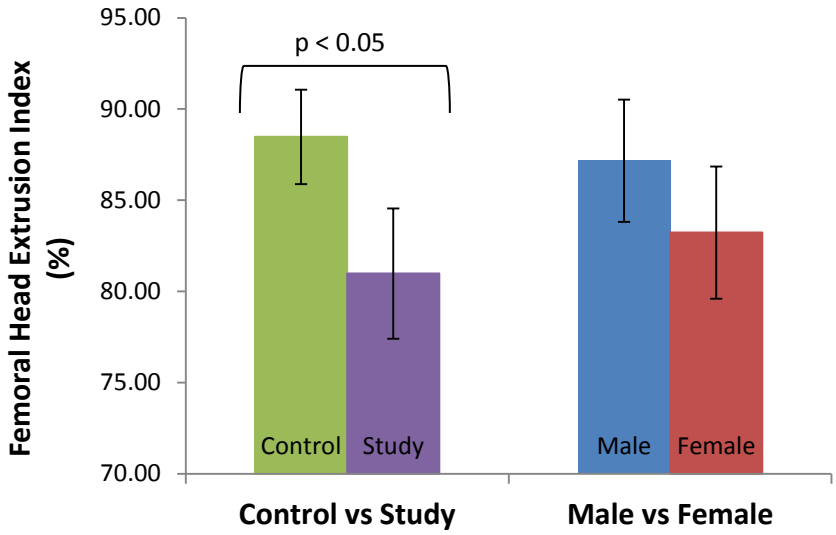

Figure 3.13: Mean % femoral head extrusion index (FHEI) ± 95 % CL for the control (n = 15) and study group (n = 14) comparison, and the male (n = 12) versus female (n = 17) comparison.

Further analysis of measurements A and B of the FHEI (see Figure 2.4 for details) revealed a significant difference ($p < 0.05$) in measurement A in the control group (4.85 ± 2.03 mm) compared to the study group (8.46 ± 2.64 mm), confirming that more of the femoral head was outside the lateral edge of the acetabulum (i.e. was uncovered) in the study group. OsiriX screenshot examples of the FHEI analysis illustrating the difference in measurement A observed between the study group and control group are shown in (Figure 3.14). Measurement of the horizontal width of the osseous aspect of the femoral head (measurement B) was significantly larger in males ($p < 0.05$) when compared to females, with dimensions of 37.64 ± 4.58 mm and 34.88 ± 1.89 mm respectively.

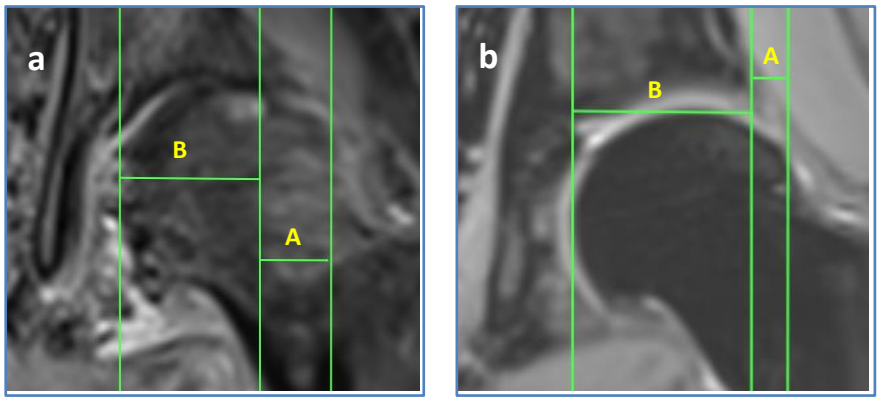

Figure 3.14: OsiriX screenshots of the FHEI analysis from a study group participant (a) and control group participant (b), illustrating the difference observed for measurement A (i.e. difference between the lateral edges of the acetabulum and femur).

3.6 Evaluation of the Acetabular Labrum and Transverse Acetabular Ligament (TAL)

The labrum and TAL were not identifiable circumferentially on the whole data set using one image sequence. It was therefore decided that a qualitative analysis of these structures on the MR images, rather a quantitative analysis using 3D surface models, was more appropriate.

3.6.1 Acetabular Labrum

The anterior and posterior sections of the acetabular labrum, which were visible on most of the axial SPACE images, had a triangular cross-sectional appearance in both the control group (Figure 3.15 a) and the study group (Figure 3.15 b). Some cystic lesions were identified around the labrum in the control group (n = 2), but none were clearly visible or defined in the study group. If present in the study group, then they could have been masked by the presence of an intra-articular joint effusion, as both have a high signal intensity on PD-weighted images, and this was evident on a number of the OA participant scans. An example of a labral, possible paralabral, cystic lesion is shown in Figure 3.15 (c). The outline of the labrum was not clearly identifiable on some slices in the image sequences, especially in the study group where participants had advanced OA with superior migration of the femoral head. A poorly delineated, and possibly degenerate, posterior section of labrum is shown in Figure 3.15 (d).

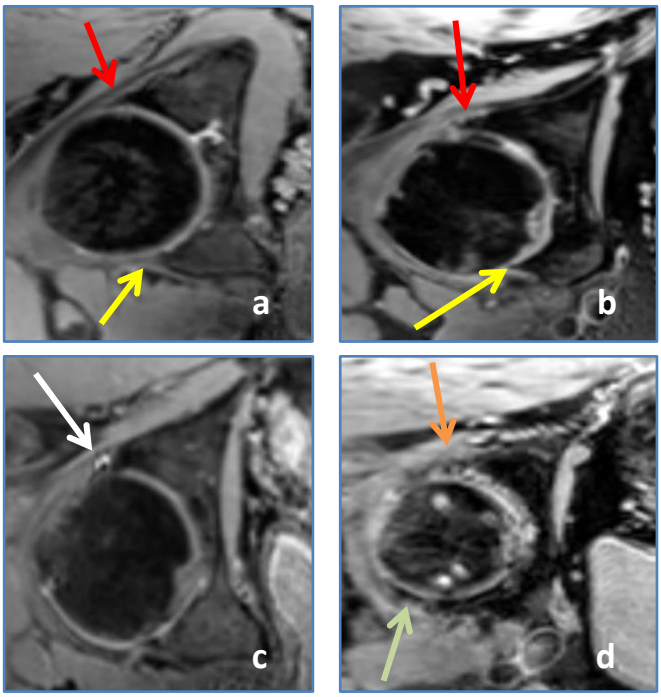

Figure 3.15: EndPoint screenshots from the axial MRI SPACE sequence scan from control group (a and c) and study group participants (b and d). Images (a) and (b) illustrate the triangular-shaped acetabular labrum posteriorly (red arrow) and anteriorly (yellow arrow). Image (c) is an example of a posterior cystic lesion (white arrow), and image (d) shows a poorly delineated labrum posteriorly (orange arrow) with better labral delineation anteriorly (green arrow).

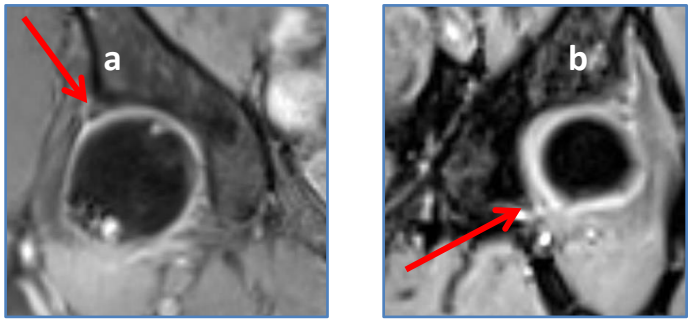

Figure 3.16: Coronal images showing a triangular cross-section of the acetabular labrum (red arrows) posterosuperiorly on a control group participant scan (a; right hip) and posteroinferiorly on a study group participant scan (b; left hip).

In general, the superior and inferior aspects of the labrum in both groups were poorly delineated in the axial plane. Superior and inferior aspects of the labrum could be viewed on some slices using coronal images (Figure 3.15), although the labrum was less well delineated anteriorly in the OA study group in this plane.

The parasagittal plane provided good views the labrum, both anteroinferiorly and posteroinferiorly, on a number of MR image slices for most participants in both groups (Figure 3.17).

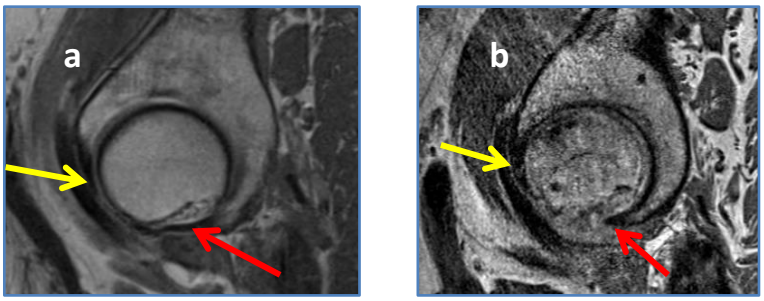

Figure 3.17: Parasagittal images showing a triangular cross-section of the acetabular labrum anteroinferiorly (yellow arrows) and posteroinferiorly (red arrows) on a control group participant scan (a; right hip) and study group participant scan (b; right hip).

3.6.2 Transverse Acetabular Ligament

The very high-resolution parasagittal MR sequence provided the clearest images of the TAL for both groups of participants, where it was visible on approximately three consecutive slices inferiorly. The TAL was visible on all parasagittal sequences in the control group (n = 15) and on 80 % (n = 12) of these scans, it was very clearly delineated. Example images from the control group of the TAL viewed using the parasagittal plane are shown in Figure 3.18.

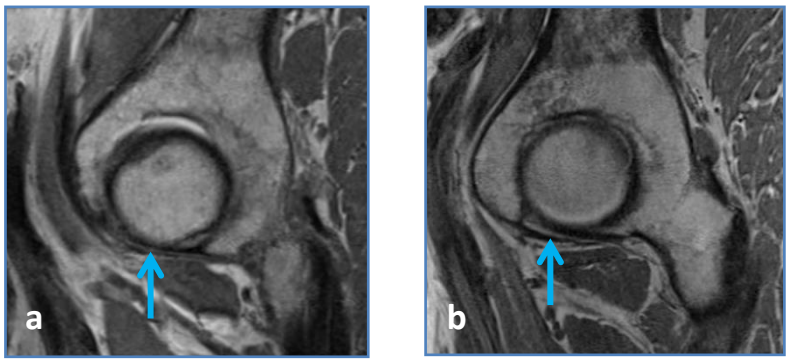

Figure 3.18: Cross-section of the transverse acetabular ligament (blue arrow) of the right hip viewed using the parasagittal image sequence (a and b are slices from two different control group participants)

It was possible to identify the TAL on 77 % (n = 10) of the 13 available parasagittal scans from the study group, and it was clearly delineated on 70 % (n = 7) of these. Examples of parasagittal image sequences from the study group where the TAL was visible (Figure 3.19 a and b) and not identified (Figure 3.19 c) are shown in Figure 3.19.

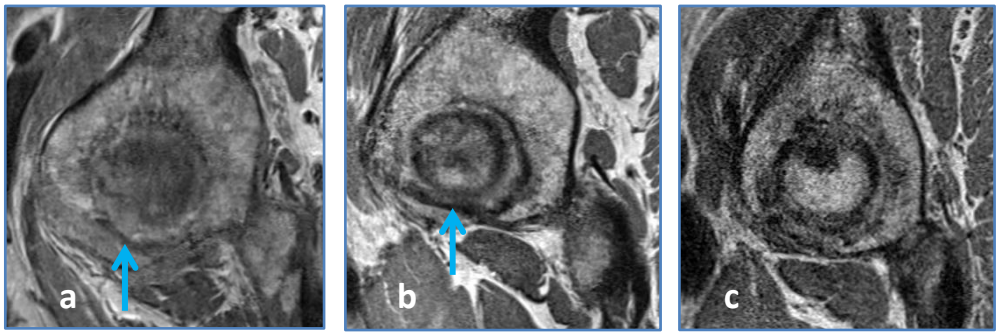

Figure 3.19: Inferior parasagittal image sequence slices from three participants in the OA study group. The TAL (cross-section) is reasonably well delineated on images (a) and (b) (blue arrows), but not identified on image (c).

3.6.3 3D Surface Models of the Labrum and TAL

The labrum and TAL were segmented in the axial plane on three isotropic SPACE scans, where these structures were considered sufficiently well delineated around the majority of the acetabular rim. This was completed for two participants in the control group and one participant in the OA hip study group (Figure 3.20).

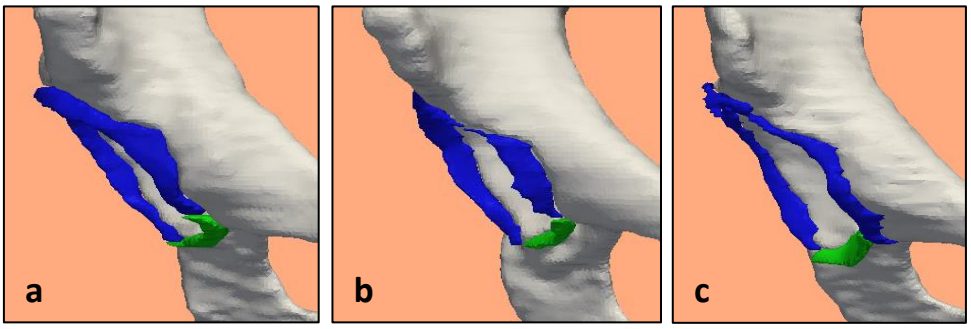

Figure 3.20: Surface models of the innominate bone (neutral), acetabular labrum (blue) and transverse acetabular ligament (green) for two control group participants (a and b) and one study group participant (c). All models are right hips viewed anteriorly in ParaView.

The labrum was noted to be deficient anterosuperiorly in the study group model (c) and one control group model (b) (Figure 3.20). The labrum followed the bony acetabular rim, filling the depression of the psoas valley anteriorly, in all models.

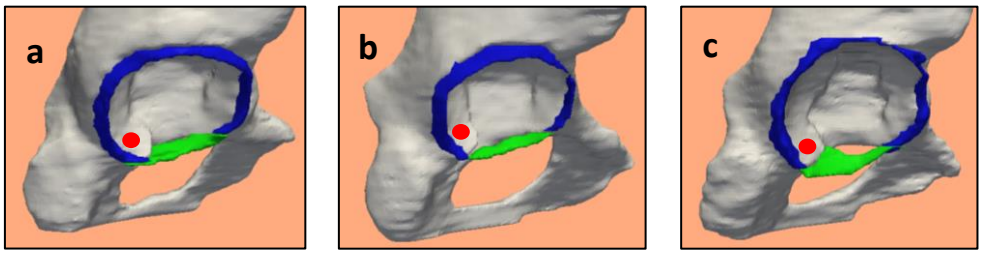

Figure 3.21: Surface models described in Figure 3.20 viewed laterally in ParaView to show the relationship between the TAL (green) and the labrum (blue). Red dot indicates the location of the posterior horn of the articular surface.

The TAL is a continuation of the labrum in Figure 3.21, traversing the acetabular notch on all three models; however, it originated from an area of bone below the posterior horn of the articular surface on model (a) but was wider and continuous with this surface on model (c). There was either incomplete segmentation of the posterior attachment on model (b) or it was deficient.

3.7 Three-dimensional Bone Morphology

The 3D morphology of the proximal femur and acetabulum was qualitatively assessed using EndPoint Surface ROI and ParaView viewing platforms (Sections 3.7.1 and 3.7.2). The principal components forming the ASMs were quantitatively analysed to compare shape distribution across the data set (Section 3.7.3) as well as 3D shape parameters (Section 3.7.4). Additionally, spheres were fitted to the femoral heads and lunate surfaces of the acetabula to investigate hip joint sphericity (Section 3.7.5).

3.7.1 Three-dimensional Morphology of the Proximal Femur

The most obvious differences between the 3D models in the control group (n = 15) and the models in the study group (n = 14) were located on or around the femoral head. The femoral head appeared to be reasonably spherical on the majority of control group models and the head and neck were well defined (Figure 3.22, C.04). Some evidence of small amounts of additional bony growth, possibly osteophytes (i.e. bone spurs), was observed on ~27 % (n = 4) of the models in the control group, which were located posteriorly on the head or superolaterally on the head-neck junction, giving the femoral head/neck a more irregular appearance.

All models in the study group with K/L grades 3 or 4 had an aspherical shaped head with evidence of osteophytic lesions located posteriorly and inferomedially on the

femoral head, and superolaterally on the femoral head-neck junction. Femoral heads were deemed aspherical if the bone deviated from a circle of best fit that was fitted to the centre of the femoral head on axial (i.e. transverse) and coronal MR images. Axial images were used to assess sphericity in the anterior-posterior directions and coronal images assessed sphericity in the superior-inferior directions. Examples of this method of assessment are shown in Appendix B, and a 3D example of an aspherical head is shown in Figure 3.22 (S.06). Most had evidence of multiple lesions with those located posteriorly appearing to be the most prominent on the majority of surface models. The study group participant classified as K/L grade 2 had evidence of a small osteophytic lesion superolaterally on the femoral head. Bony growth was also observed on the medial aspect of the femoral head around the fovea capitis on ~36 % (n = 5) models, which could have been from the formation of osteophytes and/or from calcification of the ligamentum teres. Severe wear/damage causing obvious flattening of the femoral head was observed on the superior aspect of ~57 % (n = 8) of the study group models. Variations in the FNSA and the morphology of the greater and lesser trochanters, with respect to size, position and orientation was observed on models from both groups in the data set. These morphological variations displayed no obvious trends that could be used to identify the model as being from the control or study group.

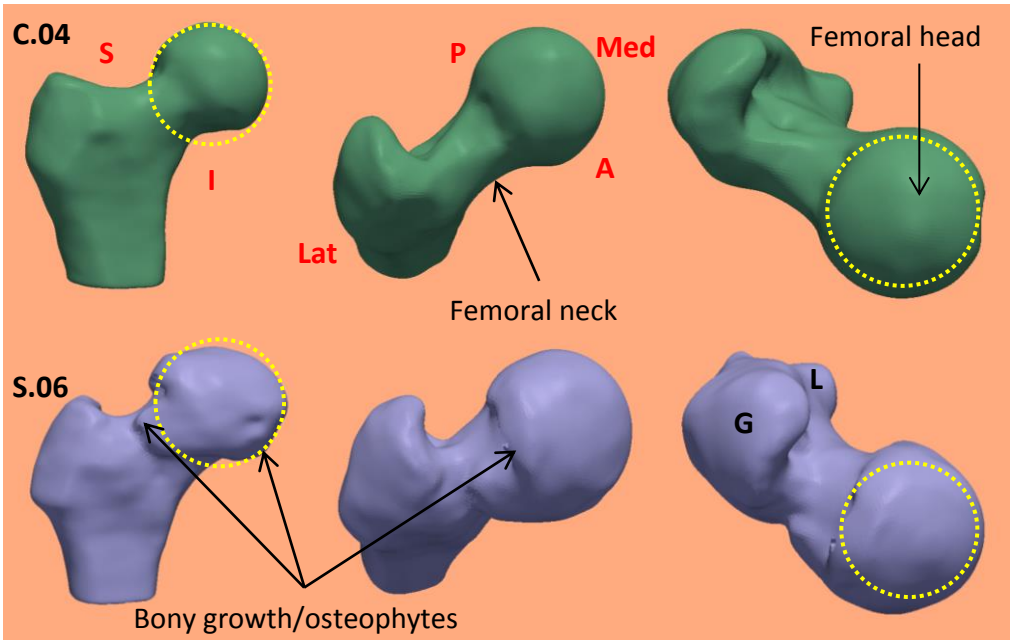

Figure 3.22: 3D ASMs of the proximal femur from a control group participant (C.04; green model) and study group participant (S.06; purple model) viewed in ParaView. The yellow circles highlight differences observed in head sphericity. S = superior, I = inferior, A = anterior, P = posterior, Lat = lateral, Med = medial, G = greater trochanter, L = lesser trochanter.

3.7.2 Three-dimensional Morphology of the Acetabulum

Morphological differences between the control and study groups were less evident in the acetabulum, and shape variations of the acetabular rim profile were observed across the whole data set (Figure 3.23). The 3D rim profiles were visually assessed and the anterior and posterior acetabular walls were and classified as irregular, straight, or curved/angular (Maruyama *et al.*, 2001; Govsa *et al.*, 2005; Vandenbussche *et al.*, 2008). The posterior rim configurations in the control group were 20 % irregular, 33 % curved or angular, and 47 % straight. In the study group, posterior rim profile shapes were more evenly distributed with 36 % irregular, 36 % curved or angular, and 28 % straight. Anteriorly, the acetabular rim was generally curved with the depth of the psoas valley varying but with no obvious trend. A small number of participants (n = 2 control; n = 3 study) had an anterior wall that was almost straight, with a very shallow psoas valley.

The only notable difference between the two groups was located superiorly, where the profile of the rim appeared to extend further laterally (i.e. over the femoral head), in the study group compared to the control group. This apparent increased depth of the acetabular roof was observed on 50 % (n = 7) of the study group models, but only n = 2 of the control models. This variation was also less well defined in the control group, an example of which is shown in Figure 3.23 (C.10).

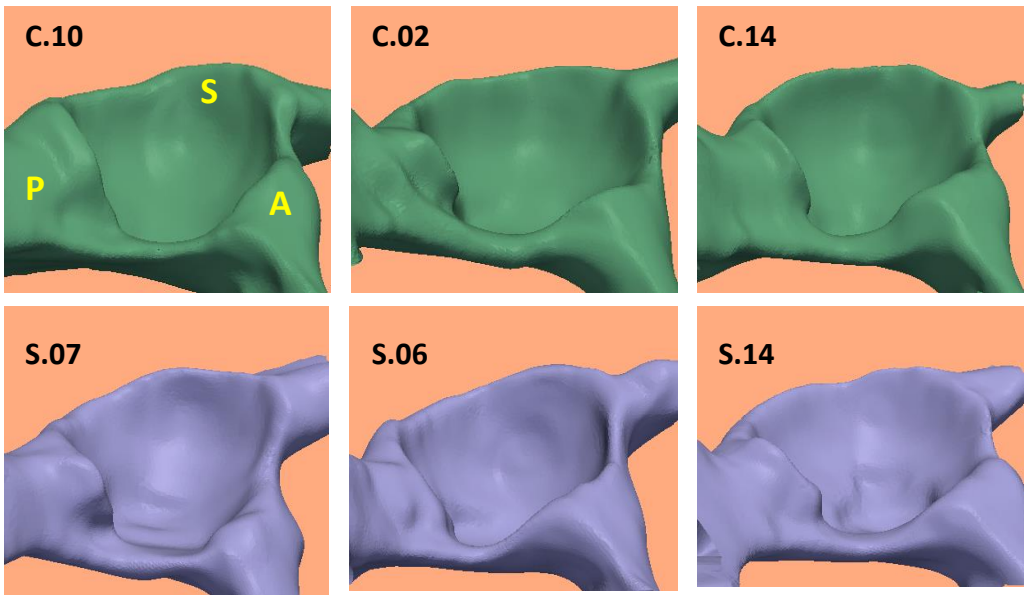

Figure 3.23: 3D ASMs of the acetabulum, n = 3 from the control group (green, C.10, 02, 14) and n = 3 from the study group (purple, S.07, 06, 14) viewed in ParaView. C.10, S.07 & S.14 are male participants and C.02, C.14 & S.06 are female participants. P = posterior, S = superior, A = anterior.

3.7.3 Shape Distributions

Sammon maps illustrating the 2D shape distributions for the control (n = 15) and study (n = 14) groups, and the male (n = 12) and female (n = 17) participants were plotted for femoral and pelvic models (Section 2.10.1). Mean x and y values for the groups were also calculated and plotted on the maps. The Sammon map created for the control versus study group femoral model data showed a random distribution of pots, with no obvious separation or boundary between the two groups (Figure 3.24). The mean group values (x, y) were 9.14, 7.12 for the control group and 9.13, 7.12 for the study group, which also suggests that a close geometric relationship exists between femoral shape in the two groups.

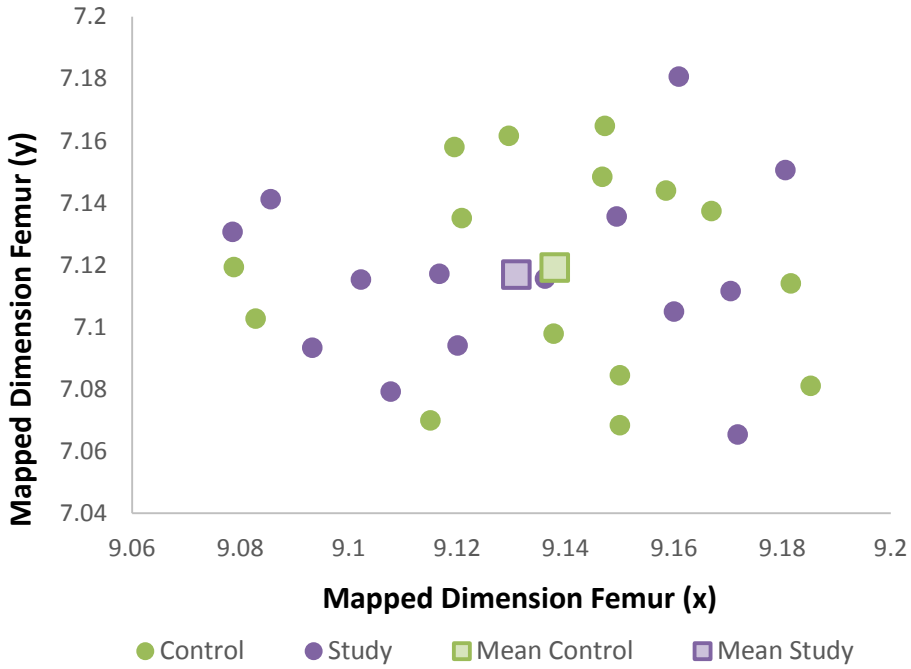

Figure 3.24: Sammon map showing the 2D shape distribution of n = 15 control group femoral models and n = 14 study group femoral models. Mean values for the two groups are also shown.

Some separation of femoral shape distribution was observed in Figure 3.25, which is a Sammon map that was plotted to compare male and female participants collectively from the control and study groups. In this map, male participants are, in the main, located on the left with slightly lower values on the x axis. Female participants are relatively well clustered on the right of the map, with higher values on the x axis. The distance between the mean plots is also larger than that observed in Figure 3.24, with

x, y values of 9.12, 7.12 and 9.15, 7.12 for male and female participants respectively, suggesting that gender-related differences in femoral shape distribution may exist.

The distribution of pelvic shape model plots on the control versus study group, and the male versus female participant Sammon maps, were similar to those observed on the control versus study group map for the femur in Figure 3.24. On both pelvic maps (not shown), the plots appeared to be randomly scattered and the mean values were located almost adjacent to each other. This suggested a close geometric relationship existed for pelvic geometry across the whole data set.

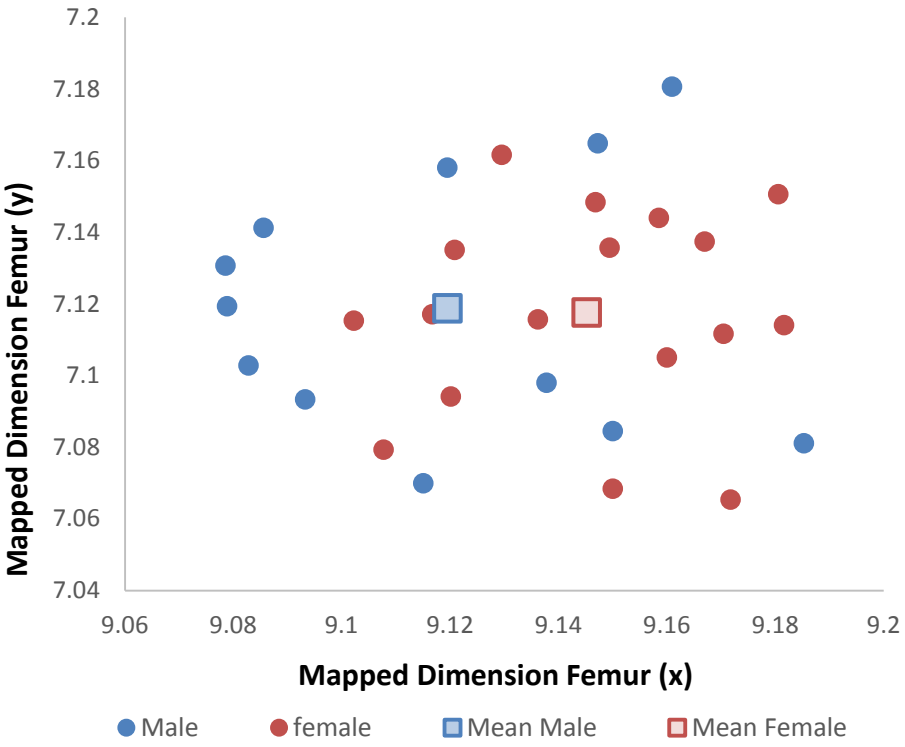

Figure 3.25: Sammon map showing the 2D shape distribution of the femoral models for n = 12 male participants and n = 17 female participants. Mean values for the two groups are also shown.

3.7.4 Shape Parameters

The Fisher's LDA conducted on the principal components of the femoral models (n = 29; n = 15 control and n = 14 study), produced a Wilks' Lambda value of 0.02. The same analysis conducted on the principal components of the pelvic models (n = 29; 15 x controls and 14 x study), returned a Wilks' Lambda value of 0.04. Wilk's Lambda values

can be used to assess the discriminatory power of the model and range from 0.0 (perfect discriminatory power) to 1.0 (no discriminatory power) (Field, 2009). Therefore, these results suggest that the femoral and pelvic shape parameters (principal components) could both potentially discriminate between control and study group ASMs, however, as Wilk's Lambda for the femoral results was closer to zero the shape parameters for these models may have greater discriminatory power.

The aim of conducting the leave-one-out analysis as part of the LDA was to predict how well the shape parameters could be used to classify a femur or pelvis into the correct group, i.e. either the control (n = 15) or study (n = 14) group (Section 2.10.2). The results of this cross-validation test for the femoral analysis revealed that 80 % (n = 12) of control femurs and 79 % (n = 11) of study group femurs were placed into the correct group, meaning that the femoral shape parameters correctly classified 79.3 % of the cross-validated group cases. The pelvic analysis showed that only 60 % (n = 9) of control pelves and only 57 % (n = 8) of study group pelves were placed into the correct group. This meant that only 58.6 % the cross-validated pelves were classified into the correct group. These classification predictions support the Wilk's Lambda results, which showed that the femoral shape parameters had greater discriminatory power.

3.7.5 Hip Joint Diameter

3.7.5.1 Sphere Dimensions

A 2D assessment of femoral head sphericity was conducted on each participant using the method described in Appendix B, however, in order to assess the sphericity of the 3D ASMs, least squares spheres were fitted to each hip joint (Section 2.10.3). The dimensions (i.e. radius) of each fitted sphere also enabled hip joint diameter to be measured and compared. The mean radius (r) ± SD of the spheres fitted to the femoral heads and lunate surfaces of the acetabula are presented in Table 3.3. The data shows that the radial range of the spheres fitted to the femurs and pelves was very similar. No significant differences in size were identified when comparing the control and study group femoral (*t*-test; $p > 0.05$) and pelvic (*t*-test; $p > 0.05$) sphere radii. When comparing the means in Table 3.3, the radius of the sphere fitted to the lunate surfaces of the pelves was ~3 mm larger than the sphere fitted to the femoral heads in both the control and study groups.

Table 3.3: Mean radius (r) ± standard deviation (SD) of the spheres fitted to the femoral heads and acetabular lunate surfaces of the pelves.

	Femoral Spheres Mean r ± 95 % SD (mm)	Pelvic Spheres Mean r ± 95 % SD (mm)
Control group (n = 15)	22.83 ± 2.07	25.89 ± 2.41
Study group (n = 14)	23.07 ± 1.78	25.68 ± 2.06
Whole data set (n = 29)	22.95 ± 1.90	25.79 ± 2.20

The Bland-Altman method was used to explore differences in femoral and pelvic sphere radius sizes in the control group (n = 15), study group (n = 14), and for the whole data set (n = 29). Differences were calculated by subtracting the radius of the sphere fitted to the lunate surface of the pelvis from the radius of the sphere fitted to the femoral head, and mean sphere radius measurements ([pelvic sphere r + femoral sphere r] / 2) were also calculated. The results of these calculations (i.e. difference and mean sphere radius measurements) were used to create Bland-Altman plots, together with the estimated bias (mean difference in sphere radius measurement), and the calculated upper and lower 95 % confidence limits of the differences. The results of these calculations have been reported in Table 3.4.

Table 3.4: Estimated bias (i.e. mean difference in sphere radius [r] measurement) and the 95 % confidence limits (CL) of the differences in sphere radius (r).

	Estimated Bias (mm)	95 % CL of the differences (mm)
Control group (n = 15)	3.06	4.43 (upper), 1.70 (lower)
Study group (n = 14)	2.61	5.78 (upper), -0.56 (lower)
Whole data set (n = 29)	2.85	5.25 (upper), 0.44 (lower)

The Bland-Altman analysis revealed 95 % confidence intervals of ± 1.37 mm for the control group and ± 3.17 mm for the study group, meaning that the spread of the differences (i.e. 95 % CL) between the control group pelvic and femoral spheres was more than double that of the study group. The inter-group analysis of the whole data set reduced the 95 % CI to ± 2.40 mm. A Bland-Altman plot of the inter-group analysis

showing the differences in sphere radius between the pelvis and the femur, for both the control group and the study group, is shown in Figure 3.26.

The data plots for the control and study group samples shown on Figure 3.26 were evenly dispersed above and below the mean difference (bias) line, however, as the mean sphere radius increased (i.e. along the x axis), the difference between the pelvic and femoral sphere size, plotted on the y axis, also increased. With the exception of one outlier, a larger radial difference with increasing sphere size was observed in data from the study group in models with mean sphere radii of ≥ 25 mm. In general, control group sphere size differences remained relatively constant regardless of size.

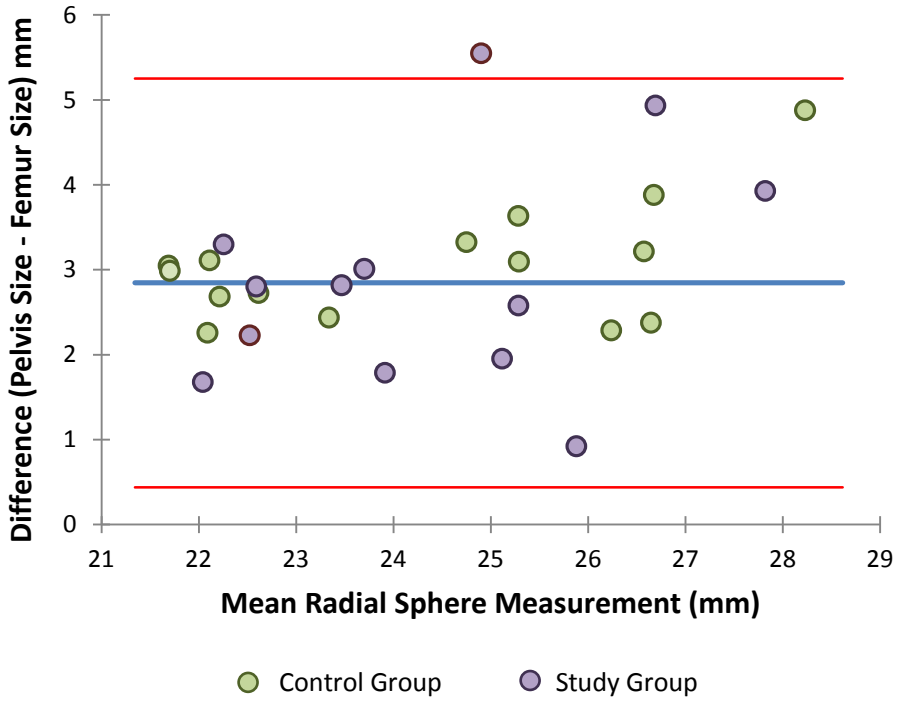

Figure 3.26: Bland-Altman plot of the difference in radial size (Pelvis – Femur) against mean radial ([Pelvis + Femur] / 2) for each sphere in the control group (n = 15) and study group (n = 14). Mean difference (blue line) and 95 % confidence limits of agreement (red lines) of the mean difference in pelvic and femoral sphere radii are shown.

3.7.5.2 Assessment of Sphericity

Least squares spheres were fitted to the femoral heads and acetabula of each ASM and the maximum and minimum departure of the 3D model from the fitted sphere (residual errors) was used to assess the shape of the hip joint models. The magnitude and

direction of any parts of the ASM lying inside or outside the fitted sphere were plotted as vector graphics so that the departure from the fitted sphere of each hip joint could be visualised in 3D. Residual errors for the femur were calculated using the superior two thirds of the femoral heads (h), as this has been described in the literature as being the spherical area (Hossain and Andrew, 2008), and the lunate surface of the acetabulum (a) was used for the pelvic residual errors. The area around the femoral fovea capitis was excluded from the analysis.

The departure from the fitted sphere of three participants from the control group are shown in Figure 3.27 as 3D vector graphics. The less intense coloured shading on residuals C.04 and C.07 denotes a small magnitude of deviation of the model from the fitted sphere, which suggests that the articulating femoral heads and lunate surfaces of these participants are relatively spherical. Example C.01 in Figure 3.27, however, displays some more intense areas of shading suggesting the presence of a slightly less spherical hip joint. The residuals from the lunate surfaces followed a similar variable pattern to that observed on the femoral heads. These three results reflect the observations made for all the residuals in the control group data, where 2/3 of the joints (n = 10) appeared to be relatively spherical with the remaining 1/3 (n = 5) displaying evidence of reduced sphericity of the femur and acetabulum.

Examples from three paired residuals from the OA study group are shown in Figure 3.28. All three femoral residuals show obvious flattening of the head superiorly (dark blue shaded areas), which is also evident posteriorly (not shown in Figure 3.28), and anteriorly in residuals S.04h and S.14h. This is contrary to S.06h, where the posterior and anterior aspects of the femoral head appear to lie outside the boundary of the fitted sphere (dark red area). Viewed collectively, the residuals for the study group femurs suggested that all were asymmetrical with superior flattening of the head being observed in the whole data set to varying degrees. Posterior to anterior changes in sphericity were more variable. The sphericity of the lunate surfaces (a) also varied posteroanteriorly with no obvious pattern, which was a similar observation made from the control group data. In the study group, the magnitude of deviation from the sphere was smaller for the pelvis than the femur; however, asphericity was greater in the study group compared to the control group, with darker colours in the residuals being observed across the whole hip joint.

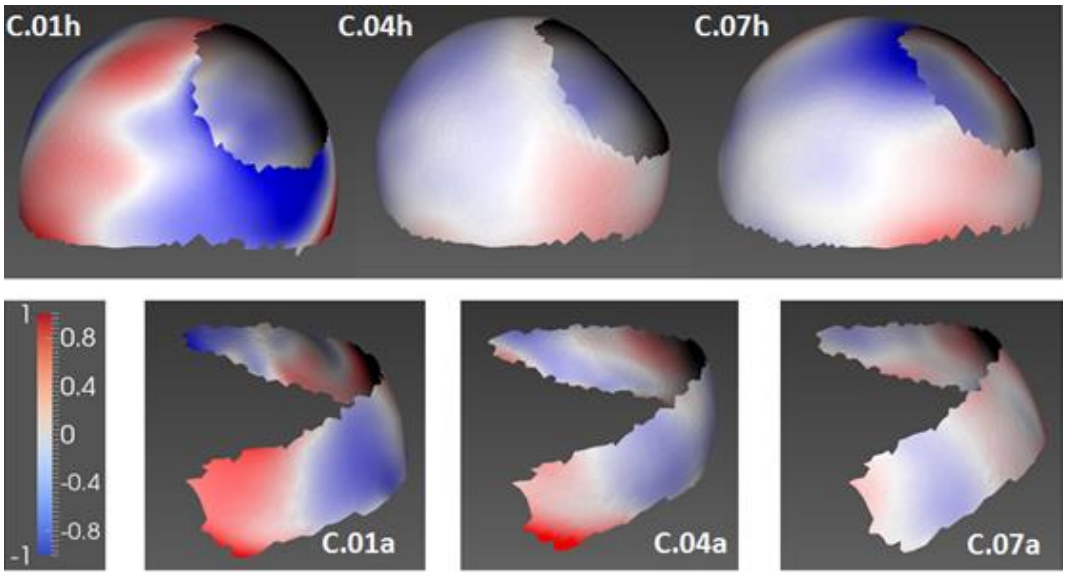

Figure 3.27: Paired examples of residual errors following sphere fitting to the femoral head (h), and acetabular lunate surface (a) of three control group participants. Residuals were viewed as 3D VRML vector graphics using Cortona3D. Areas of the model lying outside the sphere have a value of 0 to +1 and areas lying inside have a value of 0 to -1. Participants C.04 and 07 are female and participant C.01 is male.

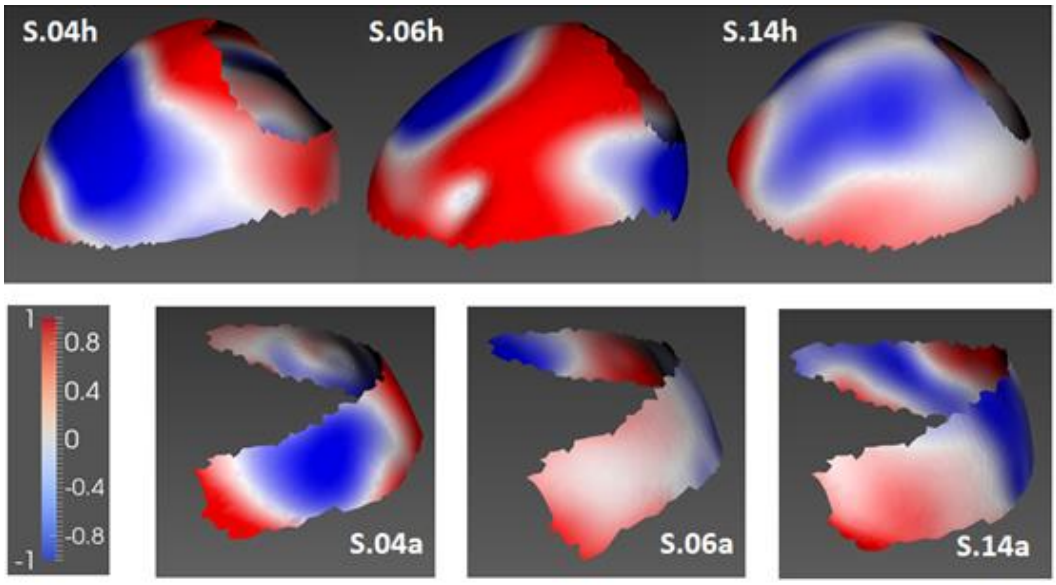

Figure 3.28: Paired examples of residual errors following sphere fitting to the femoral head (h), and acetabular lunate surface (a) of three OA study group participants (All K/L Grade 4). Residuals were viewed as 3D VRML vector graphics using Cortona3D. Areas of the model lying outside the sphere have a value of 0 to +1 and areas lying inside have a value of 0 to -1. Participant S.06 is female and participants S.04 and 14 are male.

3.8 Discussion

This study used 3.0 T MR images to compare the geometry of the hip joint in a study group of hip osteoarthritis patients and a control group of asymptomatic participants, in order investigate the hypothesis that there are fundamental differences in geometry in subjects with hip OA compared to those without. Additionally, the study of hip geometry (SHIG) aimed to segment the labrum and TAL circumferentially around the acetabulum so that the 3D surface models could be used to investigate the use of these structures as local landmarks when positioning the acetabular cup during THR. This discussion provides a review of the methods and processes developed and used in the study, and an interpretation of the results in order to address the aims of the study and the null hypothesis, which was that there are no differences in geometry in participants with hip OA when compared to age-matched asymptomatic participants.

3.8.1 Study Participants

The initial recruitment target for this study was n = 30 in each group, however, due to the recruitment process being unpredictably slow this was reduced to n = 15 in each group. At the end of the recruitment stage, which was conducted over five years, the study comprised of n = 15 control participants (n = 7 male; n = 8 female; age 50–73) and n = 14 study group participants (n = 12 male; n = 17 female; age 68–82). More female than male OA patients were referred to the candidate and subsequently included in the study group, which supports current data showing that of the 71,075 patients aged 50 to 89 years old who underwent primary THR in the UK during 2013/14, 61 % were female and 39 % were male (NJR, 2014). The attrition rate was low in both groups (control, n = 3; study n = 11), however, as summarised in Table 3.1, the number of potential participants for the study group who were either unsuitable or declined participation was large and accounted for ∼77 % (n = 83) of the 108 patients referred to the candidate for possible inclusion. Participants in the control group had voluntarily approached the candidate with a view to taking part in the study, which possibly explains why the recruitment rate was higher in this group compared to the study group, who had been referred to the candidate as potentially suitable participants by the orthopaedic team at CAH. Another reason for the extremely poor hip OA patient recruitment rate was due to their concerns about the relatively long scanning time, which was ∼50 minutes. Patients with hip OA often find periods of inactivity increases

pain (Doherty *et al.*, 2005), and therefore, although the scanning protocol was designed specifically for this project, the length of the scan time was found to be unsuitable for a number of potential OA participants.

All study group participants were assigned K/L grades by a consultant radiologist and subjectively assessed their own symptoms using the OHS. The majority of participants had radiographic features of hip OA that matched the subjective assessment of their symptoms (Table 3.2). For example, participants with K/L grades 3 (moderate OA) or 4 (severe OA) had an OHS of 8 to 25, indicating possible moderate to severe hip OA. However one participant (S. 05), had minimal radiographic features (K/L grade 2) with a perceived disability indicative of moderate to severe hip OA (OHS 24). Symptomatic hip OA with minimal or no evidence of radiographic OA, as observed in this participant, has previously been reported in the literature (Bijlsma and Knahr, 2007).

3.8.2 Image Acquisition and Accuracy of the 3D Models

Two methods were used to measure the effect of applying different distortion correction algorithms to the MR images. The first method involved fitting a data cube (cube axes) to the outer corners of the 3D models, created from the segmented images, and recording the dimensions along the x, y, and z-axes (Figure 2.2). A comparison of the 2D corrected model dimensions with the 3D corrected models showed small, non-significant differences along the x and y-axes of the pelvis and femurs. The second method involved overlaying the images, and this showed that applying 3D distortion correction reduced the amount of distortion, observed as generally bending towards the midline on the models, at the top of the pelvis and on the shaft of the femurs (Figure 3.3 and Figure 3.3). The y axis on the models (running inferosuperiorly) corresponded with the main 3.0 T magnetic field of the scanner (known as B_0), which runs longitudinally down the centre, and the x axis on the models (running horizontally from right to left) was orthogonal to B_0. The most likely explanation for the geometric distortion is slight B_0 inhomogeneity that is known to occur distally from the magnetic field isocenter, and orthogonal to this, distortion can also arise from nonlinearities in the applied gradient fields used for spatial localisation (McRobbie *et al.*, 2007; Moser *et al.*, 2009). The distortion observed around the centre of the hip joint was, however, minimal and non-systematic, and was reduced distally by the application of the 3D correction algorithm.

At higher field strengths, such as 3.0 T, it is harder to create a homogeneous static field and this can increase the risk of geometric distortion, which can affect how accurately the size, shape and/or orientation of the tissue is represented on the MR image. In addition to homogeneity of the background field (B_o), the linearity of the applied RF gradients and magnetic susceptibility of the imaged tissues can affect the geometric accuracy of the images (Baldwin *et al.*, 2007). The accuracy of the 3D distortion correction was not specifically checked in this study, it was only compared to 2D distortion correction, however, biannual checks conducted as part of the CAH quality assurance procedures (Sections 2.6.1 and 3.3) specify a maximum geometric distortion allowance of ± 2 mm when using the ACR accreditation phantom (Jackson *et al.*, 2010). To minimise the incidence of B_o inhomogeneity participants were carefully positioned with their hips in the isocenter of the scanner, and furthermore, the 3D correction algorithm was applied to all images. Considering these factors, it was therefore felt that sufficient precautions had been taken to reduce the risk of any potential experimental artefact to an acceptable level.

The process undertaken to create the 3D surface models and the accuracy and inter-rater reliability of the segmentation technique was assessed to ensure that it was repeatable, and that it provided geometric measurements that were considered accurate. Measurements taken from a 3D surface model that had been created from the segmented MR scan of a porcine tissue substitute using ParaView, and measurements taken from the actual tissue sample using ImageJ, were found to be closely matched with only a slight variation being observed around the acetabular fossa (Section 3.4.1). Only osseous structures were segmented from the porcine scan and therefore, the non-significant difference in measurement between the 3D model and the actual tissue probably arose from some of the soft tissues, namely the fat pad and ligamentum teres, being included in the tissue sample measurements. It was not possible to segment the labrum as it was very poorly delineated due to the immaturity of the tissue sample, however, as only osseous structures were segmented for the SHIG study this was acceptable. If future studies of human hip geometry are undertaken using this method that include an analysis of the labrum, then this work should be repeated using a skeletally mature tissue substitute model where the labrum should theoretically be better delineated.

The intra-rater reliability of the segmentation method and ability of the investigator (i.e. candidate) to obtain the same geometric 3D surface model on more than one occasion when segmenting the osseous structures was assessed. One control group hemi-pelvis and one study group femur, both randomly chosen, were re-segmented and compared using data cubes and by overlaying the models in ParaView (Section 3.4.2). Only a small random sample was re-segmented, however, due to the excellent agreement between the original and retest extracted 3D surface models, it was not thought necessary to do further repeats as the candidate was confident regarding the intra-reliability of the process.

3.8.3 Two-Dimensional Morphology

Morphometric hip parameters were measured directly from the 3D distortion corrected MR images to compare the two groups of participants and look for potential indicators of any underlying anatomical abnormalities, e.g. dysplasia or FAI, that may contribute to the development of hip OA (Murphy *et al.*, 1995; Ganz *et al.*, 2003; Beck *et al.*, 2005; Ganz *et al.*, 2008). Male (n = 12) and female (n = 17) participants were also compared as the groups contained both genders, and studies that have used various forms of 2D and 3D imaging methodologies provide evidence to suggest that morphometric parameters vary with gender (Jacobsen and Sonne-Holm, 2005; Traina *et al.*, 2009; Atkinson *et al.*, 2010; Gosvig *et al.*, 2010; Nakahara *et al.*, 2010). It is important to note that this could be a confounding factor for the SHIG study as it is possible that with such small group sizes, any morphological differences between the control and study groups could be influenced by gender. However, it should also be remembered that the male versus female analysis contained both control and hip OA patients, therefore this should also be considered before drawing any conclusions relating to gender.

The FNSA, AI, FHEI and AV were chosen as they have been well documented for use with MRI (see Section 2.8 for details). All mean measurements were within the reported normal ranges for adult radiographic morphometric parameters, although these vary slightly between authors, primarily due to the heterogeneous samples and methodologies used to measure them. In general, they are considered to be in the region of the following: FNSA = 120° to 130°; AI = 0° to 10°; FHEI = ≥ 75 %; AV = 13.3° to 26.3° (Palastanga *et al.*, 2002; Beall *et al.*, 2008; Clohisy *et al.*, 2008; Stelzeneder *et al.*, 2012). Control group measurements were all larger than those of the study group with

significant differences ($p < 0.05$) being observed for AV (control, 17.42 ± 3.03°; study, 15.44 ± 0.14°), and FHEI (control ~88 % [± ~3 %]; study ~81 % [± ~4 %]). Male versus female parameters were similar and not significantly different. Although the difference in some parameters was statistically significant, the group sizes were small, and the measurements fell within the reported range of normal values, therefore, these results are unlikely to be clinically significant.

In advanced hip OA, migration of the femoral head, most commonly superiorly, has been observed with superolateral, intermediate, and superomedial directions of migration having been described in the literature (Resnick, 1975; Ledingham *et al.*, 1992). Having broken down the components of the FHEI measurements, the mean value for "A", which measures how much of the femoral head lies outside the lateral edge of the acetabulum (refer to Figure 2.4 c), was significantly larger in the study group (8.46 ± 2.64 mm) compared to the control group (4.85 ± 2.03 mm) (Figure 3.14). Reduction of the joint space superiorly was evident on a number of the study group scans; therefore, this result suggests that superolateral migration of the femoral head had occurred in a number of participants in the study group.

In addition to providing quantitative measurements to compare the geometry of the two groups, these results also provided information relating to the spatial orientation of the hip joint that will be used when positioning test samples in future *in vitro* simulation studies investigating the tribology of the natural human hip (Section 7.6).

3.8.4 Intra-articular Soft Tissue Analysis

A number of authors have reported that high resolution (3.0 T) non-contrast MRI provides good quality musculoskeletal imaging of the hip joint, and is a good diagnostic tool for intra-articular pathology, for example lesions affecting the articular cartilage and labrum (Mintz *et al.*, 2005; Watanabe *et al.*, 2007; Mamisch *et al.*, 2009; Potter and Schachar, 2010). Non-invasive (i.e. non-contrast) imaging was therefore chosen for this study in preference to MR arthrographic techniques, which require the use of intra-articular injections, as there is little or no risk of complications or side effects.

Analysis of the MR images revealed that the soft tissues of interest (labrum and TAL) were visible in locations where they were orthogonal to the plane of the MR image (Section 3.6), however, it was not possible to visualise them circumferentially around the hip joint in any single image sequence. Where visible, the labrum had a triangular

appearance, which is well reported in the literature (Narvani *et al.*, 2003; Beaule *et al.*, 2009; Field and Rajakulendran, 2011), and labral pathology was detected in both control subjects and study subjects. The presence of labral tears has been suggested as a possible risk factor for hip OA and the incidence of asymptomatic labral tears has been reported in older adults (McCarthy *et al.*, 2001; Seldes *et al.*, 2001; Jessel *et al.*, 2009), therefore, it was not surprising that there was evidence of labral pathology in both groups.

Although the TAL was not segmented for the whole data set, it was visible when viewed cross-sectionally using the para-sagittal sequence on all control group images, and on 76.9 % (10/13) of the available study group images. Reports regarding the identification of the TAL intra-operatively have been mixed, with Archbold *et al.* (2006) and Miyoshi *et al.* (2012) reporting the TAL as being visible in 99.7 % (997/1000) and 81.6 % (93/114) patients respectively, and Epstein *et al.* (2011) reporting visibility of the ligament in only 46.8 % (30/64) of OA patients intra-operatively. Despite the small number of participants in the SHIG study, the results suggest that the TAL can remain intact in the presence of advanced hip OA. However, it was not possible to make any conclusions regarding the efficacy of using the TAL for cup positioning in THR, as it could not be segmented with the acetabulum in the axial plane.

The joint space between the two articular cartilage surfaces was quite poorly delineated (except in OA patients who had significant joint effusion creating a natural contrast highlighting the joint space), and similarly to the labrum, it was difficult to visualise in one plane and was therefore not included when segmenting the bone. Segmentation of the osseous structures was completed in the axial plane, as maximal cross-sectional images of the bone were visible on each slice in this plane due to the spatial orientation of the hip joint.

The findings of this study support the use of non-contrast 3.0 T MRI of the hip joint for detecting hip pathology and reporting clinical findings relating to the soft tissues. However, creating surface models of the labrum and TAL for 3D analysis was considered inappropriate from the image sequences used in this study due to the risk of error arising from a number of different views/planes being required to segment the complete structures. Recommendations for future work relating to this have been made in Chapter 7.

3.8.5 Three-dimensional Analysis

Visual assessment of the ASMs was completed systematically by the same observer (the candidate) to maintain consistency. Morphologic differences of the proximal femur observed in the study group were, as expected, consistent with osteoarthritic changes, with osteophytes and flattening of the femoral head superiorly being the most predominant features. Two types of OA have been described in the literature; hypertrophic OA, where individuals often develop large osteophytes, and atrophic OA, where individuals will develop very few osteophytes (Solomon, 1976) and of these, hypertrophic OA has been regarded as being more prevalent (Schnitzler *et al.*, 1992). The results of the SHIG study suggests that the majority of study group participants had pathology indicative of hypertrophic OA, as relatively large areas of extra bone formation were observed on all 3D femoral models created from MR images with K/L grades 3 and 4. The extra bone growth was located either superolaterally on the weight bearing areas of the femur, or inferomedially in the non-weight bearing region (Section 3.7.1). Using the classification system for describing osteophytes of the femoral head and neck created by Jeffery (1975), and later developed by Resnick (1983), the lesions observed in the SHIG study had the appearance of marginal/epiarticular osteophytes and femoral neck osteophytes. Marginal osteophytes are located peripherally around the edge of the head and/or fovea capitis, and if epiarticular, may extend onto the surface of the head. Proposed mechanisms relating to the formation of osteophytes is discussed in Chapter 7.

Differences between the two groups were observed superiorly on the acetabulum, where in half of the 3D models from the study group, the acetabular roof appeared to extend further out laterally compared to other models (Figure 3.23). This finding contradicts the 2D morphometric measurement of the FHEI, where the results indicated that the study group had less acetabular coverage of the femoral head laterally than the control group. Measurement artefact could account for this discrepancy as the 2D parameters were only measured on a single slice of an MRI sequence. Therefore, unless the superior rim extended out uniformly around the acetabulum, which it appeared not to on the majority of the 3D models, then the measurements could have been taken at a point where there was no additional coverage, and at a point where the head had migrated laterally. Two possible mechanisms could account for the apparent over coverage in the study group, the first

is that degenerative parts of the acetabular labrum had become ossified (Llopis *et al.*, 2012), and were therefore included in the osseous segmentation of the rim. The second is that marginal osteophytes were present laterally on the acetabular rim, which is often observed in patients with superolateral migration of the femoral head (Ledingham *et al.*, 1992). It is also possible that natural geometric differences existed between the two groups; however, with the small sample size and limited evidence, this theory would need further investigation beyond the scope of this study.

Exploration of the femoral and pelvic shape distributions (Section 3.7.3) and evaluation of the discriminatory power of the shape parameters (i.e. the orthogonal principal components forming the ASMs) (Section 3.7.4) was generally disappointing. Neither method of assessing how well the principal components could be used to classify a shape model as being in the control group or the study group produced definitive results that could be used to support the theory that distinct geometric shape patterns separated the asymptomatic participants from the OA participants. The most promising result was for the cross-validation analysis of the femoral principal components, where 79.3 % of the models were classified into the correct group. Given the obvious visual shape differences affecting the femoral head, it was not surprising that this result was better than that for the pelvis, which was 58.6 % and essentially meant that correct classification was probably due to chance rather than arising from the geometric shape differences between the two groups. Although disappointing in terms of discriminating group geometric shape differences, the outcome of this analysis was encouraging in terms of assessing the efficacy of the ASMs as the results were considered realistic. It was noted that there was some separation of male and female participant shape distributions (Figure 3.25), which supports the theory discussed briefly in Section 3.8.3 that gender differences may exist and, with small mixed gender group samples, this could have confounded the results of the SHIG study.

The mean difference between the radius of the spheres fitted to the femoral heads and the radius of the spheres fitted to the acetabula (Section 3.7.5.1) revealed very large 95 % CL for the study group compared to the control group (Table 3.4), meaning that the range of differences between the femoral and pelvic spheres was much wider in this group. Interestingly, the distribution of data plots on the Bland-Altman map (Figure 3.26) showed that models from both groups with a mean sphere $r \leq 24$ mm had data plots close to the bias, or mean difference line, and in the study group, (with the

exception of one outlier) it was only models with a mean sphere $r \geq 25$ mm that had larger differences between the femoral and pelvic sphere size. It is possible that the study group had a shallower acetabulum, which would have meant a larger sphere would have been fitted to the lunate surface relative to the femoral head. However, the mean pelvic and femoral sphere sizes were relatively similar in both groups (Table 3.3) and only small differences between the groups were observed in the 2D morphometric parameters (e.g. AI and FHEI), therefore, this theory is unlikely to have caused the differences observed only in the larger sizes. Likewise, flattening of the femoral head would cause a large difference in sphere radii; however, it is also unlikely that this would only be observed in larger hips. In the hip joints in the study group, especially where there was a large difference between the diameter of the lunate surface of the acetabulum and the diameter of the femoral head, the load will be distributed over a smaller area. This could reduce the contact area, increasing the contact stress in that area, which under certain conditions has been shown to have a positive correlation with frictional shear stress and wear (Walker *et al.*, 1968). These hips may also become less stable due to the reduced congruency between the two articulating surfaces. Contact mechanics is discussed further, and with reference to the *in vitro* laboratory work, in Chapter 7.

Residual error plots of the spheres (Figure 3.27 and Figure 3.28) confirmed that the morphology of the superior aspect of the femoral head, which was generally quite flattened and asymmetrical superolaterally, differed between the two groups. Slight asymmetry, possibly arising from mild age-related degenerative changes, was also observed in the residuals from the in the control group femoral heads.

3.9 Summary and Conclusions

The main aim of this chapter was to investigate the null hypothesis that there are no fundamental differences in geometry in subjects with hip OA compared to those without. Some notable differences between the two groups were observed, pertaining mainly to the femoral head, meaning that the null hypothesis should be rejected. However, the relatively small number of mixed gender participants recruited in to the study made it difficult to draw any firm conclusions regarding the existence of any underlying abnormalities or differences in geometry that may have contributed to the onset of hip OA. Despite this, the study has provided a valuable contribution to the

research in this area and a methodology has been developed that can be modified slightly to address this further in future work. A summary of the findings of this study is as follows:

- The attrition rate for the study was low; however, recruitment into the study group was very slow due to the selection criteria, particularly the requirement for participants to lie still for ~50 minutes.
- In general, the radiographic features of hip OA matched the subjective assessment of perceived disability for participants the study group.
- The magnitude of geometric distortion was kept to a minimum by applying 3D distortion correction to the MR images before the analysis, and by ensuring that participants were positioned centrally, close to the isocenter of the MR scanner.
- The segmentation process developed for this study was assessed as being accurate and repeatable.
- Two-dimensional radiographic morphometric parameters varied slightly between both groups and gender, but the small, mixed gender groups reduces the statistical power of these observations.
- A large number of participants in the study group had evidence of superolateral migration of the femoral head.
- Labral pathology was observed in both groups. The labrum could not be visualised on any single MR image sequence and therefore, 3D analysis of this structure was not included in the study.
- The MR sequence taken in the para-sagittal plane, which was developed for this study, appeared to be effective for viewing the TAL.
- The majority of study group participants had evidence of osteophytes, mainly affecting the femoral head, which is pathology indicative of hypertrophic OA.
- The superior rim of the acetabulum appeared to extend further laterally in some study group participants. The mechanism of this is unknown but possible aetiologies include calcified labrum, marginal osteophytes, or underlying abnormal geometry.
- Active shape model parameters for the femurs had greater discriminatory power in terms of classification into the correct group (i.e. control or study), than those for the pelvis.

- Larger differences between the femoral and pelvic spheres were observed on the study group with a mean sphere r ≥ 25 mm.
- Maximum and minimum departure from a least squares sphere fitted to the femoral heads of participants in the study group was greater than that observed in the control group.
- Participants from the control group had evidence of mild degenerative changes despite being asymptomatic.

Chapter 4 Validation of a New Pendulum Friction Simulator Using Total hip Replacements

4.1 Introduction

The commissioning and validation of a new piece of equipment is required in order to verify that it meets the requirements of the user and that it is able to function consistently in order to achieve the intended results, as specified by the design objectives (British Standards Institution, 2008).

This PhD thesis aimed to investigate the tribology of the natural hip joint using *in vitro* simulations. The tribological properties of various total artificial hip joints (Auger *et al.*, 1993; Williams *et al.*, 2006; Brockett *et al.*, 2007), and more recently hemiarthroplasty models using metal cobalt chrome heads and porcine acetabula (Zhang *et al.*, 2010; Taylor, 2012), have been investigated using pendulum friction simulator equipment at the University of Leeds. However, insufficient space in the test area of the existing friction simulator equipment meant that the hemiarthroplasty studies could not be progressed onto testing completely natural hip joints.

A new pendulum friction simulator was designed specifically for testing natural tissue and can therefore accommodate a complete natural hip joint, specifically a porcine acetabulum and femoral head. Once validated, a methodology was developed to enable the tribology of natural porcine hip joints to be investigated using the new pendulum friction simulator (Chapter 6).

This chapter describes the stages undertaken to validate the new pendulum friction simulator (Mark B [Mk B]) using total hip replacements and an existing, validated friction simulator (pendulum friction simulator A) as the comparator. The design of the simulator, materials and methods used for the validation, and the various processes completed from the initial handover from the manufacture to the final validation tests, are explained. The results, and where applicable a short summary of the findings of each stage in the process, are also presented in this chapter. On receiving the simulator from the manufacturer some preliminary testing and early commissioning work was completed (Section 4.5), and this was followed by an initial validation study (Section 4.6). The results of this initial study highlighted some major concerns about the functioning of the simulator, which were explored and the simulator was then modified based on the findings from this exploratory work (Section 4.8). A further

validation study was conducted and final conclusions were drawn (Section 4.12). Hemiarthroplasty tests using natural porcine tissue were also conducted on pendulum friction simulator Mk B as part of the validation process, and these have been discussed in Chapter 5. An overview of the validation process is provided in Figure 4.1.

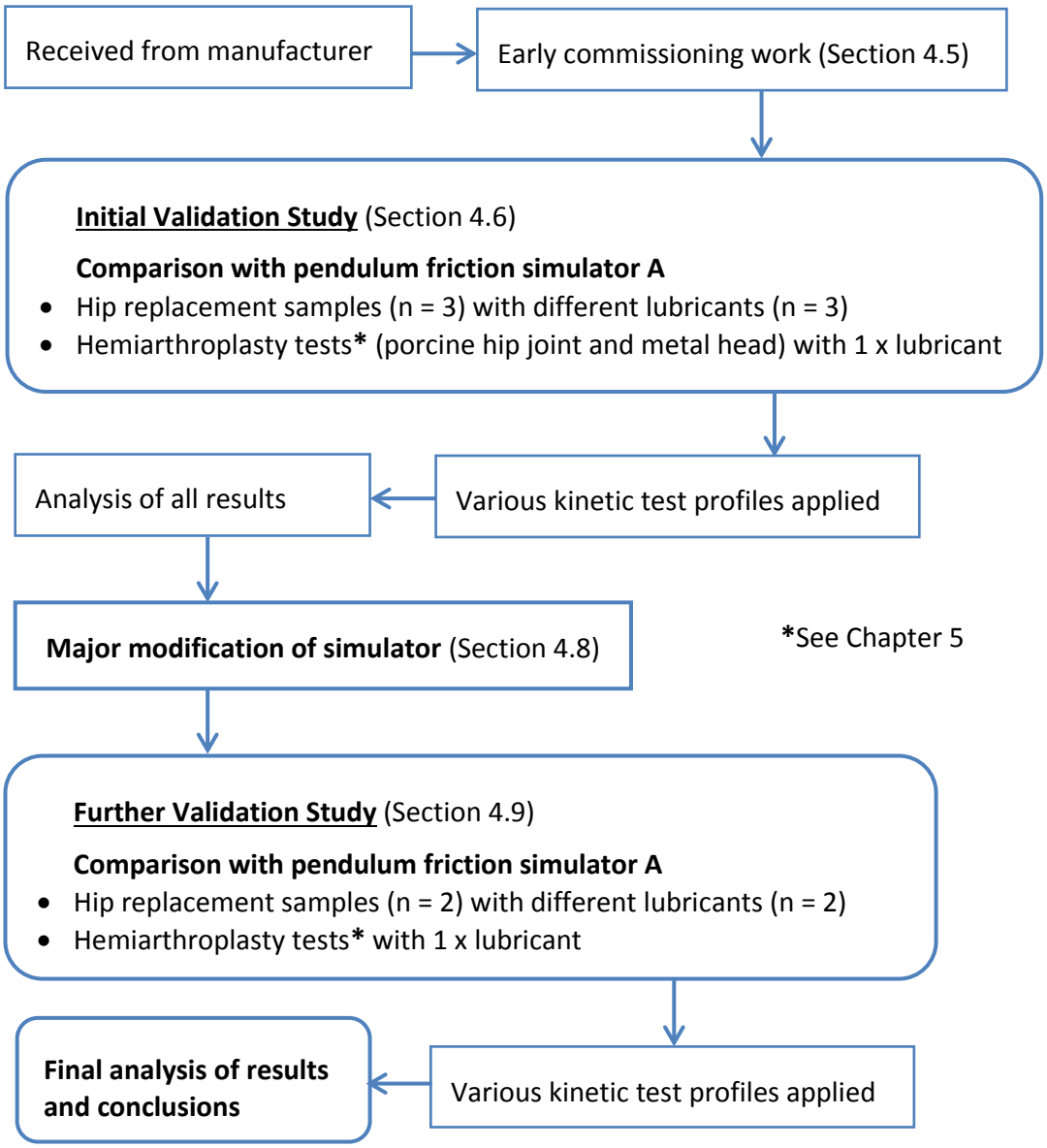

Figure 4.1: Flow chart of the validation process for pendulum friction simulator Mk B.

4.2 Pendulum Friction Simulator Mk B

4.2.1 Design Requirements

A single station pendulum simulator was required that could be used to measure frictional torque between the bearing surfaces of the sample to be tested. The

simulator needed to be able to accommodate artificial hip replacement bearings of the same size and range that can be tested *in vitro* in a ProSim Hip Wear Simulator. The simulator also needed to be able to accommodate biological tissue samples from hip joints, and the simulator needed to be designed so that the test components (artificial or biological) could be easily fitted for testing and removed. The simulator needed to be able to apply axial forces with a peak load up to 3 kN for artificial bearings, in line with the British Standard 14242-1 loading and displacement parameters for wear-testing total hip joint prostheses (British Standards Institution, 2002), and with a minimum peak load of 500 N for testing biological samples. A swing phase load in the range of 0-800 N was required, again to enable biological tissue to be tested at very low loads, and conformance with the demand load needed to be within ± 5 %, as any deviation greater than this could confound the results of biological tissue tests by affecting the integrity of the chondral surface(s) of the samples. An angular displacement sinusoidal waveform was required with an amplitude in the range of ± 25° (e.g. to deliver a flexion-extension motion), and conformance demand of ± 3° to accommodate the same British Standard, as well as biological animal tissue that require smaller amplitudes of movement. Forward and reverse motion were required so that a mean torque value could be calculated cancelling out any torques generated by slight misalignment of the test component. Low friction, self-aligning bearings were required to ensure correct positioning of the components during the test. A highly sensitive force transducer was needed as the torque generated between the cartilage surfaces of biological tissue was expected to be low, and friction factor values of animal cartilage tissue have been reported in the range of 0.002 to 0.35 (Mow *et al.*, 1993).

4.2.2 Design Solution

ProSim pendulum friction simulator Mk B (Simulation Solutions Ltd., Stockport, UK) was manufactured as a single station pneumatically loaded machine, controlled by a desktop personal computer (PC), which is able to apply both dynamic and static axial loading cycles via a loading frame and flexion-extension (FE) rocker (Figure 4.2). The simulator is designed to use a closed loop feedback system to control the demand load via a sentronic valve, and it can apply a peak load in the range of 500-3 kN ± 5 % conformity, and swing phase load in the range of 0-800 N ± 5 % conformity. The FE rocker, which is attached to the loading frame, can move forwards and backwards and is able to apply FE motion in the range of ± 45° ± 2 % conformity.

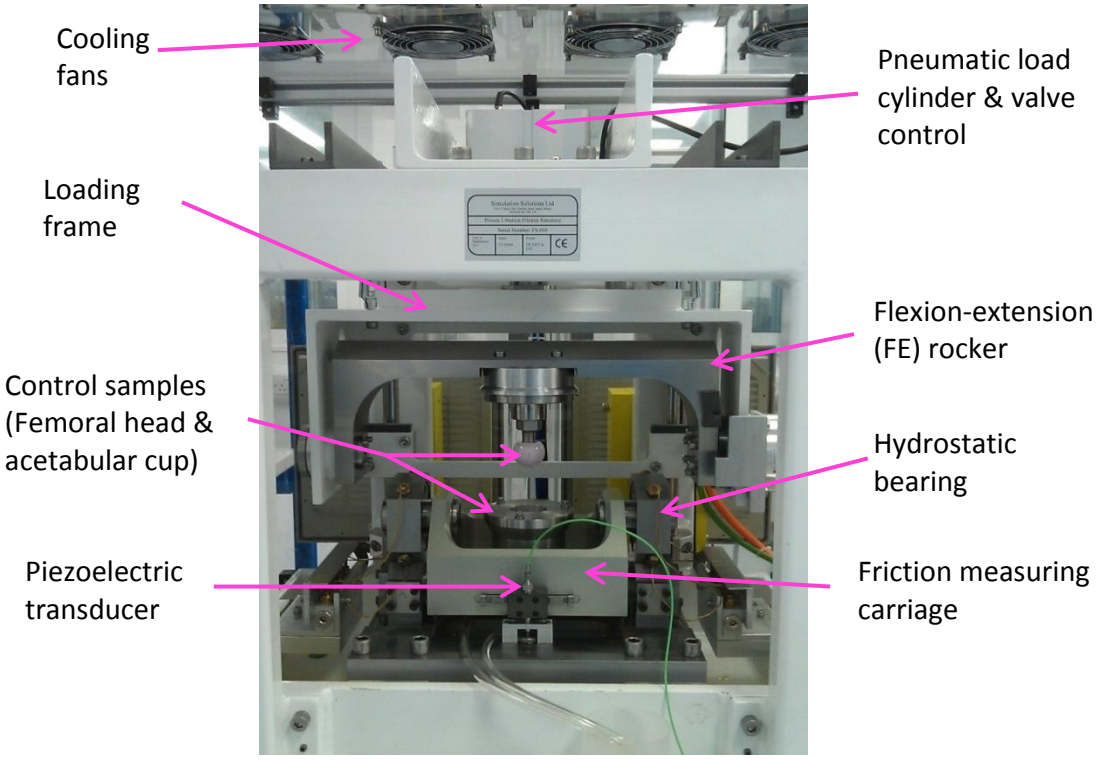

Figure 4.2: Pendulum friction simulator Mk B.

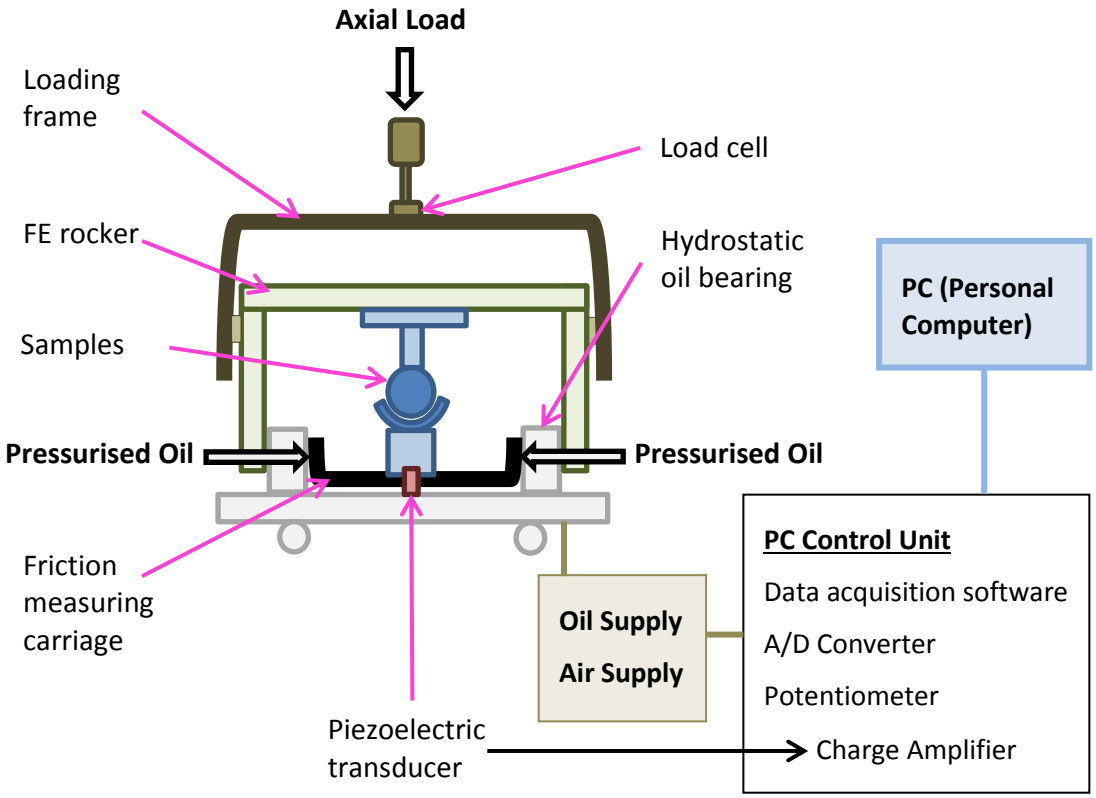

Figure 4.3: Schematic diagram of pendulum friction simulator Mk B.

A friction measuring carriage, which is housed in a fixed frame, is self-aligning and mounted on a pressurised hydrostatic oil bearing (Figure 4.3), thus enabling any friction that may be generated by the carriage itself to be regarded as negligible. Attached to the front of a friction measuring carriage is a piezoelectric force transducer, which measures the forces transferred between the carriage and the fixed frame. The piezoelectric transducer determines frictional torque within the system by measuring the forces transferred between the bearing surfaces as the FE rocker moves back and forth. The system was designed so that any torque created by incidental movement of the carriage in a medial-lateral (left-right) or anterior-posterior (forward-backward) directions, and not due to friction between the two surfaces arising from FE motion, would be negligible. This was achieved via the hydrostatic bearing, which aimed to make the friction measuring carriage effectively "frictionless" with any medial-lateral or anterior-posterior translation. This was important for testing biological tissue as, depending on the sample, the samples may not be of uniform and/or symmetrical geometry, and could therefore give rise to concomitant movement not related to friction between the two surfaces.

The piezoelectric transducer has a maximum range of 50 Nm of torque with a minimum accuracy of 1 % of the maximum, therefore, frictional torque can be measured to a minimum value of 0.5 Nm (1 % the maximum range of 50 Nm), with friction factors measured in the range of 0.01-0.5. This force data is sent to the PC, via a charge amplifier (which converts the charge signal into a voltage signal), in order to determine the frictional torque in the system created by the samples being tested.

Cooling fans in the roof and rear wall control the build-up of heat generated during long tests. Hip joint components are inverted with respect to anatomical position in the simulator meaning that the acetabulum is seated in the friction measuring carriage and the femoral is fixtured onto the FE rocker.

4.3 Simulator Control Systems

The load control simulator is controlled by two different control loops, one controlling motion (i.e. flexion-extension) and one controlling the axial load, with both loops being regulated by a main control unit via a PC (Figure 4.4).

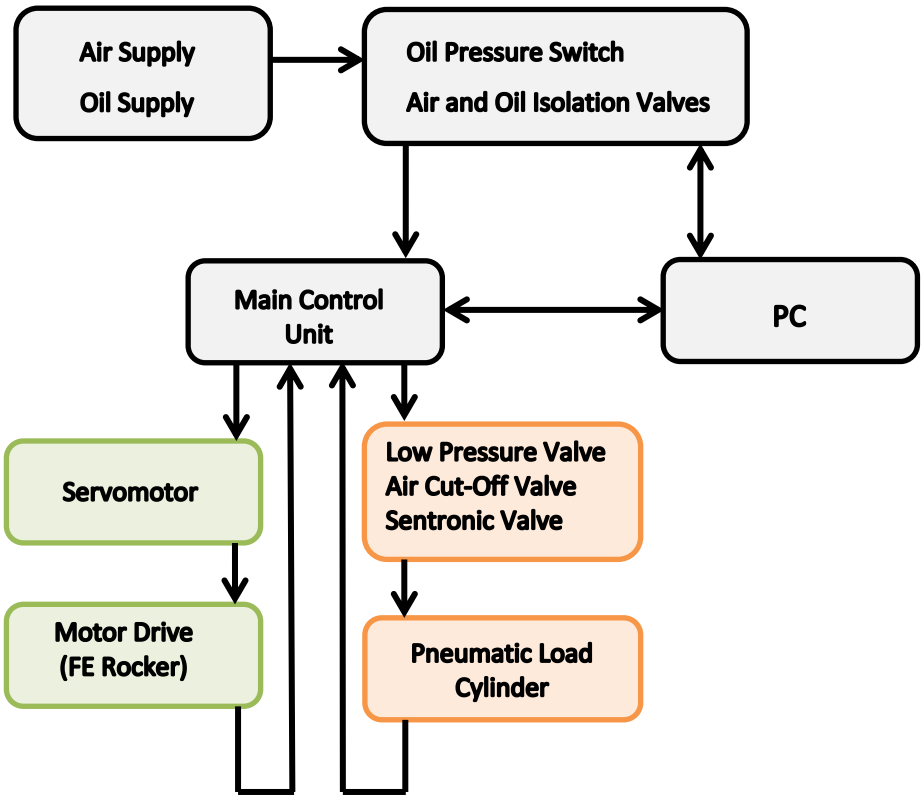

Figure 4.4: Schematic diagram of the pendulum friction simulator Mk B motor drive (green) and pneumatic load (orange) control systems, adapted from Simulation Solutions Ltd. (2012).

The FE rocker is driven by a digital motor drive with a position encoder (servomotor) attached, so that it can monitor the angular motion via a closed loop system. The motor drive, which is connected to and controlled by the PC, controls the position of the FE rocker using the positioning profile uploaded to the PC by the user.

The axial load is pneumatically driven with air entering the simulator via an isolator and filter/regulator. The air pressure supplied to the simulator is monitored by the PC, and the pressure of the air going to the sentronic valve is controlled by an air cut-off valve. The sentronic valve controls the axial load applied to the samples being tested via the load cylinder. A 5 kN load cell (with an accuracy of ± 30 N) monitors the load being applied to the samples and is able to adjust the input via the main control unit, using a closed loop feedback system.

Demand load and motion profiles are downloaded from the PC and used to control the position of the rocker, and therefore FE femoral head motion, and the axial loading regime that is required for each specific test.

4.4 Calibration

In accordance with good laboratory practice, frictional torque and load cell calibration procedures were carried out on a monthly basis or before starting a new study. This was completed using automatic calibration software supplied with the simulator.

4.4.1 Frictional Torque Calibration

Frictional torque was calibrated using an auto friction calibrate function at both high and low gain charge amplifier settings. This was done by placing calibrated test weights onto a 500 mm long loading arm, which was fixtured into the friction measuring carriage with the loading arm facing forwards (Figure 4.5). The charge amplifier was zeroed before loading the arm incrementally with 1 kg weights up to a total of 4 kg for high gain and 9 kg for low gain. Overloading the arm with weights beyond these limits would have saturated the torque sensor. After each test weight was placed onto the loading arm, the applied test weight was recorded in the 'Test Mass (kg)' box on the auto friction calibrate software dialogue box before clicking on the 'Measure' button. This was repeated until the maximum weight had been applied for the gain being calibrated. The 'Calibrate' button on the dialogue box was then activated and the software produced a calibration report. The report contained details of the test weight, and the applied and measured torque values, which it used to calculate the frictional torque calibration constants. The calibration constants were then manually entered into the 'Set Calibration Constants' dialogue box in the machine properties menu.

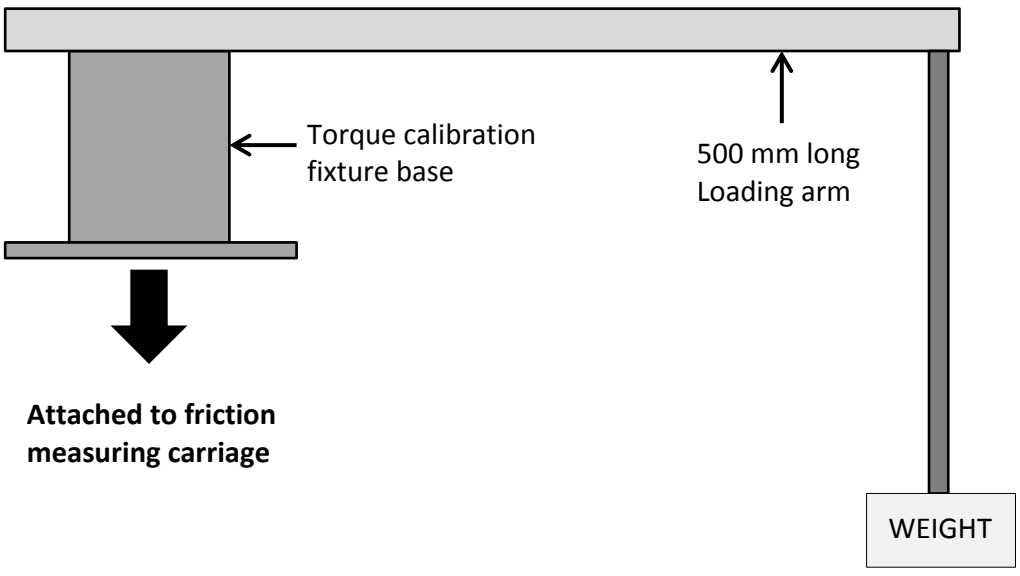

Figure 4.5: Schematic diagram of the frictional torque calibration equipment and set-up.

The simulator was checked to ensure that there was a linear relationship between the points and no significant differences in magnitude between the calculated calibration constants when loading the simulator from the front and when loading it to the rear (Figure 4.6). This was done to correspond with running the simulator in forward and reverse directions, however, reverse loading calibration is not necessary as part of the standard frictional torque calibration process and required the fixed rear panel of the simulator to be removed.

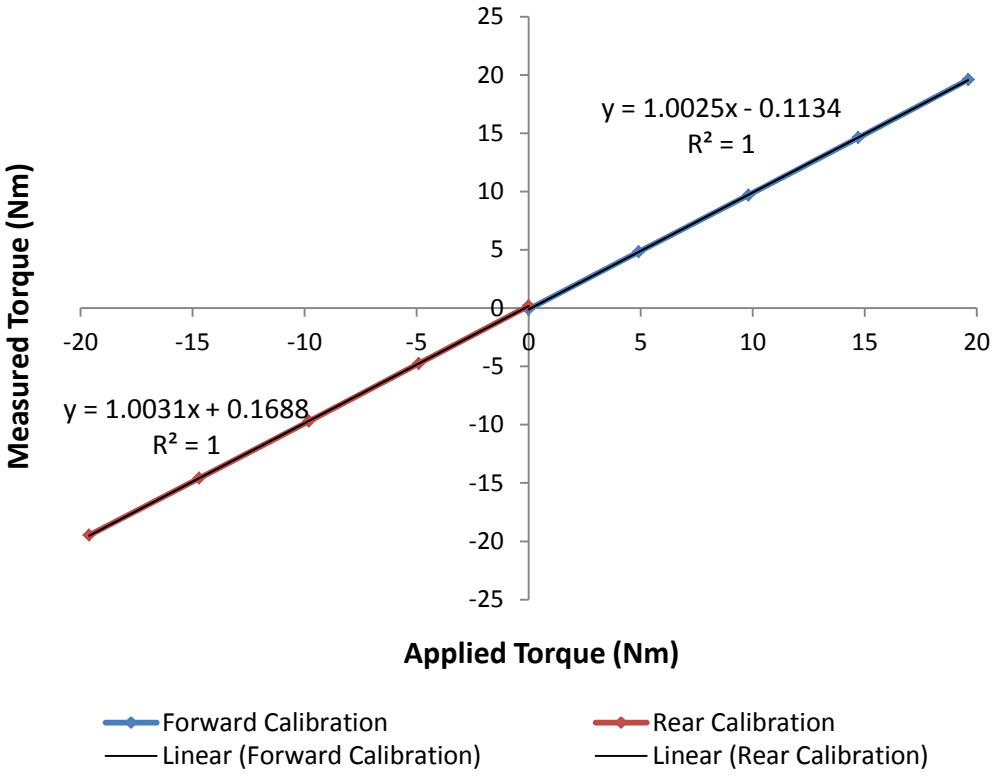

Figure 4.6: Plot of forward and rear frictional torque high gain charge amplifier calibration results for ProSim friction simulator Mk B.

4.4.2 Load Cell Calibration

The load cell, mounted in the loading frame of the simulator, was calibrated using an external calibrated load cell (Figure 4.7). The external load cell was fixtured onto the FE rocker and a load cell calibration cylinder block made from Delrin® (polyoxymethylene) was used to fill the space between the load cell and the friction measuring carriage. Activating the auto load calibrate function causes the air pressure valve in the simulator to be opened through five positions in order for the calibration constants to be calculated. The valve starts in a fully closed position and ends fully open, and at each of

the five stages the external load cell was used to record the actual force being applied by the simulator, which was recorded in the auto load calibrate dialogue box. Once the last load cell reading had been recorded with the valve fully open, the 'Calibrate' button on the dialogue box was activated and the software produced a calibration report. The report gave details of the actual loads (from the external load cell), the loads recorded by the load cell in the simulator, and the deviation of the simulator load cell value from the actual load.

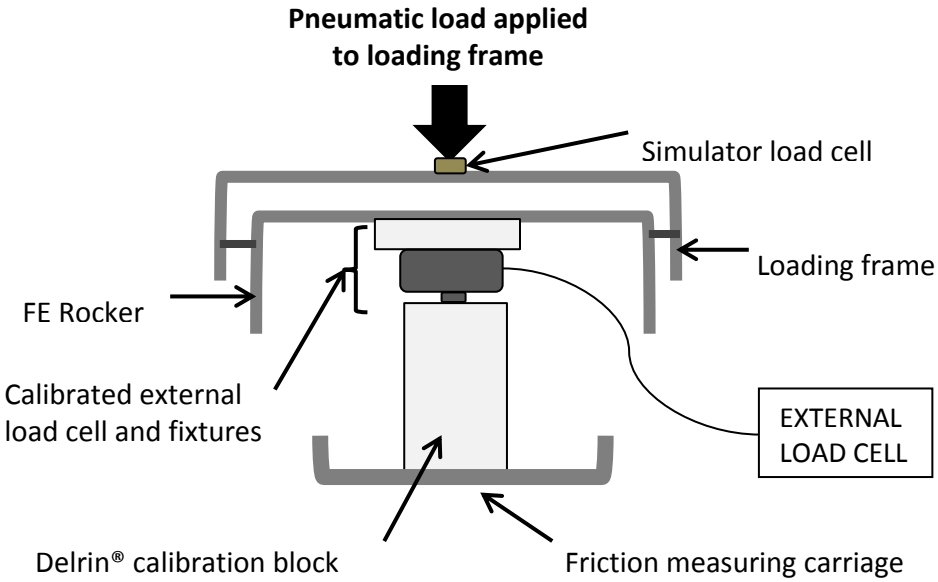

Figure 4.7: Schematic diagram of the load cell calibration equipment and set-up.

The calibration constants calculated by software at the end of this process were manually entered into the 'Set Calibration Constants' dialogue box in the machine properties menu. The calibrated load cell constants are used by the simulator to ensure that the correct demand load is applied during testing.

4.4.3 Data Analysis

Friction between the femoral head and acetabulum causes movement of the friction measuring carriage and this exerts a force on the piezoelectric transducer, the magnitude of which is proportional to the amount of friction between the two surfaces. Frictional torque is derived from the force measured in the piezoelectric transducer by the simulator software.

The average friction factor was calculated using only the data collected during the peak load (i.e. 2 kN or 800 N) high velocity phase of each of the logged one-second dynamic cycles (shaded area on Figure 4.8).

One cycle at a frequency of 1 Hz lasts for one second, during which time 255 data points are collected by pendulum friction simulator A and 127 data points are collected by pendulum friction simulator Mk B (Figure 4.8). Friction was not calculated at the beginning or end of the cycle because the motion arm is changing direction and there may be a temporary reduction in speed.

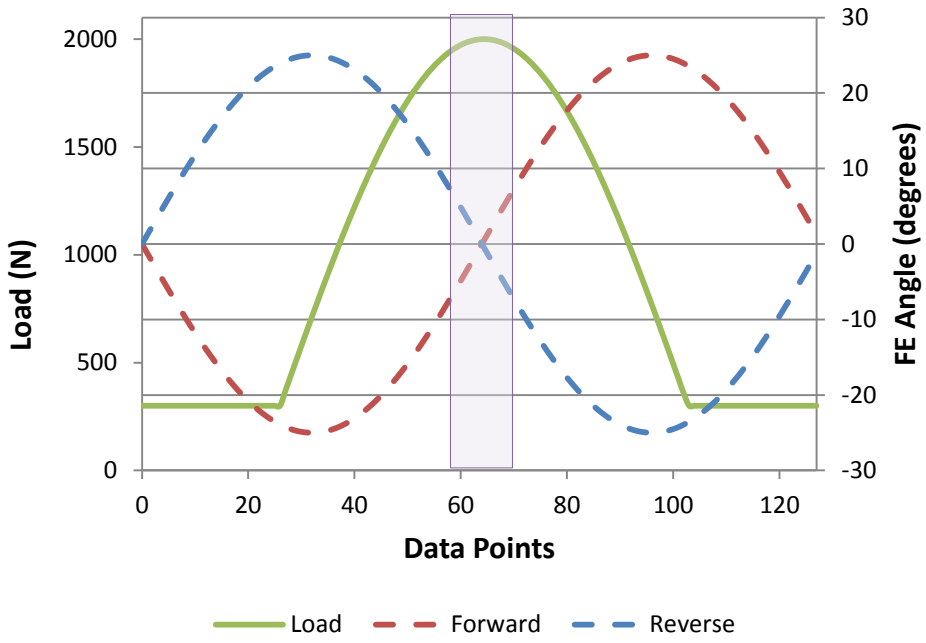

Figure 4.8: Pendulum friction simulator load profile and FE motion. The shaded area shows where the data is collected from.

Previous studies using pendulum friction simulator A reported that the friction stabilised after 90 cycles, therefore, only data taken from cycle 90 onwards was used for the analyses (Brockett, 2007).

Torque measurements from both forward (T_F) and reverse (T_R) cycles were used to calculate the true torque magnitude (T_t) for each test, which was done using Equation 4.1. This method was adopted so that the effect of any slight misalignment of the components could be eliminated (Auger *et al.*, 1993). The forward and reverse torque

values were initially calculated as follows, where $T_{frictional}$ is the total frictional torque and $T_{misalignment}$ is the torque resulting from any slight offset in the centre of rotations:

$$T_F = T_{frictional} + T_{misalignment}$$

$$T_R = T_{frictional} + T_{misalignment}$$

The forward (T_F) and reverse (T_R) torque measurements from the above calculations were then used to calculate the true torque magnitude (T_t):

$$T_t = \frac{(T_F - T_R)}{2} \qquad \textbf{Equation 4.1}$$

The mean friction factor (f) was calculated from the true torque magnitude using Equation 4.2, where r is the radius of the bearing surfaces (m) and W_p is the peak load (N):

$$f = \frac{T_t}{r \times W_p} \qquad \textbf{Equation 4.2}$$

Friction factor for the constant load tests was calculated using data taken from where the head was vertically loading the cup, i.e. where the FE arm was positioned at 0° FE, which corresponds with the high velocity phases of the cycles.

In addition to the mean friction factor results, data from the forward and reverse tests were analysed separately so that any large disparities (e.g. large offset), that may otherwise have been masked by only reporting the mean results, could be detected. Reverse friction had a negative value but should be of similar magnitude to the forward result. Data obtained under reverse conditions on charts/graphs have been presented as positive values to enable the forward, reverse and mean data to be compared more easily.

4.5 Early Commissioning of Pendulum Friction Simulator Mk B

Initial checks conducted by the candidate during the handover period for the pendulum friction simulator from the manufacturer to the university highlighted a number of anomalies that required addressing before any formal validation testing and commissioning could begin.

Pre-validation activities conducted during the early commissioning phase included:

- Initial training provided by the manufacturer to ensure the correct and safe use of the simulator, which included checking that the safety guards and emergency stop button were working.
- Calibration of the load cell and frictional torque output (Section 4.4).
- Running the simulator to check its general function (e.g. oil flow activation and smooth movement of the friction measuring carriage, hydrostatic bearing, FE rocker, and piezoelectric force transducer).
- Checking that the load output profile and data matched the demand (i.e. input) load profile. This was done by running a control sample in the simulator and visually inspecting the demand and actual load profiles on the PC monitor, and also by checking the data logged by the simulator (Table 4.1).
- The FE motion output profile was also checked whilst running a control sample in the simulator and compared to the input demand. As well as assessing the PC monitor and logged data, a calibrated digital inclinometer was used to check the position of the FE rocker against the input motion profile.
- Checking that the data log contained the correct calculations and analysis of results, for example frictional torque measurements and friction factor calculations (Section 4.4.3).

Work conducted on the simulator to rectify the issues identified during this period have been summarised in Table 4.1. A description of a subsequent modification is in Section 4.8.

Table 4.1: Summary of early commissioning work conducted on pendulum friction simulator Mk B.

Problem	How the Problem was Identified	Solution	Time Taken to Resolve
Capillary tubing feeding oil to hydrostatic bearing failed under pressure	A tube broke away from its mounting with pressurised oil flow	All capillary tubing was replaced and re-soldered	~3 months
Frictional torque was generated from the hydrostatic bearing	The carriage was moving to the left and sticking when the oil was flowing	Hydrostatic bearings were removed and re-ground	~9 months
Design fault affecting the stability of the FE rocker	The FE rocker was visibly bending when loaded	New stainless steel FE rocker designed and fitted	~4 months
No load applied at initial calibration step and unable to deliver axial loads of less than 200 N	Visually on the PC monitor and by analysing the Excel data output from the simulator	Simulator software driving load calibration process modified enabling lower axial loads to be delivered	~3 months
Large discrepancy between demand load and output (worse at lower loads)	Inspection of demand and actual load profiles on monitor (Figure 4.9 a)	Software modified to allow limited proportional-integral-derivative (PID) open control combined with closed loop control (Figure 4.9 b)	~2 months

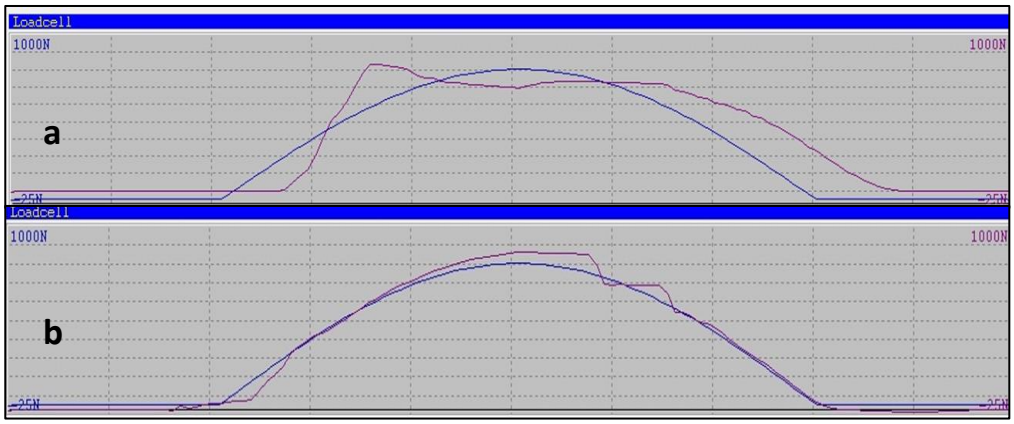

Figure 4.9: Screenshot of the demand and output axial loading profiles (blue and magenta lines respectively) before (a) and after (b) software modifications.

4.5.1 Fitting of Floating Joint

Operating the simulator with a 36 mm diameter ceramic-on-ceramic bearing *in situ*, with water lubricant, a 300 N to 2 kN load, and no FE motion produced a mean frictional torque output of 2.67 ± 0.22 Nm (n = 6). Torque measurements of this magnitude were not anticipated when applying an axial load with no motion, inferring that the friction sensor was unable to discriminate between the actual torque being generated between the two bearing surfaces and any concomitant movements of the self-aligning friction measuring carriage. An explanation relating to the hydrostatic bearing and concomitant movement of the friction measuring carriage was given in Section 4.2.2.

To enable free movement of the friction measuring carriage whilst allowing only axial tensile and compressive forces to be applied to the friction sensor, a floating joint was fitted between bottom of piezoelectric friction sensor and the hydrostatic bearing. This had the net effect of decoupling the friction sensor from any other incidental (e.g. lateral) movement of the hydrostatic bearing so that only the torque generated between the two bearing surfaces in the carriage was measured.

Following this work, the simulator was operated using the same ceramic-on-ceramic bearing couple, lubricant, and loading profile with no FE motion. The floating joint was found to have significantly reduced (paired *t-test*, $p < 0.05$) the load-only torque measured by the simulator to 0.37 ± 0.07 Nm (n = 6), which equates to a friction factor of ∼0.01. The load-only torque measured by friction simulator A under the same tribological testing conditions was 0.30 ± 0.14 Nm (n = 6).

4.6 Materials and Methods for Validation using Total Hip Replacements

4.6.1 Introduction

The validation of pendulum friction simulator Mk B was conducted using criteria that had been established in advance by the candidate. This part of the validation procedure involved measuring the frictional torque generated between a set of artificial hip bearings tested in the new simulator (Mk B) and using this to calculate the friction factor. Friction factor results from the new simulator were then compared to

the friction factor results from an existing and previously validated pendulum friction simulator (A), which is of a similar design.

4.6.2 Pendulum Friction Simulator A

Pendulum friction simulator A (Figure 4.10) is also a single station servo-hydraulic machine that measures the frictional torque generated between two test sample surfaces using a frictionless hydrostatic bearing and piezoelectric force transducer. The orientation and fixturing of the components is comparable to that of simulator Mk B, thus enabling samples to be easily moved between and tested in both simulators. The results output is also very similar and the same information (e.g. demand/applied load and motion, frictional torque, friction coefficient) can be derived from both simulators. Torque measurement and the load and motion control systems and parameters of pendulum friction simulator A are the same as those described for pendulum friction simulator MK B in Sections 4.2 and 4.3.

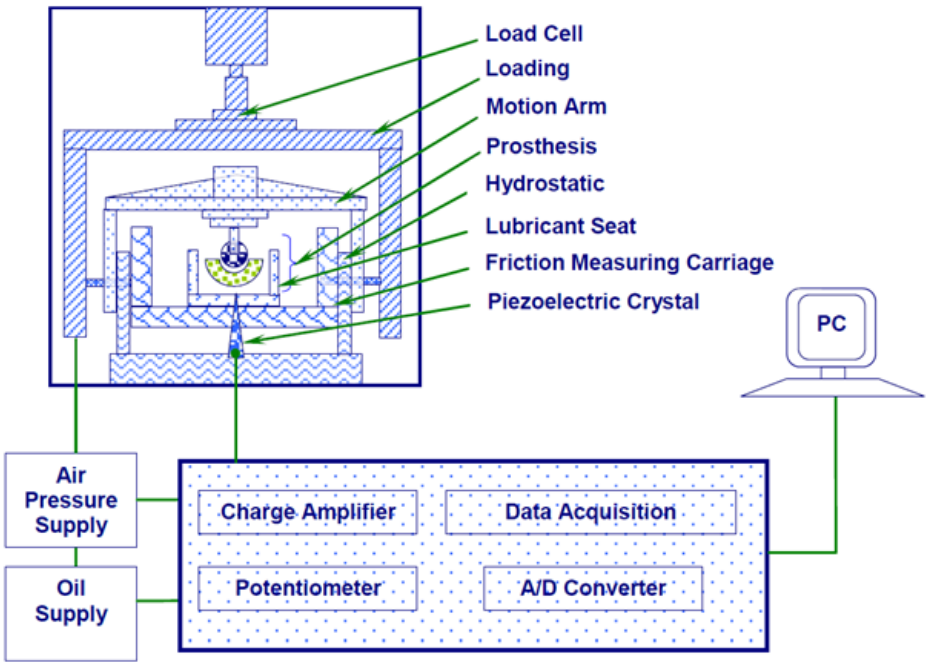

Figure 4.10: Schematic diagram of pendulum friction simulator A (Lizhang, 2010).

4.6.3 Total Hip Replacements

Three sets of control samples, (supplied by DePuy Synthes, Leeds, UK), comprising of two different bearing combinations were tested during the initial validation studies

(Figure 4.11). A metal-on-polyethylene (MoP) sample and a ceramic-on-ceramic (CoC) sample, both with a nominal diameter (Ø) of 28 mm, were used so the results could be compared to previously published work measuring friction in THRs using pendulum friction simulator A (Brockett *et al.*, 2007). Additionally, a larger CoC sample (36 mm Ø) was included in the validation plan, as this was similar to the mean diameter of the natural porcine hip joints to be used in subsequent testing (Chapter 5).

The ceramic bearing surfaces were made from BIOLOX® Delta, which is a toughened alumina matrix composite (CeramTec, 2012), and the metal femoral head was a cobalt chrome (CoCr) molybdenum alloy. The polyethylene cup was manufactured from MARATHON™ polyethylene, which is a third generation, crosslinked ultra-high molecular weight polyethylene (UHMWPE) (DePuy Synthes, 2014).

Figure 4.11: Total hip replacement control samples with simulator fixturing: 28 mm metal-on-polyethylene and ceramic-on-ceramic (28 mm and 36 mm).

4.6.3.1 Control Sample Preparation

In order to remove any potential confounding factors caused by the experimental set-up, meticulous preparation of the test samples was conducted.

4.6.3.2 Alignment of Centre Height

The centre of rotation (COR) of the acetabulum and femoral head were aligned with the COR of the friction measuring carriage and loading frame to reduce the risk of any experimental artefact. This ensured that, as far as possible, the measured frictional torque was due to friction between the two bearing surfaces being tested in the simulator. The COR of the femoral head was 27.07 mm larger in pendulum friction simulator Mk B compared to simulator A, therefore, a spacer was used in conjunction with the universal head fixture in simulator Mk B. The COR of the head (99.90 mm) and acetabulum (63.24 mm) is shown schematically in Figure 4.12.

Alignment marks were used with all samples and sample holders to maintain consistency during the set-up procedure and repeatable orientation of the fixtures during multiple repeats and different tests.

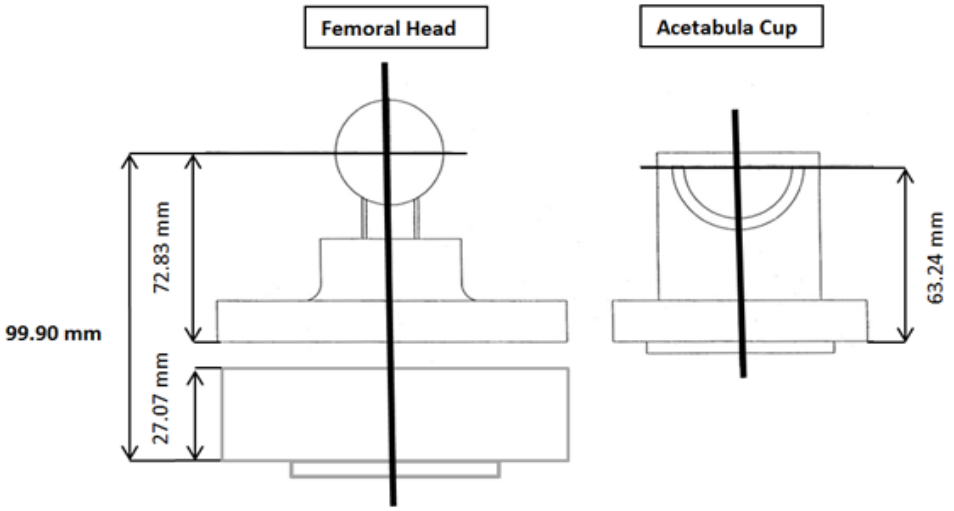

Figure 4.12: Schematic diagram showing centre of rotation heights for the femoral head and acetabulum (cup) in the pendulum friction simulator.

Femoral head centre heights were set to 72.83 mm plus the radius of the femoral head (rh), (i.e. 72.83 + rh mm) using a vernier height gauge with dial test indicator (DTI) attached and slip gauges. The cups were set up in a universal cup holder and the COR

was aligned using locking rings (specific to the sample being tested), and a small Delrin® pin (Figure 4.11). Experimental work conducted by Brockett (2007) on pendulum friction simulator A reported that the friction factor was affected if the centre heights of the samples were slightly misaligned. To reduce the risk of over-tightening and deforming the Delrin® pin, which would affect the COR of the cups, a torque screwdriver was used to secure the pin and acetabula cup in place. The repeatability of this method and accuracy of the screwdriver torque settings was assessed by setting up the cups a number of times and checking the COR with vernier height and slip gauges.

An alignment rod, supplied with the simulator, was used before starting each test. The rod was passed through holes in the FE rocker and friction measuring carriage, which are arranged in series corresponding to the COR of the simulator. Testing does not begin unless the alignment rod passes through the two holes as this could introduce experimental error and reduce the internal validity of the results.

4.6.3.3 Surface Roughness Measurement

The surface roughness of the control samples was measured using two-dimensional contacting profilometry (Form Talysurf series, Taylor-Hobson, Leicester, UK) before the start of the validation studies, after each test, and at the end of the validation studies. Any changes in surface roughness would affect the tribological performance of the control samples (Scholes *et al.*, 2000) in terms of both friction measurements and test re-test repeatability, thus making it difficult to fully assess the function of the simulator.

Two traces, positioned perpendicular to each other (P1 and P2), were taken from both the heads and cups in order to calculate the arithmetic average of the surface roughness (R_a) for each bearing surface (Figure 4.13). The heads and cups were measured with the alignment mark orientated in the same position each time to maintain consistency and repeatability of the measurements (British Standards Institution, 1998). The mean R_a values and variation from the mean, i.e. standard deviation (SD), for the control samples measured during the validation procedure are shown in Table 4.2. The profile skewness remained negative throughout the validation process, denoting a prominence of valleys on the bearing surfaces.

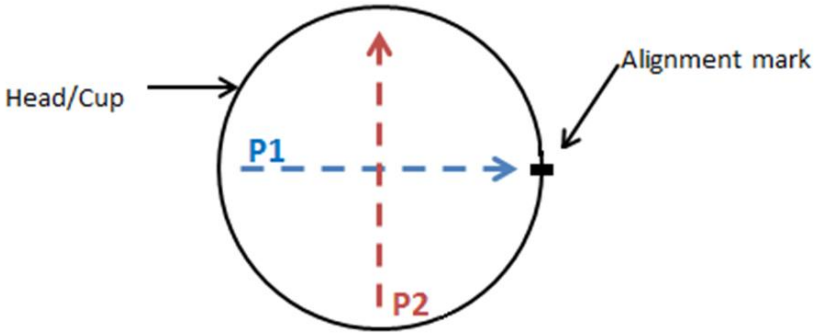

Figure 4.13: Schematic diagram showing the position of the two profilometry traces (P1 and P2) taken from the femoral heads and acetabular cups.

Table 4.2: Roughness average (Ra) values ± SD of the control sample bearing surfaces.

Sample	Head R_a µm ± SD	Cup R_a µm ± SD
28 mm Metal-on-polyethylene	0.008 ± 0.002	0.501 ± 0.053
28 mm Ceramic-on-ceramic	0.007 ± 0.000	0.008 ± 0.001
36 mm Ceramic-on-ceramic	0.008 ± 0.000	0.008 ± 0.001

4.6.4 Lubricants

Distilled water (Baxter Healthcare, Zurich, Switzerland) and newborn calf serum (Life Technologies Corporation, Auckland, New Zealand), were used to lubricate the bearing surfaces during the validation process. The newborn calf serum (NBCS) was used in 100 % and 25 % volume-to-volume (v/v) concentrations, totalling three different lubricants that could be used for comparative purposes. The protein concentration was 62.0 mg/ml in the 100 % NBCS and 15.5 mg/ml in the 25% NBCS (Life Technologies™, 2013). The 25 % (v/v) NBCS, diluted with distilled water, was used as it has a protein content similar to human synovial fluid, which is reported to be 20-40 mg/ml (Saari *et al.*, 1993; Wang *et al.*, 1998). The NBCS is generally referred to as serum throughout this thesis.

The minimum level of torque to be detected by the simulator was assessed using the CoC bearings with a water lubricant, as the frictional torque produced under these test conditions is known to be very low (Scholes and Unsworth, 2006).

The control samples were thoroughly cleaned using water with a disinfectant followed by isopropanyl, before and after each repeat to remove any debris or traces of lubricant (i.e. protein deposits) that could affect the results. The lubricant, 2 ml for the 28 mm Ø samples and 3 ml for the 36 mm Ø samples, was placed into the acetabular cup before each test.

4.6.5 Input Kinetics

The validation plan consisted of a number of different input profiles, chosen to test the performance of the simulator under different conditions and enable the results to be compared to pendulum friction simulator A and previously published work.

Samples were subjected to dynamic loads and motion ranging from 25 N to 2 kN with ± 15° or ± 25° FE motion at a frequency of 1 Hz (i.e. 1 cycle per second), via simple sinusoidal waveforms. Dynamic profiles (examples of which can be seen in Figure 4.14) were based on a very simplified standard gait cycle (Paul, 1966), with a 'standard' test being defined as a swing phase load (SPL) of 300 N, based on ISO standard 14242 (British Standards Institution, 2002), peak load of 2 kN and ± 25° FE motion. A peak load of 2 kN was used to enable the results to be compared to those from pendulum friction simulator A, which is unable to accommodate a 3 kN ISO standard peak load. A low load and motion profile (25 N SPL to 800 N peak load ± 15° FE) was included in the plan to assess the simulator working at lower dynamic loads and with less motion (Figure 4.14). This was referred to as a tissue profile, and is explained in Section 5.3.2, as it was the profile used for testing natural tissue in Chapter 5 and Chapter 6. These parameters were included to replicate the test conditions used for further subsequent validation tests using natural porcine tissue (Section 5.3.2).

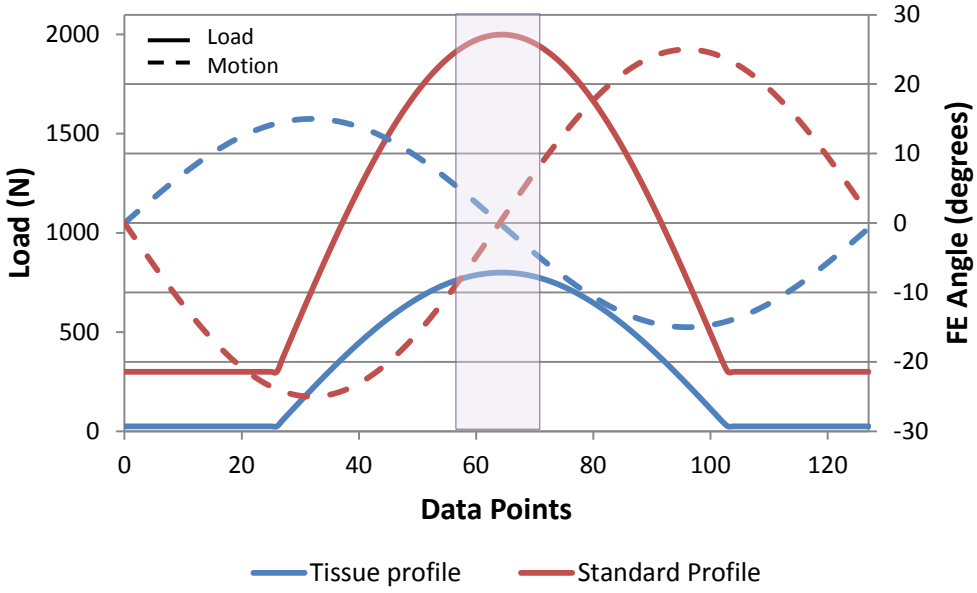

Figure 4.14: Dynamic tissue test profile and standard forward profile showing flexion-extension angles, demand load, and data collection area (shaded box).

In addition to the standard 300 N SPL test, the CoC samples were tested using two lower SPLs of 25 N and 100 N so that the function of the simulator could be assessed through a range of axial loading conditions of different magnitudes. Two constant loading conditions of 300 N and 1 kN (both ± 25° FE motion) were also used with the CoC samples to ensure that the positive and negative frictional torque output were of equal magnitude and positioned symmetrically above and below zero.

The MoP sample was used as a dynamic control sample only at this stage, and therefore, it was only tested using the standard and tissue profiles. The number (n) of tests conducted during the initial validation period is summarised in Table 4.3. The full validation plan is in Appendix C.

All testing was conducted at room temperature in both forwards and reverse directions (i.e. with the load applied as the FE rocker is moving forwards or backwards), each for 125 cycles, to eliminate the effects of any offset that may occur during loading from the sample set-up. Each test was repeated three times in order to reduce the risk of any spurious effects, increasing the probability that the averaged results were more accurate than a single repeat.

Table 4.3: Initial validation studies conducted on pendulum friction simulators A and Mk B using artificial hip replacement samples with standard, tissue and constant load tests, and n = 3 lubricants (water, 25 % serum, 100 % serum).

Sample	Tests (load ± FE motion)	Lubricants (n)	Repeats (n)	Sub Total	Total Tests for Simulators A and Mk B
28 mm Ø MoP	**1 x standard** *(300 N to 2 kN ± 25° FE)* **1 x tissue** *(25 N to 800 N ± 15° FE)*	3	3	18	36
28 mm Ø CoC	**3 x standard** *(25 N, 100 N & 300 N SPLs to 2 kN ± 25° FE)* **1 x tissue** *(25 N to 800 N ± 15° FE)* **2 x constant** *(300 N & 1 kN ± 25° FE)*	3	3	54	108
36 mm Ø CoC	**3 x standard** *(25 N, 100 N & 300 N SPLs to 2 kN ± 25° FE)* **1 x tissue** *(25 N to 800 N ± 15° FE)* **2 x constant** *(300 N & 1 kN ± 25° FE)*	3	3	54	108
		Total Number of Tests			**252**

4.6.5.1 Statistical Analysis

The level of significance for all tests was $p < 0.05$ and the standard deviation (SD) was calculated and used as a method of assessing the variability and dispersal of the measurements around the mean (i.e. mean ± SD). Statistical analysis of the data, which was normally distributed, was performed with two-tailed *t*-tests using SPSS.

The null hypothesis (H_o), therefore for the validation is that there will be no difference in friction factor results obtained from the two pendulum friction simulators:

H_o: Simulator Mk B (f) = Simulator A (f)

The alternative hypothesis (H_1) is that results from the two simulators are different:

H_1: Simulator Mk B (f) ≠ Simulator A (f)

The piezoelectric transducer has a maximum range of 50 Nm of torque with a minimum accuracy of 1% of the maximum (as explained in Section 4.2.2), therefore, the minimum torque that can be accurately measured by the transducer is 0.5 Nm. This equates to a friction factor of ~0.01 for a 28 mm or 36 mm diameter bearing tested under a peak load of 2 kN (where the data is taken from), when derived from Equation 4.2. Therefore, when comparing the two simulators, any differences in the resultant friction factor ± 0.01 will be considered as a measurement limitation of the piezoelectric transducer.

4.7 Initial Validation Study Results

The initial validation studies compared the friction factor results obtained from the two simulators (A and Mk B) after testing three artificial hip bearing samples (28 mm Ø MoP, 28 mm Ø CoC, 36 mm Ø CoC), with three different lubricants (water, 25 % serum, 100 % serum), using different kinetic input profiles. Student's *t*-tests were used to test the level of significance. The mean friction factor results for all of the tests following the completion of three repeats can be found in Appendix D.

4.7.1 Constant Load and Standard Profile Results

4.7.1.1 Constant Load Torque Plots

Torque values recorded during the CoC constant load tests were plotted and found to be asymmetrical on friction simulator Mk B (Fric Sim B), unlike the torque plots from simulator A (Fric Sim A), which were much more symmetrical. This finding is illustrated in Figure 4.15 (i), where the torque plot for simulator A lays symmetrically ± 1.6 Nm above and below zero. In contrast to this, the torque plot for friction simulator Mk B in Figure 4.15 (ii) is on average 1.4 Nm above zero and -1.7 to -1.9 Nm below zero.

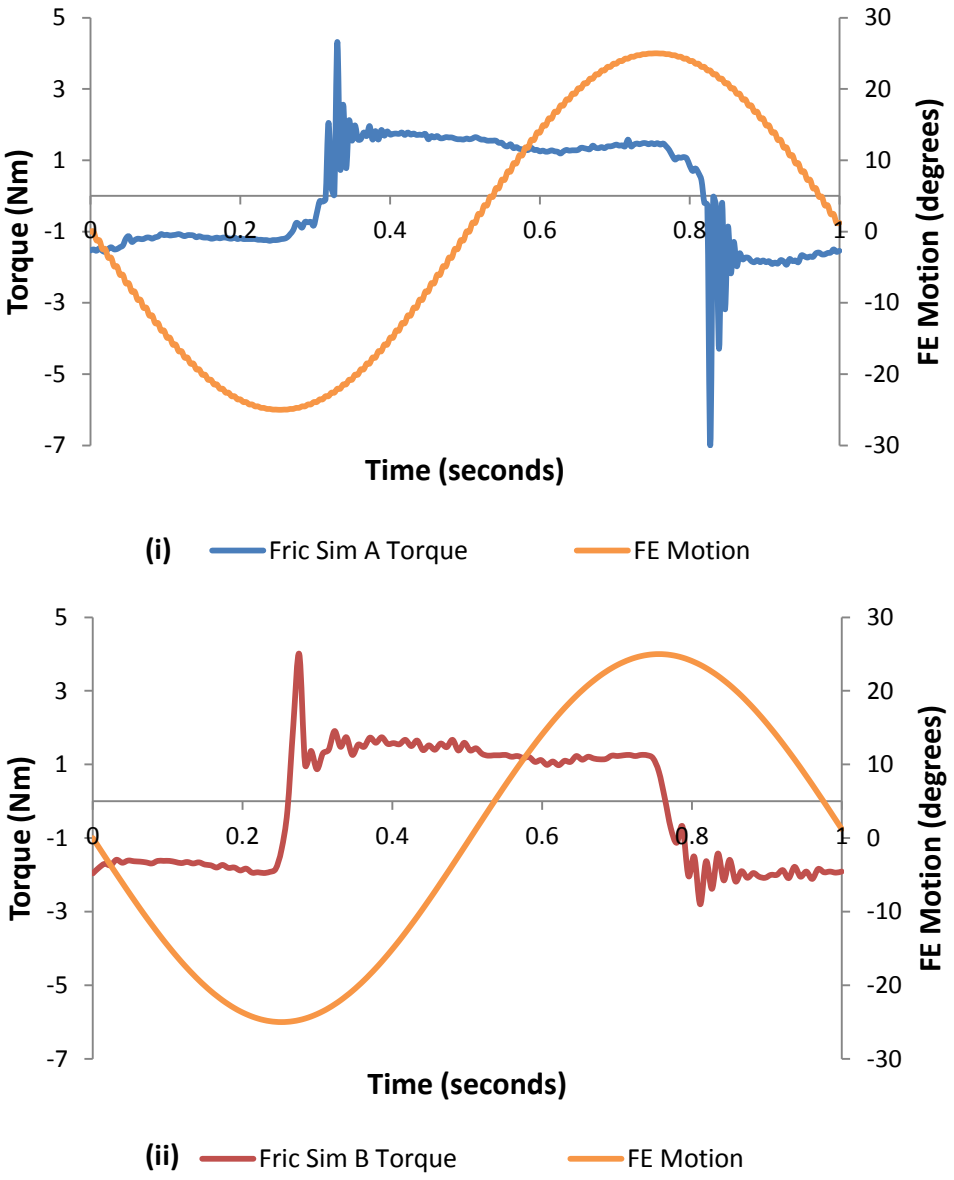

Figure 4.15: Torque for the 36 mm CoC sample tested with a 1 kN constant load and 25 % serum lubricant. Plot of measured torque taken from last cycle on simulators A (i) and Mk B (ii).

Further examples illustrating the asymmetry of the torque values measured during the constant load tests on simulator Mk B using the 28 mm CoC bearings are presented in Figure 4.16 and Figure 4.17. The negative torque value is an average of -0.8 to -0.9 Nm in both figures, i.e. both 25 % and 100 % serum lubricants, and the mean positive value is 0.4 Nm for the 25 % serum lubricant test (Figure 4.16) and 0.2 Nm for the test using 100 % serum.

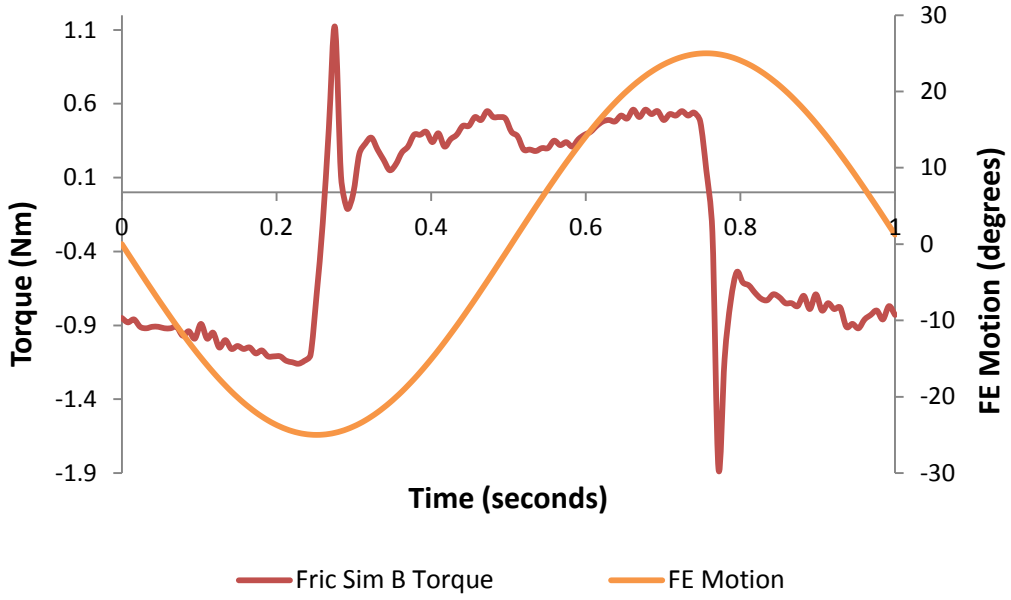

Figure 4.16: Torque for the 28 mm CoC sample tested with a 300 N constant load and 25 % serum on friction simulator Mk B. Torque plot of the last cycle.

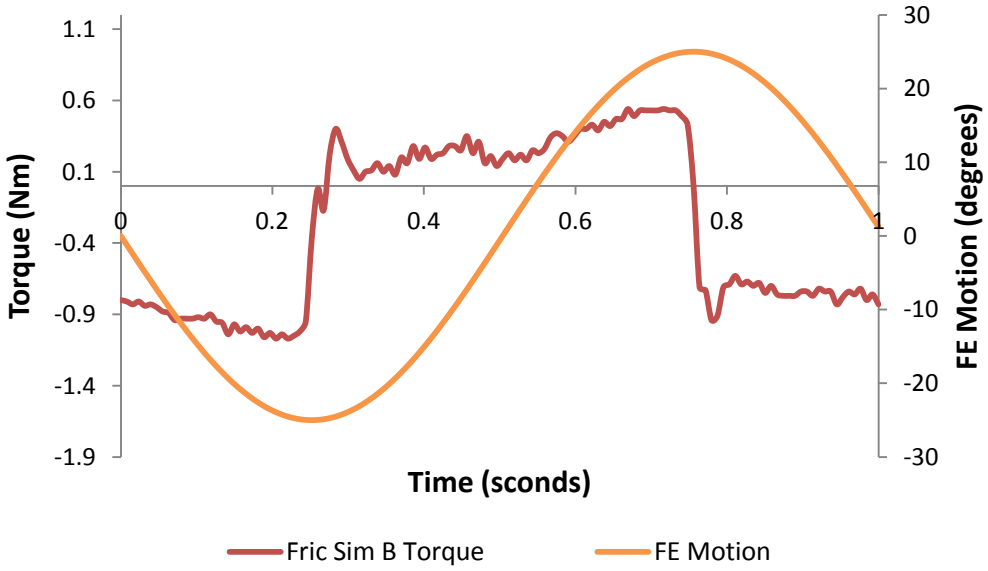

Figure 4.17: Torque for the 28 mm CoC sample tested with a 300 N constant load and 100 % serum on friction simulator Mk B. Torque plot of the last cycle.

The results and trends for the torque plots described in this section were found to be very similar for all repeats. It was also observed that there was more oscillation and variability in the torque output from friction simulator Mk B during each one-second cycle when compared to friction simulator A.

4.7.1.2 Standard Profile Test Results

There were no significant statistical differences ($p > 0.05$) in mean friction factor results for the 28 mm MoP control sample tested with the standard profile for any of the three lubricants. There was a slight difference in friction factor for the water lubricant tests, 0.031 ± 0.001 from simulator A and 0.040 ± 0.009 from simulator Mk B, but when tested with 25 % and 100 % serum lubricants the friction factor was the same on both simulators at approximately 0.06 and 0.07 respectively.

In contrast to this, the 28 mm CoC sample mean friction factor results from the two simulators were significantly different for the 25 N and 100 N SPL dynamic profile tests (Figure 4.18) and the 1 kN constant load test (Figure 4.19), (all $p = 0.00$), when tested with both a 25 % and 100 % serum lubricant. Significant differences in mean friction factor were also recorded when using the 36 mm CoC sample, however, the degree of significance was slightly less ($p = 0.01$ to $p = 0.03$). It was also observed that, unlike the 28 mm CoC sample, mean friction factor results that were significantly different were more randomly distributed and there was no obvious pattern or trend (Figure 4.20 and Figure 4.21).

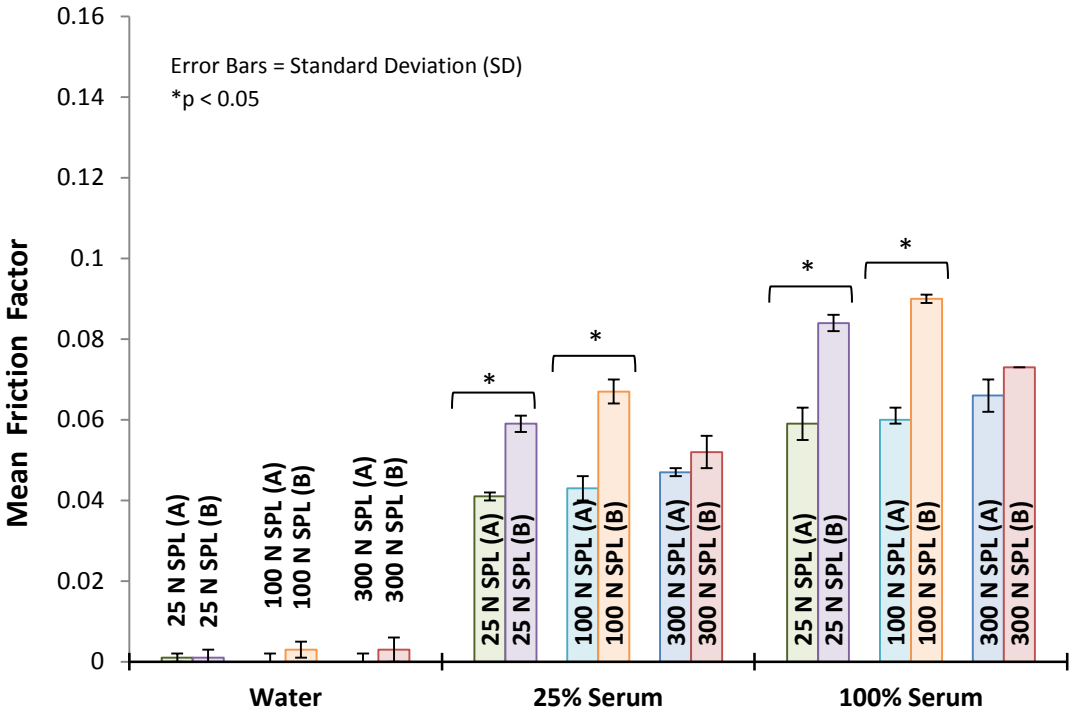

(A) = Friction Simulator A (B) = Friction Simulator Mk B SPL = Swing Phase Load

Figure 4.18: Mean friction factor results ± standard deviation (SD) (n = 3) for the 28 mm CoC sample. The motion was ± 25° FE and the peak load was 2 kN with varying SPLs for all tests carried out on friction simulators A and MK B.

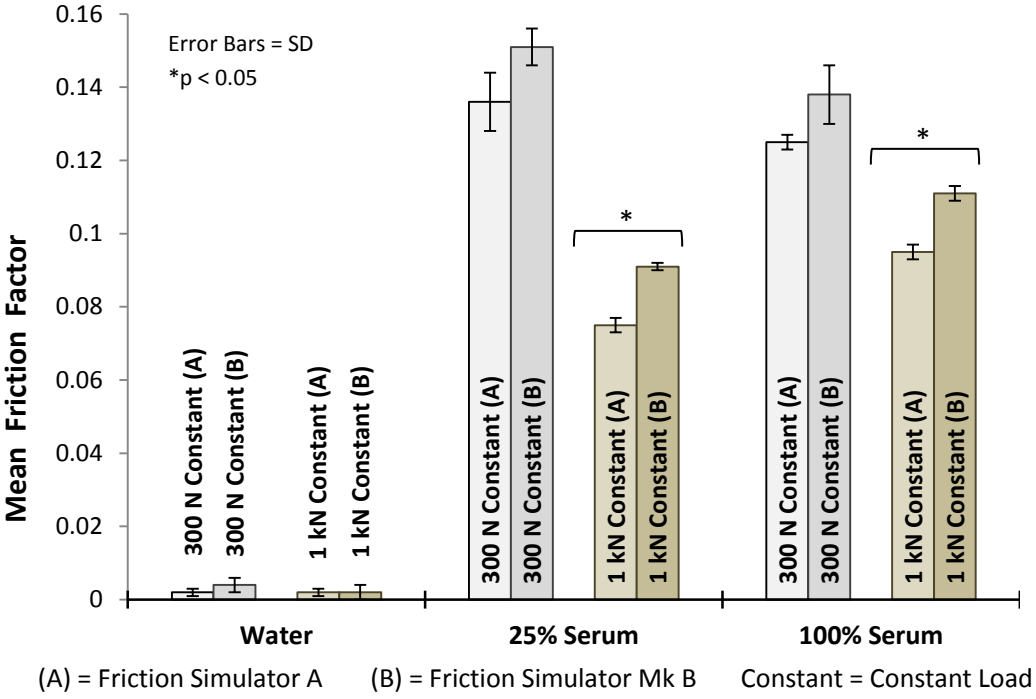

Figure 4.19: Mean friction factor results ± SD (n = 3) for the 28 mm CoC sample tests carried out on friction simulators A and Mk B with a constant load ± 25° FE.

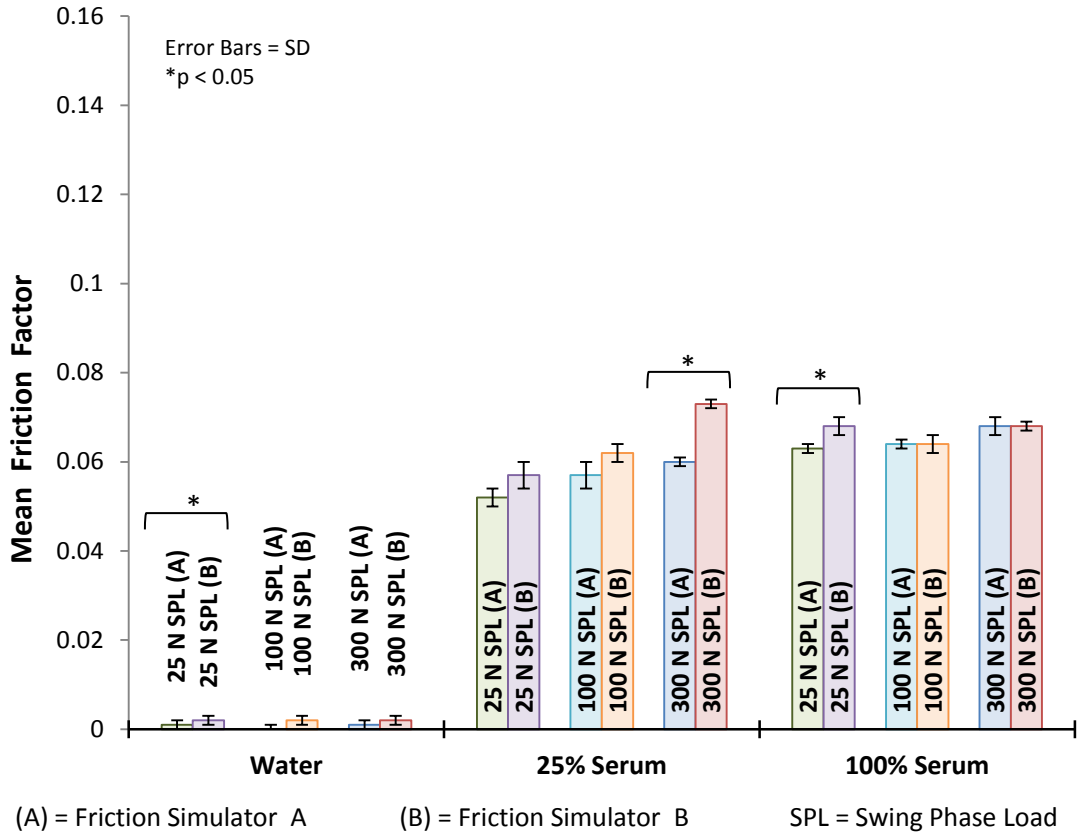

Figure 4.20: Mean friction factor results ± SD (n = 3) for the 36 mm CoC sample. The motion was ± 25° FE and the peak load was 2 kN with varying SPLs for all tests carried out on friction simulators A and Mk B.

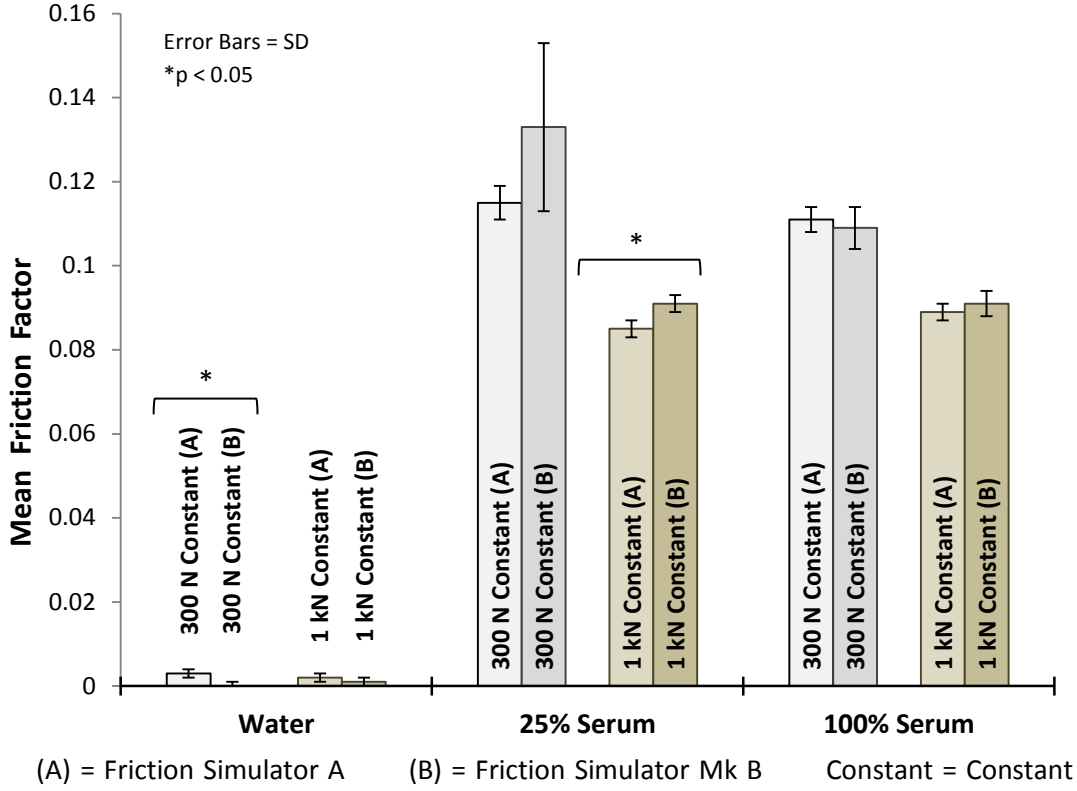

Figure 4.21: Mean friction factor results ± SD (n = 3) for the 36 mm CoC tests carried out on friction simulators A and Mk B with a constant load ± 25° FE.

The mean friction factor was also found to increase when lubricants with a greater protein concentration was used (i.e. water < 25 % serum < 100 % serum) for tests conducted on simulator A using a dynamic load, although this was not as evident on simulator Mk B for the 36 mm CoC sample (Appendix D). The measured friction of the CoC bearings also increased slightly on both simulators when the SPL was increased from 25 N to 100 N (Figure 4.18 and Figure 4.20).

The most salient data to emerge from the dynamic tests was the marked differences between the forward and reverse results measured using simulator Mk B.

The friction factor measured during forward tests on the 28 mm MoP sample was found to be significantly different to those measured during the reverse tests for all three lubricants ($p < 0.05$). The forward friction factor on friction simulator Mk B was larger than the reverse friction factor by a magnitude of 0.04 with the water lubricant and 0.06 when using 25 % and 100 % serum lubricants. Forward and reverse friction factors measured on friction simulator A were not significantly different and therefore

comparable to the mean friction factor. The results of the forward and reverse tests for the 28 mm MoP sample have been summarised in Figure 4.22.

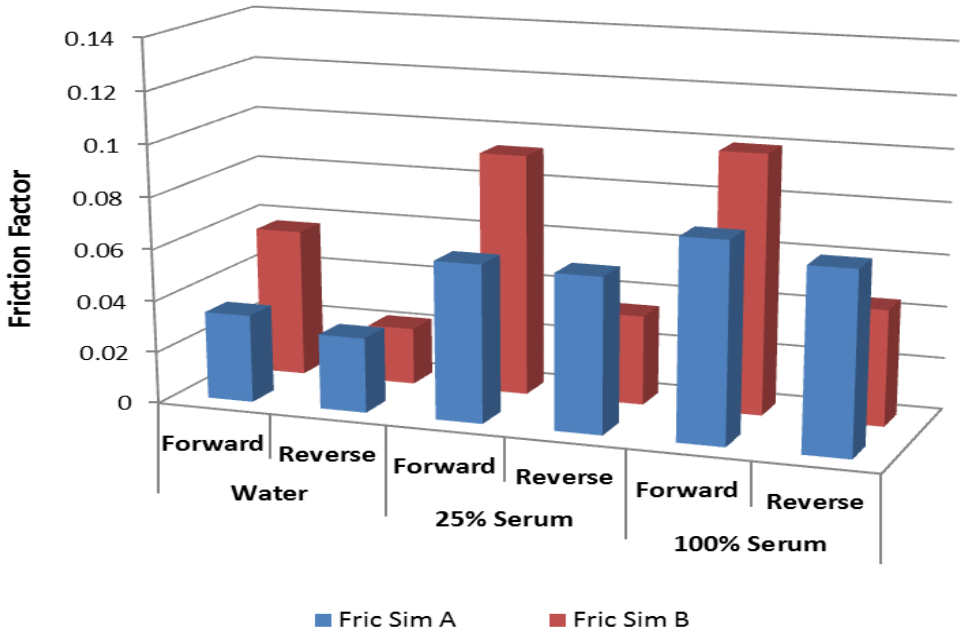

Figure 4.22: 28 mm MoP control sample standard test (i.e. 300 N to 2 kN ± 25° FE) forward and reverse friction factor results. Reverse data has been converted to positive values. Forward friction is significantly larger than reverse friction ($p < 0.05$) for all friction simulator Mk B results.

The forward friction factor of the 28 mm and 36 mm CoC samples was also significantly larger than the reverse friction factor ($p = 0.000$) for all dynamic and constant load profile tests when using 25 % and 100 % serum lubricants. The dynamic forward friction was larger than the dynamic reverse friction by an average magnitude of 0.04 ($n = 12$; 6 x 28 mm CoC and 6 x 36 mm CoC), with the smallest difference in magnitude of friction factor being 0.02 and the largest 0.07. No significant differences in friction were apparent when using a water lubricant with either of the CoC samples, where the friction factor for all tests was very small (0.000 ± 0.001).

4.7.1.3 Low Load (Natural Tissue Profile) Test Results

The mean friction factor for tests conducted on the 28 mm MoP control samples using the tissue profile (i.e. 25 N SPL to 800 N peak load ± 15° FE) and a water lubricant was 0.061 ± 0.007 for simulator A and 0.058 ± 0.021 for simulator Mk B . This value is approx. 0.03 (simulator A) and 0.02 (simulator Mk B) higher than the mean friction factor recorded for the standard tests. This increased friction at lower loads and

motion was less obvious for tests conducted using 25 % serum and not observed with 100 % serum (Appendix D). Simulators A and Mk B both recorded different friction factor values for the forward and reverse tests, although these variances were more pronounced in simulator Mk B (Figure 4.23).

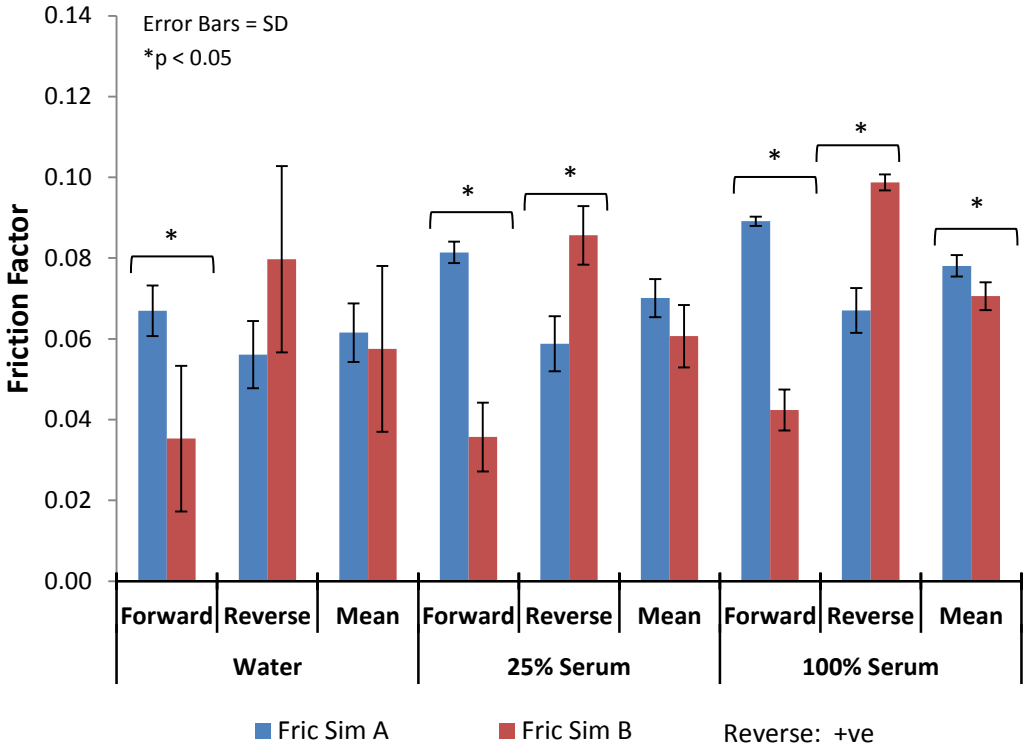

Figure 4.23: Friction factor results ± SD (n = 3) for the 28 mm MoP control sample tissue profile tests (25 N 800 N ± 15° FE) carried out on friction simulators A and Mk B. Reverse data has been converted to positive values.

In contrast to the varied results obtained from the 28 mm MoP control sample, higher friction factor results for simulator Mk B compared to simulator A were recorded for all the tissue profile tests using the CoC bearings, and very similar trends in both samples (28 mm and 36 mm) were observed. The results obtained from the 36 mm CoC sample are displayed graphically in Figure 4.24 and the mean friction factor results for all of the tissue profile tests are in Appendix D.

Values remained very low on both simulators when tested with the water lubricant. On simulator A, there was a small increase in friction with 25 % serum compared to the standard test, which again was not observed when using 100 % serum. This was dissimilar to simulator Mk B where a marked increase in friction factor was observed

when using both 25 % and 100 % serum, with the greatest variability between the repeats being seen in the 36 mm CoC sample.

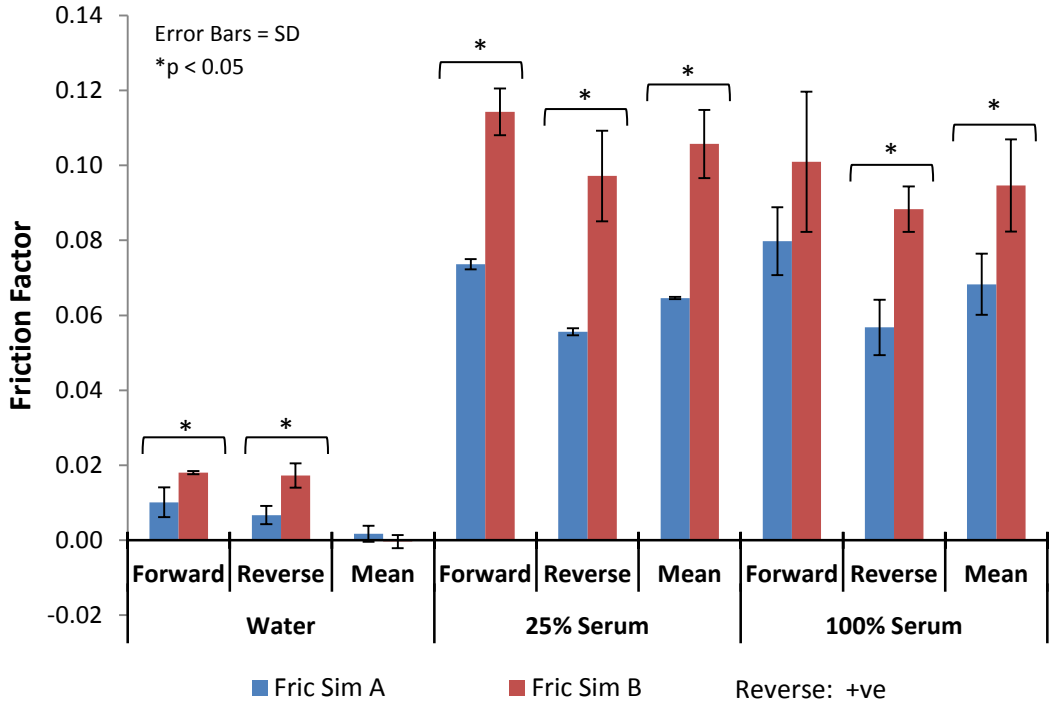

Figure 4.24: Friction factor results ± SD (n = 3) for the 36 mm CoC control sample tissue profile tests (25 N 800 N ± 15° FE) carried out on friction simulators A and Mk B. Reverse data has been converted to positive values.

Significant differences ($p < 0.05$) were identified between the results obtained from simulator A compared to Mk B for the majority of tests on all three samples (Figure 4.23 and Figure 4.24), with the 36 mm CoC significances replicating those of the 28 mm CoC sample. Separate analysis of the forward and reverse friction factor results for simulator Mk B revealed significant differences ($p = 0.00$ to $p = 0.01$) for all three samples when tested with 25 % and 100 % serum. There were no significant differences ($p > 0.05$) between the forward and reverse results for the two CoC samples tested with water, where the friction factor was very low.

4.7.2 Discussion and Conclusions Following Initial Validation Studies

A number of significant differences between the friction factor results collected from the new pendulum friction simulator (Mk B) and the existing, previously validated pendulum friction simulator (A) were observed during the initial validation studies, meaning that at this stage, the null hypothesis could not be accepted. The most noteworthy results to emerge when comparing data from the two simulators were:

- Significant differences in friction factor measured during forward and reverse dynamic profile tests on pendulum friction simulator Mk B
- Larger discrepancies in the results obtained from the two simulators when using lower dynamic loads
- Constant load torque output positioned asymmetrically above and below zero

It was also observed that the results obtained from the 28 mm MoP and 36 mm CoC bearing couples exhibited the greatest variability about the mean.

More encouraging findings from the initial studies that have been previously reported in the literature were:

- The detection of very low friction factor measurements when testing CoC bearings with a water lubricant (Scholes *et al.*, 2000)
- Higher friction factor values with larger SPLs and increased protein concentrations (Brockett *et al.*, 2007)

The theoretical predicted film thickness and lubricating regime for the 28 mm MoP bearing tested with input profiles of i) 300N to 2 kN ± 25° FE and ii) 25N to 800 N ± 25° FE, both with 25 % serum lubricant, with was calculated using the equations presented in Section 1.6.4, and the parameters listed in Table 4.4. Experimental data was taken from the point in the cycle with the highest velocity and peak load (Section 4.4.3), and therefore the loads (W) used for the calculations were 2,000 N and 800 N. The angular velocity (ω), which was calculated as the rate of change of angular displacement during the high velocity phase of the cycle (i.e. change in angular displacement/change in time), was 2.58 and 1.47 radians/second for ± 25° and ± 15° FE respectively. The 25 % serum lubricant was assumed to be Newtonian with a constant viscosity of 0.0009 Pascal-second (Yao *et al.*, 2003).

Table 4.4: Young's Moduli, Poisson's Ratios (Jin *et al.*, 1997) and roughness average values for theoretical calculation of lubricating regime.

Material	Young's Modulus E (GPa)	Poisson's Ratio ν	R_a (Table 4.2) µm
UHMWPE	1	0.4	0.5
Cobalt Chrome	200	0.3	0.008

The results of the theoretical calculations were as follows:

i) The minimum film thickness ($h_{min)}$ = 0.024 µm and the lambda ratio (λ) = 0.05

ii) The minimum film thickness ($h_{min)}$ = 0.020 µm and the lambda ratio (λ) = 0.04

The results of the theoretical calculations for the 28 mm MoP THR samples predict a boundary lubricating regime, as indicated in Figure 1.11, for both input profiles.

The objective of the initial validation studies was to assess the function of pendulum friction simulator Mk B using artificial hip prostheses and an existing friction simulator, with the aim of then extending the validation process to include natural tissue. The analysis of the results, however, highlighted a number of anomalies that needed to be addressed before completing the validation process using natural tissue samples.

The next section contains an overview of the exploratory work carried out to identify possible causes for the discrepancies in the results highlighted in this section.

4.8 Modification of Pendulum Friction Simulator Mk B

4.8.1 Introduction

The mean friction factor measured on the two simulators during the initial validation period was not found to be significantly different for any of the tests; however, significant discrepancies between the forward and reverse results were identified. This needed to be addressed because subsequent planned validation testing and future work using natural tissue would be conducted running the simulator in one direction only. The rationale for not testing natural tissue under forward and reverse loading conditions will be explained in Section 5.3.2.

4.8.2 Carriage Movement

The piezoelectric force transducer was calibrated to detect small tensile and/or compressive forces, from which the magnitude of frictional torque and friction factor are calculated. To understand how the friction measuring carriage, and therefore force transducer, moves when being subjected to constant and dynamic loads, vertical movement of the carriage was investigated. Standard forward and reverse dynamic tests (i.e. 300 N to 2 kN) and a 1 kN constant load test, all with ± 25° FE, were used to

evaluate this. The 28 mm MoP control sample with water lubricant was *in situ* throughout, aligned to the COR of the simulator as normal.

A DTI was placed on a flat surface on the top left-hand side of the friction measuring carriage so that any vertical movement occurring whilst it was running could be quantified. Once measurements had been taken for the forward, reverse, and constant load tests, the DTI was moved to the right-hand side of the carriage. Care was taken to ensure that the stylus of the DTI was placed parallel to the surface being measured to reduce the risk of cosine error, and also that its location, relative to the carriage, was the same on both sides. Small oscillations on the DTI as the simulator was running made it difficult to give definitive values; however, the approximate values, which have been presented schematically in Figure 4.25, did highlight some asymmetry in the movement of the carriage under dynamic loads. Carriage movement was found to be much greater when running under the 300 N to 2 kN dynamic load in the forward direction, where it was approximately 40 µm, compared to when it was running under reverse dynamic or 1 kN constant loading conditions, where values in the region of 5-15 µm were registered on the DTI. It was hypothesised that these results could explain why the initial validation tests showed that forward dynamic load tests produce higher frictional torque measurements than reverse dynamic load tests.

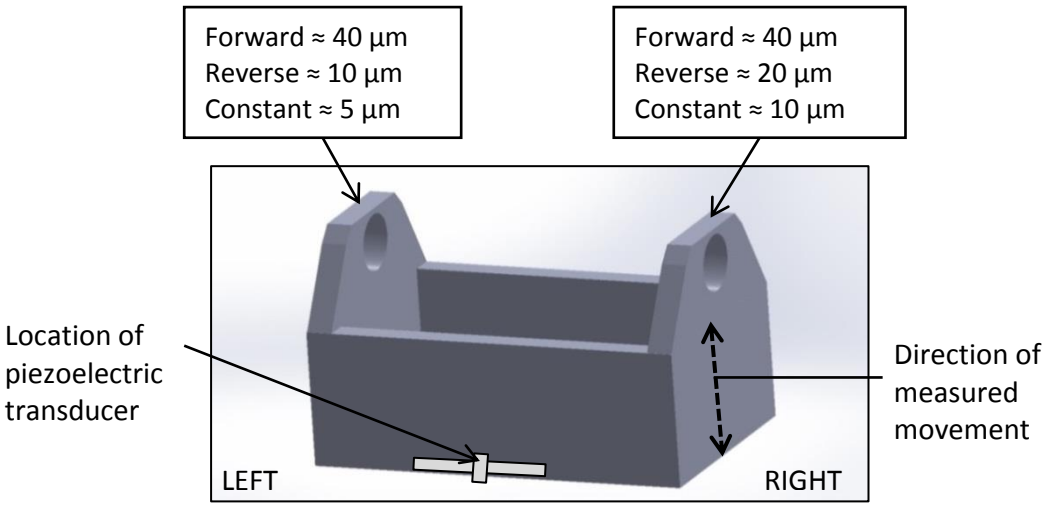

Figure 4.25: Schematic diagram of the vertical friction measuring carriage movement of friction simulator Mk B measured with a dial test indicator under dynamic and constant loads.

4.8.3 Comparator Chart

In order to see if there were any obvious differences in the design features or specifications that could have contributed to the poor agreement in results and/or the asymmetrical movement of the carriage discussed in Section 4.8.2, a chart was drawn up comparing pendulum friction simulator A with pendulum friction simulator MK B. The chart, which can be seen in its entirety in Appendix E, looked at various characteristics relating to the simulator control systems, hydrostatic bearings, and sample alignment.

The most noticeable differences between the two simulators highlighted by the comparator chart were associated with the oil supply to the hydrostatic bearing. The oil pressure was found to be considerably lower in friction simulator MK B, which was fluctuating between 1150 psi (pounds per square inch) and 1250 psi, compared to a steady state pressure of 1750 psi in simulator A.

To determine if adjusting the oil pressure affected the friction factor, the 28 mm MoP control sample was tested using a standard test in forward with water lubricant whilst manually adjusting the oil pump pressure. It was not possible to increase the oil pressure, implying that the pump was working at its maximum capacity. It was, however, possible to reduce the oil pressure and this had the following effect on the friction factor (observed values from monitor therefore approximate values given):

- Oil pressure at 1150/1250 psi Friction factor ~0.05
- Oil pressure reduced to 1000 psi Friction factor ~0.06
- Oil pressure reduced to 800 psi Friction factor ~0.08

These results should be interpreted with caution due to the small and rudimentary nature of this investigation, however, the results suggested that a link existed between oil pressure and friction factor value.

It was also noted that the capillary tubing in simulator Mk B was longer and wider than that in simulator A and that the oil flowing out of the hydrostatic bearing on simulator Mk B was quite fast and pulsating slightly, unlike the steady and constant flow observed on simulator A.

4.8.4 Discussion

It was possible that a hydrostatic bearing that was not functioning effectively could have given rise to the asymmetrical carriage movement observed in Section 4.8.2 and the unsatisfactory friction factor data collected during the initial validation tests (Section 4.7). To investigate this, the hydrostatic bearing (Figure 4.26) was removed by Simulation Solutions Ltd. (SimSol) and a coordinate measuring machine (CMM) was used to measure and assess the bearing base plate and friction measuring carriage for any tolerance or alignment issues. The report from SimSol confirmed that the bearing endplates were aligned, all cylindrical parts were concentric, and the geometry and diametral clearances were consistent with the design specification and engineering drawings.

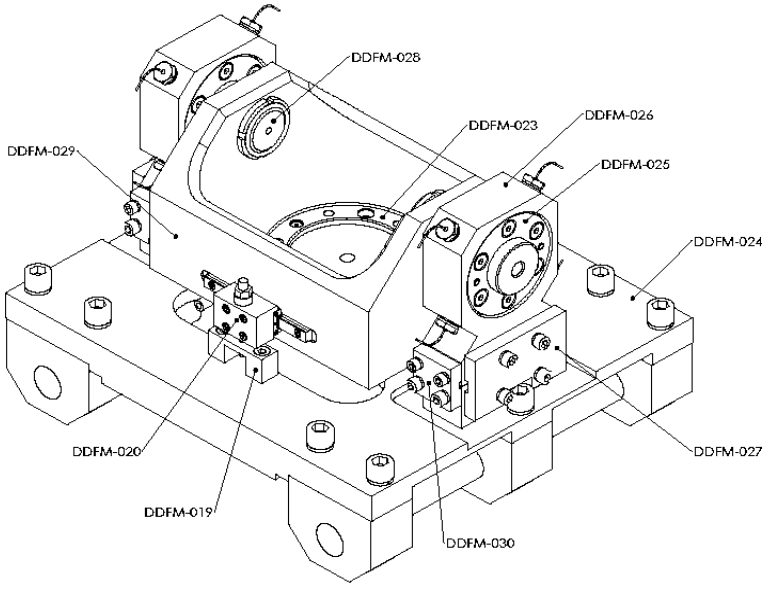

DDFM-019	Adjuster mount	DDFM-026	Hydrostatic bearing
DDFM-020	Friction sensor	DDFM-027	Parallelism key plate
DDFM-023	Cradle spacer	DDFM-028	Sample cradle shaft
DDFM-024	Hydrostatic bearing base	DDFM-029	Solid cradle
DDFM-025	Hydrostatic bearing end plate	DDFM-030	FR alignment key

Figure 4.26: Schematic diagram of hydrostatic bearing (Simulation Solutions Ltd., 2012).

As no apparent anomalies relating to the manufacture of the bearing baseplate and carriage were identified it was reasonable to suggest that the notable differences in oil supply to the hydrostatic bearings identified in Section 4.8.3 could have affected the frictional torque values (Martin, 2006).

4.8.5 Replacement of Capillary Tubing

The comparator chart (Appendix E) indicated that friction simulator Mk B was running with lower, fluctuating oil pressure and had slightly shorter capillary tubing with a greater diameter than friction simulator A. The oil pump on simulator Mk B was already running at maximum capacity, therefore, SimSol agreed that the capillary tubing supplying the oil to the hydrostatic bearing needed to be lengthened to increase resistance and oil flow, thus theoretically making the frictionless bearing more effective (Cheng and Rowe, 1995).

Assuming a laminar (i.e. non-turbulent) flow of oil, the length of the capillary tubing that would be required to increase the flow rate and provide oil to the hydrostatic bearing at a pressure similar to that of simulator A can be determined using a calculation based on Poiseuille's Law (Opitz, 1967) (Equation 4.3):

$$Q = \frac{\Delta P \pi R^4}{8\eta L} \qquad \textbf{Equation 4.3}$$

where Q is the volumetric flow rate, R is the internal radius of the tube, $\Delta\mathrm{P}$ is the pressure difference between the two ends of the tube, η is the dynamic fluid viscosity in S.I. units, which is Pa s (pascal-second), and L is the length of the tube.

SimSol assumed that the pressure drop across the tubing would be the same in simulators A and Mk B, therefore, using oil of the same viscosity (Appendix E):

$$Q = \frac{\Delta \mathrm{P} \times R^4}{\frac{8}{\pi}\eta \times L} \qquad \textbf{Equation 4.4}$$

$$Q = \frac{R^4}{L} \qquad \textbf{Equation 4.5}$$

The internal radius of the capillary tubing on simulator A was 0.250 mm (R_A) and the tubing bought to replace that on simulator Mk B was 0.355 mm (R_B). The length of the tubing fitted to simulator A was 224 mm (L_A), therefore, to give the same flow rate in both simulators the length of the capillary tubing required on simulator Mk B (L_B) was:

$$\frac{{R_\mathrm{A}}^4}{L_\mathrm{A}} = \frac{{R_\mathrm{B}}^4}{L_\mathrm{B}} \qquad \textbf{Equation 4.6}$$

$$\frac{0.250^4}{224} = \frac{0.355^4}{L_B} \quad \textbf{(4.7)}$$

$$\frac{0.250^4}{224} = \frac{0.355^4}{L_B} \quad \textbf{(4.8)}$$

$$L_B = 224 \times \left(\frac{0.355}{0.250}\right)^4 \quad \textbf{(4.9)}$$

$$L_B = 224 \times 4.066 \quad \textbf{(4.10)}$$

$$L_B = 910.78 \text{ mm} \quad \textbf{(4.11)}$$

The capillary tubing on friction simulator Mk B was replaced with longer tubing that was 912 mm in length, which is very close to the resultant value (4.11), calculated using Equation 4.6. On completion of this work, the simulator was re-tested using a standard test with the 28 mm MoP control sample, during which, the oil pressure and oil flow from the hydrostatic bearings had notably improved and were more consistent with friction simulator A. The features listed on the comparator chart pertinent to the oil supply were updated to reflect this modification (Table 4.5).

Table 4.5: Table comparing simulator features in relation to the hydrostatic bearing before and after new capillary tubing was fitted to friction simulator Mk B.

		Friction Simulator A	Friction Simulator Mk B	
			Original	Modified
Oil Viscosity (η)		0.03 Pa s	0.03 Pa s	0.03 Pa s
Oil Pressure (psi)		1750	1150 to 1250	2000
Oil Pressure Gauge		Steady state	Fluctuating	Steady state
Capillary Tubing	**Internal Diameter**	0.50 mm	0.80 mm	0.71 mm
	Length	224 mm	205 mm	912 mm
Observed Oil Flow		Steady/Constant	Fast/Pulsating	Steady/Constant

Vertical movement of the friction measuring carriage was re-assessed using the same methodology described in Section 4.8.2. This had also improved, with the amount of forward movement being halved to a mean of 20 ± 5 µm, with movement recorded under constant loading registering only 5 µm on the DTI.

4.9 Further Validation Studies

The results from the initial validation studies reported in Section 4.7 highlighted some significant differences between the new simulator being validated (pendulum friction simulator Mk B) and the existing simulator (pendulum friction simulator A). Having identified and addressed possible contributing factors for these disparities, further validation testing was necessary to re-assess the function of simulator Mk B following the fitting of new capillary tubing.

4.9.1 Materials and Methods

The main areas of concern regarding the function of friction simulator Mk B were the discrepancies between the forward and reverse friction factor values, which in some instances appeared to affect the mean friction factor, and the asymmetry of the constant load torque plots. In order to investigate whether these anomalies had been rectified by the modification of the simulator, a consolidated validation plan was implemented using the following materials:

- Pendulum friction simulator A for comparison
- 28 mm Ø MoP and 36 mm Ø CoC total hip replacements
- Lubricants: water and 25 % (v/v) NBCS

The results generated by the 28 mm CoC sample had been similar to those of the 36 mm CoC sample, therefore it was decided that only the 36 mm Ø bearing couple would be re-tested. The 36 mm sample was chosen because, as previously stated in Section 4.6.3, the diameter is comparable with that of the natural porcine acetabulum, which will be used in the next stage of the validation process. Similarly, friction factor had already been shown to increase with protein concentration, therefore only a 25 % serum lubricant was used. This was chosen rather than 100 % serum, as it is closer to the physiological environment when testing natural porcine tissue.

The 28 mm MoP sample was chosen as the second total hip replacement due to it being of a different diameter and material to the CoC sample, thus increasing the sampling validity of the study.

4.9.1.1 Input Kinetics

The standard profile (300 N SPL to 2 kN peak load ± 25° FE) and the tissue profile (25 N SPL to 800 N peak load ± 15° FE) were used to re-test the simulator under different dynamic loads and motions, and the symmetry of the torque output under constant loading was re-assessed using 800 N ± 15° FE (Table 4.6). During the initial validation studies, the same information was gained from evaluating the 300 N and 1 kN constant load tests, therefore, it seemed reasonable to re-assess the constant load torque output using just one test. A load and motion of 800 N ± 15° FE was chosen because this kinetic profile was going to be used for subsequent hemiarthroplasty testing (Section 5.3.2). In the absence of a second CoC sample, the constant load test was also conducted on the 28 mm MoP bearing couple in order to increase the sample size.

Table 4.6: Further validation studies conducted on pendulum friction simulators A and Mk B using two artificial hip replacement samples with standard, tissue, and constant load tests, and two lubricants.

Sample	Tests (load ± FE motion)	Lubricants	Repeats (n)	Sub Total	Total Tests for Simulators A and Mk B
28 mm Ø MoP	**Standard** *(300 N to 2 kN ± 25° FE)* **Tissue** *(25 N to 800 N ± 15° FE)* **Constant** *(800 N ± 15° FE)*	Water 25 % Serum	3	18	36
36 mm Ø CoC	**Standard** *(300 N to 2 kN ± 25° FE)* **Tissue** *(25 N to 800 N ± 15° FE)* **Constant** *(800 N ± 15° FE)*	Water 25 % Serum	3	18	36
			Total Number of Tests		**72**

4.10 Further Validation Test Results

On completion of the further validation studies detailed in the previous section, the mean, forward, and reverse test friction factor results were again compared and analysed using student's *t*-tests to assess the level of significance between the two simulators. Paired sample *t*-tests were also used to determine whether there was any significant difference in the results obtained using simulator Mk B before and after its modification. The mean friction factor results for all of the further validation studies can be found in Appendix F.

4.10.1 Constant Load Results

There were no significant differences in friction factor values detected between the two simulators for the constant load tests, and the torque measurements plotted from the last cycle of each test was more symmetrical than had been previously reported in the initial studies (Section 4.7.1.1).

Torque plots from constant load tests conducted on the 28 mm MoP sample with a water and serum lubricant are shown in Figure 4.27 (i) and (ii) respectively. The torque plot for the sample tested in water is laying almost symmetrically ± 1.25 Nm above and below zero (Figure 4.27 i), and the plot for the sample tested in 25 % serum is laying on average 1.7 Nm above and -1.9 Nm below zero (Figure 4.27 ii).

Examples of the torque output measured whilst testing the 36 mm CoC bearing couple, with serum lubricant, on simulators A and B has been plotted in Figure 4.28 (i) and (ii) respectively. Excluding data from around the turning spikes (i.e. where the FE rocker changes direction), the symmetry of the plots from the two simulators is similar, with the torque from simulator A approximately 0.9 Nm above and -0.7 Nm below zero (Figure 4.28 i), and from simulator Mk B approximately 0.8 Nm above and -1.1 Nm below (Figure 4.28 ii).

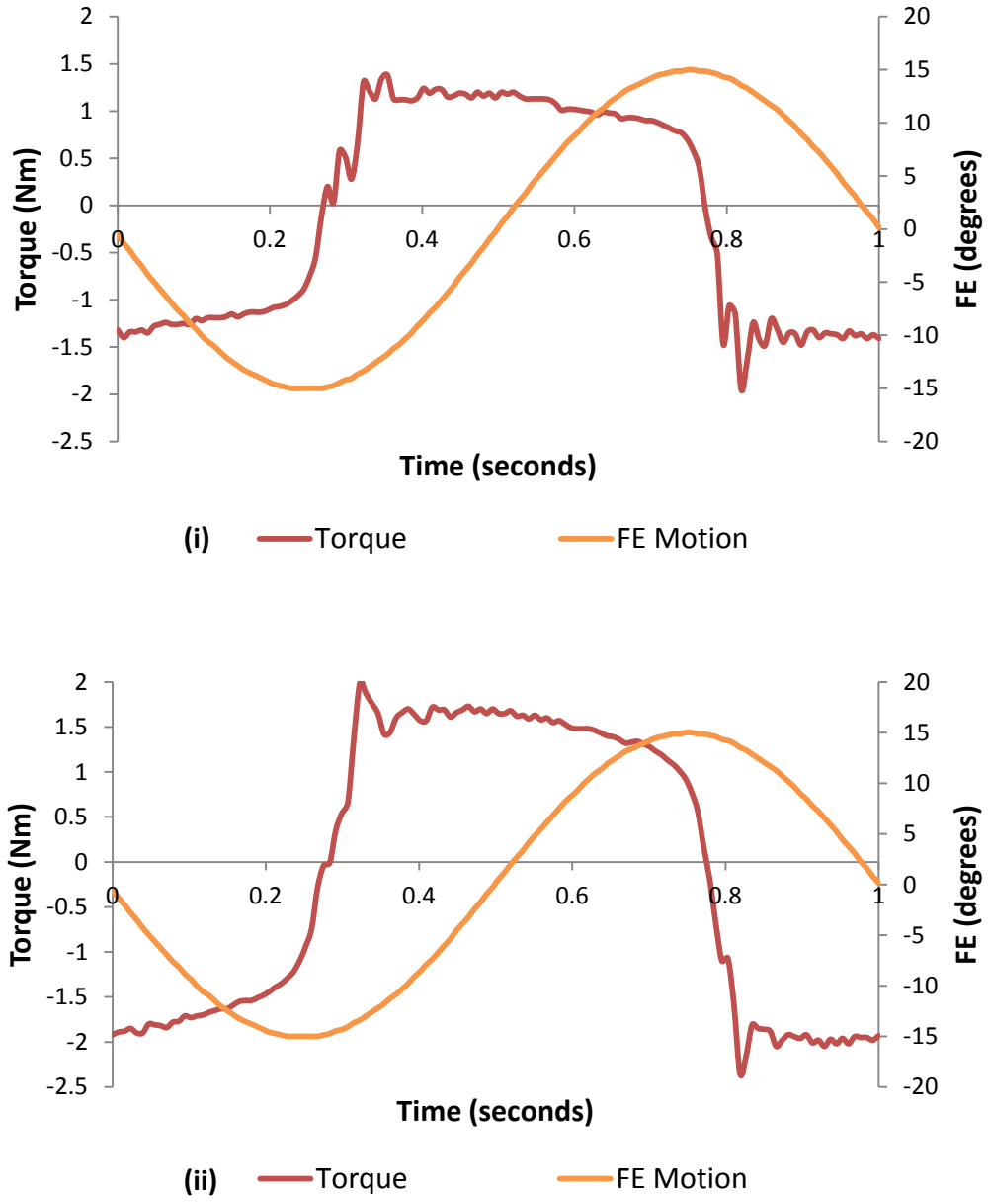

Figure 4.27: Torque for the 28 mm MoP sample tested on pendulum friction simulator Mk B with an 800 N constant load ± 15° FE, after new capillary tubing had been fitted. Plot of measured torque taken from last cycle with (i) water and (ii) 25 % serum lubricant.

It was also observed that the torque output graphs from friction simulator Mk B appeared to be less oscillatory than the graphs plotted during the initial validation phase, although there was still some variability observed at the start of each cycle.

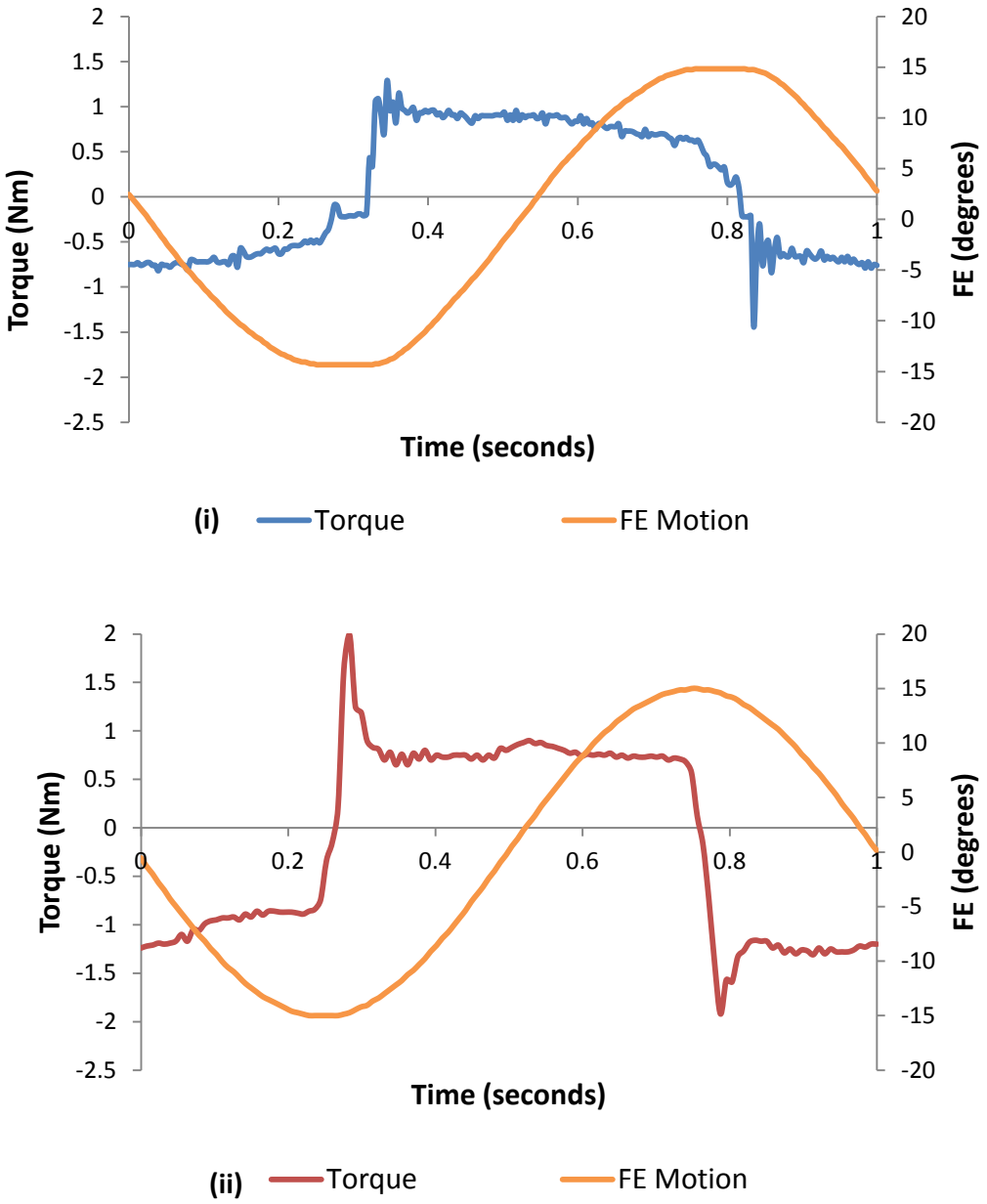

Figure 4.28: Torque for the 36 mm CoC sample tested on pendulum friction simulator A (i) and Mk B (ii), after new capillary tubing had been fitted, with an 800 N constant load ± 15° FE and 25 % serum lubricant. Plot of measured torque taken from last cycle.

4.10.2 Dynamic Profile Results

4.10.2.1 Initial Versus Modified Simulator Mk B Results

A small reduction in mean friction factor of approximately 0.01 and 0.02 ($p > 0.05$) was recorded for standard and tissue profile tests respectively, conducted on the 28 mm MoP sample with a water lubricant (Figure 4.29).

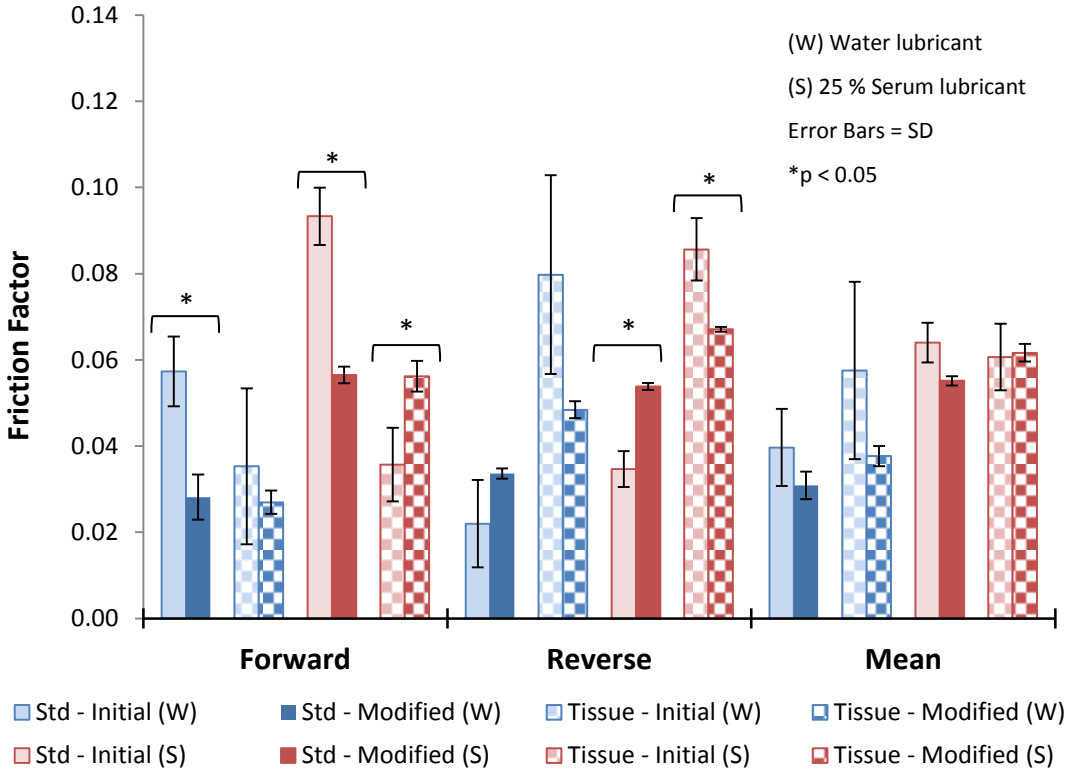

Figure 4.29: Friction factor results ± SD (n = 3) for the 28 MoP control sample standard (Std) and tissue profile tests conducted on friction simulator Mk B, before (initial) and after the fitting of new capillary tubing (modified). Reverse data has been converted to positive values.

Mean results for tests conducted with the serum lubricant remained largely unchanged; however, separate analysis of the forward and reverse test friction factors revealed significant differences between the initial results and the modified simulator results. Initially, the forward and reverse friction factors for the standard profile with serum were recorded as 0.093 ± 0.007 and -0.035 ± 0.004 respectively, however, the modified results were statistically different at 0.056 ± 0.002 ($p = 0.02$) and -0.054 ± 0.001 ($p = 0.01$). Forward and reverse friction factors for the tissue test with serum were also both significantly different ($p = 0.04$) but to a lesser degree (Figure 4.29). There was a noticeable improvement in the dispersion of the results around the mean for all 28 mm MoP tests, predominantly for those conducted with a water lubricant where there was a marked reduction of the standard deviation (SD error bars on Figure 4.29).

Friction factors for the 36 mm CoC sample tested with water remained very low (Figure 4.30) and overall, differences between the initial results and the modified results for this bearing couple were less pronounced than for the MoP sample.

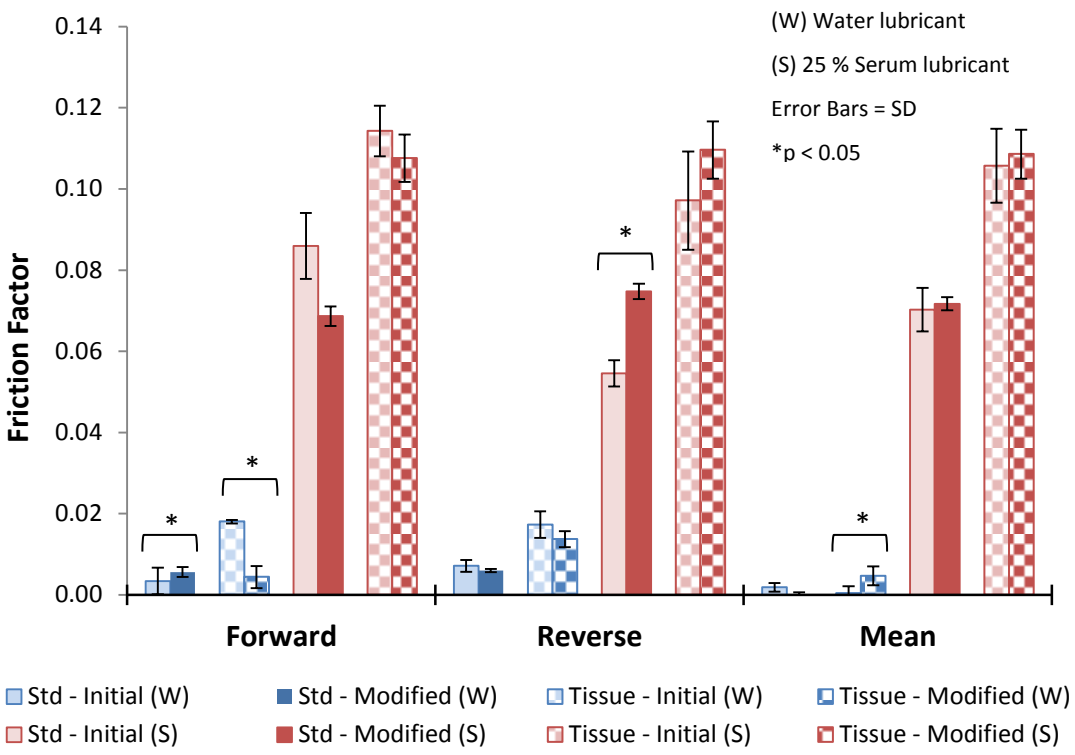

Figure 4.30: Friction factor results ± SD (n = 3) for the 36 CoC sample standard (Std) and tissue profile tests conducted on friction simulator Mk B, before (initial) and after the fitting of new capillary tubing (modified). Reverse data has been converted to positive values.

As observed with the 28 mm MoP control sample, further studies conducted on simulator Mk B using a serum lubricant showed improved forward and reverse friction factor results (i.e. of a more equal magnitude) for both standard and tissue profile tests (Figure 4.30). The most significant improvement was observed for the standard serum lubricant test, where the initial forward and reverse friction factors were 0.086 ± 0.008 and -0.055 ± 0.003 respectively and the modified simulator results were 0.069 ± 0.002 ($p = 0.003$) and -0.075 ± 0.002 ($p = 0.02$).

4.10.2.2 Further Comparison of Simulators A and Mk B

No significant differences ($p > 0.05$) in mean friction factor were identified for any of the dynamic profile tests conducted on the 28 mm MoP sample. There was some variation between the forward and reverse measurements recorded by the two simulators (Figure 4.31); however, the majority of these differences were not significant.

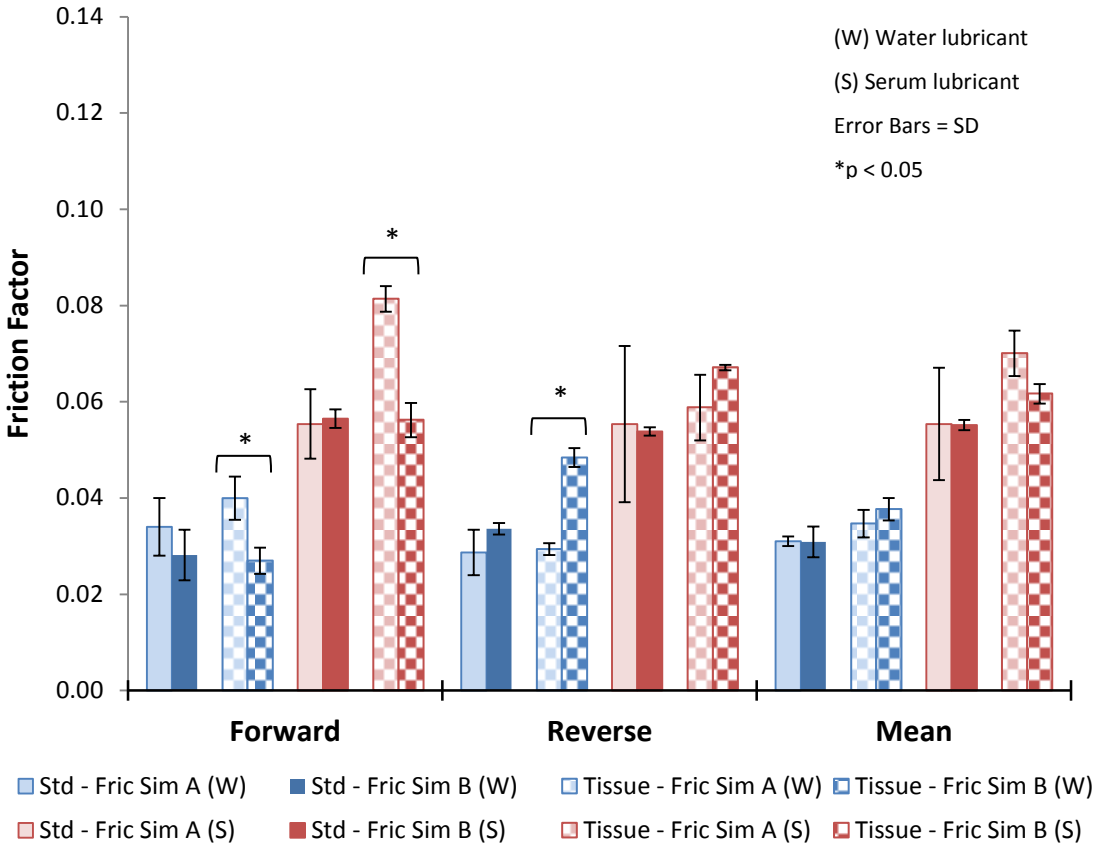

Figure 4.31: Friction factor results ± SD (n = 3) for the 28 MoP control sample standard (Std) and tissue profile tests conducted on friction simulators A and Mk B after new capillary tubing had been fitted to simulator Mk B. Reverse data has been converted to positive values.

An exception to this was the tissue profile test using a water lubricant (Figure 4.31), where for simulators A and Mk B the forward friction factors were 0.040 ± 0.004 (A) and 0.027 ± 0.003 (Mk B), which has a significance level of $p = 0.01$, and the reverse friction factors were -0.029 ± 0.001 (A) and -0.048 ± 0.002 (B), where $p = 0.00$. The only other significant difference detected for the 28 mm MoP sample was for the forward tissue test with 25 % serum lubricant ($p = 0.01$). However, it was noted that for this test the magnitude of the forward and reverse friction factors determined using simulator A were significantly different ($p = 0.00$), which could have given rise to this result.

Similarly, the friction factor values for the 36 mm CoC sample measured on the modified simulator Mk B were also much more in line with those measured using simulator A (Figure 4.32), with no significant differences in mean friction factor being observed for any of the dynamic tests ($p > 0.05$).

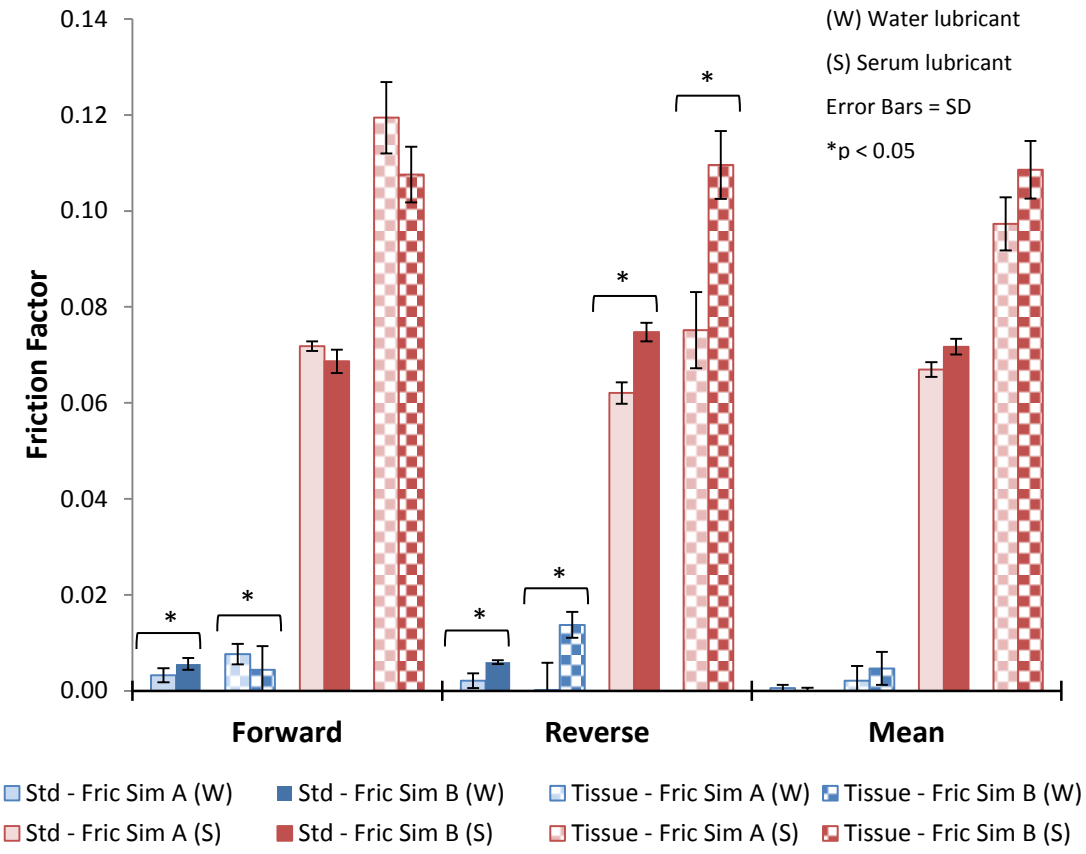

Figure 4.32: Friction factor results ± SD (n = 3) for the 36 CoC control sample standard (Std) and tissue profile tests conducted on friction simulators A and Mk B after new capillary tubing had been fitted to simulator Mk B. Reverse data has been converted to positive values.

A significant difference in the reverse friction factor values was detected when comparing simulator A (-0.075 ± 0.008) with simulator Mk B (-0.110 ± 0.007) for the CoC sample tissue profile test and 25 % serum ($p = 0.00$). A possible explanation for this result is the significant difference ($p = 0.00$) between the reverse and forward (0.119 ± 0.007) friction magnitudes on simulator A (Figure 4.32). Significant differences were also seen when using a water lubricant with the CoC sample, however, as the friction is known to be very low when lubricating CoC bearings with water, these results are not considered as important. This will be explained in more detail in the discussion (Section4.11).

Interestingly, a large number of the test results recorded on friction simulator Mk B appeared to be more consistent and with less variation between repeats compared to those from friction simulator A. This was observed for both bearing couples but was slightly more evident for the 28 mm MoP sample (error bars on Figures 4.31 and 4.32).

4.10.3 Repeatability

Repeated testing of the 28 mm MoP sample with 25 % (v/v) NBCS using the standard test profile was conducted to test the repeatability of the simulator measurement system. Repeats were conducted on the same day, and on different days, both before and after the simulator was modified by fitting new capillary tubing, so that any within day or day-to-day variations in mean friction factor measured by the simulator could be identified.

The results in Table 4.7, presented with 95 % confidence intervals (CI), demonstrate the repeatability of the mean friction factor measurements before (95 % CI = 0.002) and after the simulator was modified (95 % CI = 0.001), providing strong evidence to support the test-retest reliability of pendulum friction simulator Mk B.

Table 4.7: Repeatability of friction measurements on pendulum friction simulator Mk B conducted during the initial (n = 29) and further (n = 24) validation studies. Tests conducted using the 28 MoP control sample, standard profile, and 25 % serum lubricant. Results given as mean friction factor ± SD and with 95 % CI.

28 mm MoP Standard Test	Number of Repeats (n)	Mean Friction Factor ± SD	95 % Confidence Interval
Initial validation	29	0.058 ± 0.005	0.002
Further validation	24	0.053 ± 0.003	0.001

4.11 Discussion

A new pendulum friction simulator (Mk B), designed specifically for testing natural (biological) tissue in addition to artificial bearings, underwent a validation process that has been summarised in Figure 4.1. The validation process was designed to ensure that the simulator met the specified requirements and produced consistent friction factor results that were comparable to an existing validated pendulum friction simulator (A) of similar design, and were consistent with existing friction factor data in the literature. This chapter covers the work done to validate the simulator using THRs, and validation using hemiarthroplasties is covered in Chapter 5. To summarise, pendulum friction simulator Mk B was received from the manufacturer and a number of small modifications were made during the early commissioning period (Section 4.5). Initial validation tests followed (Section 4.6) using MoP and CoC hip replacement bearings

with different lubricants and different kinetic inputs, which included a low load and motion profile for testing biological tissue (tissue profile). Large discrepancies were observed during the initial tests, particularly when running the simulator with forward and reverse motions, and on further investigation this was found to be due to the hydrostatic bearing not functioning effectively (Section 4.8). A major modification was made to the simulator by replacing all the capillary tubing that feeds pressurised oil to the bearings, and following this the validation study was repeated (Section 4.9).

A predetermined series of tests was carried out using a set of three artificial hip bearing couples, three different lubricants and a range of dynamic and constant load kinetic input profiles. Prostheses of different sizes and materials (e.g. 28 mm Ø MoP, 28 mm Ø CoC and 36 mm Ø CoC) and different lubricants were included in the plan to provide a more heterogeneous sample and increase the external validity of the results. The main objective was to assess the function of friction simulator Mk B by comparing the friction factor results to those from an existing validated simulator (A) of similar design. Friction factor, which was calculated from the measured frictional torque, was used so that the effects of using different kinetic input profiles, different lubricants, and different bearing couples could be compared.

In general, the analysis of the results from the initial tests highlighted a tendency for greater mean friction factor values to be measured when using simulator Mk B compared to simulator A, although this difference was not always statistically significant (Section 4.7). Caution must be applied, however, with reference to the statistical analysis of the data in this study, as there is a risk of error due to the small sample size. Although a large number of different tests were conducted on the three artificial bearings (n = 252), the sample size for each test was quite small (n = 3). This was based on practical considerations such as time and resources, for example the availability of shared equipment, namely pendulum friction simulator A.

It is possible that extraneous factors, such as an undetected problem with friction simulator A, could confound the results thus introducing a source of error into the validation process. To reduce this risk and increase the validity of the process, it was important to incorporate some tests into the validation plan that were based on studies published in peer-reviewed journals.

The effect of using 25 N, 100 N and 300 N SPLs on the friction factor of MoP and CoC bearings has been previously studied by Brockett *et al.* (2007), who reported a slight increase in friction factor with increased SPL. This relationship was observed for tests conducted on both CoC bearings on simulator A, and for the 36 mm CoC bearing couple on simulator Mk B during the initial validation studies. The 28 mm CoC bearing only showed an increase in friction factor from 25 SL to the 100 SPL and not from 100 N to 300 N; however, these tests were conducted prior to simulator Mk B being modified (Section 4.7.1).

The same study by Brockett *et al.* (2007) investigated the effects of using different lubricants (water, 25 % serum and 100 % serum) on the friction of different total hip bearings. Tested with a 100 N SPL, a large increase in friction was reported for 28 mm MoP and CoC bearings when substituting water with 25 % serum, with a smaller increase being reported when substituting the 25 % serum for 100 % serum. The exact friction factor values were not given in the results, however, for the MoP bearings the column chart shows the mean friction for the three lubricants to be similar in value to the results reported in this chapter from simulator Mk B during the initial validation studies. The CoC results observed during the initial validation process for simulator Mk B are lower than those reported on the column chart presented by Brockett *et al.* (2007), but are in agreement with the results observed when using simulator A. Despite the results from simulator Mk B during the initial validation studies not being of the same magnitude, the results did display the same trends, i.e. a large increase between water and 25 % serum and a lesser increase with 100 % serum (Appendix D).

Studies by Scholes and Unsworth (2006) and Williams *et al.* (2006) measured the mean friction factor in artificial hip bearings using a 100 N SPL and 25-30 % serum lubricants. They reported values in the range of 0.03 to 0.06 and 0.062 respectively for MoP bearings, and 0.02 to 0.06 and 0.041 respectively for CoC bearings. The values reported in these studies for the MoP bearings support the findings of this thesis following the further validation studies (Section 4.10.2.2). The values reported for the CoC bearings are slightly higher than the 0.07 mean friction factors observed on simulators A and B during the further validation studies (Figure 4.32), however, this slight difference could be explained by the higher SPL (i.e. 300 N) being used for the further validation tests.

Very low friction factor values, less than 0.01, were observed when testing the CoC samples with a water lubricant during the initial and further validation studies (Section

4.7 and Section 4.10 respectively). Similarly, Scholes *et al.* (2000) reported very low friction factor values with CoC samples and the lowest reported friction factor measured using CoC samples and a thick silicon oil on simulator A is 0.005 (Brockett, 2007). The sensitivity of the friction simulator Mk B has not been measured specifically, however, as simulator Mk B will be used to test natural tissue that has a higher friction factor, the researcher can be confident that based on the CoC with water tests, the simulator can measure friction in the range required for future studies.

A more pivotal finding than the variances in mean friction factor was the large difference in magnitude observed between the forward and reverse results for a large number of the different tests conducted on simulator Mk B. This, together with the asymmetry of the constant load torque plots, was indicative of a possible large offset in the system. This could also have been caused by misalignment of the samples in the simulator as this would introduce additional friction into the system (Auger *et al.*, 1993), however, as the bearing couples were always set-up with the correct COR and the same samples were used in both simulators, this was an unlikely source of the error. Other possible explanations for the apparent large offset were manufacturing errors (e.g. incorrect tolerances) relating to the frictionless measuring carriage or hydrostatic bearing, however, these ideas were explored and subsequently dismissed by SimSol.

It was hypothesised that the anomalies in the results from simulator Mk B stemmed from the low oil pressure, which if too low to float the hydrostatic bearing, would lead to additional frictional torque being created by the simulator. It is feasible that the additional torque could be generated from grounding of the hydrostatic bearing if the pressure within the bearing system could not be maintained whilst under load (Cheng and Rowe, 1995). Having highlighted the problem to the simulator manufacturer (SimSol), the length of capillary tubing needed to maintain a pressure within the hydrostatic bearing pressure similar to that of simulator A was calculated. Modification of the simulator by fitting longer, and slightly wider, capillary tubing increased the oil pressure and appeared to alleviate the problem. The friction factor results of the further validation tests were then accepted as being consistent with those from simulator A and, where appropriate the literature. A summary of the mean friction factor results for the 28 mm MoP and 36 mm CoC THR samples tested during the further validation study (Section 4.9), is shown in Figures 4.33 and 4.34 respectively.

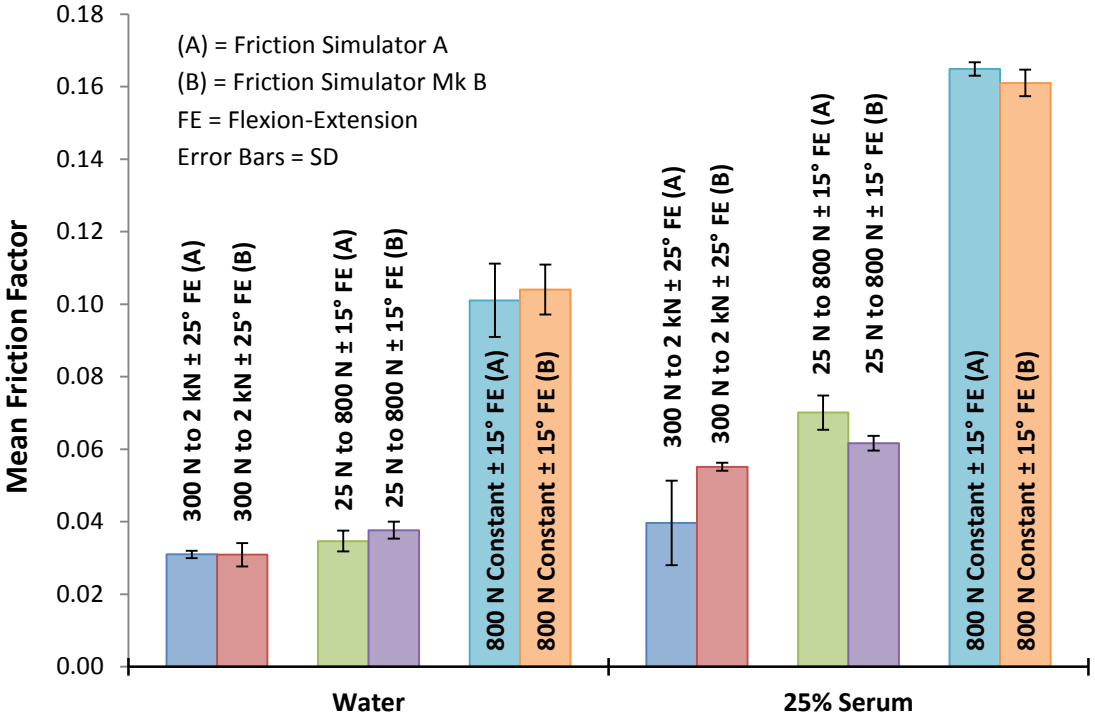

Figure 4.33: Mean friction factor results ± standard deviation (SD) (n = 3) for the 28 mm MoP sample from the further validation study carried out on friction simulators A (A) and MK B (B), following the fitting of new capillary tubing.

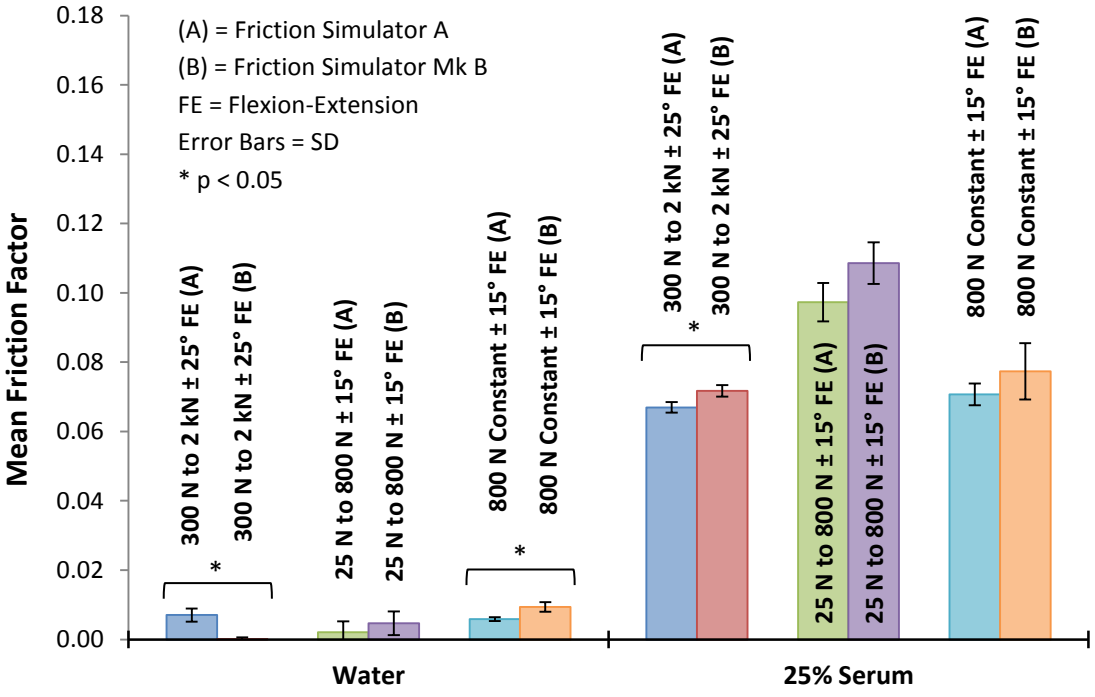

Figure 4.34: Mean friction factor results ± standard deviation (SD) (n = 3) for the 36 mm CoC sample from the further validation study carried out on friction simulators A (A) and MK B (B), following the fitting of new capillary tubing.

4.12 Conclusions

The aim of this study was to validate a new pendulum friction simulator (Mk B) using total hip replacements and an existing validated pendulum friction simulator (A). The basic function of pendulum friction simulator Mk B was checked following handover from the manufacturer to the university, and this was followed by a formal validation process, which was conducted in three parts:

A. Initial validation studies
B. Modification of the simulator by fitting new capillary tubing to the hydrostatic bearing
C. Further validation studies

The following observations were made during this study:

- It was hypothesised that the discrepancies in the results obtained using friction simulator Mk B, compared to those from friction simulator A, were originating from the hydrostatic bearing. This theory was supported when improved friction factor results and torque plot symmetry was observed following the fitting of longer and slightly narrower capillary tubing to simulator Mk B, which increased the oil pressure and oil flow to the hydrostatic bearing.
- Significant differences in friction factor were observed in the initial validation studies during forward and reverse dynamic profile tests on friction simulator Mk B, however, this discrepancy was rectified in the further validation studies following the fitting of new capillary tubing.
- Torque plots for the constant load tests conducted on pendulum friction simulator Mk B were positioned more symmetrically above and below zero when re-tested during the further validation studies.
- The mean friction factor results from the further validation studies conducted on simulators A and Mk B were of a similar magnitude.
- Friction factor results of a greater magnitude were recorded on simulators A and B when testing total hip replacements in lubricants with a greater protein content, and when increasing the swing phase load. These results are consistent with those reported in the literature.

- The further validation study results for friction simulator Mk B were comparable with the results from simulator A and, where appropriate, consistent with friction factor results for total hip replacements reported in the literature.

Having obtained acceptable results from this study using total hip replacements, the validation of pendulum friction simulator Mk B was progressed onto validation using hemiarthroplasty samples (Chapter 5), prior to developing a methodology for investigating the tribology of complete natural porcine hip joints using the new pendulum friction simulator (Chapter 6).

Chapter 5 Validation of New Pendulum Friction Simulator using Hemiarthroplasties

5.1 Introduction

Pendulum friction simulator Mk B was used to study the tribology of complete natural hip joints following the validation process; therefore, it was deemed important to include an assessment of the function of the simulator with natural tissue samples *in situ* in the validation plan.

This chapter provides details of the *in vitro* hemiarthroplasty studies, conducted using cobalt chrome (CoCr) alloy heads and porcine acetabula, as detailed in the previous chapter (Figure 4.1). An overview of the validation process conducted in this chapter using hemiarthroplasties in shown in Figure 5.1. A new test pot for conducting *in vitro* studies using porcine acetabula in the pendulum friction simulators (A and Mk B) was designed (Section 5.2.7), as was a new method for potting the samples (Section 5.3) before starting the validation process. Pendulum friction simulator Mk B underwent a small modification by having the counterbalance reduced, which was completed before any hemiarthroplasties could be tested (Section 5.5.4). This was followed by conducting the initial validation study using hemiarthroplasties. It should be noted that the initial hemiarthroplasty study ran concurrently with the THR initial validation study, as shown in Figure 4.1. A major modification was made to pendulum friction simulator Mk B by fitting new capillary tubing to increase the pressure of the oil floating the hydrostatic bearing (Section 4.8), following which the THR validation study was completed. The further validation study using hemiarthroplasties was then conducted (Section 5.6).

The results from the further hemiarthroplasty validation studies reported in this chapter were used as control data for subsequent *in vitro* simulation studies using complete natural porcine hip joints conducted on friction simulator Mk B (Chapter 6). A comparison of the hemiarthroplasty and complete porcine hip joint results is presented in Chapter 7.

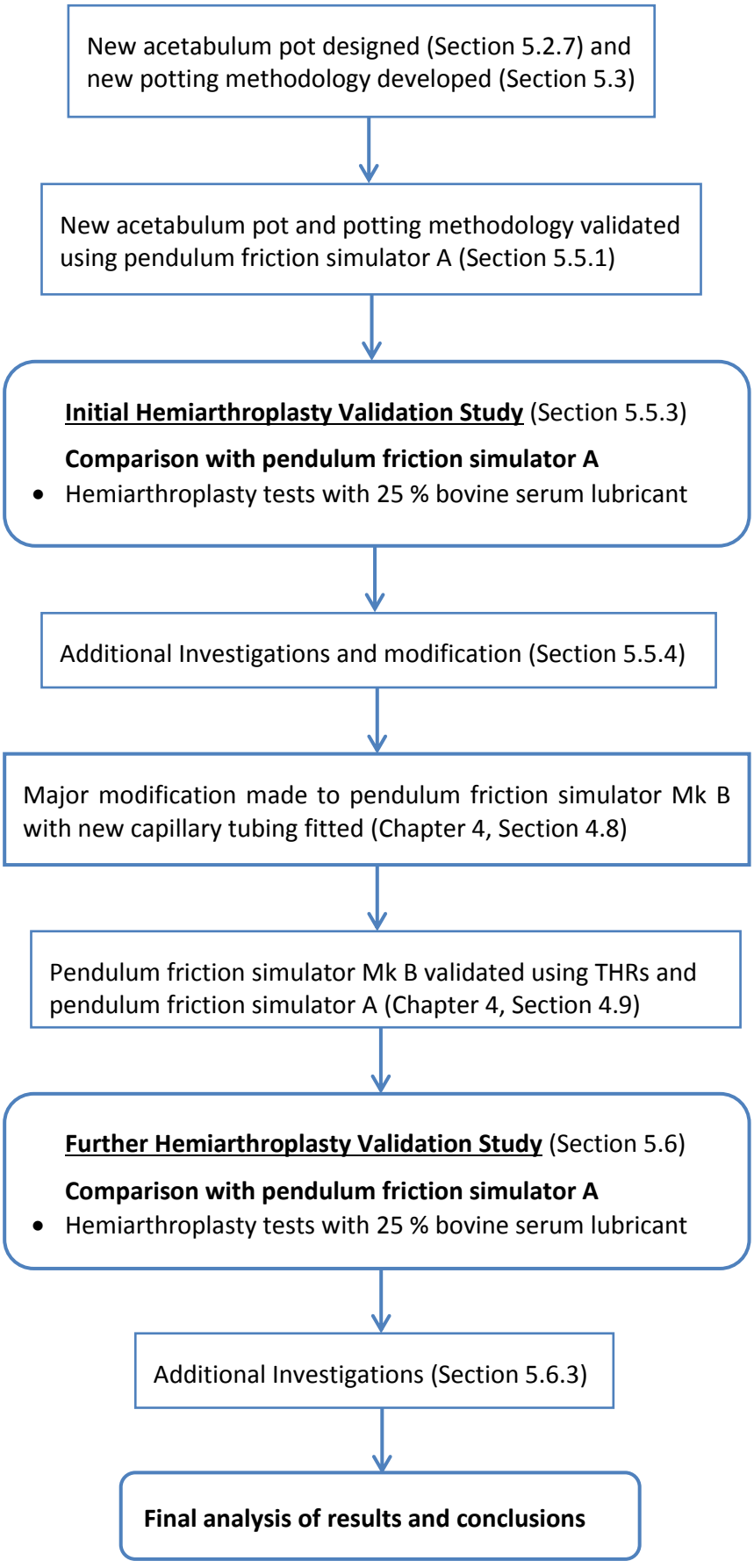

Figure 5.1: Flow chart of the validation process using hemiarthroplasties for pendulum friction simulator Mk B.

5.2 Materials

Materials used in this set of hemiarthroplasty friction studies are described in this section.

5.2.1 Newborn Calf Serum

The lubricant used to test the hemiarthroplasty samples for the validation studies was a 25 % (v/v) concentration of NBCS which, as stated previously, has a protein content similar to that of synovial fluid (Section 4.6.4). This facilitated physiological *in vitro* test conditions to be generated and maintained throughout this part of the validation process.

5.2.2 Phosphate Buffered Saline

Hydration of exposed articular cartilage was maintained using phosphate buffered saline (PBS), which is a non-toxic isotonic salt-based water solution (Table 5.1). The PBS used in this study was supplied in tablet form (MP Biomaterials LLC, Illkirch, France) and reconstituted by dissolving one tablet in 100 ml of sterile distilled water, as per the manufacturer's guidelines.

Table 5.1: Organic salt content of phosphate buffered saline, which is used to maintain hydration of articular cartilage (MP Biomedicals LLC, 2014).

Contents (Organic Salts)	Concentration (mg/litre)	Molecular Weight (Daltons)	Molarity (millimoles per litre)
Potassium chloride	200.00	74.55	2.68
Potassium phosphate monobasic	200.00	136.09	1.47
Sodium chloride	8000.00	58.44	136.89
Sodium phosphate dibasic (Na_2HPO_4)	1150.00	141.96	8.10

5.2.3 Cobalt Chrome Heads

Cobalt chrome alloy femoral heads (DePuy Synthes, Leeds, UK) were used to articulate against the lunate surface of the porcine acetabula during the *in vitro* hemiarthroplasty studies. Heads of different diameters (32, 34, 35, 36, and 37 mm) were available, which

enabled the harvested porcine acetabula to be matched and tested with a suitable sized CoCr femoral head. The methodology used to size-match the acetabula and CoCr femoral heads is described in Section 5.3.1.1.

Surface roughness measurements using the methodology described in Section 4.6.3.3, and a Gaussian filter with a cut-off 0.08 mm, were performed on each femoral head. The mean ± standard deviation average roughness (R_a) value for all of the CoCr femoral heads used in the hemiarthroplasty studies was 0.006 ± 0.001 µm.

5.2.4 Polymethyl Methacrylate (PMMA) Bone Cement

Non-sterile polymethyl methacrylate (PMMA) bone cement was used to secure the porcine acetabula in the correct position and orientation in a test pot, which was then attached to the friction measuring carriage for the *in vitro* simulation studies. PMMA cement, which is frequently used in orthopaedic procedures to aid the fixation of artificial prostheses, is formed by mixing a pre-polymerised cold cure powder with a liquid monomer (Rapid Repair Liquid).

The cold cure powder and liquid monomer, (obtained from WHW Plastics, Hull, UK), were mixed on a downdraft table with a powder to liquid component ratio of 2:1, according to the manufacturer's instructions. The polymerisation process results in a relatively high exothermic reaction (Haas *et al.*, 1975), and therefore a PBS soaked tissue was placed on the surface of the articular cartilage to reduce the risk of any cell death or damage that could have been caused by the increasing temperature of the cement as it hardened against the backside of the acetabulum.

5.2.5 Microset® High Resolution Replicating Compound

Microset® 101 silicon polymer compound (Microset Products Ltd., Leicestershire, UK) was used to create highly accurate three-dimensional (3D) replicas of the articular surfaces in order to assess cartilage volume loss and wear following *in vitro* testing. Microset® 101 is a two-part silicon polymer comprising of a base material and catalyst, which are dispensed using a manual dispensing gun and static mixing nozzle that is attached to the outlet of the cartridge. Once applied to the surface/area of interest to be replicated, the compound cures in five minutes at room temperature to produce a silicon replica with a resolution of 0.1 µm (Microset Products Ltd., 2014).

5.2.6 Porcine Acetabula

The acetabula were harvested from skeletally immature porcine right hind legs that were 24 to 26 weeks old at the time of slaughter, a source that was constantly and reliably available. The average weight of the donor pig was approximately 80 kg, and the tissue was dissected in the bioengineering laboratory 24–48 hours following its slaughter at a local abattoir (Figure 5.2).

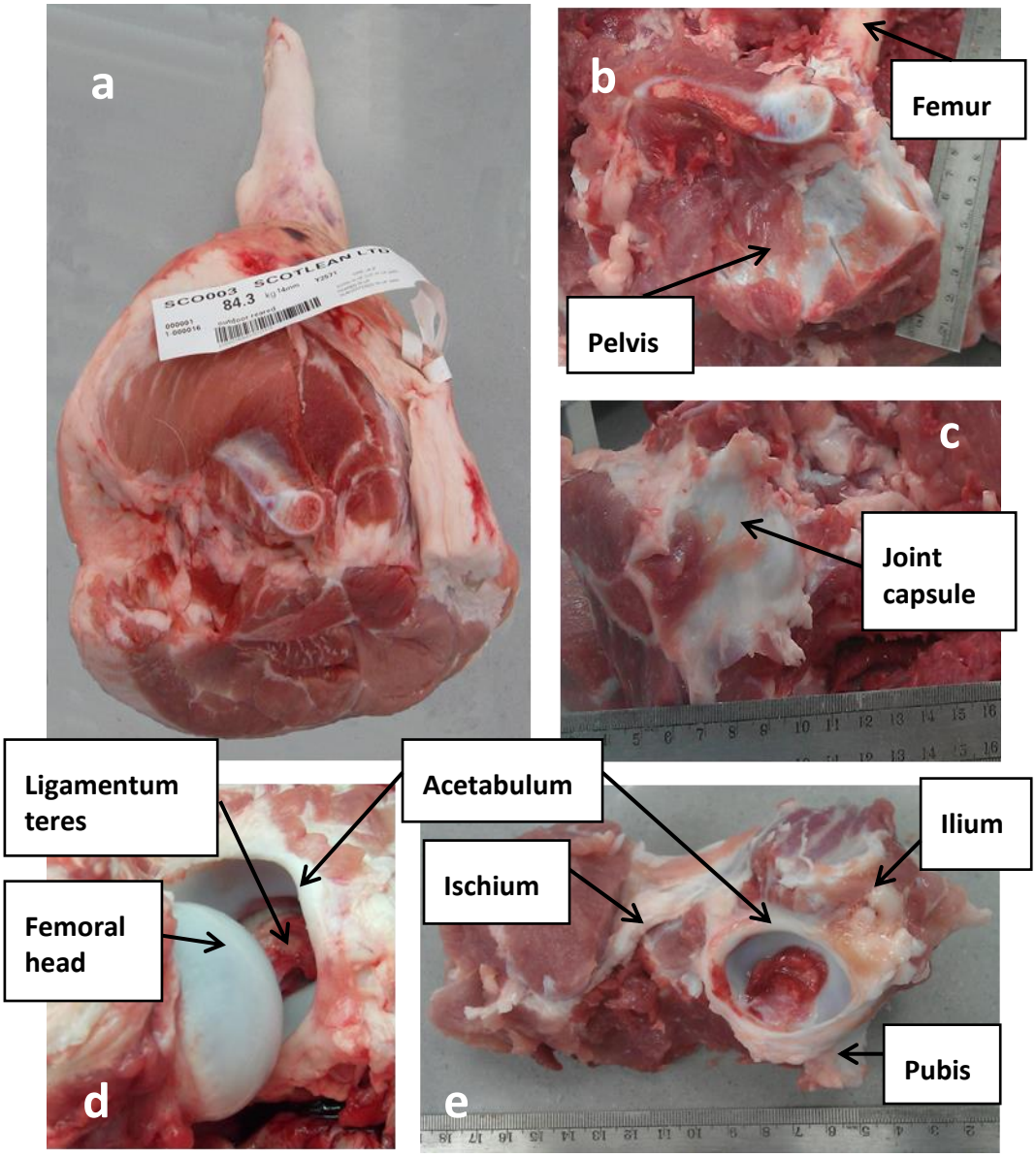

Figure 5.2: Harvesting of porcine acetabulum: (a) entire right rear porcine leg; (b) soft tissues excised from around hip joint exposing femur and deep muscles; (c) exposure of joint capsule around the hip joint; (d) separation of the femoral head and acetabulum by cutting the ligamentum teres; (e) the harvested acetabulum and pelvic bone.

The porcine leg was dissected using a non-sterile scalpel blade and handle. The weight of the pig, which is on a label attached to the porcine leg (Figure 5.2 a), was recorded (note this is the weight of the whole animal) and used as part of the identification number given to each specimen.

The bulk of the superficial soft tissue (e.g. muscle, tendon) was excised from around the hip joint to expose the proximal aspect of the femur and pelvic bones (Figure 5.2 b).

Deep muscle was then carefully removed from around the hip joint and pelvis to expose the synovial joint capsule (Figure 5.2 c). The joint capsule was left intact at this stage to protect the articular surfaces of the hip joint from damage and maintain hydration using the synovial fluid contained in the capsule. Removal of the capsular ligaments (e.g. iliofemoral, ischiofemoral, and pubofemoral) from around the hip enabled the joint to be distracted prior to the separation of the head from the acetabulum.

Once distracted, the joint capsule was opened and the joint separated by cutting the ligamentum teres, which attaches the acetabulum to the fovea capitis on the femoral head (Figure 5.2 d). Any remaining tissue, for example joint capsule, that prevented complete separation of the acetabulum from the femur was removed. At this stage, extra care was taken not to damage the acetabula labrum or articulating surfaces of the head and acetabulum (lunate surface). All exposed cartilage surfaces were covered with PBS-soaked tissue for protection and hydration.

Once the pelvis had been separated from the rest of the leg (Figure 5.2 e), any residual soft tissue around the acetabulum was excised. Excess pelvic bone (ischium, ilium and pubis) was then removed from around the acetabulum using a hacksaw so that the harvested specimen would fit into the acetabulum test pot.

The main structures of interest (e.g. lunate surface, acetabular labrum, transverse acetabular ligament [TAL], intra-articular fat pad, and acetabular portion of the ligamentum teres) were then identified on the harvested acetabulum and checked to ensure they were intact. For reference purposes, the lunate surface was divided into three regions namely caudal, central and cranial (Figure 5.3). Acetabula either accidentally damaged during the harvesting procedure, or with any obvious defects or pathology (e.g. haematoma within the acetabula fossa occasionally arising from the slaughter process), were discarded.

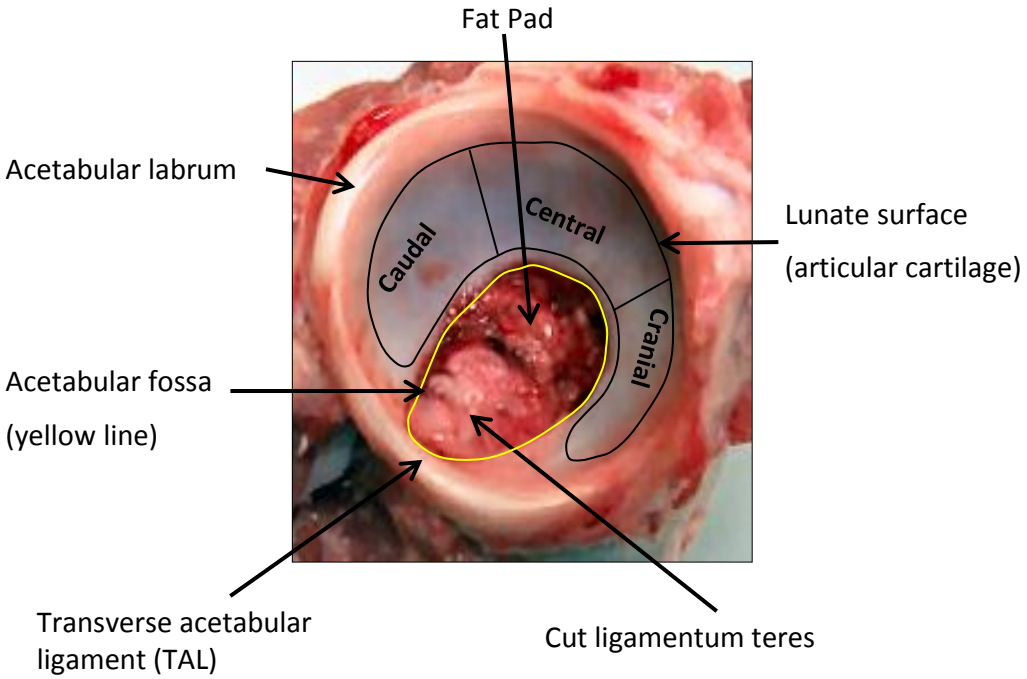

Figure 5.3: Right porcine acetabulum illustrating the main structures of interest and nomenclature of lunate surface.

Previous studies have reported that freezing does not affect the friction coefficient of articular cartilage (Forster and Fisher, 1996) and therefore following harvesting, tissue specimens not tested the same day were frozen at -20°C (which can be for up to four weeks) with a PBS-soaked tissue covering the articular surface, again to ensure that it remained hydrated. The storage bag (resealable plastic freezer bag) was marked with the date of harvesting and the identification number of the specimen. The day before testing, frozen specimens were taken out of the freezer and put into the fridge to ensure that they were fully defrosted.

5.2.7 Development of an Acetabulum Test Pot

A Delrin® acetabulum pot that had been designed for hemiarthroplasty studies previously conducted on pendulum friction simulator A (Lizhang, 2010; Lizhang *et al.*, 2013), was deemed to be unsuitable for *in vitro* simulation studies using complete porcine hip joints. Porcine femurs have very short necks and a large greater trochanter (Figure 5.4 a), meaning that during *in vitro* simulation studies in the pendulum friction simulator, there was a very high risk that the inverted natural femur would impinge against the deep sides of the existing acetabulum pot (Figure 5.4 b). The femur was

also wider than the metal spigot that metal femoral heads are mounted on for testing (Figure 4.11), which would have increased the risk of impingement in the simulator.

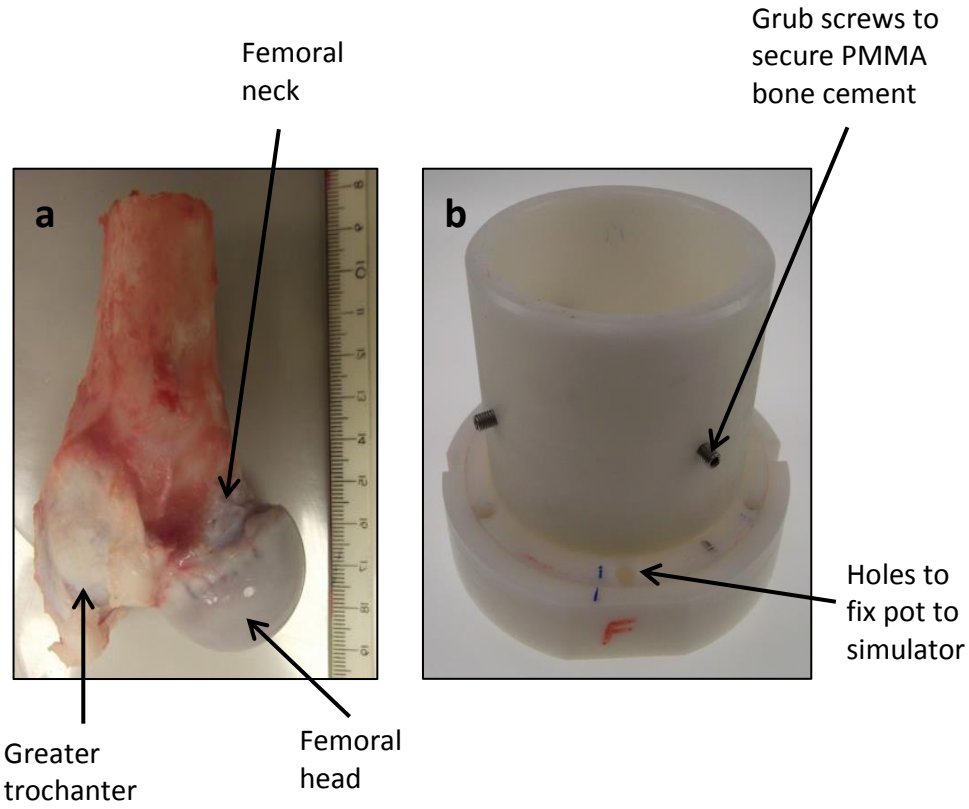

Figure 5.4: (a) A proximal porcine femur and (b) deep acetabulum pot used for previous hemiarthroplasty studies conducted in pendulum friction simulator A.

As the results from the hemiarthroplasty validation study were to be used as control data for the complete natural joint studies, it was deemed important to use the same fixturing for the acetabulum for all *in vitro* tissue testing in order to control this variable. Considering this, a new acetabulum pot was designed prior to starting the validation study using SolidWorks 3D computer aided drawing (CAD) software (2009 version, Dassault Systèmes, Waltham, US). The new design took into consideration the intended use of the pot for both hemiarthroplasty studies and complete natural hip joint studies. Design requirements for the pot are shown in Table 5.2 and a 3D SolidWorks illustration of the pot is shown in Figure 5.5. The engineering drawing used to manufacture the test pot is in Appendix G.

Table 5.2: Design requirements and solutions for the new acetabulum test pot.

Feature	Requirement/Specification	Design Solution(s)
Dimensions	Pot must be large enough to accommodate different sizes of acetabula, with attached pelvic bone, and PMMA cement for fixation	Manufactured with an internal diameter of 80 mm, based on the largest specimen of a sample group being 50 mm wide (n = 10)
	Must be able to cement the acetabulum in the pot with the correct COR (i.e. 63.24 mm)	Designed with the centre of the pot corresponding to the COR of the simulator
	Must be able to secure pot into the friction measuring carriage of the pendulum friction simulator	Same dimensions used for the base and as existing fixtures, and screw holes of same size and location as existing fixtures used (details in Appendix G)
Operation	Able to pot acetabulum in correct orientation with ease before PMMA cures Low risk of impingement between the pot and porcine femur during FE motion	Designed with shallow sides for easy access to specimen during potting and to reduce the risk of any impingement
	No movement of the cement mantle and/or the specimen during testing	Shallow recesses drilled on internal surface of the pot to provide fixation points for the PMMA cement. This would theoretically prevent any movement of the sample during testing with the application of an axial load
	Easy removal of the specimen without causing damage	Tapped hole with grub screw that can be used to dislodge the PMMA from the pot
Material	Durable enough to withstand repeated use and fixturing in the simulator Able to clean thoroughly with disinfectant after use to remove residual natural tissue and PMMA cement, with no degradation of the material	Manufactured from stainless steel 303, which is a chromium-nickel alloy that can be machined easily (British Stainless Steel Association, 2014)

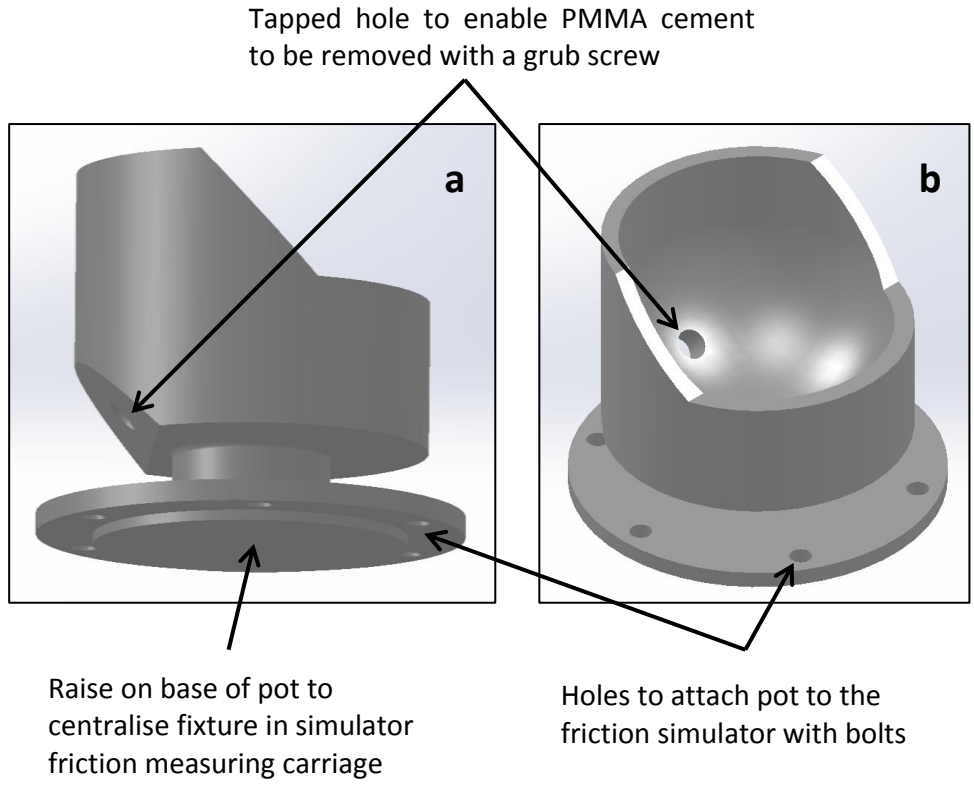

Figure 5.5: Front (a) and oblique (b) views of the new stainless steel acetabulum test pot, designed using SolidWorks 3D software.

Post manufacture, shallow holes (recesses) were drilled on the internal surface of the pot and, during initial hemiarthroplasty tests using the methods described in Section 5.3, no rotation of the cement was observed. However, some linear movement of the cement mantle was observed during FE motion under dynamic axial loading. The most likely explanation is that this was caused by the small amount of volume shrinkage that occurs as the cement cures (Haas *et al.*, 1975). In order to eliminate all movement, the acetabulum pot was slightly modified by drilling three small equally spaced holes around the sides of the pot, so that grub screws could be screwed into the PMMA cement before it was fully cured. This method of holding the specimen in place had been used previously by Lizhang (2010) in the Delrin® pot (Figure 5.4 b), and was found to be a satisfactory method of securing the PMMA cement and specimen in the new stainless steel pot. This method of securing the specimen had not been included in the original new pot design due to the potential for serum to leak from the holes and contaminate the oil in the hydrostatic bearing of the friction simulator.

5.3 Methods

This part of the validation process was adapted from the methodology developed by Lizhang (2010), who investigated the tribology of porcine hip hemiarthroplasty using natural acetabula and metal femoral heads on pendulum friction simulator A. Friction simulator A was again used as the comparator for the results obtained from pendulum friction simulator Mk B in this chapter.

5.3.1 Sample Preparation

5.3.1.1 Femoral Head

Hemiarthroplasty studies conducted by Lizhang (2010) and Lizhang *et al.* (2013) measured the diameter of the acetabulum in the flexion-extension direction (Figure 5.6) using vernier callipers, and a CoCr femoral head was selected that would give a radial clearance of 0.6 mm to 1.2 mm. In clinical practice however, the size of the head is measured and not the acetabulum. This is done using either vernier callipers or circular gauges, and with the latter method being deemed the most accurate (Jeffery and Ong, 2000; Athapattu *et al.*, 2013), this method was used for the hemiarthroplasty validation studies conducted in this thesis.

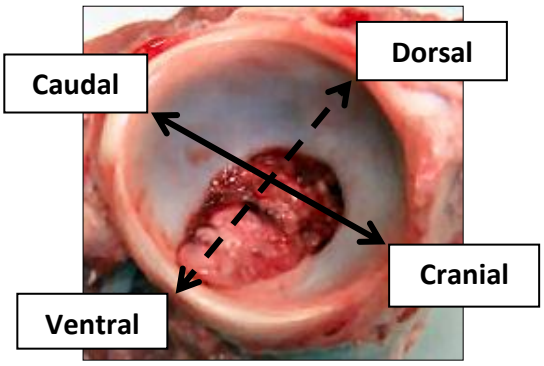

Figure 5.6: Cranial-caudal (i.e. flexion-extension) and dorsal-ventral dimensions of a right porcine acetabulum.

Circular gauges covering a range of femoral head sizes from 32.5 mm to 39.0 mm, in 0.5 mm increments, were designed and manufactured from 10 mm thick sheets of white PVC sheet (Figure 5.7). This range of sizes was based on the observations of the candidate and previous hemiarthroplasty studies (Lizhang, 2010; Taylor, 2012). All edges were smoothed and fillets with radii of 1.5 mm were created around the internal

diameters of the holes to reduce the risk of damage to the articulating surface of the femoral head during measurement. This was important as the same templates were also used for the complete natural hip joint *in vitro* simulation studies in Chapter 6. This was also the reason for creating a range of head gauge sizes that extended beyond the range of CoCr heads available for the hemiarthroplasty validation studies.

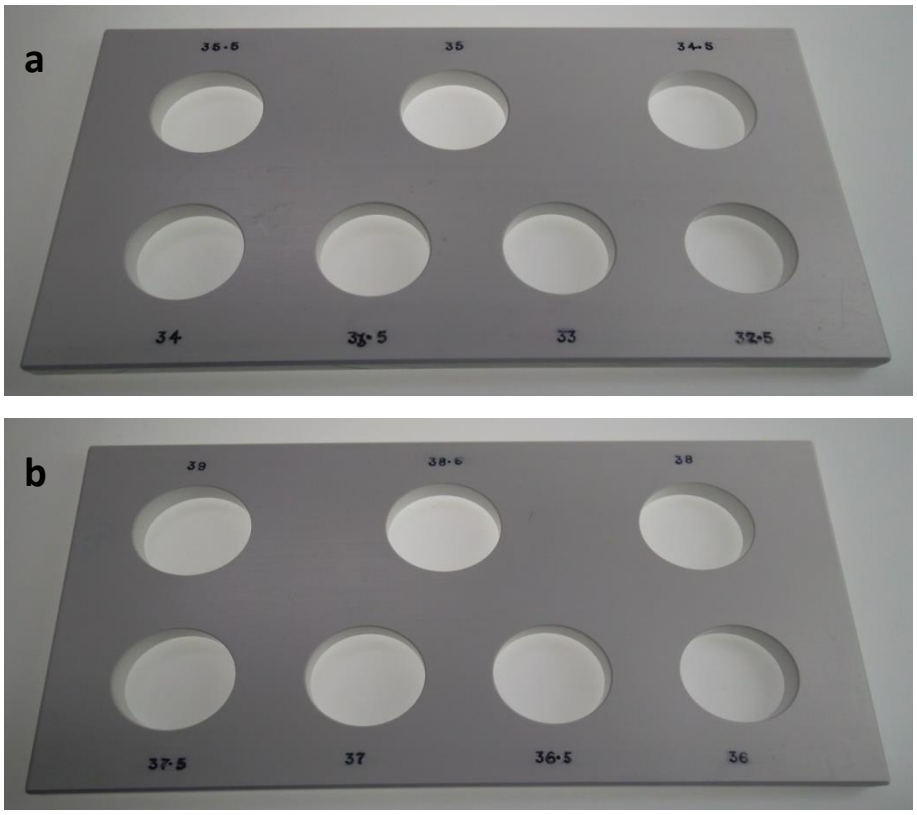

Figure 5.7: Circular gauges used to measure natural porcine femoral head size. Sizes (a) 32.5 mm to 35.5 mm and (b) 36.0 mm to 39.0 mm.

Circular templates used by Taylor (2012) to measure the femoral head size for hemiarthroplasty studies were available to use but were deemed unsuitable due to them only available in 32, 34, 35, 36 and 37 mm sizes. This range of sizes was not sufficient for use with the complete porcine hip joint studies that followed.

The porcine femoral head was gently pushed through the gauges (starting with a large size) and a CoCr femoral head of a size nearest the smallest diameter gauge that the head comfortably fitted through, which also corresponded to the FE direction of motion, was selected for use. Size selection was based on there being no interference of the femoral head from the gauge. Specimens were discarded if they could not be matched with one of the available CoCr head sizes (Section 5.2.3).

The metal femoral head was placed onto the same fixture that had been used for the THR samples (Figure 4.11) and the COR of the head and fixturing was set up using the method described in Section 4.6.3.2.

5.3.1.2 Porcine Acetabulum

Ten harvested porcine acetabula (n = 5 for each simulator) were cemented into the new stainless steel acetabulum pot in an anatomically inverted position, using PMMA bone cement with a powder to liquid ratio of 80 g to 40 g respectively. A generic rig, used for a number of different potting applications, was adapted for use by designing and manufacturing a Delrin® base plate that ensured the distance between the centre of the acetabulum and the base of the acetabulum pot was equal to the COR of the friction simulator (i.e. 68.24 mm). The rig set-up for potting a porcine acetabulum is shown in Figure 5.8.

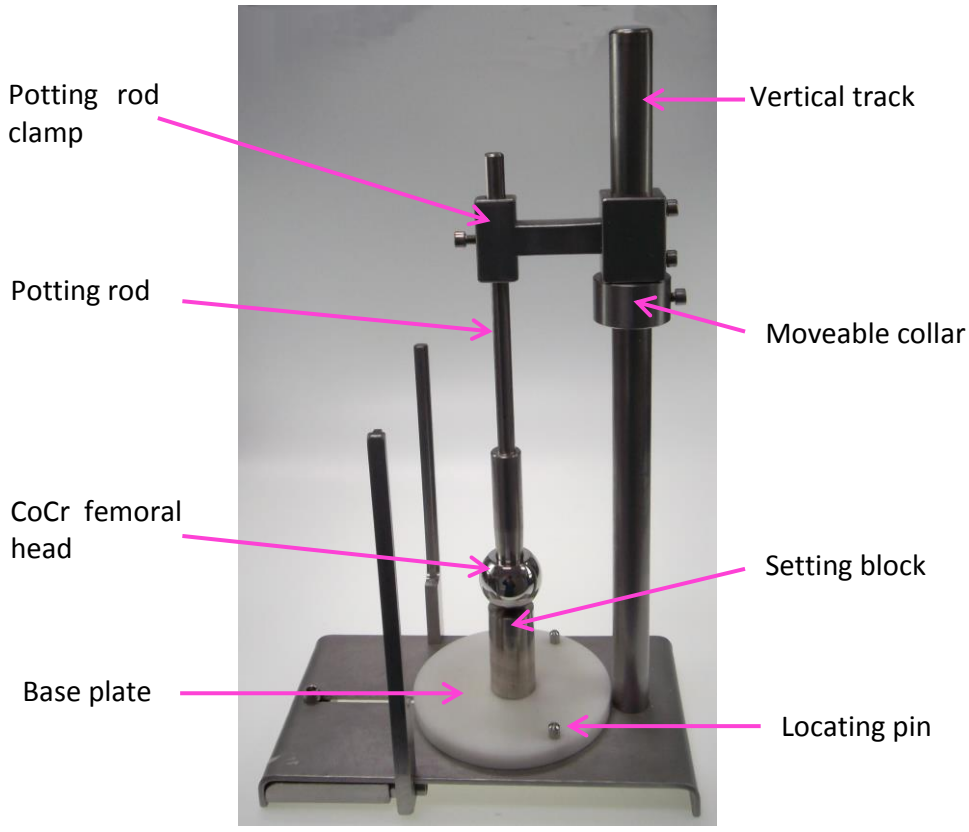

Figure 5.8: Lateral view of acetabulum potting jig with CoCr femoral head, potting rod, setting block and base plate *in situ*.

The CoCr femoral head was placed onto the potting rod and clamped to the vertical track of the rig. The correct COR height was established by lowering the femoral head down onto a setting block, corresponding to the radius of the femoral head, which was placed onto the base plate of the rig. The rod was locked in place using a moveable collar that was fixed to the vertical track underneath the potting head clamp using a grub screw. The base plate was specially designed for use with the new pot and the rig so that it would give the correct COR when combined with the setting blocks. The sum of the height of the setting block, the width of the base plate and the radius of the CoCr head was 68.24 mm.

Once clamped in place, the setting block was removed and replaced with the acetabulum pot, which was placed onto two locating pins on the upper surface of the base plate (Figure 5.9). The locating pins had been included in the design to ensure that the centre of the pot corresponded with the centre of the CoCr femoral head during the potting process in order minimise the offset of the specimen.

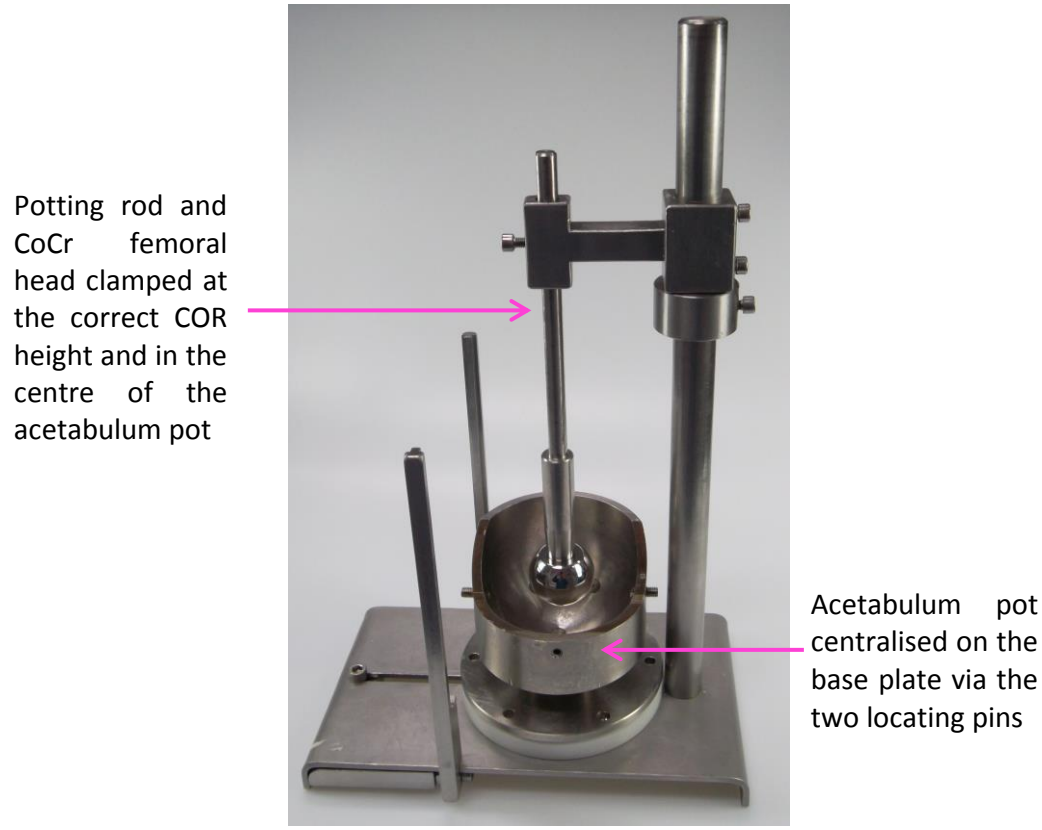

Figure 5.9: Lateral view of acetabulum potting jig with CoCr femoral head set to the correct height and the acetabulum pot centralised on the base plate.

The PMMA bone cement was placed into the bottom of the pot and whilst in a workable state before being fully cured, the porcine acetabulum was pushed into the centre of the cement with the TAL uppermost and the central area of the lunate surface at the bottom (Figure 5.10 b). The femoral head located on the potting rod was moved down the vertical track to push the acetabulum further into the cement until the potting rod clamp touched the top of the moveable collar, thus ensuring that the centre height of the acetabulum was correct.

In addition to maintaining the correct centre height, the acetabulum was also orientated with neutral version (i.e. orientation in then transverse plane) and an inclination angle (i.e. orientation in the coronal plane) of 45° for each test. In order to maintain consistency when positioning the specimens, a small attachment was designed to fit onto an inclinometer (Figure 5.10 a), and this was used to pot the specimens with the same orientation (accurate to approximately ± 5°) for each test.

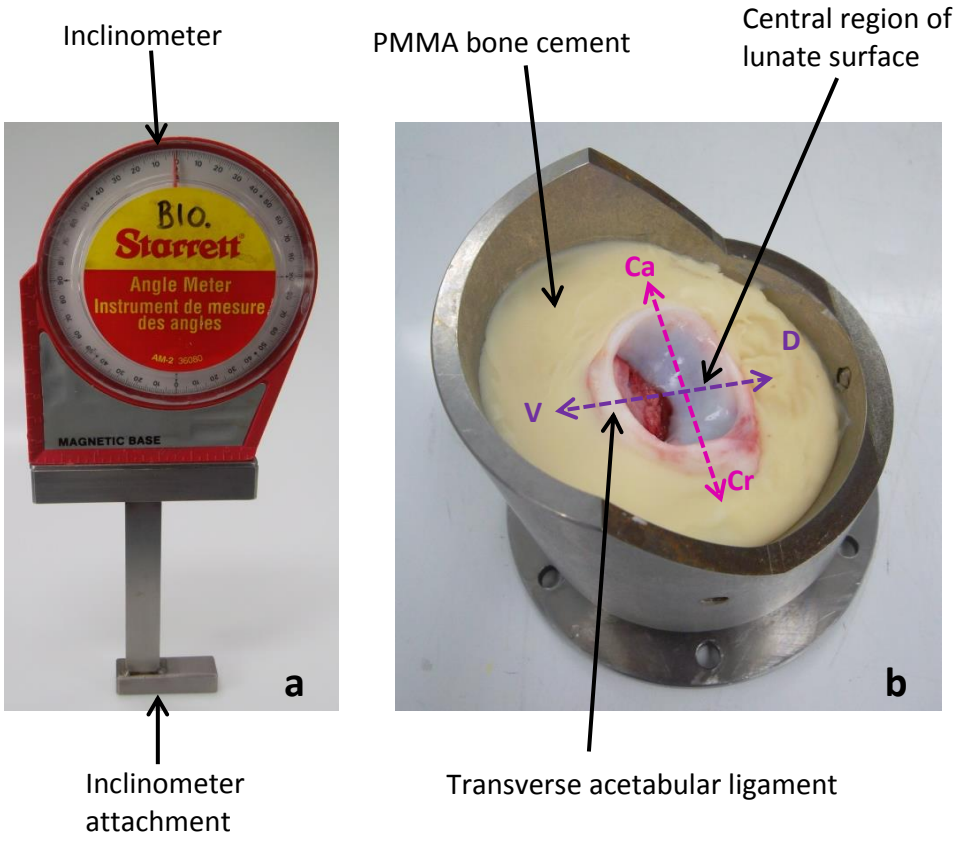

Figure 5.10: (a) Inclinometer with attachment used to orientate the porcine acetabulum and (b) a potted porcine acetabulum showing position of the specimen in the acetabulum pot. The dorsal (D) – ventral (V) and cranial (Cr) – caudal (Ca) directions correspond to the inclination and version angles respectively.

Inclination was measured by placing the bottom surface of the inclinometer attachment across face of the acetabulum in the dorsal-ventral direction, and acetabula version was measured across the cranial-caudal face of the acetabulum (Figure 5.10 b). This orientation ensured that contact between the femoral head and central region of the articular cartilage on the acetabulum was maintained.

Once the PMMA cement had cured and cooled, the acetabulum pot was secured into the friction measuring carriage of the simulator and the porcine acetabulum was filled with enough 25 % serum lubricant (~50–70 ml) to completely cover the articular cartilage, thus keeping it hydrated throughout the test. A small wall of PMMA cement was subsequently placed at the front of the pot to prevent any spillage of the serum from the pot during testing.

This method of positioning the acetabulum differs from how previous researchers (Lizhang, 2010; Taylor, 2012) orientated the specimen, as they used a line drawn at 45° on the CoCr potting head as a visual cue to estimate the degree of inclination. This technique did not control version and the repeatability of the method was considered poor due to the irregular shape of the acetabulum. The new method was developed so that the effects of varying the angle of inclination and/or acetabula version could be controlled, and therefore investigated in future studies (Chapter 6).

A small study was conducted to validate the new method of orientating the acetabulum in the new stainless steel pot against the previously established potting method. This involved running standard tissue profile tests on pendulum friction simulator A with porcine acetabula cemented in the old Delrin® pot (Figure 5.4 b) using the 45° line method (n = 3), and in the new acetabulum pot using the inclinometer method (n = 3) described earlier. Friction simulator A was used for this study as pendulum friction simulator Mk B had not been validated using natural tissue at this stage.

5.3.2 Input Kinetics

Hemiarthroplasty samples (n = 5 samples for each simulator) were tested with a dynamic cyclic load of 25 N to 800 N ± 15° FE motion, at a frequency of 1 Hz for 2 hours (i.e. 7,200 cycles). This loading and motion profile was referred to as the tissue profile and is shown in Figure 4.14. The tissue dynamic loading profile was comparable with loads experienced through the hip joint in quadrupedal gait (Bergmann *et al.*, 1984; Bergmann *et al.*, 1999; Biewener, 2003), and was designed to simulate non to full

weight-bearing through one hind limb in the gait cycle of a donor pig weighing on average 80 kg. A motion of only ± 15° of flexion to extension was chosen as it was thought that greater degrees of movement would cause an impingement of the femoral head and/or neck against the rim of the natural porcine acetabulum. Although porcine range of motion at the hip joint has not been reported, in quadrupeds such as pigs, the hip joint is slightly flexed when in the anatomical position and therefore they are assumed to have a smaller range of motion during normal gait than bipedal humans (van Ingen Schenau and Bobbert, 1993; Biewener, 2003). This kinetic input profile was also used for the complete natural hip joint study in Chapter 6.

As per the manufacturer's instructions, the cooling fans were used for all hemiarthroplasty tests to control the build-up of any heat generated from running the simulator for longer. In quadrupeds, FE motion occurs in the cranial (flexion) and caudal (extension) directions of the acetabulum (Figure 5.10 b). Unlike the spherical THR samples used in the previous section that were tested in forward and reverse directions, natural porcine acetabula have a more complex and slightly aspherical geometry, which creates additional torque due to the COR of the acetabulum and simulator being slightly misaligned. In order to calculate this additional torque, each sample was tested with a constant load of 800 N ± 15° FE at 1 Hz for two minutes both before and after the dynamic tissue test. This input profile was developed by Lizhang (2010) and used more recently by Taylor (2012) in their hemiarthroplasty work on friction simulator A.

5.3.3 Assessment of Wear and Surface Deformation

5.3.3.1 Classification of Wear

A number of different grading systems have been developed for use during arthroscopic knee surgery for classifying chondral defects (Noyes and Stabler, 1989; Curl *et al.*, 1997), two of which were considered for use in this study as methods of evaluating any wear or defects present on the acetabula following *in vitro* testing.

The first classification system evaluated by the candidate was developed by the International Cartilage Repair Society (ICRS) as part of a Cartilage Injury Evaluation Package. This system has five main grades with a number of different sub-grades, enabling the user to give a very detailed and accurate description of the lesion with particular reference to the depth (Table 5.3).

The second grading system appraised as a potential method was the Outerbridge classification system. This tool also has five grades describing normal to exposed subchondral bone; however, the grades are not sub-divided meaning less detail is required about the nature of the damage (Table 5.4).

Table 5.3: ICRS Cartilage Injury Classification System (Brittberg *et al.*, 2000).

Grade	Definition
0	**Normal**
1 (A & B)	**Nearly Normal**. Superficial lesions with soft indentation **(A)** and/or superficial fissures and cracks **(B)**
2	**Abnormal**. Lesions extending down to < 50 % of the cartilage depth
3 (A to D)	**Severely Abnormal**. Cartilage defects extending down > 50 % of the cartilage depth **(A)** as well as down to the calcified layer **(B)** and down to but not through the subchondral bone **(C)**. Blisters are included in this Grade **(D)**
4	**Severely Abnormal**. Cartilage defects extend through to the subchondral bone

Table 5.4: The Outerbridge Classification System used to classify damage to the articular cartilage following *in vitro* simulation testing (Outerbridge, 1961).

Grade	Definition
0	Normal cartilage
I	Cartilage with surface roughness, swelling
II	A partial-thickness defect with fissures on the surface that do not reach subchondral bone or exceed 15 mm in diameter
III	Fissuring to the level of subchondral bone in an area with a diameter more than 15 mm
IV	Exposed subchondral bone

After carefully considering both grading tools, it was decided to use the Outerbridge Classification System for assessing wear/chondral damage following the *in vitro* simulation studies. This classification system has been reported as being reliable with good inter-observer agreement when classifying chondral lesions in the knee (Curl *et*

al., 1997; Cameron *et al.*, 2003; Marx *et al.*, 2005). It has also been successfully used for classifying acetabula chondral lesions in patients with FAI undergoing arthroscopy (Konan *et al.*, 2011), supporting its validity as an assessment tool for use in this study. This system was also chosen as it was considered more practical for this particular application when compared to the ICRS grades, which would have required a quantitative assessment of the depth of the lesions. To verify this, both assessment tools were trialled on tested acetabula samples, and the Outerbridge classification system was confirmed as being the most workable option for the validation process.

Outerbridge classification grades were assigned by conducting a macroscopic evaluation of the tested specimens 24 hours after testing, and where appropriate, prior to making a Microset® replica. The length of any identifiable wear scars was measured using a vernier calliper (± 0.01 mm). A mapping system that divided the lunate surface equally into caudal, cranial, and central sections (Figure 5.3) was used to report the grade, location, and quantity of any lesions. This system was a simplified version of a geographical chart developed by Ilizaliturri *et al.* (2008) for reporting intra-articular lesions. Their method also divided the three regions into superior and inferior zones. This level of precision was not required for this study.

5.3.3.2 Measurement of Surface Deformation

Following *in vitro* testing in the friction simulator, surface deformation of the articular surface of the tissue sample was used as an additional secondary outcome measure for the validation process. It was assessed with a Microset® silicon replica of the acetabulum and two-dimensional (2D) contacting profilometry, using the Talysurf equipment described in Section 4.6.3.3. Silicon replicas, which have been used in other tribological studies of articular cartilage (Katta *et al.*, 2007; McCann *et al.*, 2008; Lizhang *et al.*, 2013), were taken from six randomly chosen tested acetabula (n = 3 from each simulator), 24 hours after *in vitro* testing to allow any elastic deformation or non-permanent damage time to recover. The sample was stored at ∼3° C in the laboratory refrigerator during this relaxation period, and a PBS-soaked tissue was used to restore and maintain hydration of the articular cartilage. A re-hydration period of 24 hours with PBS before measuring surface deformation and wear was chosen based on a cartilage pin-on-plate study by Lizhang *et al.* (2011), who reported this as being sufficient time for any non-permanent cartilage deformation to recover. Replicas were

created by inserting Microset® quickly into the tested acetabulum (to avoid the entrapment of air bubbles), which was positioned horizontally to enable the cavity to be completely filled with the silicon compound. The acetabular fossa was used as a reference point to orientate the replicas, as this roughened area was easily distinguishable from the smoother replica of the lunate surface (Figure 5.11). Approximately nine parallel traces of the replica were taken orthogonally to the direction of FE motion, across the region of interest (ROI). The ROI was identified by the presence of scratches or damage on the surface of the acetabulum, and each trace extended beyond both sides of the ROI so that unworn/undamaged areas could be used as a reference.

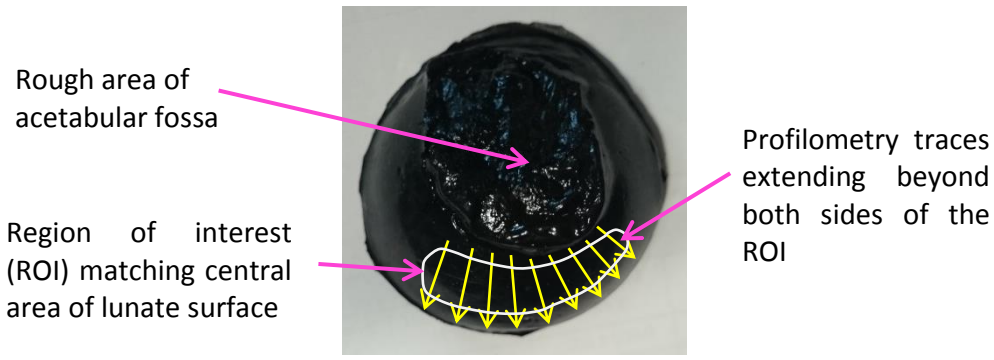

Figure 5.11: Microset® replica of tested hemiarthroplasty sample showing region of interest (white area) and direction of profilometry traces (yellow arrows).

The profilometry traces, which were performed by a qualified metrology technician, had a 1.5 mm gap between them and therefore, the exact number of traces taken from each replica was dependant on the size of the ROI being assessed. Measurements were taken with the replica fixed in position between two V-blocks using a metal pin, which was inserted through the centre of the replica and held in place using plasticine (Figure 5.12).

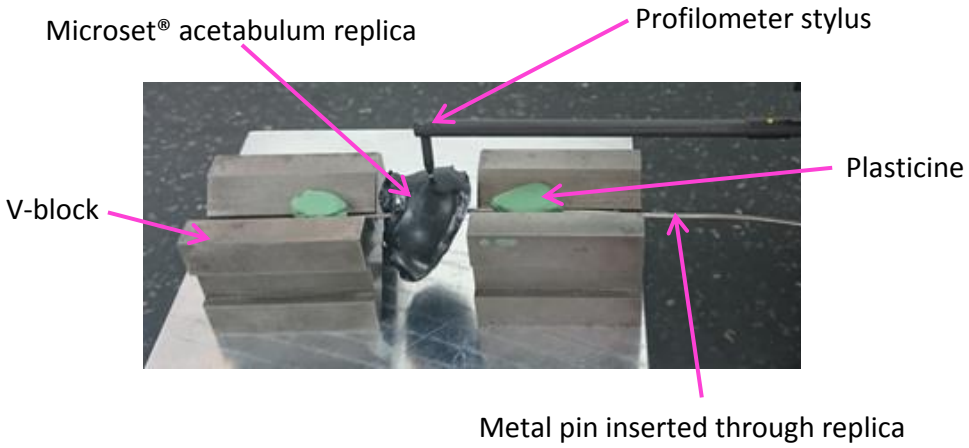

Figure 5.12: Microset® replica set-up for 2D contacting profilometry measurements.

5.4 Data Analysis

5.4.1 Friction Factor

Data was logged in the pendulum friction simulator during the two-hour dynamic load test period every 30 cycles up to cycle number 100, and then every 150 and 300 cycles up to cycle numbers 1,000 and 10,000 respectively, and every 30 cycles for the two-minute constant load tests. To account for the additional frictional torque created by the misalignment of the aspherical porcine acetabula, the data was normalised using a mean frictional offset value (f_o), which was calculated from the constant load tests conducted before (pre-test) and after (post-test) each dynamic profile study. The mean friction factor for the two-minute constant load tests was calculated using the methodology described in Section 4.3.3.

The frictional offset for each hemiarthroplasty study was calculated using Equation 5.1, where f_b is the mean pre-test friction factor and f_a is the mean post-test friction factor:

$$f_o = \frac{f_b + f_a}{2} \qquad \text{Equation 5.1}$$

The mean dynamic friction factor (f_d) for each of the logged one-second cycles was calculated from the data collected during the peak load (i.e. 800 N) high velocity phase of the cycle (Figure 4.11). The friction data was then normalised (f_n) by subtracting the

frictional offset (f_o) from the mean dynamic friction factor of each logged cycle (Equation 5.2) to give a friction value for the hemiarthroplasty test:

$$f_n = f_d - f_o \quad \text{Equation 5.2}$$

5.4.2 Surface Deformation

Talysurf 2D contacting profilometer measurements were analysed using TalyMap Gold 5.1 software (Taylor Hobson, UK) by which the form, excluding the wear scar, was removed. The traces were processed using a number of different functions, which are listed in Table 5.5.

Table 5.5: Functions used to process profilometry traces using TalyMap Gold software.

Function	Rationale/Details
Zoom (if required)	To excluded distal ends of the trace that appear to have been outside the boundaries of the replica
Levelling	By rotation to level the trace making it horizontal
Symmetry	To invert the profile due to the wear scar on the replica being a mirror image of the cartilage (i.e. peak instead of trough)
Form Removal	Using a polynomial order of three

The deformation area (mm^2) and maximum depth (mm) of the deformation under the mean line was then calculated for each trace using the '**surface of hole or peak**' studies option on the software. These values were then used to calculate the volume of the surface deformation (V_d) (mm^3) and mean depth ($\overline{D_d}$) (mm) of the wear scar using Equation 5.3 and Equation 5.4 respectively:

$$V_d = \sum_{i=1}^{n} (A_d \times G_t) \quad \text{Equation 5.3}$$

$$\overline{D_d} = \sum_{i=0}^{n} A_d \div \sum_{i=0}^{n} L_t \quad \text{Equation 5.4}$$

where A_d is the deformation area of each trace (mm^2), G_t is the gap between each trace (i.e. 1.5 mm), and L_t is the length of each trace (mm). This method was developed by Lizhang (2010), who validated it using a pyncometer and Microset® replica of known volume.

5.4.3 Statistical Analysis

Data is presented with mean values ± standard deviation (SD), or ± 95 % confidence limits (CL) for data with more than three values. Due the normalisation of data to account for frictional offset arising from the porcine acetabulum, data is presented to two decimal places, rather than the three used for the THR samples. Statistical analysis of the friction factor results using *t*-tests, for two sample means, or one-way ANOVA for more than two mean values, was performed using SPSS software on normally distributed data taken from specific time points during the tests. Scheffé post-hoc analysis, which is suitable for unequal sample sizes, was used to determine significant differences between group means on significant ANOVA results where $p < 0.05$. Data was analysed at the start and end of each test at the one-minute (60 cycles) and two-hour (7,200 cycles) time points respectively, so that the results could be compared to similar studies reported in the literature (Lizhang, 2010; Lizhang *et al.*, 2013). An additional arbitrary time point of 20 minutes (1,200 cycles) was chosen by the candidate to enable data from the initial stage of the tests to be compared, as this is where a large increase in friction factor has been reported to occur (Forster and Fisher, 1996; Katta *et al.*, 2007; Lizhang *et al.*, 2013).

5.5 Initial Hemiarthroplasty Validation Study Results

Results from the validation of the new pot and potting methodology (which was conducted on pendulum friction simulator A), pendulum friction simulator A hemiarthroplasty comparator data, and the initial findings following testing on pendulum friction simulator Mk B are presented in this section. All friction factor data is normalised with respect to frictional offset as described in Section 5.4.1.

5.5.1 Validation of New Acetabulum Pot and Potting Methodology

Pendulum friction simulator A was used for this study as pendulum friction simulator Mk B had not been validated using natural tissue at this stage. The mean friction results of the study to validate the new acetabulum pot (Section 5.2.7) and new potting

methodology using the inclinometer (Section 5.3.1.2) before continuing with the validation of pendulum friction simulator Mk B are presented in Figure 5.13. Slight fluctuations in the mean friction factor value with an increase in the magnitude of friction were observed throughout the two-hour tests for both methodologies.

Mean friction factor for the samples tested using the Delrin® pot and old potting methodology increased from 0.03 ± 0.02 to 0.11 ± 0.03 during the two-hour test, and the mean friction values for the new stainless steel pot and inclinometer method increased from 0.02 ± 0.01 to 0.12 ± 0.01. A slightly larger change in friction over time was observed for the new method (0.11) compared to the old method (0.08).

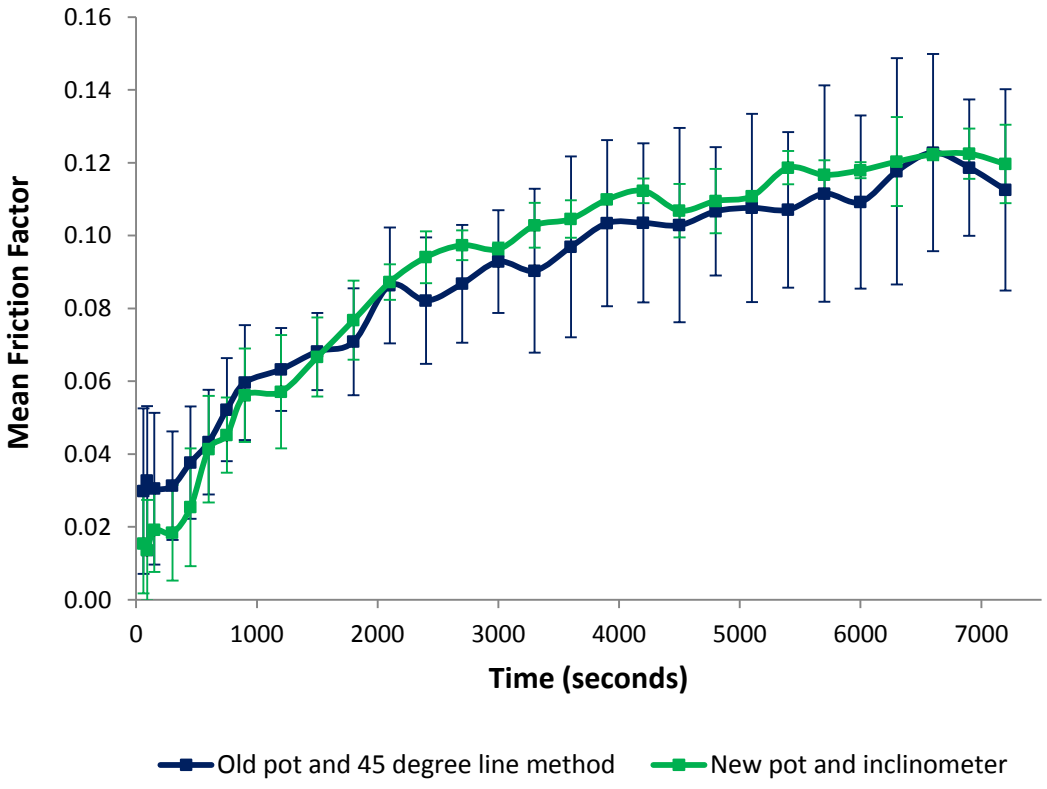

Figure 5.13: Mean friction factor ± SD for hemiarthroplasty tests conducted on porcine acetabula cemented in the old pot positioned using the 45° line method (n = 3) and in the new pot positioned using the inclinometer (n = 3). This work was conducted on pendulum friction simulator A.

There was no significance difference between the mean friction factor determined in the hemiarthroplasty samples tested using the two methods (*t*-test, $p > 0.05$) and less variability in the results was observed obtained using the new method.

Hemiarthroplasty validation studies were conducted using the new acetabulum pot and positioning method.

5.5.2 Pendulum Friction Simulator A

The friction factor of all five hemiarthroplasty samples tested in friction simulator A increased with time. The rate of friction increase was higher for all samples during the first 15-25 minutes of the test (Figure 5.14).

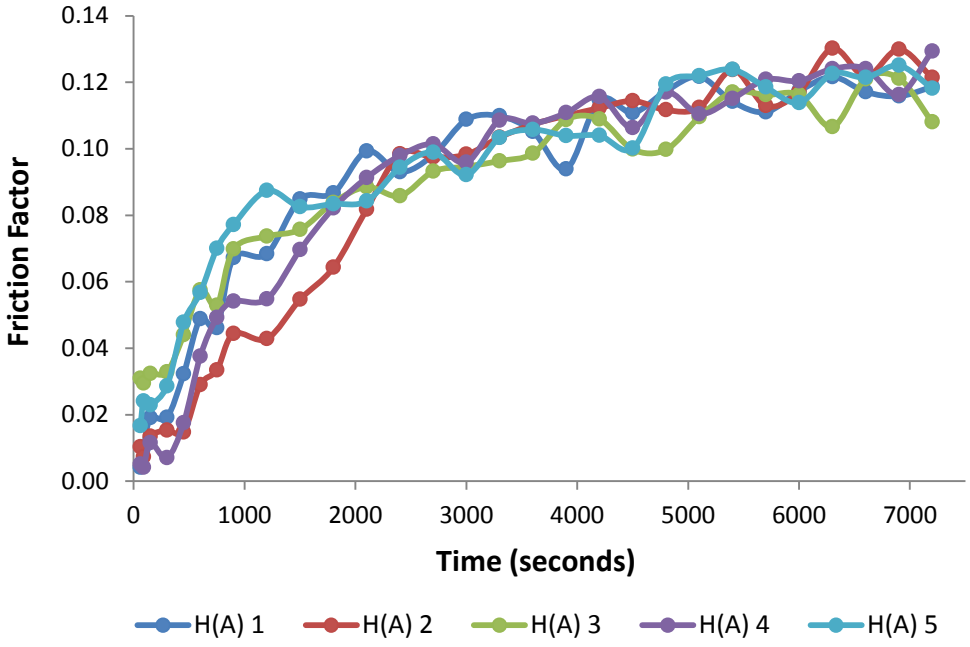

Figure 5.14: Friction factor of hemiarthroplasty samples (n = 5) tested in pendulum friction simulator A for two-hours.

The mean friction factor (n = 5) presented in Figure 5.15 increased over two hours from 0.02 ± 0.01 to 0.12 ± 0.01 and there were no significant differences between repeats (ANOVA, $p > 0.05$). Greater variability in the friction factor with larger error bars was observed during the 5-10 minute period.

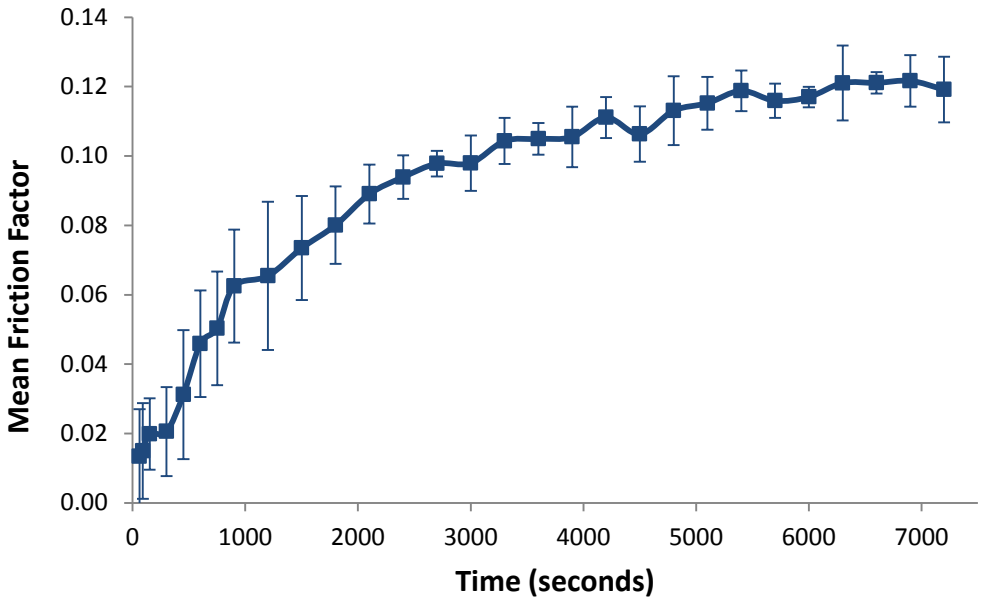

Figure 5.15: Mean friction factor ± 95 % confidence limits (CL) for hemiarthroplasty samples (n = 5) tested in pendulum friction simulator A.

5.5.3 Preliminary Results – Pendulum Friction Simulator Mk B

Initial attempts at running hemiarthroplasty tests in pendulum friction simulator Mk B were unsuccessful due to the friction measuring carriage moving laterally away from the CoCr femoral head when the oil flow to the hydrostatic bearing was activated. This created a gap between the articulating surfaces of the head and the acetabulum. An attempt was made to test three different hemiarthroplasty samples in simulator Mk B; however, the hip joint of each sample disarticulated as the CoCr femoral head moved laterally away from acetabulum by varying amounts as soon as the oil flow was switched on. An example of the position of the CoCr head in relation to the porcine acetabulum before and after activation of the oil is shown in Figure 5.16. All three samples were placed into pendulum friction simulator A to check for any problems (e.g. offset) with the potting or fixturing, and the CoCr head and porcine acetabulum remained congruous with the activation of oil flow and application of a dynamic load (25 N to 800 N ± 15° FE motion) for all three samples.

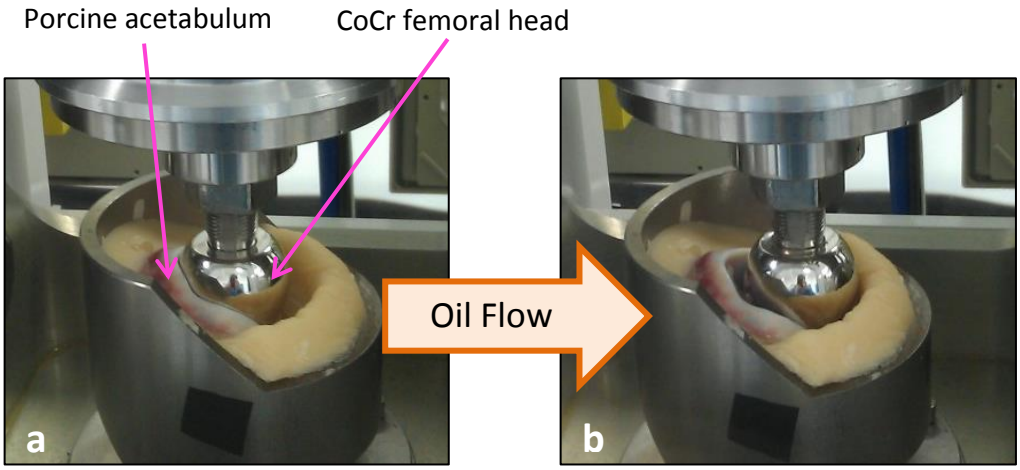

Figure 5.16: Position of hemiarthroplasty samples in pendulum friction simulator Mk B before (a) and after (b) the oil to the hydrostatic bearing was activated.

5.5.4 Additional Investigations – Pendulum Friction Simulator Mk B

A number of basic investigations, detailed below, were conducted on friction simulator Mk B in order to explore possible reasons for the lateral movement of the friction measuring carriage with a porcine acetabulum *in situ*.

a) The oil flow was activated with a porcine hemiarthroplasty sample *in situ*, but without the femoral head located in the acetabulum. A small amount of lateral movement of the frictionless carriage was observed in the direction of the centre of mass of the acetabulum cup holder. The centre of mass was offset due to the acetabulum being positioned in the PMMA with an inclination angle of 45°.

b) Pendulum friction simulator Mk B was designed with a counterweight fitted to the loading frame in order to reduce the effort required to pull down/position the FE rocker. The mass of the counterweight however, was greater than that of the loading frame, thus producing a slightly negative force. The loading frame on friction simulator A does not have this design feature. To offset the counterweight, free weights were placed incrementally on top of the loading frame (with a hemiarthroplasty sample *in situ*) until it was balanced with a total of 4.08 kg (Figure 5.17 a). Once balanced, only a minimal amount of lateral movement of the acetabulum was observed when the oil flow was activated (Figure 5.17 b).

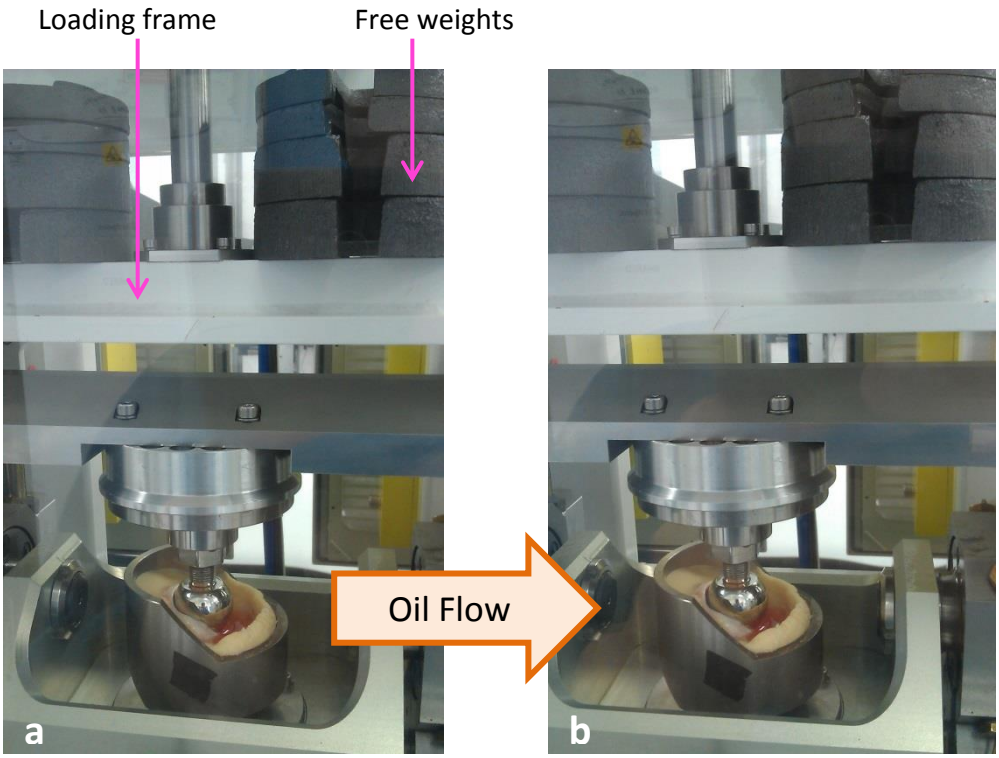

Figure 5.17: Pendulum friction simulator Mk B with free weights totalling 4.08 kg placed on the loading frame. Position of hemiarthroplasty samples before (a) and after (b) the oil to the hydrostatic bearing was activated.

c) The 36 mm Ø CoC THR sample (used for the validation studies detailed in Chapter 4) with 25 % serum lubricant was fixtured into the simulator with the cup angled at 45°. No obvious movement of the friction measuring carriage was observed when the oil was switched on or when the dynamic tissue kinetic profile was applied.

5.5.4.1 Adjustment of Pendulum Friction Simulator Mk B Counterweight

The results of investigations conducted in Section 5.5.4 indicated that reducing the counterweight on the loading frame would enable the CoCr head and porcine acetabulum to remain congruent with activation of the oil flow to the hydrostatic bearing. In order to test this hypothesis, a 4.5 kg section was removed from the counterweight. A fresh hemiarthroplasty sample was placed in the simulator and no movement of the friction measuring carriage was observed when the oil flow was activated.

The THR control samples were re-tested under the conditions specified in Section 4.9 to check that reducing the counterweight had not affected the general function of the simulator. Friction factor values for the THR samples remained unchanged.

5.5.5 Initial Hemiarthroplasty Validation Study Results for Pendulum Friction Simulator Mk B

The hemiarthroplasty results reported in this section were conducted on pendulum friction simulator Mk B during the initial validation period. This study was conducted following the reduction of the counterbalance and before the simulator was modified by fitting new capillary tubing.

It was possible to run hemiarthroplasty tests in pendulum friction simulator Mk B following the reduction of the counterbalance, however, variable results were recorded for all tests (n = 4). After an initial short increase, generally a reduction in friction factor over time was observed in three of the four hemiarthroplasty tests (Figure 5.18), with the fourth (H[B]4) oscillating between 0.03 and 0.04 throughout the two-hour period. All tests produced graphs with trends that were dissimilar to those tested in friction simulator A (Figure 5.14) and therefore, testing a fifth sample at this stage would not have been beneficial.

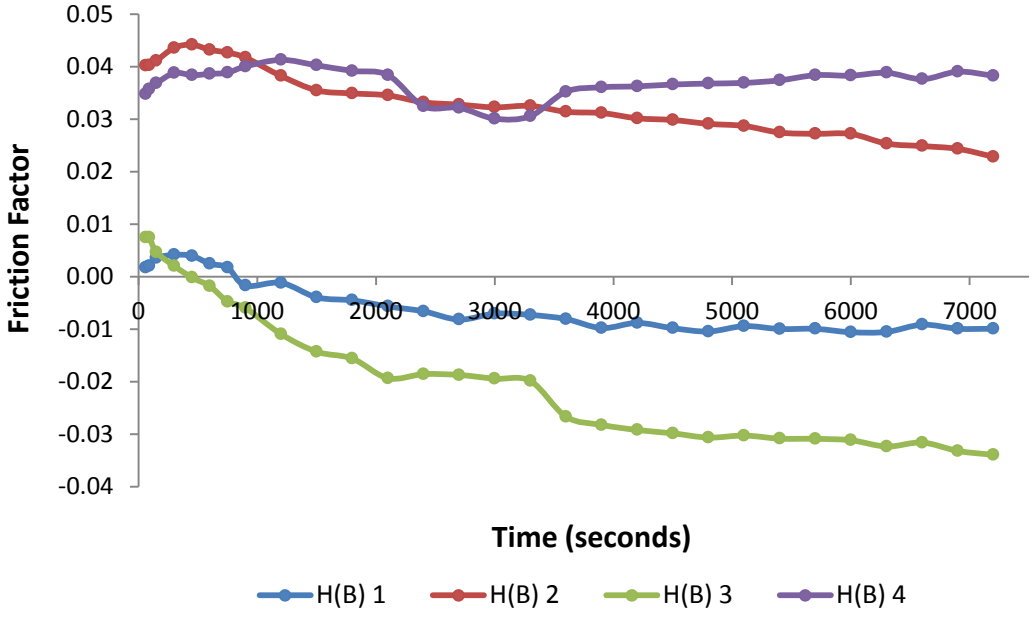

Figure 5.18: Friction factor of hemiarthroplasty samples (n = 4) tested in pendulum friction simulator Mk B for two-hours during the initial validation study.

Mean friction factor for the initial validation study was variable throughout the two-hour test period, with confidence intervals ranging from ± 0.03 to ± 0.05 for the four samples tested (Figure 5.19). Overall, the mean friction for the study started to decrease after 25 minutes (1,500 cycles) from 0.02 ± 0.02 to ≈ 0.00 ± 0.03.

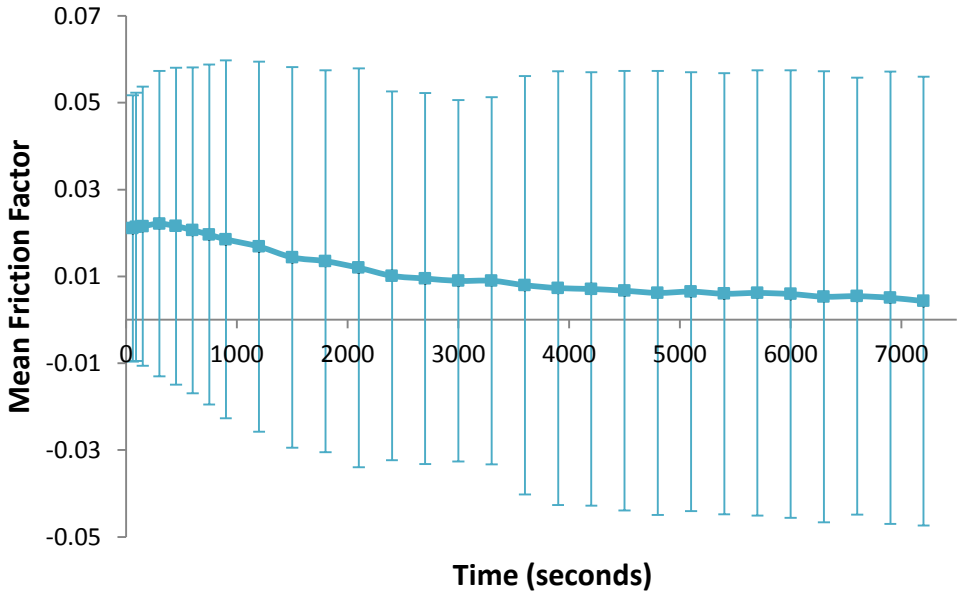

Figure 5.19: Mean friction factor ± 95 % CL for hemiarthroplasty samples (n = 4) tested in pendulum friction simulator Mk B during the initial validation study.

The mean results of the initial hemiarthroplasty validation study conducted on friction simulator Mk B were significantly different to the hemiarthroplasty results from friction simulator A at the 20-minute and two-hour time points (*t*-test, p = 0.02 and p = 0.00 respectively), but not at the start of the test, where p > 0.05 after one minute (Figure 5.20). Larger confidence intervals were observed in the friction factor results obtained using friction simulator Mk B compared to simulator A.

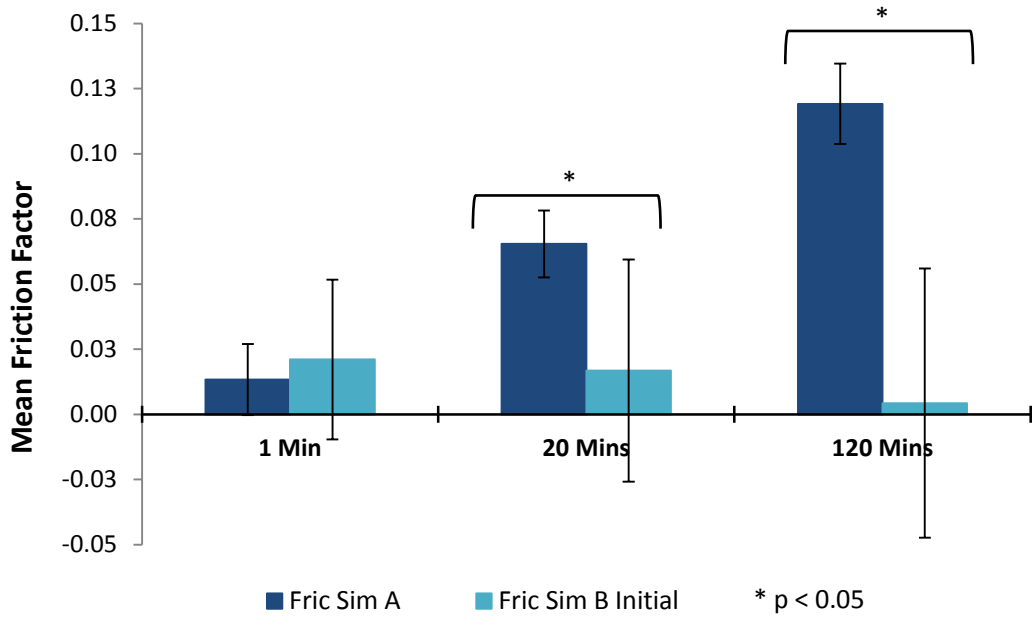

Figure 5.20: Mean friction factor results ± 95 % CL for hemiarthroplasty tests conducted on friction simulator A and friction simulator Mk B at the three time points.

5.6 Further Hemiarthroplasty Validation Study

Further hemiarthroplasty validation tests were conducted on five porcine acetabula in pendulum friction simulator Mk B following its modification with new capillary tubing (Section 4.8). The same methodology (described in Section 5.3 and Section 5.4) was used, all tested acetabula specimens were assessed for surface wear, and three tested samples were randomly chosen for 2D profilometry surface deformation measurements. Friction factor was the primary variable used to validate the new simulator and therefore, three acetabula surface deformation measurements was deemed sufficient to be used as an additional measurement variable for the validation study.

5.6.1 Friction Factor Results

The friction factor generally increased rapidly during the first 20 minutes of the hemiarthroplasty tests, with the exception of sample H(B) 6, in which a very slight decrease in friction from ≈ 0.05 to ≈ 0.04 was observed (Figure 5.21).

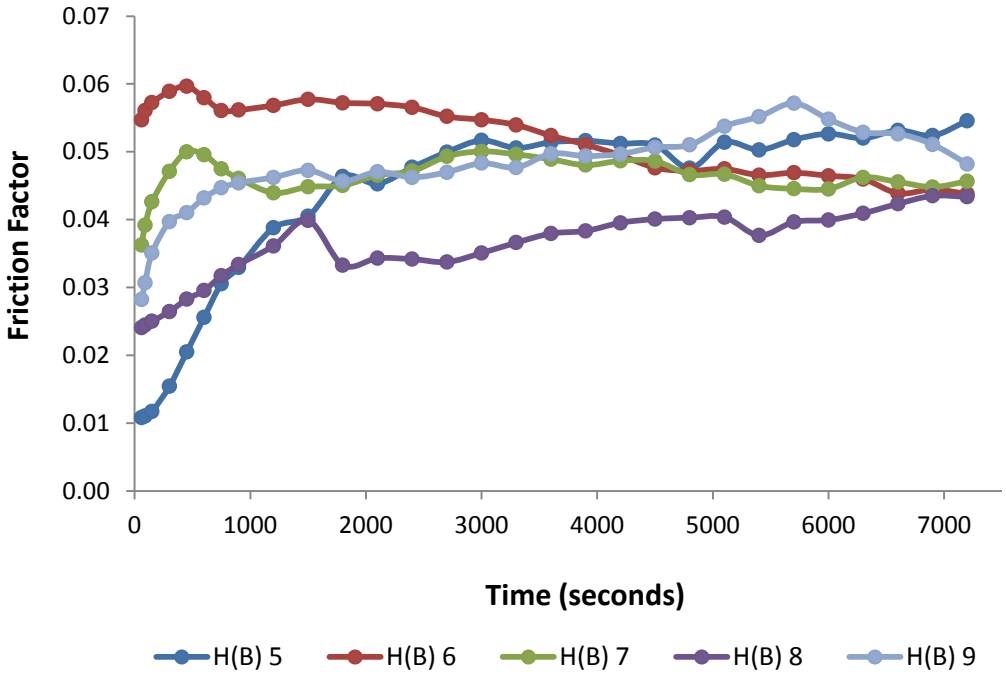

Figure 5.21: Friction factor of hemiarthroplasty samples (n = 5) tested in pendulum friction simulator Mk B for two-hours for the further validation study.

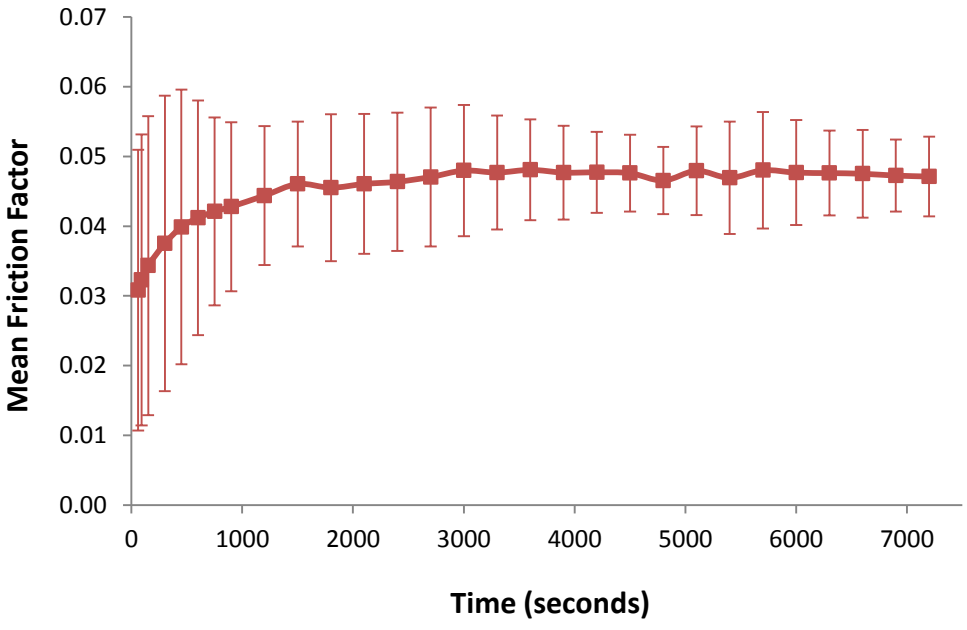

Figure 5.22: Mean friction factor ± 95 % CL for hemiarthroplasty samples (n = 5) tested in pendulum friction simulator Mk B for the further validation study.

Mean friction factor increased during the initial part of the study from a value of 0.03 ± 0.02 before plateauing at 1,500 cycles (25 minutes) to ≈ 0.05 ± 0.01 (Figure 5.22). The large variability in friction factor values at the start of the tests compared to the end of the tests observed in Figure 5.21 is reflected by the confidence intervals calculated for the mean results, which are shown in Figure 5.22. Clearly visible differences were observed in the friction factor results from the initial validation study and the further validation study, in terms of both values and trend over time (Figure 5.23).

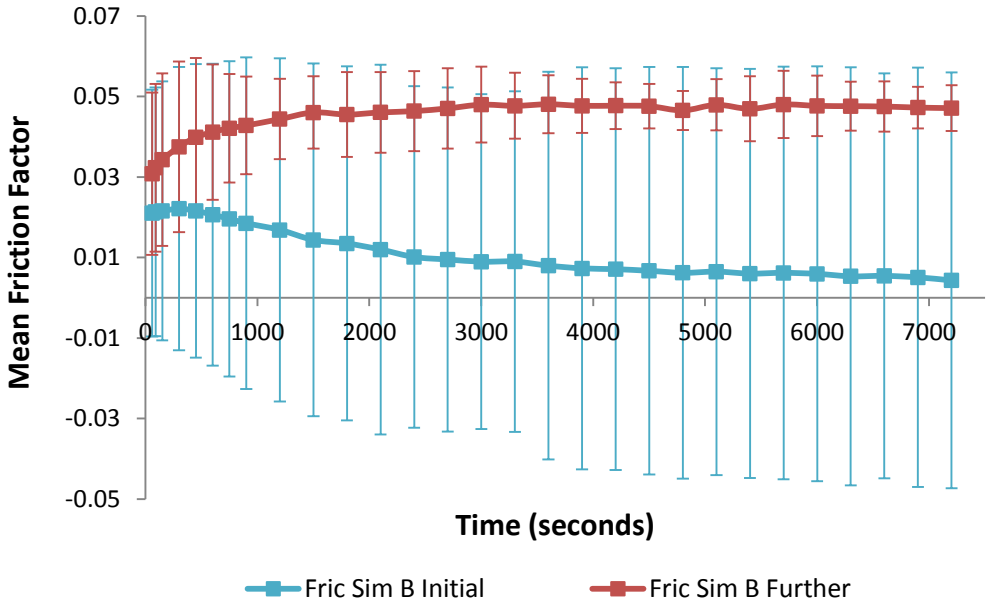

Figure 5.23: Mean friction factor ± 95 % CL for hemiarthroplasty samples tested in friction simulator Mk B during the initial (n = 4) and further (n = 5) hemiarthroplasty validation study.

Initial validation study results were more widely dispersed than the further validation study results, with a significant difference in mean friction factor (*t*-test, p = 0.02) being detected after two hours of testing (Figure 5.24). There were no statistically significant differences in mean friction factor values at the start of the test or at the 20-minute time point (p > 0.05).

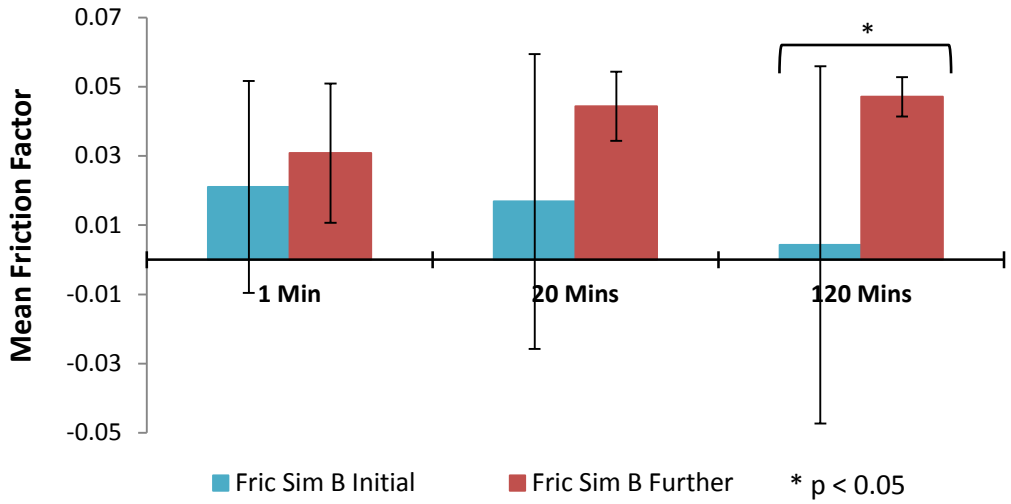

Figure 5.24: Mean friction factor ± 95 % CL for the initial and further hemiarthroplasty validation tests conducted on friction simulator Mk B at three time points.

A comparison of the mean friction factor results from the further validation study conducted on friction simulator Mk B and the results from friction simulator A is presented graphically in Figure 5.25. Hemiarthroplasty samples tested in the two simulators behaved differently over time, with simulator A recording mean friction factor values of 0.01 ± 0.01 increasing to 0.12 ± 0.01 after two-hours, and simulator Mk B recording mean values of 0.03 ± 0.02 increasing to 0.05 ± 0.00.

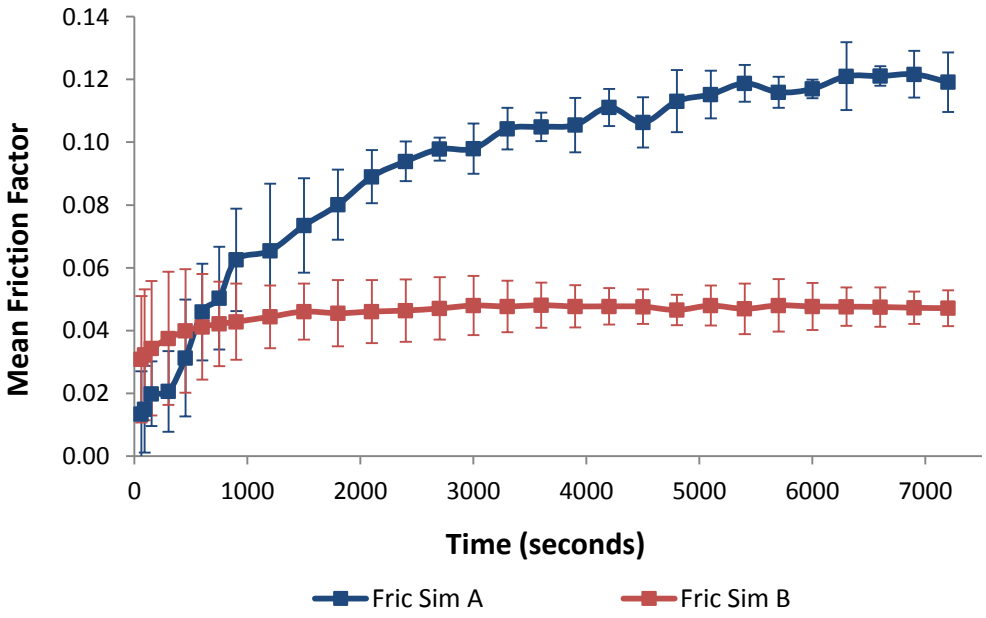

Figure 5.25: Mean friction factor ± 95 % CL for hemiarthroplasty samples tested in friction simulator Mk B during the further (n = 5) hemiarthroplasty validation study and in friction simulator A (n = 5).

The mean friction factor plateaus on simulator Mk B but continues to increase gradually over time on simulator A. Greater variation in mean friction factor during the initial stages of the test is evident on both simulators, were there is a more rapid increase in friction factor. Statistical analysis of the hemiarthroplasty friction factor results from simulator A and the further validation results from simulator Mk B showed a significant difference at the end of the two-hour test (*t*-test, p = 0.00). No significant differences were observed after one minute or at the 20-minute time point (p > 0.05) (Figure 5.26).

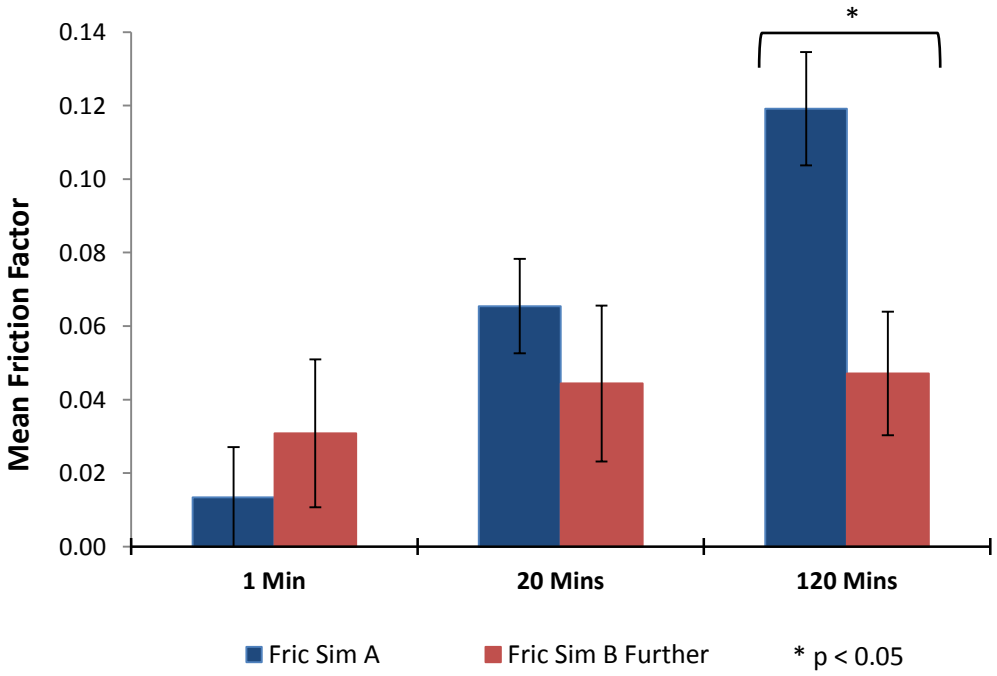

Figure 5.26: Mean friction factor ± 95 % CL for hemiarthroplasty validation tests conducted on friction simulator A and further validation testing on simulator Mk B at three time points.

5.6.2 Classification of Wear and Surface Deformation Analysis Results

The results of the wear and surface deformation analyses performed on porcine acetabula tested *in vitro* using friction simulator A (H[A] 1 to 5) and simulator Mk B during the further validation study (H[B] 5 to 9), are presented in this section.

5.6.2.1 Wear Analysis

The lunate surfaces of each tested acetabulum from the two sample groups (A and Mk B), were macroscopically evaluated, with all discrete wear lesions being recorded and graded individually using the Outerbridge Classification System. Four different types of

chondral damage were identified on the lunate surfaces (Figure 5.27) and these were described as 1) roughening and discolouration; 2) scratches; 3) partial thickness defect; or 4) fissuring.

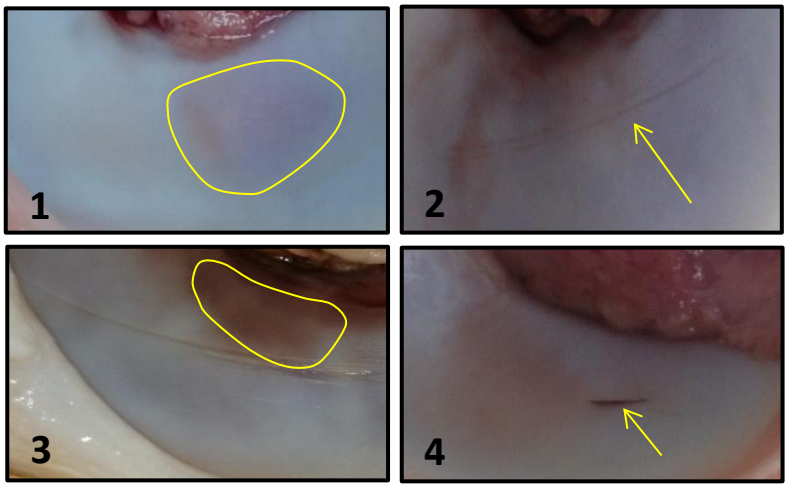

Figure 5.27: Examples of chondral damage observed on the acetabula following *in vitro* hemiarthroplasty testing in the pendulum friction simulators. The four types of lesion (highlighted in yellow) were 1) roughening and discolouration; 2) scratches; 3) partial thickness defect; 4) fissure.

A protractor was held over the lunate surface to divide it into three equal sections (cranial, central, caudal). The grade, type and location of any wear lesions on the cartilage was then recorded on the mapping system chart (Figure 5.28). Scratches that were located immediately adjacent and parallel to each other were classified as one lesion, and damage spanning across a boundary was logged in both regions.

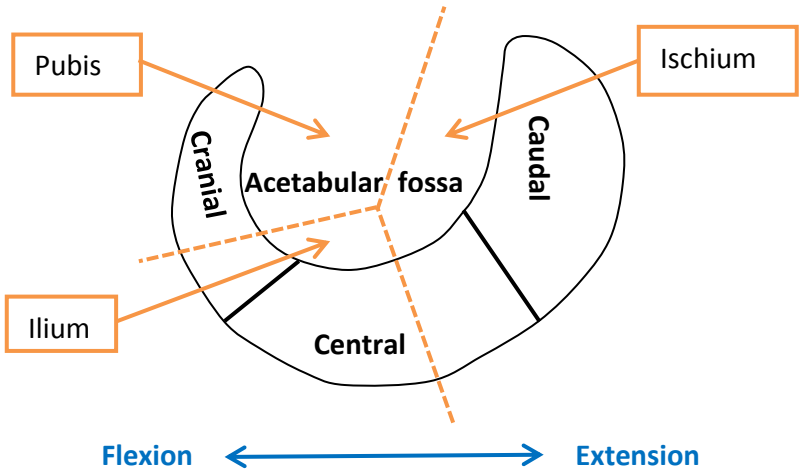

Figure 5.28: Mapping chart used to record the location, type, grade, and number of lesions identified on the lunate surface of the tested acetabula. The direction of FE motion (blue arrow) and location of triradiate cartilage (orange dashed lines) and pelvic bones are displayed for reference.

Roughening and discoloration of the lunate surface was the predominant type of lesion mapped, as this was observed in all specimens from both groups (n = 10). Partial thickness defects were also a common feature, which in the main were located in the central region either side of the triradiate cartilage. Large (> 15 mm), deep Grade 3 lesions were observed in the central region of two samples, one from each simulator (H[A]3 and H[B]5), and a small fissure had formed in the caudal region of specimen H(B)9. No exposure of the subchondral bone (Grade 4 wear) was observed in any of the acetabula that had been tested. Scratches of varying depths and lengths were observed in six acetabula (H[A]2, 3, 4, and H[B]5, 6, 8), all located centrally and orientated in the direction of the FE motion of the simulation.

The total number wear lesions observed on the lunate surface of porcine acetabula following *in vitro* simulation testing in friction simulator A and friction simulator Mk B was n = 14 and n = 12 respectively. The number, location and grade (assigned using the Outerbridge Classification System) of lesions is presented in Figure 5.29, which shows the cumulative number of lesions of each grade, in each region of the lunate surface observed on the tested samples from each simulator.

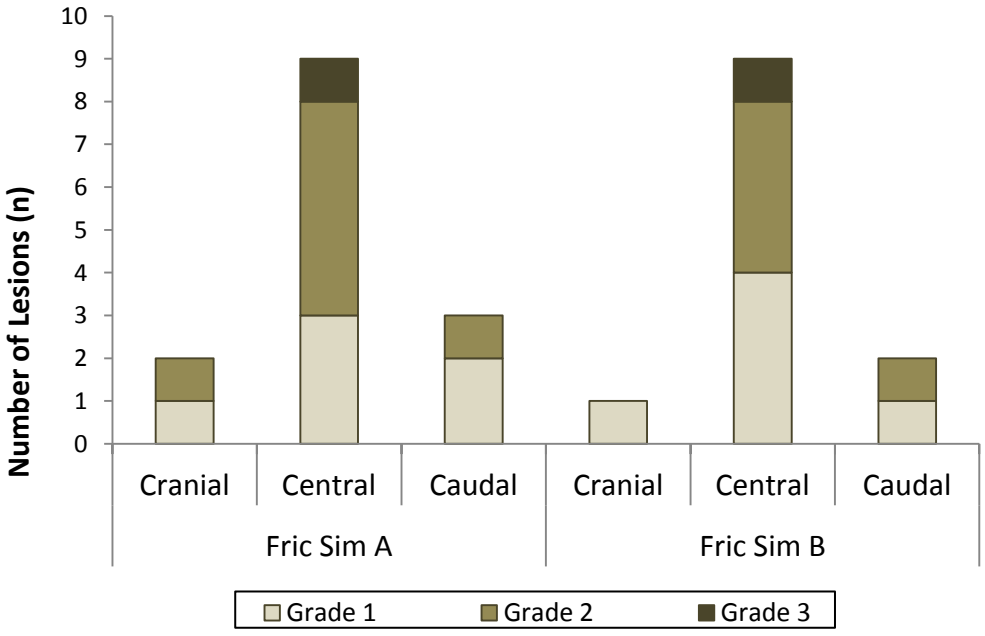

Figure 5.29: Location and grade of chondral lesions identified on hemiarthroplasty samples tested in pendulum friction simulators A (n = 5) and Mk B (n = 5) during the validation procedure. The total number of lesions recorded for each sample group was: A: n = 14 lesions and Mk B: n = 12 lesions.

The majority of damage was observed in the central region, just proximal to the acetabula fossa, with 64 % (n = 9) of the wear lesions being located centrally on specimens tested in simulator A, and 75 % (n = 9) being located centrally in specimens tested in the further validation study on simulator Mk B. The frequency of wear lesions located in the cranial (14 % simulator A; 8 % simulator Mk B) and caudal (21 % simulator A; 17 % simulator Mk B) regions was smaller than the frequency of those located centrally. There were no significant differences in the frequency of wear lesions observed in the cranial, central, or caudal regions, when comparing specimens from the validation studies conducted on the two simulators (ANOVA; $p > 0.05$).

The percentage of wear lesions on specimens tested using simulators A and Mk B that were classified as either Grade 1 (A: 43 %; MK B: 50 %), Grade 2 (A: 50 %; Mk B: 42 %) or Grade 3 (A: 7 %; B: 8 %) were evenly matched and not significantly different (ANOVA, $p > 0.05$). Unworn areas of cartilage (i.e. Grade 1), was not quantified in this study and, as stated previously, no Grade 4 lesions were observed in either data set.

5.6.2.2 Surface Deformation

Two-dimensional contacting profilometry was performed on Microset® replicas taken from acetabula specimens H[A]1 H[A]2 and H[A]3 (n = 3) from the friction simulator A validation study data set, and from H[B]5 H[B]8 and H[B]9 (n = 3) from the pendulum friction simulator Mk B further validation study data set. Profilometry traces from the six replicas were analysed using Talymap software analysis (Section 5.4.2). Acetabula cartilage deformation volume loss (mm^3) and depth (µm) results from simulator A were compared with the results from simulator Mk B (Figure 5.29).

Mean cartilage volume loss (Figure 5.29 a) measured using replicas from the friction simulator A hemiarthroplasty validation study was 13.87 ± 3.88 mm^3 (n = 3). This was less than the 20.49 ± 3.79 mm^3 (n = 3) mean deformation volume measured using replicas from the friction simulator Mk B further validation study, however, this difference was not statistically significant (*t*-test, $p > 0.05$). The mean depth of the cartilage deformation (Figure 5.30 b) was 28.78 ± 6.61 µm (simulator A; n = 3) and 41.93 ± 3.83 µm (simulator Mk B; n = 3), which was marginally significant ($p = 0.04$).

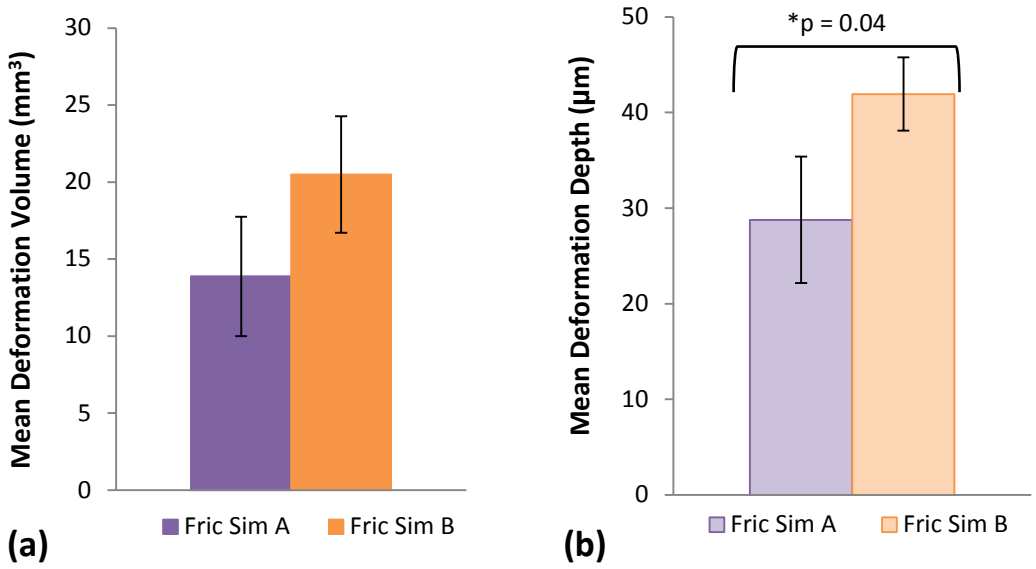

Figure 5.30: Talysurf 2D profilometry results of acetabula cartilage deformation following hemiarthroplasty studies conducted on friction simulators A (n = 3) and Mk B (n = 3). Comparisons of (a) mean deformation volume (mm^3) ± SD and (b) mean deformation depth (µm) ± SD.

A strong positive correlation was found in the relationship between deformation volume and mean deformation depth (r^2 = 0.92) in both simulators (Figure 5.31). A weaker negative correlation was found between mean friction factor and both deformation volume (r^2 = 0.48) and mean deformation depth (r^2 = 0.61).

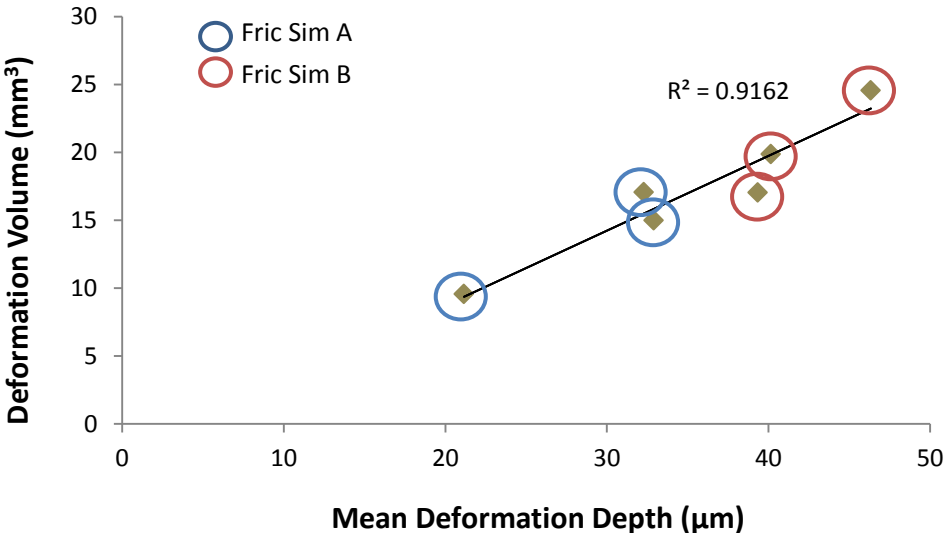

Figure 5.31: Regression analysis (Microsoft Excel) showing the correlation between acetabula cartilage deformation volume and mean deformation depth for hemiarthroplasty specimens tested in pendulum friction simulators A (n = 3) and Mk B (n = 3).

5.6.3 Summary of Hemiarthroplasty Validation Friction Factor Results

The two most noteworthy differences observed between the initial and further hemiarthroplasty validation studies on simulator Mk B were:

1. Reduced variation of the mean friction factor values, which was evident throughout the two-hour test (Figures 5.23 and 5.24)
2. An increase in friction factor recorded over the first 20-25 minutes of the test (Figure 5.22)

Increasing the oil pressure to the hydrostatic bearing improved the performance of the frictionless carriage, and this lead to reduced variability of the friction factor values and a trend during the first part of the test that was similar to that observed in hemiarthroplasty tests conducted on simulator A. This is discussed further in Section 5.7.4. Despite improved results being obtained following the modification of simulator Mk B however, the mean friction factor measured at the end of the two-hour test remained significantly lower than the friction factor measured over the same time-period using friction simulator A (Figure 5.26). Additionally, on simulator A the friction factor continued to increase gradually during the latter stages of the test, whereas on simulator Mk B the mean friction factor plateaued approximately 25 minutes after the start of the test. Potential causes of the different hemiarthroplasty results observed on Simulator A compared to the modified simulator Mk B were investigated in Section 5.6.3.1 and Section 5.6.3.2.

5.6.3.1 Increased Swing Phase Load Study

Review of the Excel data output files from both simulators revealed a larger discrepancy between the demand load and the actual load delivered during the swing phase on friction simulator A. The magnitude of this discrepancy varied between tests and recorded cycles, with the delivered SPL load ranging from ∼15 N to ∼150 N greater than the demand SPL of 25 N, compared to delivered loads of approximately -5 N to + 50 N difference on friction simulator Mk B. To investigate any possible effects increasing the SPL would have on the friction factor, three hemiarthroplasty tests were conducted on friction simulator Mk B using a 120 N instead of 25 N SPL. This SPL value was an approximation of the mean SPL delivered by simulator A, calculated using randomly selected output data from two cycles from each of the five hemiarthroplasty validation study tests.

The mean friction factor at the start and end of the two-hour test remained largely unchanged from the results observed during the further validation study, with recorded mean values of 0.03 ± 0.02 and 0.05 ± 0.00 respectively (Figure 5.32). The only notable difference was a more rapid rise in friction factor during the first 10 minutes (600 cycles) of the test, where the gradient of the graph for simulator A is almost parallel to that of the tests conducted on simulator Mk B with a higher SPL.

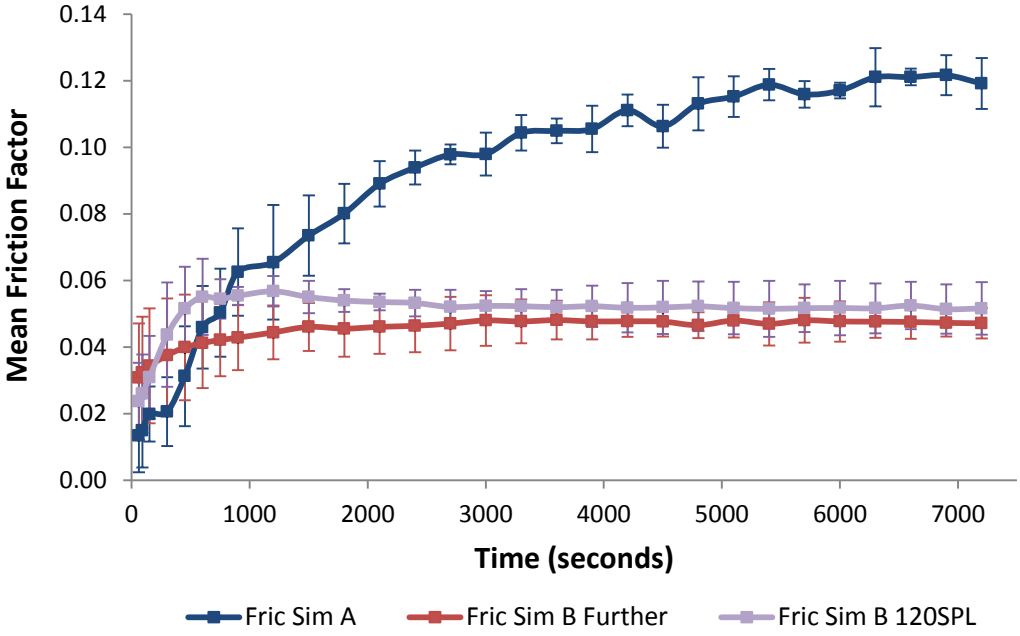

Figure 5.32: Mean friction factor ± SD for hemiarthroplasty samples tested in friction simulator A (n = 5) and friction simulator Mk B during the further validation study (n = 5) and with a 120 N Swing Phase Load (n = 3).

5.6.3.2 Drift Measurement

The change in friction factor over time was investigated in order to ascertain the presence of any of measurement drift in the two pendulum friction simulators and, where appropriate, quantify the magnitude of the drift. This was investigated by running the 28 Ø MoP control sample (used for the THR validation study), for two hours under the tissue test dynamic kinetic profile (i.e. 25 N to 800 N load ± 15° FE), with 25 % serum lubricant. Three repeats were performed on each simulator. Total hip replacement bearings, rather than a hemiarthroplasty sample, were used to reduce the risk of introducing confounding factors arising from the complex geometry and cartilage wear associated with running biological tissue samples *in vitro*.

The magnitude of drift for each repeat was calculated by subtracting the friction factor value of the first recorded cycle from all logged cycle values. After two hours, the mean friction factor drift measured on simulators A and Mk B was 0.078 ± 0.016 and 0.006 ± 0.006 respectively (Figure 5.33).

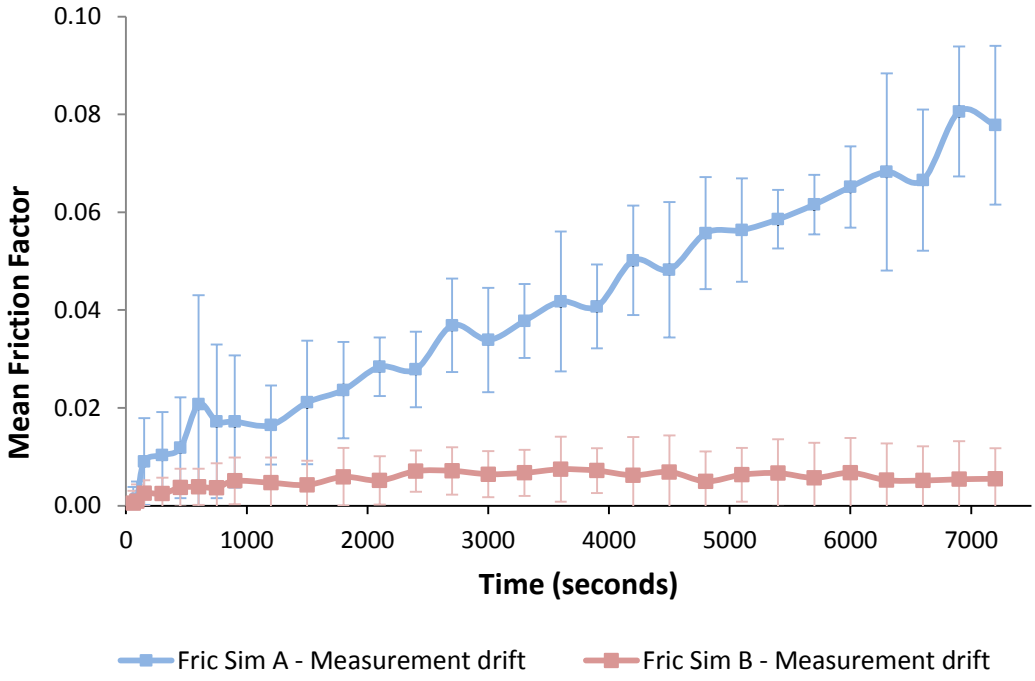

Figure 5.33: Mean drift (friction factor ± SD) for pendulum friction simulators A (n = 3) and Mk B (n = 3) calculated using a 28 MoP THR sample, 25 % serum and 25-800 N load ± 15° FE.

The calculated mean friction factor drift for each simulator was subtracted from the respective results from the hemiarthroplasty validation studies. For example, the mean drift values for simulator A were subtracted from the validation test results from simulator A (n = 5), and the drift values for simulator Mk B were subtracted from the further validation test results from simulator Mk B (n = 5). The 120 N SPL results from simulator Mk B (n = 3) were also included in the analysis. The mean friction factor using the drift-adjusted values was then calculated for the three study groups. Statistical analysis of the adjusted study results detected no significant differences (ANOVA, $p > 0.05$) in mean friction factor at the start or end of the test, or at the 20-minute time point (Figure 5.34).

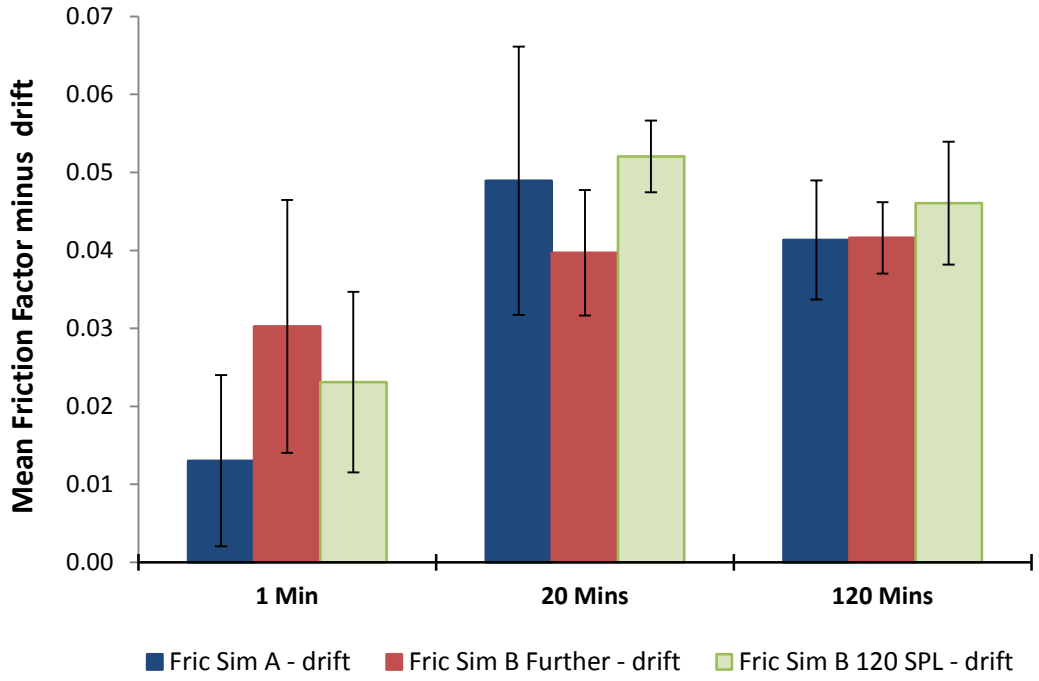

Figure 5.34: Mean friction factor with mean measurement drift subtracted ± SD for hemiarthroplasty studies conducted on pendulum friction simulator A (n = 5), further hemiarthroplasty studies conducted on pendulum friction simulator Mk B (n = 5), and hemiarthroplasty studies conducted on friction simulator Mk B with a 120 N swing phase load (n = 3).

A comparison of the non-adjusted results from the three studies (simulator A, simulator Mk B further and simulator Mk B 120 N SPL) with the drift-adjusted results from the same studies detected no significant difference (ANOVA, $p > 0.05$) in mean friction factor at the start of the test or at the 20-minute time point. The results were however, significantly different after two hours ($p = 0.00$) and the post hoc analysis revealed significant differences (Scheffé, $p = 0.00$) between the non-adjusted results from friction simulator A and all five other study group results (simulator A - drift, simulator Mk B further ± drift and simulator Mk B 120 N SPL ± drift).

5.7 Discussion

The main aim of this study was to validate pendulum friction simulator Mk B using biological tissue through *in vitro* hemiarthroplasty simulations. As in Chapter 4, this was done by conducting the same studies on pendulum friction simulator A and comparing the results. This section will therefore discuss the methodology used for the

in vitro hemiarthroplasty simulations, but focus on comparing the results from the studies conducted on the two simulators.

Pendulum friction simulator Mk B was designed for use with biological tissue, therefore, it was important that natural tissue samples were included in the validation process. This part of the validation process was completed using *in vitro* hemiarthroplasty simulations, which consisted of porcine acetabula and CoCr femoral heads. An overview of the sequence of events is shown in Figure 5.1. Prior to stating the validation study, a new test pot and potting method for the acetabulum was devised, which was validated using pendulum friction simulator A (due to simulator Mk B not having been validated at this stage). Initial validation testing (Section 5.5) was conducted concurrently with the THR initial validation study (Section 4.6), following a small modification to friction simulator Mk B. The capillary tubing was replaced on pendulum friction simulator Mk B, which constituted a major modification, to make the hydrostatic bearing more effective. This work has been described in Section 4.8, and following the further validation study using total hip bearings, the further validation study using hemiarthroplasties was then conducted (Section 5.6).

5.7.1 General Methods

Porcine acetabula were tested *in vitro* in pendulum friction simulators A and Mk B using a kinetic profile of 25 N to 800 N ± 15° FE for two hours. Additional frictional torque produced by the asymmetrical acetabulum was measured using a pre and post-test constant load, which was used to normalise the friction factor data. This methodology, which was developed by Lizhang (2010) and subsequently utilised by Taylor (2012) for a longer, medium term *in vitro* study, was considered to be sound. Acetabula were fixtured in a pot with 45° of inclination using PMMA bone cement to simulate the approximate orientation of the acetabulum *in vivo* (Vandenbussche *et al.*, 2007; Murtha *et al.*, 2008), before *in vitro* tribological testing in the friction simulators against a CoCr femoral head. The CoCr femoral was size-matched to the natural porcine femoral head using circular gauges, designed by the candidate for this study and subsequent complete natural hip joint simulations (Chapter 6). Using circular templates to measure the size of the femoral head is used clinically for patients requiring hip hemiarthroplasty procedures, usually following a fracture, where a prosthesis matching the size of the patients excised femoral head is implanted (Jeffery and Ong, 2000; Sharif and Parker,

2002; Athapattu *et al.*, 2013). This method, however, was slightly limited due to the femoral head not being a perfect sphere, meaning that the radial clearance of the CoCr head in the cranial-caudal direction would be slightly different to the dorsal-ventral direction. To control this extraneous variable, the size most closely matching the cranial-caudal dimensions of the porcine femoral head was used, as this corresponded to the FE direction of motion when placed in the simulator. Porcine hemiarthroplasty studies conducted by Zhang *et al.* (2010) in friction simulator A also selected metal femoral heads based on measurements taken in the anterior-posterior (i.e. FE) direction, however, in this study the dimensions were taken from acetabulum using vernier callipers. The internal dimensions of the natural porcine acetabulum varies at different locations due to its complex asymmetrical geometry, therefore, an erroneous measurement of the FE diameter using vernier callipers could result in an inappropriately size-matched head.

A 25 % (v/v) NBCS lubricant was used for all hemiarthroplasty testing throughout the studies, which provided an *in vitro* protein concentration similar to that of synovial fluid (Saari *et al.*, 1993). This lubricant has been used extensively by other researchers for tribological investigations of the hip joint (Scholes *et al.*, 2000; Müller *et al.*, 2004; Williams *et al.*, 2008; Flanagan *et al.*, 2010; Zhang *et al.*, 2010; Duong *et al.*, 2012; Lizhang *et al.*, 2013), and the rationale for using it in this hemiarthroplasty validation study was to simulate physiological biphasic lubrication mechanisms (Forster and Fisher, 1996; Caligaris and Ateshian, 2008; Ghosh *et al.*, 2014).

5.7.2 Development of New Acetabulum Pot and Potting Methodology

Mean friction factor results for hemiarthroplasty tests conducted using simulator A with the newly designed stainless steel acetabulum pot and inclinometer potting method were comparable to those observed when using the existing fixtures and methodology developed by Lizhang (2010). The new pot was designed to improve access and control over the acetabulum whilst positioning it in the PMMA cement, and to reduce the risk of impingement between the components during complete natural hip joint testing. The inclinometer potting methodology was developed to provide a more consistent and repeatable way of orientating the acetabulum, and to enable the degree of inclination and version to be varied, thus providing two additional independent variables that can be explored during future *in vitro* simulations. The use

of the new methodology was supported with less variability being observed in the mean friction factor results when compared to using existing methods, suggesting improved test re-test reliability.

5.7.3 Preliminary Hemiarthroplasty Testing in Friction Simulator Mk B

The first *in vitro* simulation experiments to test porcine acetabula with paired CoCr femoral heads were unsuccessful. This was due to the friction measuring carriage moving laterally towards the centre of mass, causing the head and acetabulum to separate when the oil flow to the hydrostatic bearing was activated. Two potential causal factors for this phenomenon (45° inclination angle and the offset centre of mass), were both explored and subsequently dismissed. No obvious movement was observed with the 36 mm Ø CoC control sample at 45° inclination *in situ*. This could be explained by the spherical artificial head and cup being more conforming than the aspherical porcine acetabulum with CoCr head bearing couple, which is less constrained. The offset centre of mass, arising from the position of the PMMA cement in the new stainless steel acetabulum pot, was investigated by activating the oil flow with the CoCr head disengaged from the porcine acetabulum. A very small amount of lateral movement of the frictionless carriage was still observed; probably due the oil pressure being too low to float the asymmetrically loaded hydrostatic bearing effectively, as this work was completed before new capillary tubing was fitted to the simulator to modify it.

Reducing the counterweight to remove the slightly negative force that was acting on the loading frame enabled hemiarthroplasty samples to be tested. Gravitational force and the mass of the loading arm appeared to be sufficient to maintain contact between the porcine acetabulum and CoCr femoral head prior to being actively loaded during the simulation.

5.7.4 Friction Factor

A nonlinear time response was observed as the increase in mean friction factor was initially quite rapid, before increasing more gradually during the later stages of the two-hour tests. A similar time-dependant frictional response has been reported in studies by Müller *et al.* (2004), Katta *et al.* (2007) and Taylor (2012), who investigated the tribology of articular cartilage from animal and/or human synovial joints. The increase in mean friction factor from 0.01 ± 0.01 to 0.12 ± 0.01 observed on friction simulator A

(n = 5) was similar to the mean friction observed by Lizhang *et al.* (2013) for hemiarthroplasty studies using the same kinetic profile, lubricant and simulator. In their study, with what was described as a large radial clearance of 1.2 to 1.75 mm, an increase in mean friction from 0.04 ± 0.02 to 0.12 ± 0.02 was reported during a two-hour test.

The initial validation study that was conducted on friction simulator Mk B (i.e. before the oil pressure of the hydrostatic bearing was rectified), produced results that were dissimilar in terms of both values and trend to those observed in friction simulator A. The mean results showed a very small increase in friction initially, which then gradually decreased over time, which is a response that does not appear to have been reported previously. The same methodology had been used for the studies conducted on simulators A and Mk B, therefore, it was feasible to hypothesise that one or more extraneous factors had confounded the results. A reasonable explanation was that the hydrostatic bearing had been unable to provide enough support to control the frictionless carriage under a dynamic load and motion profile with bearing couples *in situ* that were not fully congruent. This could have led to a small amount of migration of the spherical CoCr head away from the asymmetrical load-bearing articular surface of the acetabulum. This would explain why the friction initially increased and then decreased as the bearing surfaces separated. A small amount of displacement would not have been detected visually due to the bearing surfaces being covered by the translucent lubricant.

Mean friction factor for the further hemiarthroplasty study (n = 5), which was conducted on pendulum friction simulator Mk B after its modification by fitting new capillary tubing, increased from 0.03 ± 0.02 to 0.05 ± 0.00 (Figure 5.22). An initial rapid increase in mean friction factor was observed, which then plateaued approximately 25 minutes into the two-hour test. At this stage of the validation process, very similar friction factor results from tests conducted on simulators A and Mk B using THR samples had been observed (Section 4.10), however, the *in vitro* hemiarthroplasty results from simulator Mk B were not in agreement with those from simulator A, or with those reported by Lizhang *et al.* (2013) for large clearance tests. Interestingly, the same hemiarthroplasty study by Lizhang *et al.* (2013) investigating the effects of using different radial clearances and reported a negative correlation between clearance and mean friction, with a lower value of 0.08 ± 0.02 being observed after two hours of

testing with extra-large clearances (1.8-3.5 mm). Conversely, a positive correlation between clearance and friction was reported in an *in vitro* hemiarthroplasty study using porcine acetabula and CoCr femoral heads by Taylor (2012). Although the outcome of these results was different, they demonstrate how friction can vary with changes in radial clearance and contact area. The findings of these studies, however, did not explain the different results observed in the candidate's validation studies, as the same method was used to select the CoCr head for all of the hemiarthroplasty tests. Any slight variations in clearance arising from the complex geometry of the acetabula would therefore have been a factor for both sample groups.

The magnitude of change in mean friction factor over time (i.e. drift) when measured using an artificial THR sample (28 mm Ø MoP) tested with 25 N to 800 N ± 15° FE and a 25 % serum lubricant, was found to be greater in simulator A than in simulator Mk B (Figure 5.33). This measurement drift was then subtracted from the friction factor results of the hemiarthroplasty studies conducted on simulator A and on the modified simulator Mk B, and a similar trend over the two-hour test period was observed when the drift-adjusted mean friction factor values from the two simulators were compared (Figure 5.35). No significant differences in mean friction factor were detected at the start or end of the test, or at the arbitrary 20-minute time point (Figure 5.34).

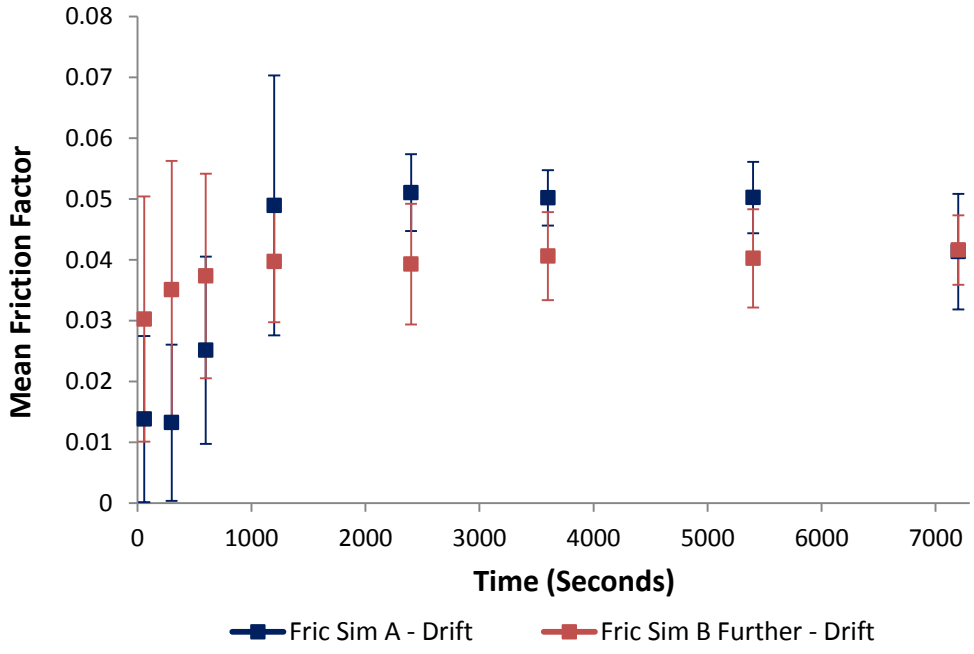

Figure 5.35: Drift-adjusted mean friction factor values ± CL for hemiarthroplasty samples tested in friction simulator A (n = 5) and friction simulator Mk B during the further validation study (n = 5). Values at the 1, 5, 10, 20, 40, 60, 90 and 120 minute time points have been plotted.

The friction factor of a MoP THR should remain relatively constant when measured at different times during a two-hour test, as any changes to the bearing surfaces (e.g. R_a) would not be expected under these test conditions. The charge amplifier, which amplifies and converts the electrical piezoelectric transducer signal to a voltage, would be expected to display a positive or negative linear change in output over time that is not caused by the input signal. In a calibrated system this undesired change, known as drift, should be relatively small, however, an increase in operating temperature has been identified as a possible cause of measurement drift in piezoelectric material (Gautschi, 2001). It is possible that the cooling fans in friction simulator Mk B, which are not fitted to simulator A, helped control the build-up of heat and, therefore, the magnitude of drift over the two-hour test period.

Increasing the SPL from 25 N to 120 N on friction simulator Mk B accelerated the rate of increase in friction factor at the start of the test, due to a more rapid exudation of fluid, but this did not affect the mean friction factor values. With the exception of the decrease in friction observed during the simulator Mk B initial validation tests, the time-dependant response that was observed during the two-hour hemiarthroplasty studies has been attributed to exudation of interstitial fluid from the articular cartilage. This causes a reduction in fluid load support with the applied load gradually being transferred to the solid phase, thus increasing the friction. The rate of increase in friction slows, before eventually plateauing, as more of the load is supported by the solid phase (Forster and Fisher, 1996; Mow and Wang, 1999; Katta *et al.*, 2007; Ateshian, 2009).

5.7.5 Surface Wear and Cartilage Deformation

The primary outcome measure for the validation of pendulum friction simulator Mk B was friction factor, with surface wear and cartilage deformation being used as additional outcome measures. Using a triangulation of methods, and therefore more than one variable to assess the outcome of the hemiarthroplasty validation study, provided a method of assessing the results whilst compensating for any weaknesses in the three methods.

The articular cartilage of the tested acetabula was macroscopically assessed, and any identifiable wear scars were graded using the Outerbridge Classification System and mapped on chart, which had been created by the candidate. There were no significant

differences in the frequency, grade, or location of the lesions when comparing specimens from simulator A (n = 5) to specimens from the further validation study on simulator Mk B (n = 5). The majority of wear in both sample groups was in the central region of the lunate surface; located predominantly at either side of the dorsal section of the triradiate cartilage were the ilium and ischium join. The triradiate cartilage in pigs fuses at 12-18 months (Dewey, 2006; König and Liebich, 2009), and therefore it is possible that, due to the acetabula being harvested from immature pigs approximately 6-months old, there was some displacement of the pelvic bones when the acetabulum was loaded in the simulator.

Surface deformation was measured using a high-resolution silicon replica of the tested acetabulum on a random sample of n = 3 specimens from both simulators. No significant difference in mean deformation volume was detected, however, statistically the mean depth of the wear area in the two sample groups was marginally significant ($p = 0.04$). However, given that the two other dependent variables measuring the wear scar (i.e. surface deformation volume and wear grade) were not significantly different, and there was a strong correlation between mean deformation volume and depth for the whole data set ($r^2 = 0.92$; n = 6), this result was not a major concern.

A number of different methods for assessing cartilage wear have been reported in the literature, making direct comparisons of the results to other studies difficult, however, cartilage deformation was measured using the methodology developed by Lizhang (2010) with good agreement between the results. Average deformation depth from the validation study was ∼29 µm (simulator A; n = 3) and ∼42 µm (simulator Mk B; n = 3), which are similar to the results reported by Lizhang (2010) in hemiarthroplasty studies with medium (∼29 µm; n = 3) and large (∼36 µm; n = 3) radial clearances. Results reported for deformation volume by the same author were more varied ranging from ∼3 mm^3 to ∼21 mm^3 for a number of different radial clearances ranging from 0.1 mm to 3.5 mm (Lizhang, 2010; Lizhang *et al.*, 2013), however, the results from the validation study fell within this range with values of ∼14 mm^3 and ∼20 mm^3 for simulators A and Mk B respectively.

A considerable difference in mean friction factor was observed for the two sample groups; however, the comparison between cartilage wear and deformation was acceptable, and in agreement with a similar study. Increased friction has been linked with greater cartilage wear (Mow and Wang, 1999; Katta *et al.*, 2007; McCann *et al.*,

2009; Taylor, 2012), however, this correlation was not observed in the hemiarthroplasty validation study where the higher friction factor observed from the sample group from simulator A was not reflected in the wear assessment. It is therefore feasible to attribute the larger, and more continuous increase in friction factor measured in simulator A to a measurement drift, rather than damage to the articular surface.

5.8 Conclusions

This conclusion will focus on the results of the hemiarthroplasty validation study presented in this chapter, however, reference to the conclusions from the validation studies conducted using THRs (Chapter 4) will be made to enable conclusions from the complete validation process for pendulum friction simulator Mk B to be drawn.

The results from *in vitro* hemiarthroplasty testing conducted on pendulum friction simulator A was used as control data, to which data from pendulum friction simulator Mk B was compared. The primary outcome measure was friction factor, which had been normalised to account for acetabula asymmetry and therefore any potential misalignment of the samples, and cartilage wear and surface deformation were used as secondary outcome measures. The experimental methodology and conditions were the same for both friction simulators; it is therefore possible to draw the following conclusions from the validation study:

- The new pot and inclinometer attachment provided a repeatable method of controlling the orientation of the acetabulum during potting.
- Modifications to the design of pendulum friction simulator Mk B, which entailed reducing the counterweight on the loading frame (Section 5.5.4.1) and replacing the capillary tubing to the hydrostatic bearing (Section 4.8), were required in order for hemiarthroplasty tests using porcine acetabula and CoCr femoral heads to be conducted successfully.
- The friction factor results from both simulators displayed a nonlinear time-dependant response, indicative of the load being transferred from the fluid phase to the solid phase.
- It is postulated that the larger increase in mean friction factor observed on friction simulator A was due to the larger magnitude of drift measured on simulator A compared to simulator Mk B.

- There was good agreement between the cartilage wear and surface deformation results from hemiarthroplasty specimens tested in simulator A and those tested in the modified simulator Mk B.
- Following the modifications made to pendulum friction simulator Mk B, the results of the validation studies conducted with THR bearings in Chapter 4 and the results of the hemiarthroplasty studies conducted in this chapter, it can be concluded that the null hypothesis set out in Section 4.6.5.1 can be retained under the following conditions:
    1. Short-duration tests (e.g. two minutes).
    2. Providing the results are corrected for drift with longer test durations. This is due to the existence of measurement drift of greater magnitude on pendulum friction simulator A compared to pendulum friction simulator Mk B, thus causing a discrepancy in friction factor results when running tests for a duration of two hours.
        - Simulator Mk B (f) = Simulator A (f) (time dependent)

Chapter 6 Development of a Complete Natural Hip Joint Simulation Model

6.1 Introduction

In the past, tribological investigations exploring the friction and wear between two contacting natural cartilage surfaces have been mainly limited to reciprocating motion friction studies with cylindrical bone and cartilage plugs. Tribological research using the more complex geometry of complete natural hip joints is limited and difficult to appraise due to the heterogeneous methodologies that have been used (Unsworth *et al.*, 1975; O'Kelly *et al.*, 1978; Furey and Burkhardt, 1997; Ferguson *et al.*, 2003; Katta *et al.*, 2008; Song *et al.*, 2012). Joint vulnerability as a causative factor for abnormal joint mechanics has been proposed as an underlying mechanism that adversely affects the tribology of the hip joint. Increased stress on the articular cartilage from abnormal loading may ultimately lead to mechanical failure and the development of OA, and joint vulnerability arising from abnormal morphology of the femoral head and/or acetabulum is a recognised aetiology in the development of hip OA (Harris, 1986; Felson, 2004; Mavcic *et al.*, 2004; Karachalios *et al.*, 2007). Morphologic information gained from the study of human hip geometry (SHIG) in Chapter 3 will be used to inform future tribological studies of the natural hip joint, using the *in vitro* simulation model developed in this chapter, in order to explore this theory.

Therefore, the aim of this chapter was to develop a novel complete hip joint *in vitro* simulation model that could be used for the tribological testing of natural porcine tissue. Additionally, the methods developed for this chapter aimed to provide a robust system for testing complete human hip joints in future tribological studies.

The chapter explains how the fixture design and methodology was developed to enable complete porcine hip joints (i.e. natural acetabulum and natural femoral head) to be tested using pendulum friction simulator Mk B. Test parameters and the methods used to analyse the experimental data from *in vitro* simulation tests conducted on the complete hip joint are also explained.

6.2 General Materials

Pendulum friction simulator Mk B (validated, as described in Chapters 4 and 5) was used for all tribological testing conducted in this chapter. As with the hemiarthroplasty

studies, *in vitro* testing of the complete natural joint was conducted using a 25 % bovine serum lubricant to simulate the protein content of synovial fluid and *in vivo* joint lubrication conditions (Section 5.2.1). Likewise, exposed articular cartilage on the acetabulum and the femoral head was kept hydrated using a PBS solution (Table 5.1) throughout the harvesting and sample preparation processes.

The acetabula and porcine femoral heads were secured in the required testing position using the same non-sterile PMMA bone cement used in the hemiarthroplasty study (Section 5.2.4).

Microset® silicon replicating compound (Section 5.2.5) was used to create accurate 3D replicas of the acetabula articular surfaces following *in vitro* testing in order to assess cartilage volume change and wear.

6.3 Development of Porcine Femoral Head Test Fixtures

6.3.1 Introduction

The acetabulum test pot used in the hemiarthroplasty study was designed by the candidate so that it could also be used for complete natural hip joint simulation studies in the same simulator (i.e. pendulum friction simulator Mk B), as stated in Section 5.2.7. *In vitro* testing of complete natural porcine hip joints had not been conducted prior to this study and therefore, new fixtures enabling the porcine femoral heads to be secured in the simulator and tested with natural acetabula were required.

The design process for the development of the fixtures was based on the British Standard BS 7000: Part 2, which outlines the different stages involved in product design from concept generation through to delivery and marketing (British Standards Institution, 2008). Although the intention was not to commercialise the fixtures designed for this study, BS 7000 provided a good management framework for the design process, enabling femoral head test fixtures to be produced that met the standards required for their intended use.

An overview of the design process used for the development of the fixtures is given in Figure 6.1. The performance requirements identified at the start of the process were used throughout, from the initial concept development stages through to the design specification and subsequent design solution.

It should be noted that the methodology for conducting complete hip joint *in vitro* simulations (Section 6.5) was developed concurrently during the fixture design process.

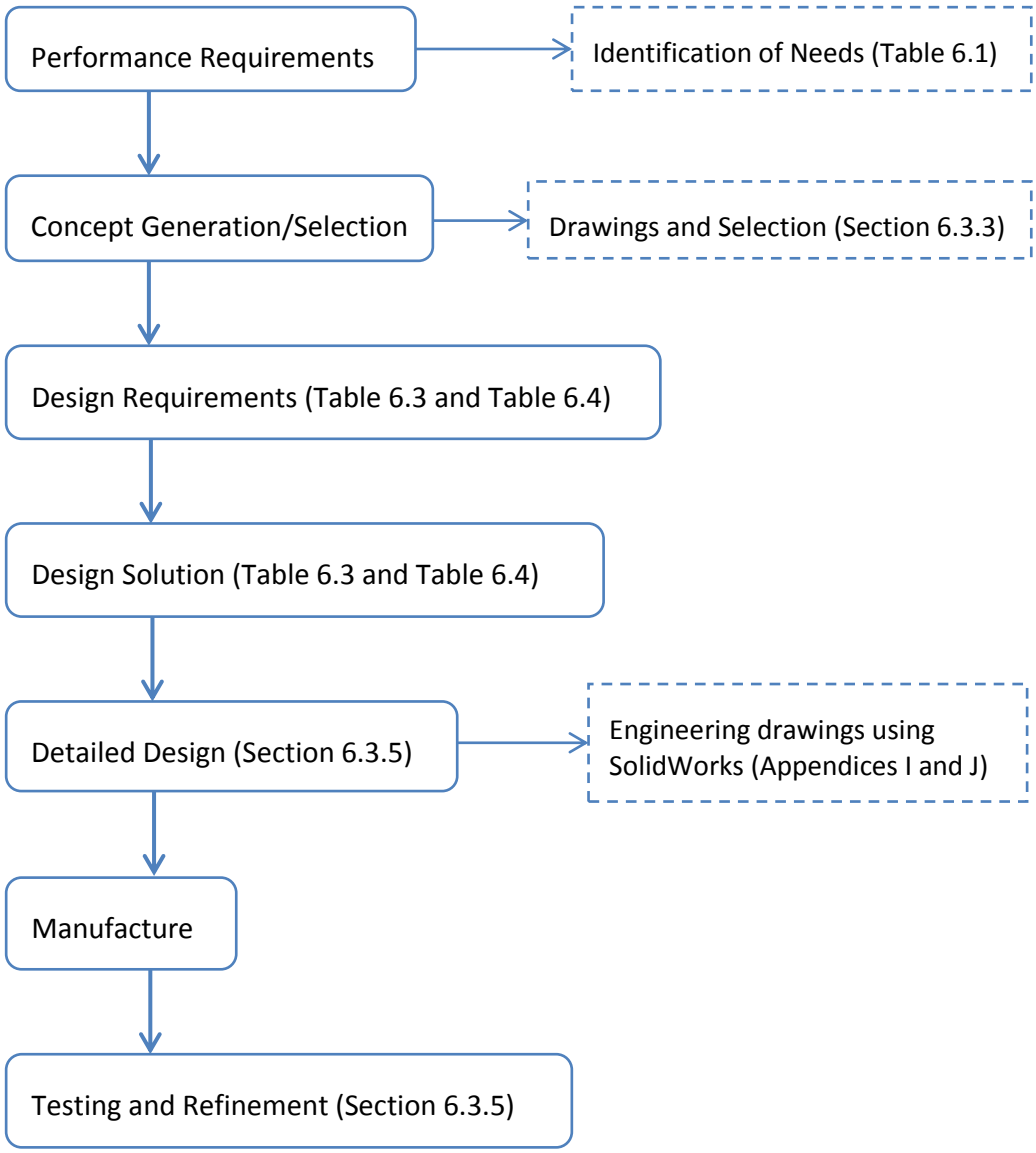

Figure 6.1: Flowchart of the design process for the porcine femoral head test fixtures.

6.3.2 Performance Requirements

The performance characteristics and requirements deemed necessary for the fixtures to function effectively were identified and listed, in no particular order, in Table 6.1. These requirements were then used for the concept development stage, which followed.

Table 6.1: Performance requirements and needs deemed essential for the development of the femoral head *in vitro* simulation fixtures.

Number	Performance Requirement/Need
1	Fixture must be able to accommodate different sized natural femoral heads
2	Sample can be held securely in an inverted position (i.e. withstand the effects of gravity) and without movement/loosening during testing
3	Test fixture fits on the FE rocker of pendulum friction simulator Mk B
4	Enough femoral head/neck is visible to test with ± 15° FE without risk of impingement
5	Specimen can be removed easily without causing damage
6	Able to withstand repeated use and fixturing in the simulator
7	Test fixture must not impinge on acetabulum pot
8	Sample can be fixed in place with the correct COR (i.e. 99.90 mm)
9	Femoral head can be secured in the correct anatomical orientation for testing
10	Resistant to permanent contamination (e.g. from animal tissue or bovine serum) and can be cleaned with disinfectant after use
11	Easy assembly of fixtures when preparing the sample for testing
12	Test fixture is easy to handle and fasten into the simulator
13	Able to centre the femoral head on the FE rocker so that it is aligned with the acetabulum (in the frictionless carriage)

6.3.2.1 Exploration of Porcine Proximal Femur Morphology

Performance requirements numbers 1, 2, 4, and 8 listed in Table 6.1, highlighted the need for the morphology of the porcine femora to be considered when designing the fixtures. There is very little information about this in the literature, therefore, a small exploratory study was undertaken to gain a better understanding of the geometry of the proximal aspect of the porcine femur.

The morphology of the proximal femur in quadruped animals differs to that of the bipedal human proximal femur. Compared to a human femur, the porcine femur has a more aspherical head, very short neck, larger neck shaft angle, smaller lesser trochanter, and much larger greater trochanter (Figure 6.2).

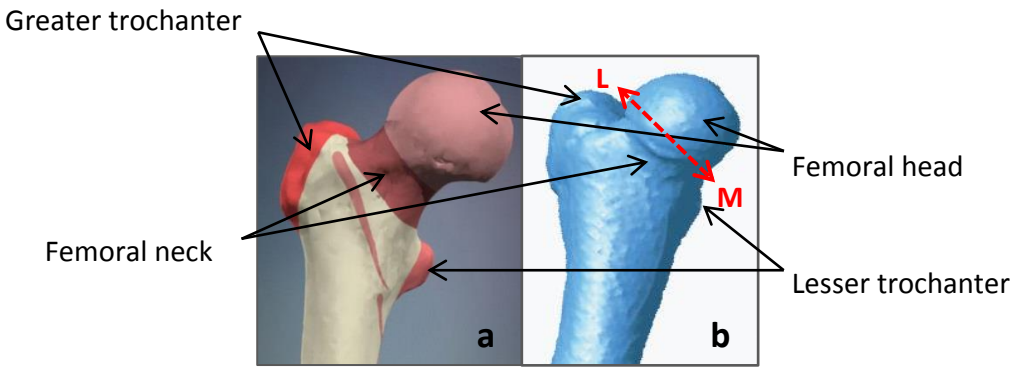

Figure 6.2: 3D computed tomography-derived reconstructions of the proximal femur (A) human (Primal Pictures, 2006) and porcine (B) (Lee *et al.*, 2008). Red dashed arrow indicates the medial (M) and lateral (L) dimensions.

The geometric information required for the design specifications was obtained by measuring the diametral range of femoral head, neck, and shaft sizes on a sample of donor pigs (n = 20), following the removal of the hemi-pelvis (Section 5.2.6). Measurements were taken from two orthogonal directions (medial-lateral [Figure 6.2] and cranial-caudal) using a vernier calliper, and approximated to the nearest millimetre (Table 6.2). All femoral shaft measurements were taken ~80 mm below the top of the femoral head. Femoral offset was estimated by measuring the horizontal distance from the centre of the femoral head to a notional line bisecting the femoral shaft (Lecerf *et al.*, 2009).

Table 6.2: Diametral and femoral offset measurements of proximal porcine femurs (n = 20) used when designing the porcine femoral head test fixtures. Results given as range and mean ± 95 % confidence interval.

Measurement	Direction	Range (mm)	Mean (mm) ± 95% CI
Femoral Head	Medial-lateral	33 – 39	36 ± 0.6
	Cranial-caudal	30 – 38	35 ± 0.8
Femoral Neck	Medial-lateral	32 – 37	34 ± 0.8
	Cranial-caudal	31 – 36	32 ± 0.6
Femora Shaft (~80 mm below top of head)	Medial-lateral	28 – 34	32 ± 0.8
	Cranial-caudal	29 – 35	33 ± 0.8
Femoral Offset	N/A	25 – 32	28 ± 1.3

During the same exploratory study, the spatial relationship between the femoral head and greater trochanter was also examined. The risk of the prominent greater trochanter impinging on the acetabulum test pot, or cement mantle surrounding the natural acetabulum, was considered high. This concern was substantiated when manually simulating the FE motion of a porcine femoral head articulating against a potted porcine acetabulum. Three options for trochanteric osteotomy prior to testing were considered (Figure 6.3). Option (b) was considered the better option as this removed the impinging trochanter whilst maintaining the integrity of the remaining part of the proximal femur, unlike option (a). Option (c) was considered an alternative if the femoral head and shaft needed to be vertically aligned without the medial distal end of the sample abutting against the side of the test pot.

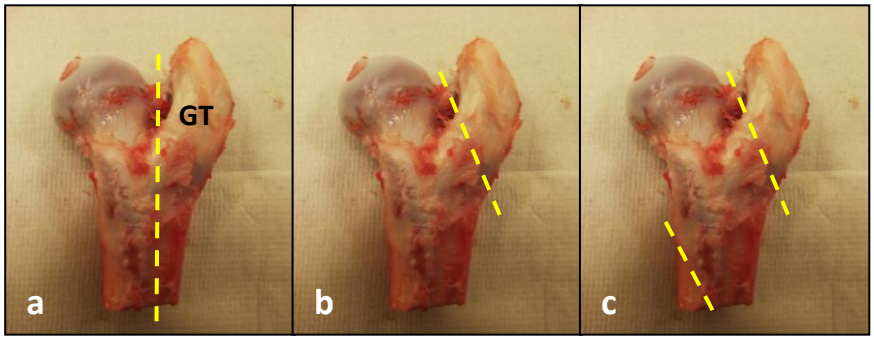

Figure 6.3: Proximal porcine femur illustrating different locations where bone (primarily greater trochanter [GT]) could be removed (yellow dotted lines) to reduce the risk of impingement during complete porcine hip joint simulation studies.

6.3.3 Concept Generation and Selection

The list of needs and performance requirements (Table 6.1) was reviewed before starting the concept generation process, and from this, it was concluded that a test fixture and a separate potting jig was required for the successful *in vitro* testing of natural femoral heads in the pendulum friction simulator. The rationale for having two separate fixtures was to enable samples with different geometries to be positioned and then secured in or on the test pot/fixture with the correct COR and orientation.

Concept designs were generated for both the test fixture, for securing the femoral head in place during the simulation, and the potting jig, to be used for positioning the sample in or on the test fixture. The fixture and jig designs were then rated against the performance requirements in order to select one from each group that satisfied these

criteria and had the potential to be developed further. The principal concept drawings considered for the test fixture and potting jig designs are contained in Appendix H.

The concept selected for the test fixture design was an offset pot (to accommodate femoral offset), which could be moved on a base plate to accommodate different shaft sizes/shapes/positions, and filled with PMMA cement to secure the sample in place (Figure 6.4 a). The concept selected for the potting jig was a modular design with interchangeable fixtures to position femoral heads of different sizes centrally and with the correct COR (Figure 6.4 b).

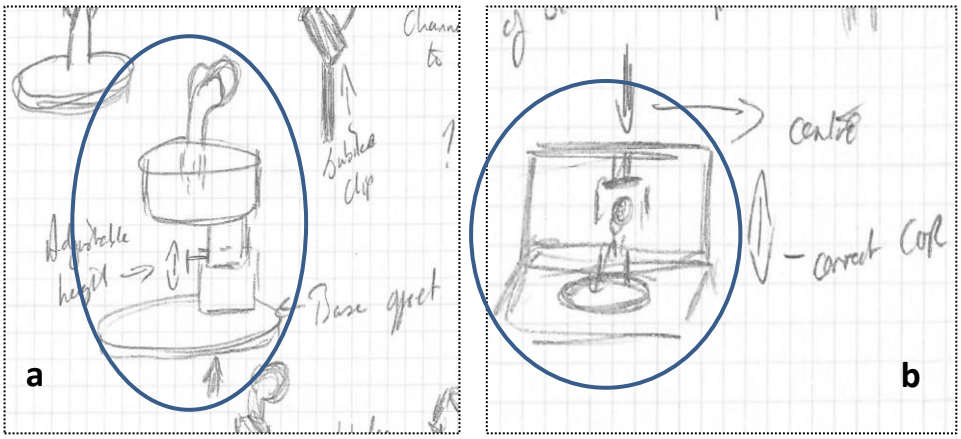

Figure 6.4: Concept drawings for (a) the test fixture and (b) the potting jig, selected for further development in the design process.

6.3.4 Design Requirements and Design Solution

Having selected the concepts, the design requirements and parameters deemed critical for a functional femoral head test pot and potting jig to be manufactured were defined together with the design solutions (Table 6.3 and Table 6.4). These were based on the performance requirements and needs (Table 6.1), the results of the exploratory study exploring proximal femoral geometry (Section 6.3.2.1), and evolving methodological development for sample preparation and testing.

Table 6.3: Design requirements and solutions for the femoral head test pot.

Feature	Requirement/Specification	Design Solution(s)
Dimensions	Wide enough and deep enough to accommodate different sized femoral shafts and enough PMMA cement for secure fixation of sample during testing	Manufacture with internal diameter of 55 mm and depth of 45 mm, based on largest shaft and head/neck Ø in the sample group n = 20 (Table 6.2)
	No Impingement of femur or femoral pot against acetabulum pot or cement mantle during FE motion	Keep height and width of pot to a minimum whilst maintaining secure sample fixation. (*Also - greater trochanter to be removed during sample preparation as in* Figure 6.3 *b*)
	Test post can be secured and centralised on the FE rocker of the simulator	Location of holes and central raise in base plate to correspond with those on the FE rocker of friction simulator MK B
Operation	Samples must be potted at the correct COR for friction simulator Mk B (i.e. 99.90 mm)	Overall height of test pot plus potted sample (to centre of femoral head) must not exceed the COR of the simulator
	Femoral head must be potted in the correct orientation	Test pot to be slightly offset and fitted to an adjustable base and top plate (with 2 degrees of freedom [DOF] in total), enabling a range of sample sizes to be tested (based on the mean offset of a sample of n = 20, Table 6.2)
	Femoral shaft to be potted centrally in test pot for stability	
	No movement of the cement mantle or sample during testing	Tapped holes (x 4), equispaced around test pot for anti-rotation grub screws to be fitted and screwed into PMMA cement
	Easy removal of tested specimen without damage	Tapped hole in base of test pot that can be used to dislodge the PMMA cement from the pot
Construction	Test pot is easy to handle and can be secured onto FE rocker in an inverted position	Manufacture base plate from stainless steel 303 for stable fixation onto FE rocker. Top plate and test pot to be manufactured from Delrin® to reduce the weight of the fixture. Delrin® is a rigid, fatigue resistant material that is moisture resistant (DuPont Engineering Polymers, 2001)
	Resistant to contamination and easy to clean with disinfectant after use with no degradation	
	Able to withstand repeated use and fixturing in the simulator	

Table 6.4: Design requirements and solutions for the femoral head potting jig.

Feature	Requirement/Specification	Design Solution(s)
Dimensions	Femoral head test pot fits onto jig and can be removed easily	Create recess centrally in base of fixture with the same dimensions as the base plate of the test pot. Place removable square pegs on either side of recess to prevent rotation of the base plate
	Test pot can be centred on jig with no movement/rotation	
Operation	Samples must be potted at the correct COR for friction simulator Mk B (i.e. 99.90 mm)	Design a hemisphere to enable samples to be potted with the correct COR. Have a range of sizes for various femoral head Ø based on Table 6.2. Attach hemispheres in vertical alignment on top bar of jig over the centre of the base recess
	Femoral head can be centred on FE rocker so that it is aligned with the acetabulum	
	Sample to be held in position until PMMA cement cures	Include a component to hold the sample in position during potting. Attach the holding component to a slotted side post so that the height and orientation of the sample can be adjusted. Component must be detachable so the sample can be removed from jig following cement curing
	Sample can be removed easily from jig after potting	
Construction	Easy assembly of fixture when preparing samples for testing	Design a modular based system made from stainless steel 303. Fasten components together with socket head cap screws for easy assembly and disassembly. Consider thumb screws to attach sample holding component
	Side posts and top bar able to maintain shape when holding component and hemisphere are attached to jig	
	Easy to clean with disinfectant after use with no degradation	

6.3.5 Detailed Design

Detailed designs and 3D models, based on the design solution, were created for the test pot fixture and potting jig using SolidWorks. The engineering drawings used to manufacture the fixtures are in Appendices I (test pot) and J (potting jig).

6.3.5.1 Femoral Head Test pot

SolidWorks schematics of the femoral head test pot assembly, which was designed in three parts, are shown in Figure 6.5:

1. Base plate

This backside of the base plate was used to fasten the test pot fixture onto the FE rocker of pendulum friction simulator Mk B, and was therefore designed with holes and dimensions to match those of the FE rocker. A full-length groove, running in the FE direction of motion (i.e. cranial-caudal anatomically) was cut into the upper surface of the base plate, along with two tapped holes, enabling the top plate to be moved and secured in the required position. Slots were created on the medial and lateral sides of the base plate to match the position of two locating pegs on the potting jig. The base plate was manufactured from stainless steel 303.

2. Top plate

The backside of the top plate was designed with a tongue that fitted into, and could slide back and forth along the groove in the top of the base plate. Slotted holes in the top plate (housing socket head cap screws) controlled the amount of sliding movement possible. A full-length groove was cut into the upper surface of the top plate, and this was orthogonal to the tongue and groove assembly beneath it allowing two DOF in total for the test pot. Two tapped holes were drilled into the upper surface for fixation of the test pot. The top plate was manufactured from Delrin®.

3. Test pot

The test pot, which was manufactured from a single piece of Delrin®, consisted of a pot with an external Ø of 65 mm (for the femoral head), that was offset by 6.5 mm from the centreline on a larger base (88 mm Ø). As annotated in Table 6.3, the offset and internal dimensions of the pot (i.e. 55 mm Ø x 45 mm) were based on the information gained from the exploratory study to assess various geometric parameters of the proximal porcine femur (Section 6.3.2.1).

The backside of the test pot base had a full-length tongue that fitted into, and could slide back and forth along the groove in the upper surface of the top plate. As with the top plate, slotted holes in the test pot base and socket head cap screws controlled the amount of sliding movement possible. Additional movement of the pot in this direction

meant that the fixture could accommodate natural variations in femoral offset across the sample set whilst maintaining central alignment of the femoral head. A tapped hole in the base of the pot, for easy removal of the specimen using a grub screw, and four circumferential holes around the pot for anti-rotation grub screws, were included in the design.

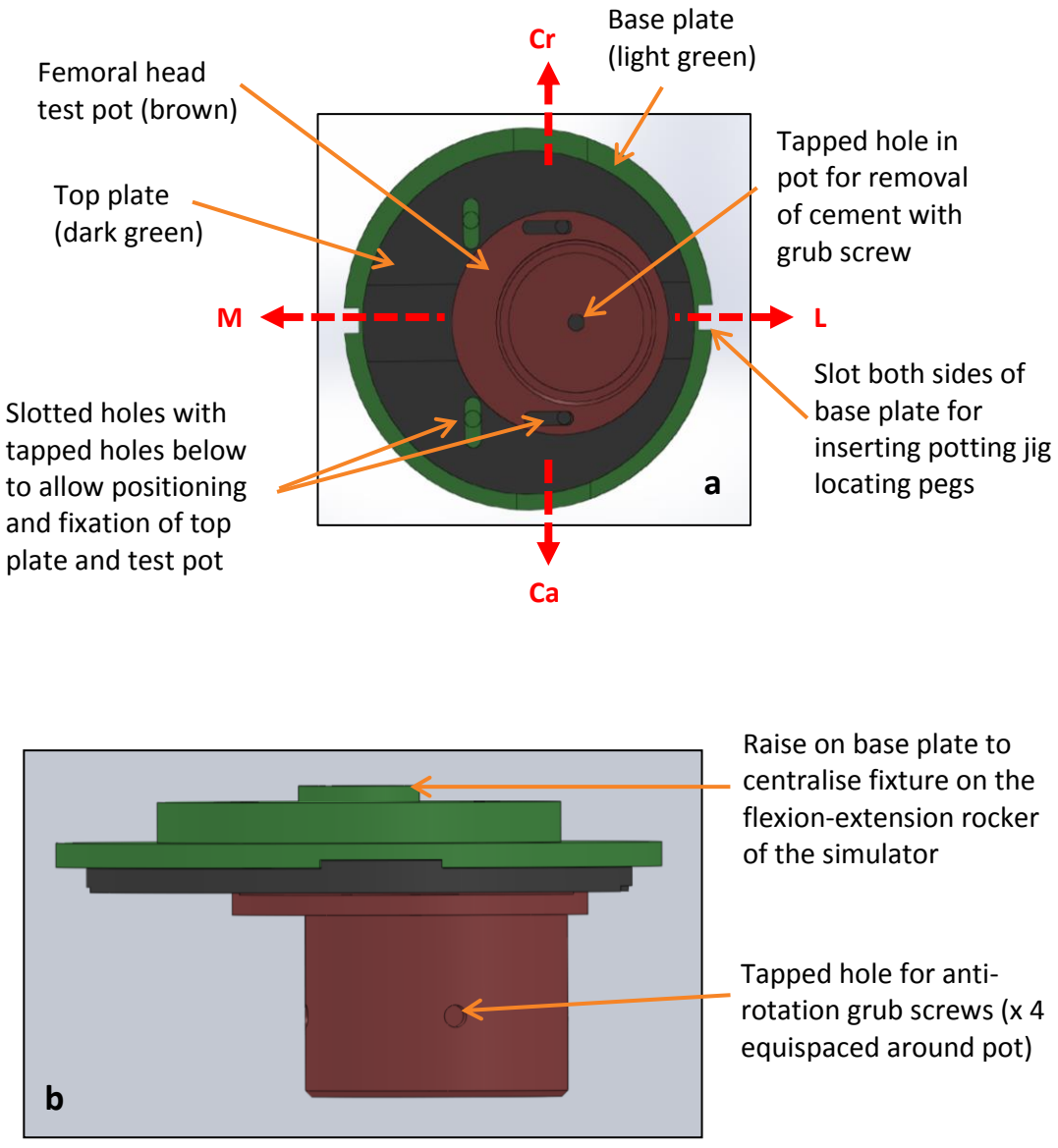

Figure 6.5: Porcine femoral head test pot assembly designed using SolidWorks viewed from (a) the top and (b) from the front in an inverted position, as it was when secured on the FE rocker of the simulator. Arrows indicate the medial-lateral (ML) and cranial-caudal (CrCa) directions the test pot was able to move in.

6.3.5.2 Femoral Head Potting Jig

The jig was designed to facilitate the potting of porcine proximal femurs with the femoral head orientated in the desired position, set to the correct COR (99.90 mm), and centred with respect to the FE rocker of the simulator. SolidWorks illustrations of the jig are shown in Figure 6.6 and details of the potting methodology developed for this study are in Sections 6.5.1 and 6.5.2. All components were manufactured from stainless steel 303.

The potting jig (Figure 6.6) consisted of three main sections:

1. The frame

A base, left and right base posts, and a top bar formed the frame to which the potting hemisphere and potting ring assembly were attached. One base post (right base post on Figure 6.6) was manufactured with a slot, running 60 mm longitudinally down the centre, for the attachment of the potting ring assembly. The recess, designed to centralise the base plate of the test pot fixture, was located in the base with two rectangular centralising pegs either side of it, which were designed to prevent rotation of the test pot. The distance from the top surface of the jig base to the upper, internal surface of the potting hemisphere was 99.90 mm (i.e. the COR of the simulator).

2. Potting ring assembly

This part of the fixture was designed to hold the sample in place during positioning and potting, and comprised of a base post attachment, arm, and potting ring (see Appendix J for details). The potting ring had six tapped holes equispaced around it, one to attach it to the arm and five to hold “pins”, which could be inserted into the sample at different angles to hold it firmly in place but without causing damage. The pins were manufactured from M6 threaded rods, finished with a cone point allowing penetration into the tissue. The ring assembly was designed to rotate in four directions to facilitate sample positioning, with adjustable movement being possible between the ring and the arm (inclination), and between the assembly attachment and the slotted base post (version).

3. Potting hemisphere

The potting hemisphere, which was attached to the top bar via a cylindrical block, was designed to position the femoral head with the COR at 99.90 mm and centre aligned on

the FE rocker. Six potting hemispheres were manufactured with radii of 17.0, 17.5, 18.0, 18.5, 19.0, and 19.5 mm, meaning that natural femoral heads with diameters of 35, 36, 37, 38, and 39 mm could be potted and subsequently tested *in vitro*. The centre of the hemisphere was vertically aligned with the centre of the recess in the potting fixture base.

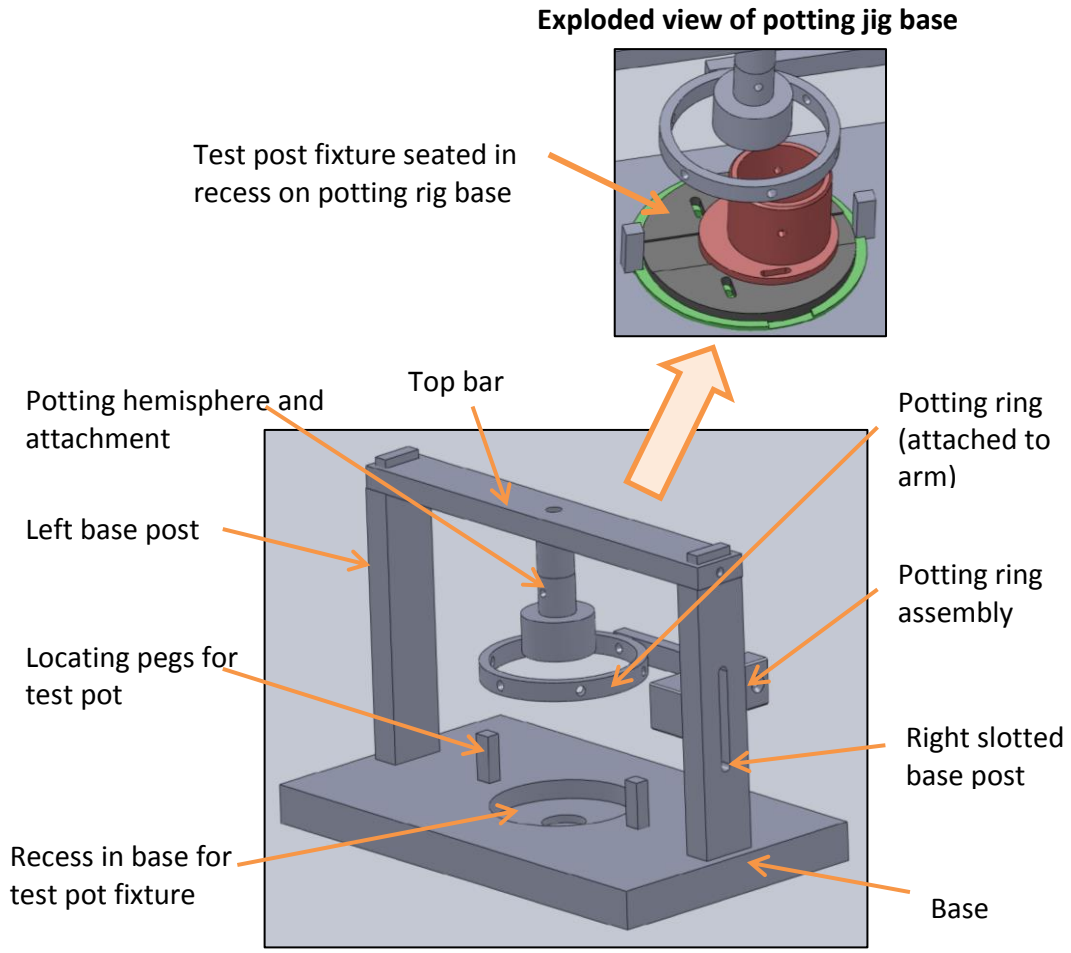

Figure 6.6: Femoral head potting jig designed using SolidWorks, shown without fasteners, including exploded view of the potting jig base with the test pot fixture *in situ*.

6.4 Harvesting Porcine Hip Joints

All porcine tissue used in this chapter was the same age and acquired from the same source as that used for the hemiarthroplasty tests in Chapter 5. Dissection was completed using a non-sterile scalpel blade and handle, the weight of the whole animal (as it appeared on the abattoir label) was used as part of the unique identification

number given to each specimen, and PBS-soaked tissue was used throughout the dissection to keep exposed areas of articular cartilage hydrated.

The harvesting procedure started by carefully removing the bulk of the muscle and extra-capsular soft tissues from around the hip joint to expose the joint capsule. The shaft of the femur was also exposed at this stage by removing the surrounding muscles and soft tissues (Figure 6.7 a). The hemi-pelvis was then removed and the acetabula were harvested using the method described in Section 5.2.6.

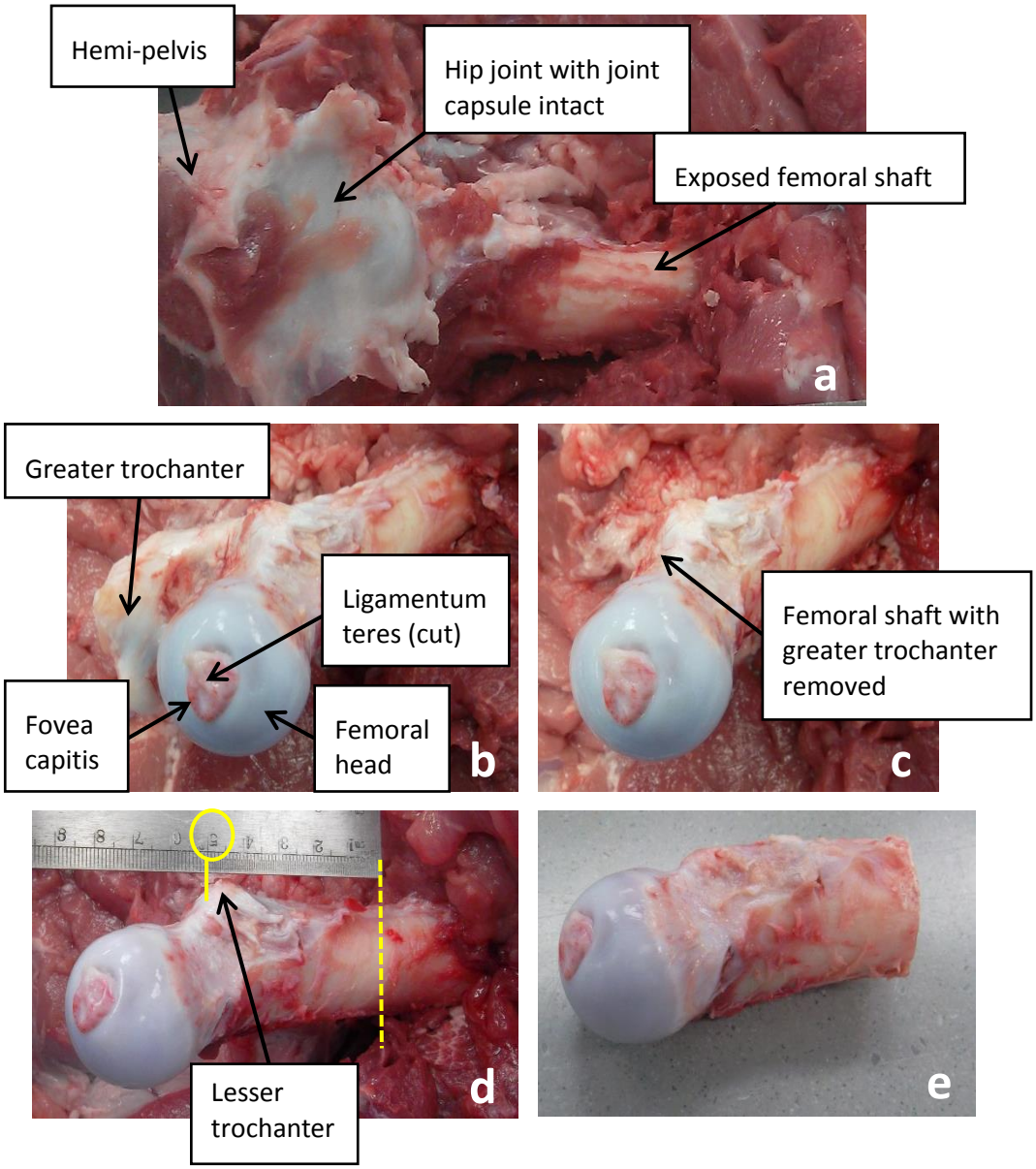

Figure 6.7: Harvesting of porcine femoral head: (a) right rear porcine leg with hemi-pelvis, joint capsule and femur exposed; (b) Proximal femur isolated from hemi-pelvis; (c) proximal femur with greater trochanter removed; (d) position of femoral osteotomy (yellow dotted line), 50 mm from lesser trochanter (yellow circle); (e) the harvested femoral head and proximal shaft of the femur.

Once the section of pelvis had been removed, the proximal aspect of the femur was mobilised by removing the remaining soft tissues surrounding it (Figure 6.7 b). The articulating surface of the femoral head was inspected and the specimen was discarded if there was any damage visible. An avulsion fracture of the fovea capitis was noted on a number of femoral heads. An avulsion fracture occurs when a small piece of bone that is attached to a tendon or ligament gets pulled away from the main part of the bone. In the porcine hip specimens from the abattoir, this was most likely due to excessive force applied to the ligamentum teres following slaughter. These specimens were always discarded as it was postulated that the rough edge around the fracture site would have increased the friction and wear in the joint, therefore confounding the results.

Osteotomy of the greater trochanter was performed (see Section 6.3.2.1), and this was done with the femur *in situ* to minimise handling of the specimen after it had been removed (Figure 6.7 c). The femoral head and proximal shaft was removed by performing a femoral osteotomy, using a hacksaw, approximately 50 mm below the lesser trochanter (Figure 6.7 d). The length of the shaft required on each specimen was derived from the depth of the pot, which was 45 mm (Table 6.3). A 50 mm shaft length meant that enough bone would be inside the pot for it to be securely fixed in place, and the head would be sufficiently clear of the top of the pot enabling articulation with the acetabulum in the simulator without risk of impingement. The harvested specimens were stored using the same method described in Section 5.2.6.

The articular surface of the femoral head was divided into four anatomical regions for reference purposes (Figure 6.8), with the cranial and caudal areas of the head corresponding with the cranial and caudal areas of the acetabulum (Figure 5.2).

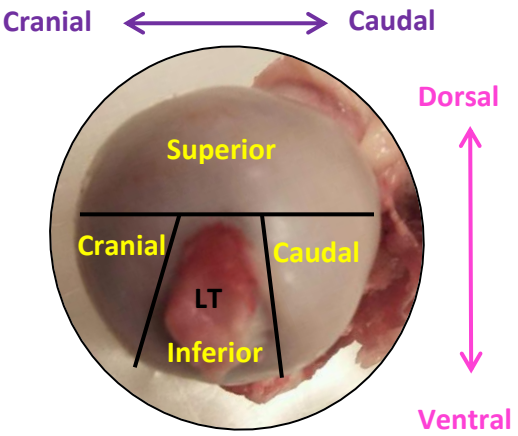

Figure 6.8: Right porcine femoral head showing the position of the ligamentum teres (LT) and location of the anatomical regions of the articular surface. Cranial–caudal (flexion–extension) and dorsal-ventral dimensions are also shown.

6.5 Methods

6.5.1 Porcine Acetabulum Sample Preparation

The diameter of the harvested porcine femoral head was measured using the PVC circular gauges and matched with a CoCr femoral head using the method described in Section 5.3.1.1. Extra care was taken to ensure that the articular surface was not damaged when using the gauges, as this could have affected the tribology of the joint. The acetabulum, harvested from the same porcine hip joint, was then potted using the equipment and methodology developed for the hemiarthroplasty *in vitro* simulation studies (Section 5.3.1.2).

6.5.2 Porcine Femoral Head Sample Preparation

The development of the methodology used for preparing and potting the natural femoral head for the *in vitro* simulations was synchronous with the design of the fixtures for the study, and evolved over the same period. This section describes the definitive method that was used in the study.

A reference circle, which matched the circumference of the acetabulum pot base, was drawn onto the base of the potting fixture using a permanent marker. This enabled consistent and repeatable positioning of the pot, centrally on the base. The centre of the reference circle corresponded with the centre of the fixture base. In order to apply

in vitro FE motion in the pendulum friction simulator, the hip joint needed to be aligned vertically in the sagittal plane. All articular surfaces were kept hydrated with PBS during the potting procedure.

Potting the porcine femoral head was a two-stage process. The first stage (Stage One) was to orientate and position the head in anatomical alignment with the matched acetabulum (Figure 6.9), and the second stage (Stage Two) involved setting the COR and securing it in the test pot with PMMA cement (Figure 6.10).

Stage One (Completed with the top bar of the potting jig removed)

- The potted acetabulum was placed onto the fixture base, within the reference circle, and held loosely in position using plasticine (Figure 6.9 a). Plasticine was used as this allowed the acetabulum pot to move if the femoral head started to push against the acetabulum as it was being positioned, thus reducing the risk of damaging the articular surfaces of the samples.

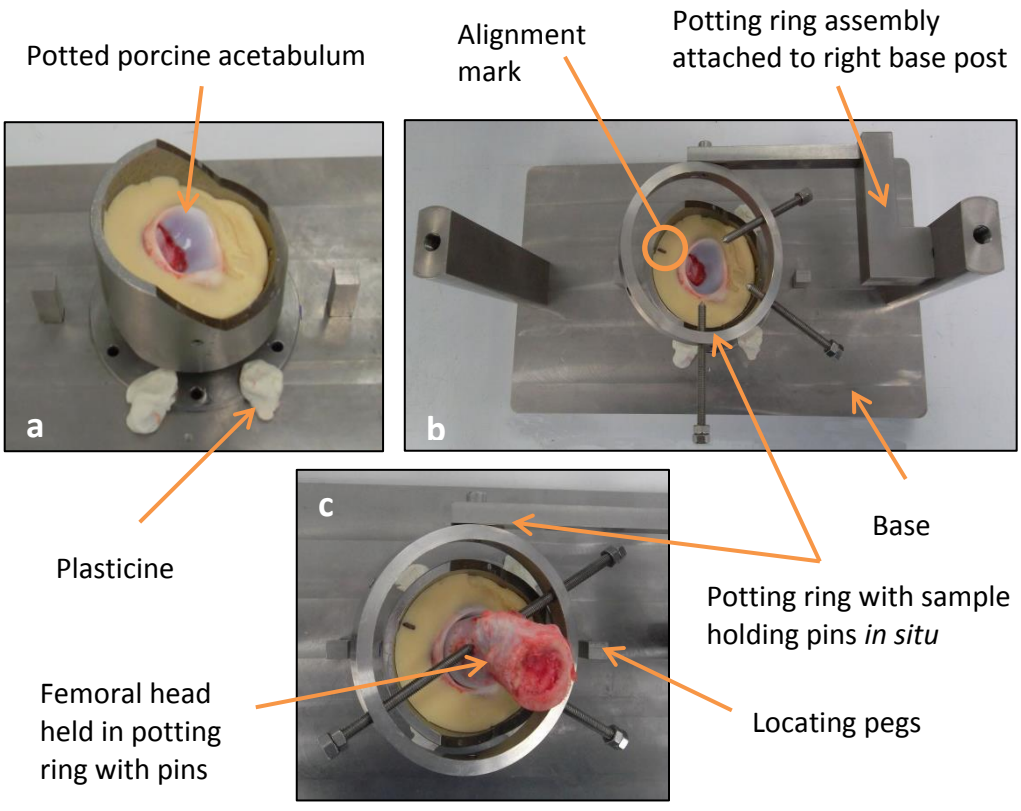

Figure 6.9: Potting Stage One – orientating and aligning the porcine femoral head with the matching potted porcine acetabulum using the femoral head potting jig. (a) positioning the potted porcine acetabulum centrally on the base; (b) attaching the potting ring assembly to the right base post (also showing position of fossa/TAL centre alignment mark); (c) porcine femoral head positioned in acetabulum and held in place using the holding pins.

- An alignment mark (Figure 6.9 b) was placed on the PMMA of the potted acetabulum in line with the midpoint of the TAL, as this was used as an anatomical reference point when orientating the femoral head. The potting ring assembly (including the pins) was attached to the slotted base post with the ring positioned approximately 10 mm above the acetabulum pot, and similarly inclined to the plane of the acetabulum and cement mantle (Figure 6.9 b).
- The harvested porcine proximal femur was then held firmly in the potting ring by screwing the cone points of the pins into the femoral neck/proximal femur. The potting ring was loosened at its attachment to the base post, and the femoral head was lowered into the potted acetabulum, taking care not to cause any damage the articular surfaces. The femoral head was then matched with the potted porcine acetabulum so the ligamentum teres/fovea capitis of the femoral head was aligned with the reference point (indicating the mid-point of the acetabular fossa/TAL), on the cement (Figure 6.9 c). This ensured that *in vitro*, the central superior aspect of the femoral head corresponded with the central area (roof) of the lunate surface, as it does *in vivo*. A thin layer of PBS in the acetabulum provided hydration between the two cartilage surfaces as the head was being positioned. The fixtures, including pins, were loosened and moved and/or re-positioned as required for each sample in order to achieve the optimum femoral head position.

Stage Two

- An inclinometer was used to measure any rotation that had been applied at the attachment between the ring assembly and the base post. The potting ring assembly, with proximal femur *in situ* and firmly positioned in the pins, was then removed. The potted acetabulum was replaced with the test pot fixture, which was fitted into the recess between the two locating pegs on the base of the potting jig (Figure 6.10 a).

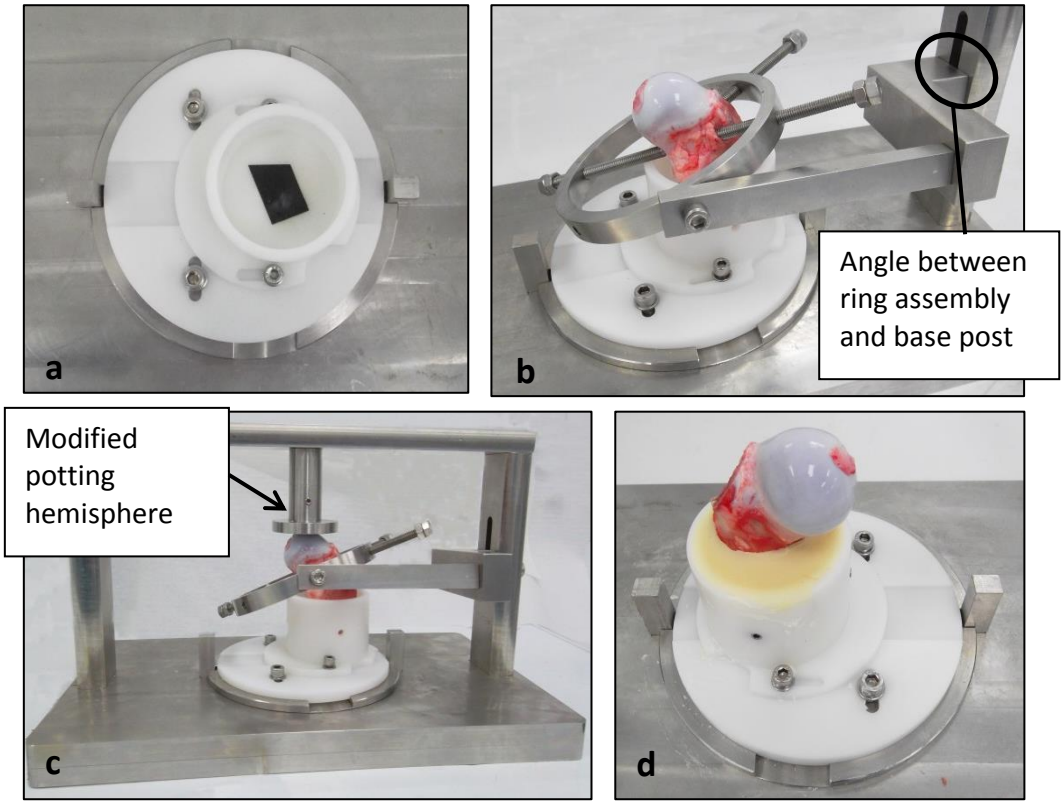

Figure 6.10: Potting Stage Two – setting the COR using the femoral head potting jig and securing the femoral head in the test pot with PMMA cement. (a) test pot *in situ* in recess on base with black tape protecting grub screw from PMMA; (b) Porcine femoral head correctly orientated and positioned centrally in test pot; (c) top bar attached and COR set; (d) porcine femoral head cemented in test pot.

- The potting ring assembly was re-attached to the base post, with the shaft of the femur in the test pot (Figure 6.10 b). Any angle between the ring assembly and post measured during the previous stage was reversed due to the sample and assembly having been rotated 180°.
- The top plate and test pot were adjusted and secured with the distal end of the shaft sitting centrally in the pot. Aligning the femoral head anatomically with the acetabulum meant that the proximal end of the shaft was not central in the pot, due to the femur being slightly angled.
- The COR of the femoral head was then fixed by placing the top bar onto the jig with a potting hemisphere of the correct size attached. The size matched the diameter of the head measured before potting the acetabulum (Section 6.5.1). The ring assembly was moved so the superior surface of the femoral head was just in contact with the flat surface of the potting hemisphere (Figure 6.10 c). Note that

the original hemisphere design had been modified, making it into a flat surface during the testing and refinement stage (see Section 6.5.3).

- Once the ring assembly had been clamped in place, the top bar was removed to prevent any prolonged and unnecessary contact between the articular surface of the head and the fixture. The sample was secured in the test pot by pouring in PMMA bone cement, mixed from a powder to liquid ratio of 70:35. The cement was allowed to fully cure before removing the potting ring (Figure 6.10 d), and test pot from the potting jig.

6.5.3 Testing and Refinement of Porcine Femoral Head Test Fixtures

As the methodology for potting the femoral heads was being developed, a problem was identified where the COR was found to be incorrect when the complete hip joint was fixtured into the simulator. The alignment rod would not pass through the FE rocker and friction measuring carriage, which meant that if the simulations had been run, inconsistent torque measurements due to experimental artefact would have been recorded (see Section 4.6.3.2).

To ascertain if the source of the problem was a deviation from the COR in the acetabulum or the femoral head, a CoCr femoral head was fixtured into the simulator with the potted acetabulum. The CoCr head was selected and set up to create the same experimental conditions reported previously for the hemiarthroplasty study (Section 5.3.1). The alignment rod passed through the two holes, confirming that the acetabulum was potted with the correct centre height. This was repeated on a small number of complete hip joint samples (n = 5), and each time, the COR for the acetabulum was found to be correct and the femoral head was observed to be at a height < 99.10 mm. This was deduced from the alignment hole of the FE rocker being above the height of the alignment rod with the complete joint *in situ*.

On investigation, the original design of the potting hemisphere was found to be unsuitable for porcine femoral heads due to the asymmetry of the non-articulating area of femoral head inferiorly, and the very short femoral neck. This meant that the femoral head was not being fully engaged in the hemisphere and therefore, the superior surface was not reaching the upper, internal surface of the fixture. The hemispheres were modified incrementally (Figure 6.11) by initially removing part of the wall, however some impingement of the head on the fixture was still observed. They

were then modified further by removing the entire exterior wall, leaving just the upper, internal surface. The final version (Figure 6.11 c), with just the flat upper surface, was the one used for the study (Section 6.5.2).

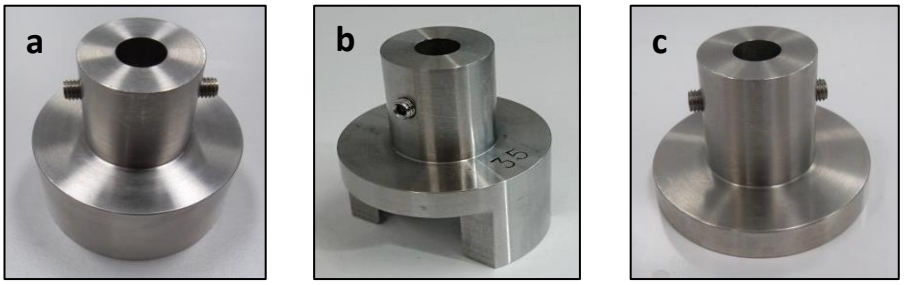

Figure 6.11: (a) Original potting hemisphere design, (b) first modification, and (c) the final version used in the study.

6.5.4 Test Conditions and Input Kinetics

The samples were secured in pendulum friction simulator Mk B in an anatomically inverted position, with the acetabulum in the friction measuring carriage and the head on the FE rocker. The acetabulum was filled with ~70-80 ml of 25 % serum, which was enough to cover the articular surfaces during the simulation. Electrical tape was used to prevent spillage of any serum from the pot as placing a small wall of cement around the pot to do this, which had been used in the hemiarthroplasty tests (Section 5.3.1.2), was deemed unsuitable for the complete natural hip joint study due to the risk of the impingement against the femur. The position of the samples in the simulator was checked using the alignment rod before each test, and the test was not conducted if this did not pass through the alignment holes as the validity of the results could not be assured due to the risk of experimental error. The *in vitro* experimental set-up in the simulator is shown in Figure 6.12.

Tribological testing of complete matched porcine hip joint samples (n = 5) was conducted under the same loading and motion conditions (tissue test profile), used previously in the hemiarthroplasty study (Section 5.3.2). To summarise, the *in vitro* simulation consisted of a two-hour dynamic load of 25 N to 800 N ± 15° FE motion (Figure 4.11), with a two-minute 800 N ± 15° FE constant load test before and after the cyclic dynamic load to account for any offset (see Section 5.4.1 for details).

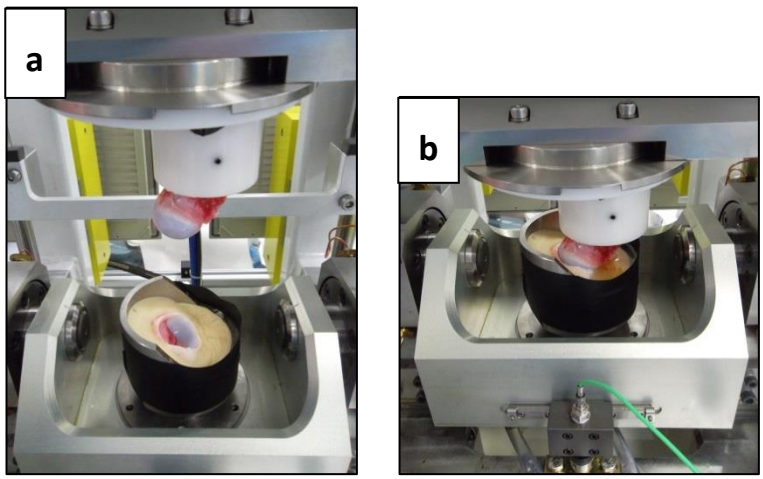

Figure 6.12: Complete porcine hip joint fixtured in pendulum friction simulator Mk B before testing. (a) potted porcine femoral head secured on FE rocker and potted acetabulum secured in frictionless carriage; (b) porcine femoral head and acetabulum coupled in simulator with 25 % bovine serum lubricant *in situ* before testing.

6.5.5 Classification of Wear and Surface Deformation Analysis

Tested acetabula and femoral heads were stored in the laboratory refrigerator in PBS-soaked tissue for a relaxation period of 24-hours before beginning any wear or surface deformation analyses. This allowed any non-permanent damage time to recover and replicated the surface analysis method used for the hemiarthroplasty tissue samples in Section 5.3.3. Using the same methodology enabled the surface wear and deformation results from the tested acetabula from the hemiarthroplasty study, and tested acetabula from the complete natural joint study to be compared.

6.5.5.1 Porcine Acetabula

Chondral lesions resulting from simulator testing, macroscopically visible on the tested porcine acetabula (n = 5), were classified using Outerbridge grades and recorded using the mapping system described in Section 5.3.3.1.

Microset® replicas of the acetabula were taken following Outerbridge grading, and 2D contacting profilometry measurements were taken from the replicas using the equipment and method described in Section 5.3.3.2 so that surface deformation could be assessed. The most obvious area of surface deformation was in the central region of the acetabulum, therefore as with the hemiarthroplasty study, nine parallel traces were taken across this area of the replicas (Figure 5.10). Talymap Gold software was used to

calculate the deformation area (mm^2) and maximum depth (mm) from the profilometry measurements for each tested acetabulum (n = 5), using the method explained in Section 5.4.2. Using this data, the surface deformation volume (mm^3) and mean depth (mm) of the wear scar on each acetabulum was calculated using Equation 5.3 and Equation 5.4 respectively.

6.5.5.2 Porcine Femoral Heads

Femoral heads were all macroscopically evaluated and Outerbridge classification grades were assigned to any chondral damage identified on the articular surface. A mapping system, similar to the one created for the acetabula, was used to report the grade, location, type and number of lesions identified on each tested femoral head (n = 5). The system, which like the acetabulum map was also a simplified version of a geographical zone chart developed by Ilizaliturri *et al.* (2008), divided the femoral head into cranial, caudal, superior, and inferior regions using the ligamentum teres/fovea capitis, as the anatomical landmark for the divisions (Figure 6.13). Ilizaliturri *et al.* (2008) also subdivided the superior region into nine areas for reporting femoral head defects during hip arthroscopy; however, this level of refinement would have been difficult to achieve with smaller asymmetrical porcine heads, and this level of detail was not necessary for this non-clinical study.

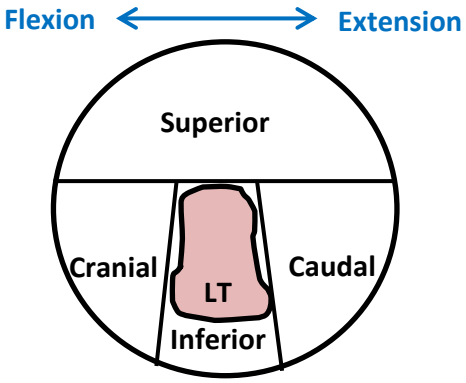

Figure 6.13: Mapping chart used to record the location, type, grade, and number of lesions identified on tested porcine femoral heads with the direction of FE motion displayed for reference (blue arrow). LT = ligamentum teres.

6.5.6 Analysis of Friction Factor

The friction factor data logged in pendulum friction simulator Mk B following each test was processed using the method described for the hemiarthroplasty study in Section

5.4.3. Once processed, statistical analysis of the data was also performed using the method adapted for the hemiarthroplasty study (Section 5.4.3), so that the results from the two studies could be compared. The results were not normalised for drift of the transducer/charge amplifier, and the data is presented to two decimal places as mean values with 95 % confidence limits (CL). Using the results from the study reported in Section 5.6.3.2 to explore drift, the mean magnitude of drift calculated over the two-hour test period on pendulum friction simulator Mk B was 0.005 ± 0.002. A drift value of this magnitude was thought to be negligible for this study of complete porcine hip joints when taking into consideration natural variations arising from using tissue samples with complex and heterogeneous geometry.

6.6 Results

Results following the tribological testing of complete porcine hip joints (n = 5) have been reported and discussed in this chapter. The *in vitro* hemiarthroplasty study and complete natural hip joint study results have been compared and discussed in Chapter 7. A very small amount (∼5 mm) of medial-lateral translation of the friction measuring carriage was observed towards the end range of FE motion (i.e. at ∼10-15° flexion and ∼10-15° extension) during all the complete hip joint *in vitro* simulations, probably due to the asymmetric geometry. A small amount of blood seeped into the joint space, mixing with the 25 % serum, over the two-hour period during all tests. This had also been observed with the hemiarthroplasty study but to a lesser extent.

6.6.1 Friction Factor

Friction factor continued to increase throughout the two-hour test period in all of the complete porcine hip joint (CpH) samples included in this study (n = 5). Overall, a more rapid increase in friction factor was observed over the first 15-20 minutes (900 to 1,200 cycles) of each test compared to the remainder of the test; however, a very small transient drop in friction was recorded after ∼2-3 minutes for all samples except CpH 1 (Figure 6.14). The initial transient change was particularly evident in sample CpH 5, where the friction factor decreased from ≈ 0.02 to ≈ 0.01 at 150 cycles before returning to ≈ 0.02.

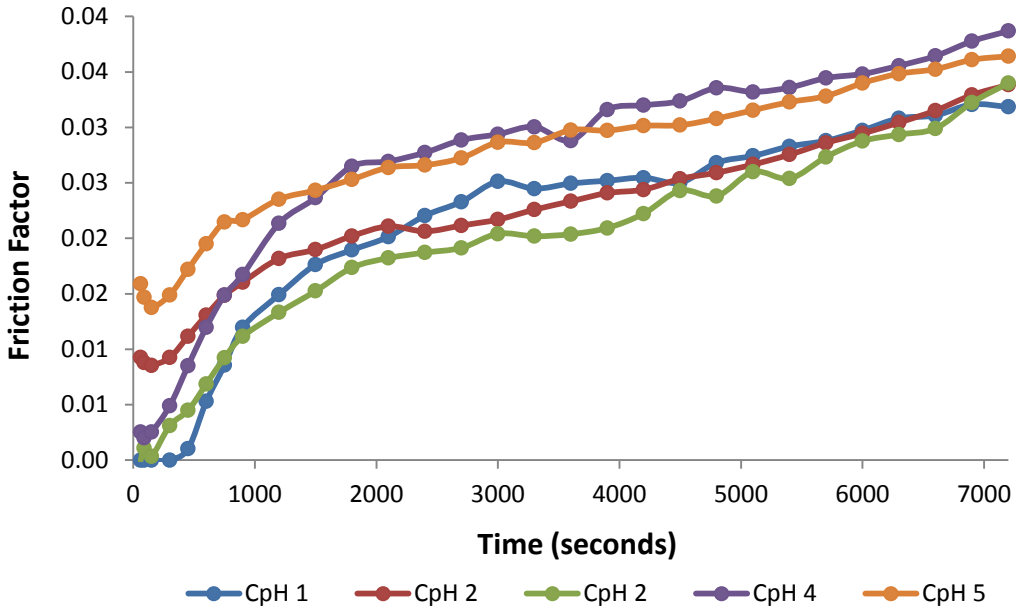

Figure 6.14: Friction factor of complete porcine hip joint (CpH) samples (n = 5) tested in pendulum friction simulator Mk B for two-hours.

Mean friction factor increased from a value of ≈ 0.00 ± 0.01 at the start of the study (recorded at 1 minute), to a value of ≈ 0.02 ± 0.01 after 20 minutes. The increase in friction was more gradual over the remaining 100 minutes (i.e. 6000 cycles) of the simulation, reaching a mean value of ≈ 0.03 ± 0.00 after two-hours (Figure 6.15).

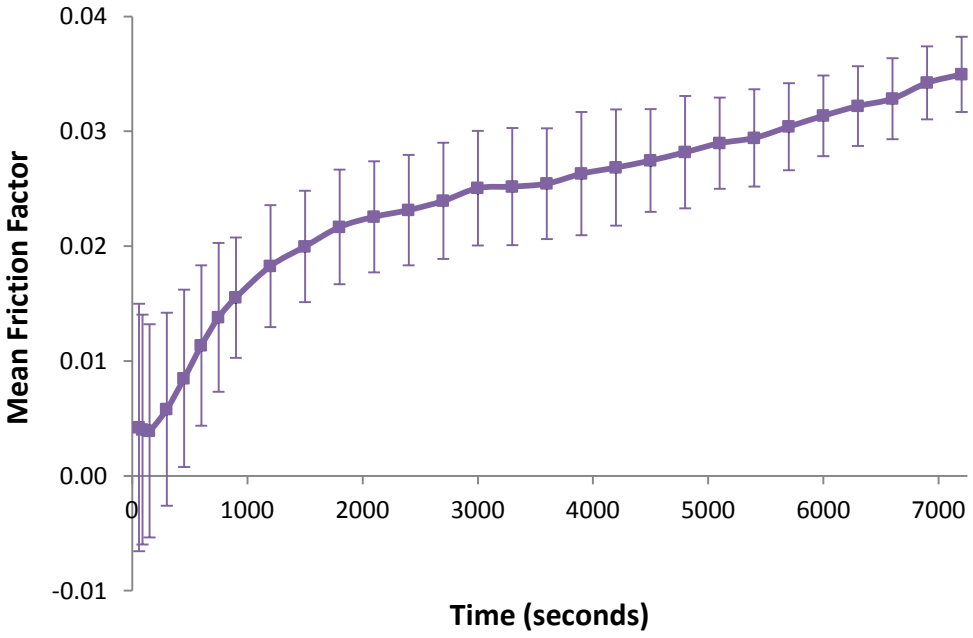

Figure 6.15: Mean friction factor ± 95 % CL for complete porcine hip joint samples (n = 5) tested in pendulum friction simulator Mk B for two-hours.

Mean friction factor over the whole test was ≈ 0.02 ± 0.00. The mean friction factor was more variable, and therefore had larger confidence limits, at the start compared to the end of the simulation, which is also evident in Figure 6.14 where the individual sample plots are initially wider apart.

The natural hip joint undergoes elastic deformation of the cartilage surfaces both *in vivo* and *in vitro* during the simulation, which affects the lubrication fluid film thickness. Porcine hip joints are not hemispherical and the exact radii of the bearing surfaces, and therefore radial clearance of the joints were not measured in this study, nor was the surface roughness of the cartilage. Taking all of these factors into consideration, a theoretical analysis of the predicted lubricating regime was not conducted. However, based on friction factor results illustrated in Figure 6.15 and the Stribeck diagram in Figure 1.11, it is reasonable to hypothesise that the joints started under a fluid film lubricating regime moving towards mixed or boundary lubricating conditions as the tests progressed.

6.6.2 Wear Analysis

Chondral lesions observed on the femoral heads and acetabula of the porcine hip joints following *in vitro* testing in pendulum friction simulator Mk B were described as either 1) roughening and/or cartilage discolouration; 2) scratches or 3) partial thickness defect. Surface damage that spanned across a boundary was logged in both regions, and any scratches that were located immediately adjacent and parallel to each other were classified as one lesion to ensure consistency with the method used for the hemiarthroplasty study (Section 5.6.2.1). Examples of wear identified during the macroscopic evaluation of the articular surfaces of the tested specimens are shown in Figure 6.16.

The total number of lesions graded using the Outerbridge classification system on the femoral heads and acetabula was n = 13 and n = 15 respectively. The majority were Grade 1 lesions, with a small number of Grade 2 lesions observed superiorly on the femoral head (n = 1) and centrally on the acetabula (n = 2). The number, grade, and location of chondral lesions identified on the tested acetabula are presented in Table 6.5, and the number, grade, and location of chondral lesions identified on the tested femoral heads are presented in Table 6.6.

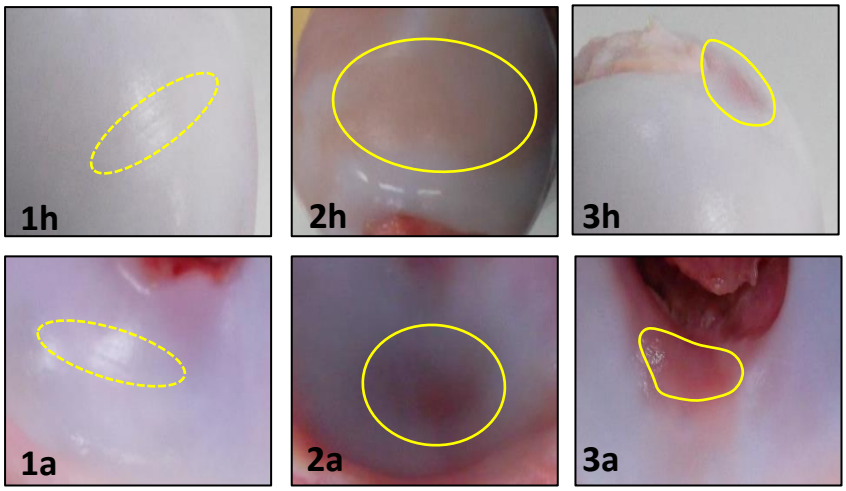

Figure 6.16: Examples of chondral damage observed on porcine femoral heads (h) and acetabula (a) following in vitro testing of complete porcine hip joints in pendulum friction simulator Mk B. The three types of lesion (in yellow circles) were: 1) scratches; 2) discolouration/roughening; 3) partial thickness defect.

The majority of lesions were identified superiorly on the head (54 %) and centrally on the acetabulum (46 %), with all specimens having evidence of wear in these regions. Wear was also observed caudally and cranially, with the number of identifiable caudal lesions being greater than the number of lesions observed cranially on both the acetabula (Table 6.5) and the heads (Table 6.6). Scratches were the main type of damage observed on the acetabula with discolouration and roughening of the articular cartilage being observed most frequently on the femoral heads. No Grade 3 lesions were identified on any of the specimens

Table 6.5: Location and grade of chondral lesions (total n = 15) identified on the acetabula following complete porcine hip joint simulation tests (n = 5) in pendulum friction simulator Mk B. The table shows the number of lesions identified on the acetabulum of each tested specimen (CpH 1–5).

	Caudal	Central	Cranial	
	Grade 1 (Acetabulum)			Total Grade 1
CpH 1	1	1	1	**3**
CpH 2	1	1	1	**3**
CpH 3	1	1	1	**3**
CpH 4	1	1	-	**2**
CpH 5	1	1	-	**2**
Total	**5**	**5**	**3**	**13**
	Grade 2 (Acetabulum)			Total Grade 2
CpH 1	-	-	-	**0**
CpH 2	-	-	-	**0**
CpH 3	-	-	-	**0**
CpH 4	-	1	-	**1**
CpH 5	-	1	-	**1**
Total	**0**	**2**	**0**	**2**

Table 6.6: Location and grade of chondral lesions (total n = 13) identified on the femoral heads following complete porcine hip joint simulation tests (n = 5) in pendulum friction simulator Mk B. The table shows the number of lesions identified on the femoral head of each tested specimen (CpH 1–5).

	Caudal	Superior	Inferior	Cranial	
	Grade 1 (Femoral Head)				Total Grade 1
CpH 1	1	2	-	-	**3**
CpH 2	1	1	-	1	**3**
CpH 3	-	1	-	-	**1**
CpH 4	1	1	-	-	**2**
CpH 5	1	1	-	1	**3**
Total	**4**	**6**	**0**	2	**12**
	Grade 2 (Femoral Head)				Total Grade 2
CpH 1	-	-	-	-	**0**
CpH 2	-	-	-	-	**0**
CpH 3	-	-	-	-	**0**
CpH 4	-	1	-	-	**1**
CpH 5	-	1	-	-	**0**
Total	**0**	**2**	**0**	**0**	**1**

6.6.3 Acetabular Cartilage Deformation

Cartilage deformation from the wear scars on all of the tested acetabula from the complete porcine hip joint in vitro simulations (n = 5) was assessed using Microset® replicas and 2D contacting profilometry with Talymap Gold software. The mean deformation volume and depth (± 95 % CI) calculated from these measurements was 7.04 ± 1.64 mm^3 and 14.44 ± 3.47 μm respectively.

6.7 Discussion

Historical studies reporting friction and lubrication regimes following tribological testing of human natural hip joints have been reported in the literature. These include studies by Unsworth *et al.* (1975), O'Kelly *et al.* (1978), and Roberts *et al.* (1982), who used a pendulum machine to explore the effects of impact and dynamic loading, with a mixture of synovial fluid and synthetic lubricants. However, there is very little information presented about the alignment of the femoral head, relative to the acetabulum, which makes this work difficult to repeat and critique in terms of the experimental methodology. More recently, Ferguson *et al.* (2003) and Song *et al.* (2012) have investigated the tribology of the hip joint and function of the acetabular labrum using *in vitro* testing of human hip specimens, however, both authors used a servo hydraulic testing machine to apply loads with no motion.

The main aim of this study was to develop a method of conducting *in vitro* tribological simulations on complete natural porcine hip joints using pendulum friction simulator Mk B. The following sections will discuss the methodological development, including fixture design, and the results of the study.

6.7.1 Methodological Development

Natural porcine acetabula had been tested *in vitro* in pendulum friction simulators A and Mk B (Chapter 5); however, complete natural hip joints had not been previously tested, meaning that simulator fixtures for the natural femoral head and the experimental methodology for testing them needed to be developed. The main requirements for the simulation model were focussed on the need to fixture the hip joint with the correct COR and anatomical orientation into the simulator, and the capability of the fixtures and methodology to accommodate the complex and varying geometry of porcine hip joints. Adapting the management framework outlined in BS

7000: Part 2, which is used for product development in industry, provided a logical and methodical approach to the fixture design process (Figure 6.1).

The performance requirements determined as being necessary for an effective product and experimental method to be designed, highlighted the need to design a test pot and separate potting jig. Concepts were generated and selected for both parts of the femoral head test fixture. The concept chosen for the development of the test pot was based on its ability to hold the sample securely throughout the simulation, without risk of impingement during FE motion, and the concept for the potting jig fixture was chosen based on its potential to position femoral heads with different diameters at the correct centre height. The initial stages of the design process, including the exploration of proximal porcine femoral geometry, provided the information required for a successful design solution and subsequent detailed design to be developed of for both parts of the fixture.

A risk of impingement from the greater trochanter was identified during the initial method development stage, and therefore the candidate decided to perform a trochanteric osteotomy during the harvesting procedure (Section 6.3.2.1). The risk of impingement was considered sufficiently high to outweigh the potential for any experimental error that may be introduced due to this structure being removed. The greater trochanter is considered a non-weight bearing structure in quadrupeds (König and Liebich, 2009), and therefore it is feasible to assume that this structure is not part of the principal compressive group of trabeculae in the proximal femur (Jang and Kim, 2008). Therefore, the mechanical properties of the femoral head, neck and proximal shaft, with respect to its ability to withstand compressive forces from axial loading during the simulation, should be unaffected by the osteotomy (Garden, 1961).

The femoral head test pot fixture was designed so that it could be moved in two orthogonal directions, facilitating central positioning of the femoral shaft within the PMMA cement mantle to give maximum stability during the simulation (Section 6.3.5.1). This design feature was essential to accommodate the heterogeneous proximal femoral geometry and consequential variations in anatomical alignment of the head and acetabulum. An adjustable height feature was not included in the final test pot design, despite being part of the selected concept design (Figure 6.4), as any vertical displacement in height occurring during the simulation through the application of an axial load, would have changed the COR of the femoral head.

Modifying the original design of potting hemisphere by reducing it to a flattened surface (Section 6.5.3) did not adversely affect the positioning of the femoral head. Locating the head centrally in the simulator was achieved by anatomically aligning the head with the potted acetabulum, whilst the acetabulum was seated centrally on the base of the potting jig. This method also enabled the asymmetrical, but conforming articular surfaces of the convex femoral head and concave acetabulum to be orientated in their natural position.

6.7.2 Friction Factor

Complete porcine natural hip joints (n = 5) were tested *in vitro* in pendulum friction simulator Mk B for a period of two-hours, with a 25 % serum lubricant and the same kinetic profile of 25 N to 800 N ± 15° FE that had been used in the hemiarthroplasty study. The method of normalising the data to account for any additional frictional torque arising from the asymmetrical geometry or misalignment of the samples was also the same as that used in the hemiarthroplasty study (Section 5.3.2). It was recognised that testing samples that were both aspherical, as opposed to the aspherical porcine acetabulum and spherical CoCr head in the hemiarthroplasty study, may have given rise to additional biomechanical torque (i.e. not related to friction associated with the loading or FE motion), that was not accounted for by this method. As reported in Section 6.6.1, only small amounts of medial-lateral translation of the friction measuring carriage was observed (~5 mm), and this was towards the end of FE motion. It was therefore assumed that it was frictional torque that was being measured and that the method used to account for the asymmetrical geometries was satisfactory. If appropriate, this could be investigated further in future studies, possibly by rotating the samples by 180°, or by using a multi-axis simulator that is able to apply a physiological motion rather than just FE. In this study, friction factor increased rapidly at first before increasing at a more gradual rate throughout the test period, with a mean value of ≈ 0.03 ± 0.00 after two-hours (Figure 6.15). The overall mean for the whole two-hour test was ≈ 0.02 ± 0.00. Friction values ranging from 0.003 to 0.08 have been reported following *in vitro* cartilage-on-cartilage tribological studies (Unsworth *et al.*, 1975; Roberts *et al.*, 1982; Macirowski *et al.*, 1994; Forster and Fisher, 1996; Katta *et al.*, 2007; McCann *et al.*, 2008), however, the different anatomical locations of the cartilage samples and heterogeneous methodologies reported in the literature makes it difficult to make any direct comparisons to this study. The friction factor values reported in this

chapter from the complete natural hip joint study did however, fall within the range of values published in these cartilage-on-cartilage studies.

The non-linear time response observed in this study, where there is a rapid increase in friction followed by a more gradual increase, could be attributed to the viscoelastic response and biphasic nature of the cartilage, where exudation of interstitial fluid reduces the fluid support, initiating a gradual transference of the load to the solid phase (Macirowski *et al.*, 1994; Mow and Wang, 1999; Ateshian, 2009). Continued dynamic loading throughout the simulation, where the cartilage is unloaded for relatively short periods, could gradually reduce the re-hydration capabilities of the cartilage matrix. This in turn would lead to some consolidation of the cartilage and the load being increasingly sustained by the solid phase, resulting in the gradual increase in friction that was observed in this study. Friction continued to increase very gradually over the two-hour test period, indicating that the samples had not reached equilibrium at the end of the test. A similar continued increase in friction over time without reaching equilibrium was also reported by McCann *et al.* (2008), who studied *in vitro* friction and wear in the medial compartment of the natural knee using a pendulum friction simulator. In order for equilibrium to be reached, fluid flow must cease and support of the load must be transferred to the solid matrix (Mow *et al.*, 1980; Woodhouse *et al.*, 2015). The results of this study suggest that some fluid support was still being maintained by the interstitial fluid pressure, generated from mechanically loading the tissue, and that fluid exudation was not complete.

6.7.3 Surface Deformation and Wear

Chondral lesions observed on the femoral heads and acetabula of the tested hip joints was macroscopically assessed and graded using the Outerbridge classification system. Grade 1 and Grade 2 lesions were observed on both femoral heads and acetabula in the central and peripheral (i.e. cranial and caudal) regions, inferring that the two articulating surfaces were relatively conforming. Chondral lesions were relatively superficial with Grade 2 being the highest level of damage observed. No wear was observed inferiorly on any of the tested femoral heads. *In vivo*, the fovea capitis and ligamentum teres corresponds with the non-articular fossa of the acetabulum in the human jip joint, and the inferior chondral surface of the head only becomes weight bearing, or in contact with the anterior wall of the acetabulum, when the hip is placed

in extreme flexion (e.g. sitting) (Athanasiou *et al.*, 1994; Palastanga *et al.*, 2002). This could explain why no evidence of wear was observed *in vitro* inferiorly on the femoral heads in this region, however, this association has to be interpreted with caution as very little is known about the contact mechanics; particularly the contact area, of porcine hip joints *in vivo*. Wear was most frequently observed centrally on the lunate surface (Table 6.5) and superiorly on the femoral head (Table 6.6), and this was generally a slightly higher grade than peripheral lesions. Surface deformation was also more evident along the central region of the lunate surface; hence, the 2D profilometry traces were taken across this area of the Microset® replicas. Axial loading was applied through the centre of the femoral head, which was vertically aligned with the central region of the acetabulum during the *in vitro* simulation, and this could explain why more damage was observed in these areas.

6.8 Conclusions

This study aimed to develop an *in vitro* model for the tribological testing of complete natural hip joints, specifically porcine samples in pendulum friction simulator Mk B. Fixtures for the femoral head and experimental methods for the simulation were developed, following which, five complete natural hip joints were successfully tested. The following observations have been made following this study:

- The design process, culminating in the design solution and detailed designs, enabled the needs and performance requirements to be successfully addressed.
- The femoral head test pot and potting jig, which were designed for the study, accommodated the natural geometric differences and sizes observed in the porcine samples.
- The methodology enabled the femoral heads to be centred in the simulator, with the correct COR, and anatomically orientated to the acetabulum.
- Hip joints were aligned vertically in the sagittal plane, enabling FE motion to be applied.
- There was good reproducibility of friction factor values across the sample group.
- The friction factor trend for all samples (n = 5) displayed a non-linear time response, indicative of a transition of the load from the fluid phase to the solid phase.
- Equilibrium did not appear to have been reached after the two-hour test period as the friction factor was still gradually increasing.

- Friction factor remained low with a mean value of ≈ 0.03 ± 0.00 at the end of the two-hour test period, and overall mean value of ≈ 0.02 ± 0.00 for the whole test.
- Chondral lesions were observed centrally and in the caudal and cranial regions of femoral head and acetabulum, however wear/damage was observed most frequently in the central areas.
- Chondral damage was generally superficial, with the majority of lesions being classified as a Grade 1 using the Outerbridge classification scale.

Chapter 7 Overall Discussion and Conclusions

7.1 Summary

In vitro studies investigating cartilage-on-cartilage tribology using animal and human tissue samples harvested from different anatomical locations are well documented. However, studies investigating the tribology of the complete natural hip joint are limited and have reported heterogeneous methodologies that do not appear to be well suited to investigating the effects of varying hip geometry or pathology (Furey and Burkhardt, 1997; Mow and Huiskes, 2005; Katta *et al.*, 2008). The tribology of the hip joint using *in vitro* hemiarthroplasty samples (porcine acetabula tested with CoCr femoral heads) tested using a pendulum friction simulator has been investigated (Taylor, 2012; Lizhang *et al.*, 2013), however these studies were not progressed onto using complete natural hip joints. There is evidence to suggest that underlying morphometric abnormalities of the hip joint affects the mechanical loading of the joint, and may be associated with the onset, and potentially the progression of hip OA by causing increased contact stresses on the articular cartilage (Harris, 1986; Felson, 2009; Castaño-Betancourt *et al.*, 2013). In addition to *in vivo* evidence, this area of research has been explored computationally (Heller *et al.*, 2001; Mavčič *et al.*, 2002; Adeeb *et al.*, 2004; Daniel *et al.*, 2008; Chegini *et al.*, 2009), however *in vitro* studies of hip joint morphology using complete natural hip joints is currently poorly researched.

Therefore, to improve the understanding of any potential associations between tribology and variations in hip geometry, a methodology that enables complete natural hip joints to be tested *in vitro* is required.

This thesis aimed to explore and identify any fundamental geometric variances in patients with hip osteoarthritis compared to asymptomatic participants of a similar age, and develop a novel *in vitro* simulation model to be used in future tribological investigations using complete natural hip joints.

7.2 Variations in Natural Hip Geometry

A study of hip geometry (SHIG) was undertaken (Chapters 2 and 3) in order to investigate geometric variances in two groups of participants, a study group with a diagnosis of hip osteoarthritis (K/L grade ≥ 2), and a control group of age-matched asymptomatic participants. Following an extensive five-year recruitment period a total

of n = 29 participants were entered into the study, with n = 15 in the control group and n = 14 in the OA study group. Participants underwent 3.0 T MR imaging with a series of sequences that enabled the whole pelvis to viewed in any plane (isotropic SPACE sequence), and detailed sequences to facilitate viewing the intra-articular structures, specifically the labrum and TAL, in more detail (Section 2.4.2). A methodology was developed for analysing and processing the images that was considered reliable and repeatable following a number of small quality assurance tests (Sections 3.3. and 3.4). It was concluded from the initial observations and preliminary segmentations of the images (whilst the candidate was undergoing training), that the study needed to focus on the osseous structures, e.g. the innominate bone and proximal femur. It was not possible to view the labrum and cartilage circumferentially in any single image sequence and this could have introduced a measurement error had some, but not all of these structures been included in the segmentations and 3D models. Imorphics Ltd. used their custom software to create active shape models (ASMs) from the extracted segmentations, each of which had 25 or 26 anatomically aligned floating model points on the surface, and were comprised of ~15-20 principal components. The method/algorithms used by Imorphics Ltd. for creating the 3D ASMs from medical imaging data has been reported in the literature for studies involving the knee joint (Balamoody *et al.*, 2010; Bowes *et al.*, 2010; Williams *et al.*, 2010; Neogi *et al.*, 2013; Bowes *et al.*, 2015), but not currently for studies involving the hip joint. The use of a 3D distortion correction algorithm, which can be applied as part of the post-processing procedure on the MRI scanner, was investigated and found to reduce the slight distortion arising from the inhomogeneity of the 3.0 T magnetic field (B_o) and orthogonal gradient fields. It was therefore, applied to all MR image data before it was processed to heighten the accuracy of image data and subsequent 3D models.

Spheres were fitted to projected model points on the femoral head and acetabular lunate surface (pelvis) of each hip joint ASM, primarily to explore any deviations in sphericity. Sphere fitting is a technique that has been used to characterise or model the geometry of the hip joint in both experimental and computational studies, mainly for comparing male and female geometry (Menschik, 1997; Thompson *et al.*, 2000; Murtha *et al.*, 2008; Anderson *et al.*, 2010; Cereatti *et al.*, 2010; Cerveri *et al.*, 2012), however, associations between femoral and pelvic sphere size in hip OA and asymptomatic participants do not appear to have been described in the literature. The

residual errors from the sphere fitting were viewed as 3D vector graphics (i.e. magnitude and direction of any points of the sphere lying inside or outside the model), and these showed some asphericity of varying degrees of magnitude of the femoral head and acetabulum on both control, and study group participant models (Section 3.7.5.2). In the study group, larger deviations from the sphere were observed in the femoral heads compared to the acetabula, reflecting the characteristic flattening of the femoral head following degeneration of the articular cartilage and subchondral bone that is often observed in the advanced stages of hip OA (Harrison *et al.*, 1953; Altman and Gold, 2007; Braun and Gold, 2012). Deviations in sphericity of the head and acetabulum in the control group, (observed in n = 5 models), were more subtle and less pronounced than the study group. Small deviations could have been a reflection of the natural morphology of a non-pathological hip joint, where the shape of articulating surfaces have been described as conchoid or ellipsoidal by some authors (Menschik, 1997; Cereatti *et al.*, 2010; Cerveri *et al.*, 2012; Gillard *et al.*, 2013). Radiographic evidence of hip OA in asymptomatic older participants has been has been widely reported in the literature (Cobb *et al.*, 1957; Lanyon *et al.*, 2003), therefore, it is also reasonable to hypothesise that some control group participants had mild degenerative joint disease (K/L grade < 2). This may be particularly pertinent to those with evidence of bony growth on the head or head-neck junction (Section 3.7.1), or labral pathology on the MRI scans (Section 3.6.1).

Interestingly, an analysis of the actual sphere dimensions (Section 3.7.5.1) revealed larger differences between the radius of the two spheres (i.e. pelvic sphere r - femoral sphere r) in participant models from the study group with a mean sphere size (i.e. [pelvic sphere r + femoral sphere r] / 2) ≥ 25 mm, compared to the control group. Control group data plots on the Bland-Altman map, with the exception of one outlier, were located close to the bias/mean difference line, as were data plots from the OA patient models in the study group with a mean radius ≤ 24 mm (Figure 3.26). Patients in the study group had slightly lower anteversion angles than participants in the control group (Figure 3.11), meaning they could have slightly shallower acetabula which would require a larger sphere to connect the anterior and posterior horns of the lunate surface. However, this does not explain why the large differences in sphere sizes were only observed in larger diameter hips. Empirical research by Bullough *et al.* (1968) measured the radius of curvature on n = 53 hips at post mortem (no gender

information given) using a three-legged gauge, and determined that both articulating surfaces of the hip joint were aspherical. They also reported that the acetabulum was more aspherical than the head in younger hips, and that a reduction in acetabular asphericity was observed with increasing age. Primary visual analysis of the 3D acetabular models showed some differences between the two groups relating to the superior rim, which appeared to be more prominent, extending further laterally over the femoral head on some areas of the acetabulum in 50 % (n = 7) of the study group models, and only n = 2 control group models (Section 3.7.2). A discussed in Section 3.8.5, this could have been due to osteophytic growth or calcified labrum being segmented as bone, however, another possible explanation is a geometric variance due to acetabular roof dysmorphia. Three types have been described in the literature: (A) an excessively arched roof; (B) an excessively flat roof; (C) a roof with a prominent segment (Lequesne *et al.*, 2004). It is therefore possible that the prominent segment observed on the superior rim of some models could be due to Type (C) acetabular dysmorphia, generally referred to as an angular roof. This abnormality has not been recognised as a risk factor for OA, however depending on the size and exact location of the abnormality, it is theoretically possible that it could give rise to a pincer type impingement and this could have led to joint degeneration (Beall *et al.*, 2005; Beck *et al.*, 2005; Anderson *et al.*, 2009). The presence of Type (B) could have contributed to the large difference in sphere size described above; however, again this does not explain why marked differences were only observed in large mean diameter hips.

The main differences observed between the two groups was the asphericity of the femoral head and/or head-neck junction, presence of osteophytic bone growth around the region of the femoral head, reduced acetabular version angle, obvious joint space narrowing, and superolateral migration of the femoral head. Asphericity of the femoral head or head-neck junction (i.e. cam FAI) is a recognised risk factor for the development of OA (Ganz *et al.*, 2008; Tannast *et al.*, 2008; Gosvig *et al.*, 2010), and dysplastic acetabula have also been associated with an increased risk of developing hip OA (Jacobsen *et al.*, 2005; Reijman *et al.*, 2005; Johnsen *et al.*, 2009; Harris-Hayes and Royer, 2011). Osteophytes generally arise from the periosteal membrane between the cartilage and the bone (intramembranous osteophytes), possibly due to remodelling as an adaptation to the mechanical environment (i.e due to Wolff's law), although the exact aetiology is still unclear. Flattening of the superior aspect of the femoral head

with subsequent superolateral extrusion causes the joint space to increase inferomedially, however, the contact area between the head and acetabulum is reduced superiorly thus increasing the contact stresses in this region, especially where the head has been displaced laterally onto the rim. In more advanced OA, as the head continues to flatten due to failure of the trabeculae in the constantly loaded subchondral bone, the joint space continues to widen inferiorly and medially (i.e. in the non-weight bearing area), allowing room for the new osteophytic bone growth to spread (Harrison *et al.*, 1953; Jeffery, 1975; Resnick, 1983; van der Kraan and van den Berg, 2007). The morphologic appearance of the flattened femoral head and inferomedial osteophytes was observed on a number of models/MRI scans in the study group (Section 3.7.1).

7.3 Validation of a New Pendulum Friction Simulator (Mk B)

A new pendulum friction simulator (Mk B) was validated using MoP and CoC artificial hip bearing couples (Chapter 4), and later, hemiarthroplasty samples consisting of porcine acetabula and size-matched CoCr metal heads (Chapter 5). An existing previously validated pendulum friction simulator (A), which was smaller but of a similar design (i.e. flexion-extension rocker housing the femoral head and friction measuring carriage mounted on a hydrostatic bearing housing the acetabulum), was used as the comparator for the validation process. The null hypothesis for the validation process and Chapters 4 and 5 was that there would be no difference in mean friction factor values obtained from the two simulators (A and Mk B). Pendulum friction simulators have been used to investigate the tribological properties of various total artificial hip joints (Auger *et al.*, 1993; Williams *et al.*, 2006; Brockett *et al.*, 2007), and more recently to investigate the friction, and indirectly cartilage volume loss and wear of hip hemiarthroplasties (Taylor, 2012; Lizhang *et al.*, 2013). The simulator is designed to measure torque transmitted to the acetabular cup, which is seated in a frictionless carriage, as the femoral head oscillates forwards and backwards. Providing the set-up of the samples is perfectly symmetrical with the exact COR (i.e. corresponding to that of the simulator), then only the torque generated between the articulating surfaces should be recorded by the piezoelectric transducer, which is attached to the front of the frictionless carriage. In reality, however, this is difficult to achieve and therefore, mean THR friction factor values were calculated using Equations 4.1 and 4.2, and mean friction factor values using natural tissue were calculated using Equations 5.1 and 5.2 to

eliminate any measurement error (i.e. additional torque) arising from the misalignment of the bearing couples (Auger *et al.*, 1993; Lizhang *et al.*, 2013).

A number of modifications were required before the validation process could be started, the most instrumental of which was fitting a floating joint to the piezoelectric friction sensor to decouple it from the hydrostatic bearing (Section 4.4). Prior to the floating joint being fitted, a mean frictional torque output of 2.67 ± 0.22 Nm (n = 6) was recorded when a 36 mm Ø CoC THR was tested with a 300 N to 2 kN dynamic axial load, water lubricant, and no FE motion. This suggested that additional torque arising from concomitant movement of the self-aligning frictionless carriage was being recorded. Torque measurements were reduced to 0.37 ± 0.07 Nm (n = 6) for the same test after the modification and fitting of the floating joint.

Validation tests using the MoP and CoC THR samples were conducted using different input profiles, which included the profile to be used with natural tissue (Section 4.6.5), and a combination of lubricants (distilled water, 25 % v/v and 100 % v/v bovine serum) (Section 4.6.4). The materials, viscosity of the lubricant, and loading profile have all been shown to affect the lubricating regime and friction factor of artificial hip bearing couples tested *in vitro* using friction simulators (Usworth, 1976; Scholes *et al.*, 2000; Scholes and Unsworth, 2006; Williams *et al.*, 2006; Brockett *et al.*, 2007). Therefore, varying the combination of THR bearings, lubricants and loading regimes tested during the validation process was essential to ensure that friction simulator Mk B was able to function effectively under a range of different operating conditions.

The results from the initial validation study highlighted a number of major discrepancies between the data output recorded by pendulum friction simulator Mk B and the data output from pendulum friction simulator A, the results from which were supported by the literature. Constant load test torque plots positioned asymmetrically above and below zero (Figures 4.15 ii, 4.16 and 4.17) and significantly different friction factor values for forward and reverse dynamic tests, with forward values being higher and reverse values being lower than the expected means (Section 4.7.1.2 and Section 4.7.1.3), were the main areas of concern following THR testing. The results calculated following initial hemiarthroplasty testing, which only became possible after the counterbalance on the loading arm had been reduced (Section 5.5.4.1), were significantly different both in magnitude and trend over time to those obtained from friction simulator A (Section 5.5.5).

The simulator has an externally pressurised hydrostatic bearing that requires a film of fluid lubricant, supplied under pressure, to separate the hydrostatic bearing parts. This enables non-contacting operation of the moving parts of the bearing, thus reducing any friction generated between them to a minimum. The fluid film hydrostatic bearing on simulators A and Mk B was supplied with pressurised oil via capillary tubing, which when functioning efficiently, was able to maintain separation of the bearing parts under different speeds and loading conditions (Cheng and Rowe, 1995; Martin, 2004; Martin, 2006). A detailed evaluation of the test results and specification for friction simulator Mk B, together with observations of the oil pressure being relatively low and fluctuating during operation, led to the hypothesis that there was a fault with the oil supply to the hydrostatic bearing (Section 4.8.3). The load-bearing capacity of the hydrostatic fluid film, which supports the bearing, is derived from a combination of pressure versus flow resistance and therefore, a calculation based on Poiseuille's Law (Section 4.8.5) was used to investigate this hypothesis. This identified that the capillary tubing fitted to friction simulator Mk B was of an incorrect length and diameter (too short and too wide), to enable oil to be supplied at the pressure required to float the hydrostatic bearing. This constituted a major modification being made to friction simulator Mk B, following which, a further validation study was conducted where constant load test torque plots were more symmetrical, and more equal forward and reverse test dynamic friction factor values were observed using the THR samples (Section 4.10). The results of the further hemiarthroplasty testing, conducted following modification of the hydrostatic bearing, also improved considerably with a nonlinear time-dependent friction response and cartilage wear/volume change values being observed that were similar to those from friction simulator A (Section 5.6).

7.4 Tribology of the Natural Hip Joint

Hemiarthroplasty studies conducted as part of the validation process for pendulum friction simulator Mk B were undertaken using an adaptation of the methodology developed by Lizhang (2010), so that the same method could be used for the complete natural hip joint study. This was achieved by modifying the porcine acetabular test pot (Section 5.2.7) and potting method (Section 5.3.1), enabling consistent acetabulum sample preparation for the porcine hemiarthroplasty and complete hip joint studies reported in this thesis, and in future natural hip joint simulations using human tissue samples. A new acetabulum test pot with lower walls was designed to reduce the risk

of impingement on the greater trochanter of the proximal femur, and an attachment was designed for use with an inclinometer to orientate and position the acetabulum. The original method enabled acetabula to be potted with 45° inclination and did not control acetabular version. It is well reported in the literature that both inclination and version angles vary in natural, human hip joints (Stem *et al.*, 2006; Murtha *et al.*, 2008; Atkinson *et al.*, 2010; Bargar *et al.*, 2010; Buller *et al.*, 2012; Goudie *et al.*, 2015), and there is evidence to suggest that reduced acetabular version, particularly retroversion, may be associated with the risk of developing hip OA (Reynolds *et al.*, 1999; Tonnis and Heinecke, 1999; Giori *et al.*, 2003; Ecker *et al.*, 2007; Goudie *et al.*, 2015). Acetabular version was measured in the SHIG study (Section 3.5), and the angle was found to be marginally significantly lower ($p = 0.04$) in the study group (15.44 ± 1.06; $n = 13$) compared to the control group (17.42 ± 1.06; $n = 15$). A gender-specific analysis of the SHIG data set revealed larger mean acetabular version angles in females (17.20 ± 1.48; $n = 16$) than males (15.56 ± 1.46; $n = 12$), which is in agreement with the literature (Stem *et al.*, 2006; Murtha *et al.*, 2008; Atkinson *et al.*, 2010; Nakahara *et al.*, 2010; Buller *et al.*, 2012; Goudie *et al.*, 2015). This was an interesting finding given that the study group, which had a smaller mean version angle, contained more females compared to males ($n = 8$ and $n = 5$ respectively), which in theory would have meant larger mean version angles being reported in this group. The results from the SHIG study, therefore, appear to support the theory that there may be some association between reduced acetabular version and hip OA. Theoretical models have investigated the relationship between dysplasia and OA, and have reported higher contact stresses in dysplastic hips due to the load being distributed over a smaller weight bearing surface (Mavčič *et al.*, 2002; Daniel *et al.*, 2008). Increased contact stresses have been shown to increase articular cartilage wear rates (Katta *et al.*, 2009; Lizhang *et al.*, 2011), possibly governed by an associated increase in frictional shear stress (Walker *et al.*, 1968). The new acetabulum test pot and potting methodology developed in Chapter 5 can therefore, be used to investigate the tribological effects of varying the angle of acetabular version (and/or inclination) during future *in vitro* simulation studies using complete natural hip joints.

A novel complete natural hip joint *in vitro* simulation model was developed in Chapter 6, which aimed to test natural porcine hip joints for this thesis, but with a view to testing human hip joints in the future. This meant that a robust methodology was

required that could adapt to variations in method parameters, for example different specimen types, sizes and orientations. To account for this, future use and variations in porcine specimens were considered in the design process. The fixtures and potting method were developed concurrently, using BS 7000: Part 2 (product design management framework), as a guide. The fixtures consisted of two parts 1) the femoral head test pot, and 2) the potting fixture, which was designed to enable the user to have control over positioning of the femoral head. The test pot (Figure 6.5) was adjustable and could be moved in cranial-caudal and medial-lateral directions on the base. This was to ensure that the femoral head could be positioned centrally in the simulator irrespective of the morphology of the sample, or the desired positioning of the proximal femur. The potting fixture (Figure 6.6) also enabled positioning of the femoral head centrally and with the correct COR, whilst also being able to accommodate samples of different sizes and morphologies. The potting ring, which held the sample, and the potting ring assembly, were both designed so that the user had control over the orientation and potting of the femoral head sample (Section 6.3.5.2), which for the complete natural hip joint study conducted in Chapter 6 meant anatomically aligning matched samples.

The input parameters for all testing conducted on natural porcine tissue was a two-hour reverse dynamic 25 N to 800 N axial loading profile with ± 15° FE (Figure 4.14). In addition to the frictional torque being generated between the two articulating surfaces, extra biomechanical torque was created when testing natural tissue due to the complex geometry of the samples causing a slight misalignment of the COR of the hip joint with respect to the driven COR of the friction simulator. The magnitude of the extra biomechanical torque (i.e. not frictional torque due to the loading and motion) needed establishing as this was also transmitted to the acetabulum, and therefore piezoelectric transducer, which would have caused a measurement error. The extra torque was measured by running a constant load test of 800 N ± 15° for two-minutes before and after each natural tissue test, so that the difference in magnitude between the flexion-extension phases could be calculated. In perfectly aligned samples, the constant load torque output would be symmetrically distributed above and below zero, therefore any differences in forward and reverse torque magnitudes could be averaged and used to normalise the dynamic test data (Section 5.3.2 and Section 5.4.1). A 25 % bovine serum lubricant was used for all natural tissue tests to mimic *in vivo* conditions, as the protein

content is similar to that of synovial fluid (Saari *et al.*, 1993; Wang *et al.*, 1998; Scholes and Joyce, 2013).

7.4.1 Hemiarthroplasty versus Complete Natural Porcine Hip Tribology

The hemiarthroplasty study results conducted as part of the validation process in Chapter 5, and the results from the complete natural hip joint study in Chapter 6 were compared, and the outcome of this is shown in Figure 7.1 (mean friction factor), Figure 7.2 (acetabular chondral lesions), and Figure 7.3 (wear scar volume change and deformation depth). The trend over time was similar for both studies (Figure 7.1); however, the mean friction factor value for the hemiarthroplasty study was larger than that for the complete natural joint study by ≈ 0.03 for the first 1,500 cycles, ≈ 0.02 for the next 4,800 cycles, ≈ 0.01 for the final 900 cycles (i.e. 15 minutes). This showed that the mean friction for the complete porcine test continued to rise gradually over the two-hour test period, whereas than the mean friction factor for the hemiarthroplasty study plateaued after ~50 minutes. Mean friction factor was significantly lower (*t*-test; $p < 0.05$) for the complete natural porcine joint study when analysed at the three time points (i.e. 60, 1,200 and 7,200 cycles), described in Section 5.4.3.

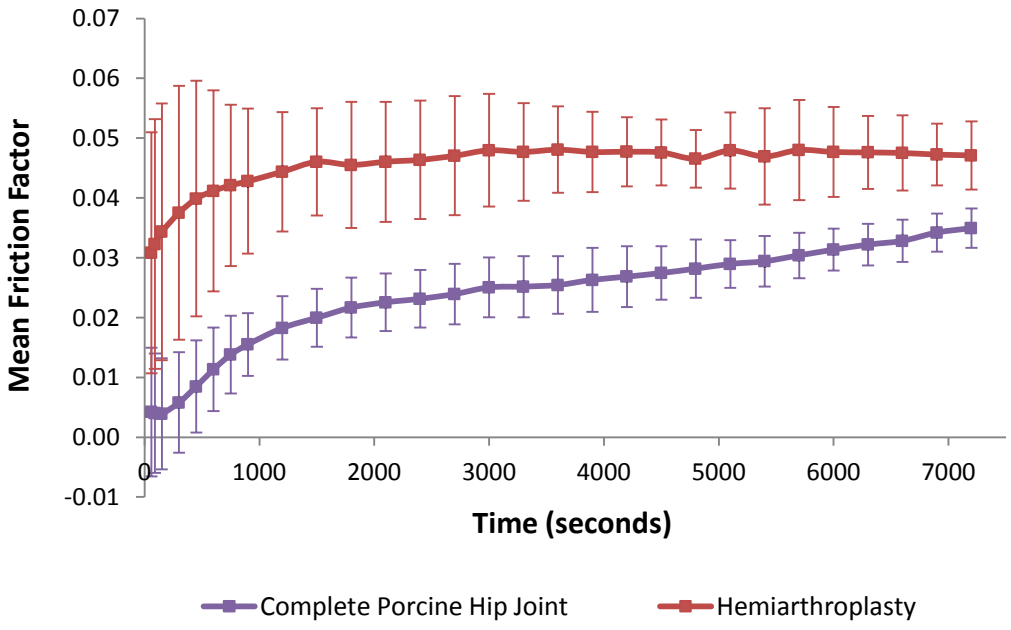

Figure 7.1: Mean friction factor ± 95 % confidence limits for the complete porcine hip joint study (n = 5) and porcine hemiarthroplasty study (n = 5) conducted on pendulum friction simulator Mk B for two-hours.

Macroscopic wear analysis and grading using the Outerbridge classification system (Section 5.6.2.1 and Section 6.5.5.2) revealed a larger number of chondral lesions on the lunate surfaces of porcine acetabula specimens tested with a natural femoral head (n = 15) compared to those tested with a CoCr head during the hemiarthroplasty study (n = 12). However, wear lesions following complete natural hip joint testing were of a lesser grade than those observed following the hemiarthroplasty study (Figure 7.2). It was also noted that the distribution of damage was more evenly dispersed around the lunate surface following the complete natural joint study. The most likely explanation for this is the greater conformity between the matched natural head and acetabulum compared to the natural acetabulum and spherical CoCr head.

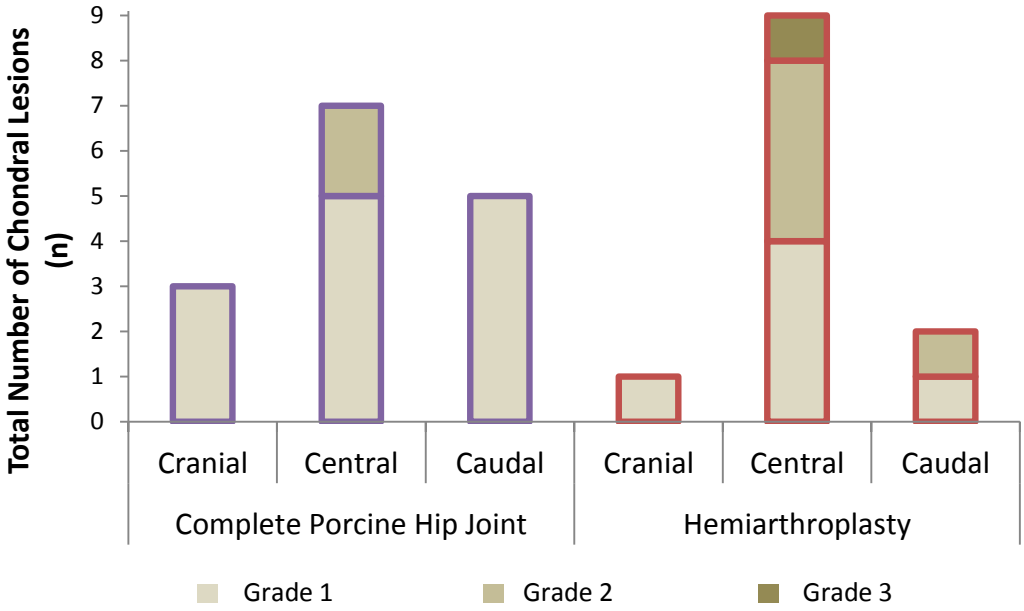

Figure 7.2: Location and grade of chondral lesions identified on the acetabula following complete porcine hip joint simulation tests (n = 5) and hemiarthroplasty tests (n = 5) in pendulum friction simulator Mk B. The chart shows the total number of lesions identified on the acetabulum of each tested specimen.

Wear scar measurement results, calculated using Equations 5.3 and 5.4 in Section 5.4.2, were not statistically analysed due to contacting profilometry being completed on only a small sample (n = 3) of tested acetabula following the hemiarthroplasty study during the validation processes (Section 5.3.3.2). However, obvious differences for both mean deformation volume (mm^3) and mean deformation depth (µm) were observed, as shown on Figure 7.3. The smaller deformation volume and wear scar depth observed on the porcine acetabula following complete natural hip joint testing supports the

findings of the macroscopic analysis, where on these specimens, chondral lesions of a lower grade were generally observed (Figure 7.2).

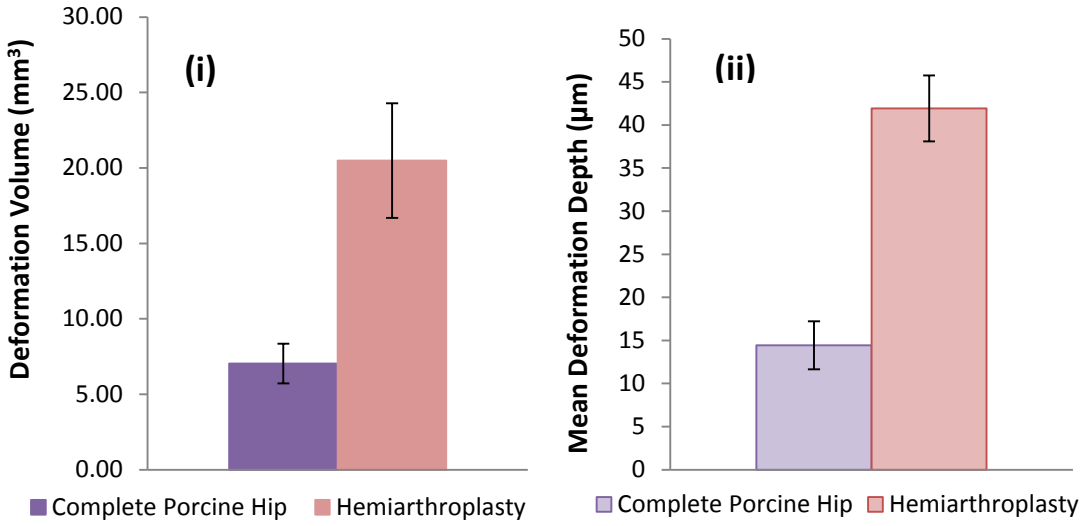

Figure 7.3: Talysurf 2D profilometry results of acetabula cartilage volume loss following complete porcine hip joint (n = 5) and porcine hemiarthroplasty (n = 3) studies conducted on pendulum friction simulator Mk B. Comparisons of (i) mean deformation volume (mm^3 ± SD) and (ii) mean deformation depth (µm ± SD).

Frictional shear stress has been suggested as an important factor in cartilage tribology, as it has been shown to cause an increase in the mechanical degradation and fibrillation of articular cartilage. Increased friction and increased shear stresses have both been associated with an increase in contact stress, which can arise from larger clearances leading to a reduction in the contact area between the articulating surfaces (Kosashvili *et al.*, 2008; Katta *et al.*, 2009; Lizhang *et al.*, 2011). Shear stress was not formally calculated for either study, as the actual contact area was not measured. However, it is reasonable to assume that the conformity, and therefore contact area between the articular surfaces of the matched porcine natural hip joint samples was greater than that for the hemiarthroplasty samples, which in theory therefore will have had larger, more variable clearances. Elastic deformation of the articular cartilage during loading also increases the contact area due to improved geometrical congruency, thus distributing the load more widely (Ateshian and Wang, 1995; Murakami *et al.*, 1998), and it is hypothesised that the effects of this were slightly greater in the complete natural joint due to both contacting surfaces being covered with cartilage. These theories support the findings of the natural hip joint studies where lower mean friction

values (Figure 7.1), more evenly distributed, lower grade chondral damage (Figure 7.2), and reduced mean wear scar deformation volume and depth (Figure 7.3) were observed the following the complete natural hip joint study compared to the hemiarthroplasty study.

The difference in contact area and congruity of the articulating surfaces may also have influenced the lubrication regime for the two studies. The nonlinear increase in mean friction observed during the two-hour test period for both the porcine hemiarthroplasty and porcine complete natural hip joint studies, suggests a change in lubrication mode from fluid film, where the two surfaces are completely separated, towards the solid-phase due to the exudation of fluid. The surface roughness of animal and human articular cartilage has been reported by a number of authors, who despite their heterogeneous methodologies and results, all agree that it is not completely smooth and that microscopic asperities exist on the surface (Forster and Fisher, 1999; Northwood *et al.*, 2007; Katta *et al.*, 2009; McCann *et al.*, 2009). Cartilage surface roughness has also been shown to increase progressively in the presence of osteoarthritis by Lee *et al.* (2012), who measured the surface roughness of cartilage from harvested femoral heads of patients with advancing OA undergoing THR using atomic force microscopy, and by Walker *et al.* (1968), who measured the surface roughness of an osteoarthritic femoral condyle using an acrylic cast and contacting stylus. Fluid pooling in the asperities between the articular surfaces has been reported as a mechanism affecting squeeze film lubrication, the effectiveness and duration of which is increased during the application of a load to surfaces that deform, such as articular cartilage, as this will trap the fluid for longer between the two opposing surfaces (Walker *et al.*, 1968; Higginson, 1978). It is possible, therefore, that fluid in between the articulating surfaces of the complete natural hip joint was being exudated more slowly, due to being trapped between the deforming asperities of the cartilage, compared to the hemiarthroplasty study where only one surface deformed. If so, the lubrication regime in the hemiarthroplasty study could have moved towards the solid phase more quickly, therefore plateauing compared to the complete natural joint study, which continued to rise gradually throughout the test and had a lower mean friction factor (Figure 7.1). This theory is supported by an experimental and computational study of contact stress and contact area by Pawaskar *et al.* (2011), who concluded that the smaller local contact area and variable clearance observed when

testing porcine hemiarthroplasty samples made the exudation of fluid easier, thus reducing fluid load support more quickly, which in turn can lead to an increase in friction.

7.5 Clinical Importance

Para-sagittal imaging of the transverse acetabular ligament (TAL) enabled it to be visualised in the majority of patients, suggesting that this ligament often remains intact in the presence of advanced hip OA, and therefore may be a suitable landmark for cup positioning in THR. The use of 3D distortion correction was found to reduce distortion of the 3D models arising from scanner inhomogeneities. The difference in the magnitude of distortion when comparing 3D to standard 2D distortion correction was observed as being small, however, the application of this algorithm should possibly be considered when using 3D surface models for surgical planning or creating patient specific implants. This could also be an important factor to be considered for non-orthopaedic procedures such as imaging-guided radiotherapy treatment planning using 3D MRI.

The development of the complete natural hip joint tribological model could have an important use in the pre-clinical testing of tissue-engineered osteochondral grafts, and other treatments for cartilage or labral lesions in the hip. The *in vitro* simulation model could also be used to add to the body of evidence regarding risk factors for the development of OA by simulating different geometries and pathologies. It is also possible that when used with natural human hip joints, cup placement in THR using anatomical landmarks (e.g. TAL) could be simulated and explored, as could the tribological outcome of early intervention surgical techniques for OA, such as osteotomies.

7.6 Limitations

7.6.1 Study of Hip Geometry

The main limitation of the SHIG study was the poor recruitment meaning that both groups had small numbers of participants, and both groups contained males and females. Small sample sizes can increase the risk of obtaining a Type II error, i.e. not finding a significant difference that exists due to the power of the study being too low. As discussed earlier in this chapter and in Section 3.8, some obvious differences were

observed between the two groups in the SHIG study (e.g. changes in the femoral head shape, reduced acetabular version, superolateral migration of the femoral head, osteophytic growth), therefore this may not have been a major problem. However, the small number of participants, combined with them being of mixed gender, did potentially reduce the power of the study and may have contributed to the poor shape distribution and discriminatory power of the principal components forming the models, as discussed in Sections 3.7.3 and 3.7.4. Male and female geometric differences in the hip have been widely reported (Lanyon *et al.*, 2003; Lequesne *et al.*, 2004; Ecker *et al.*, 2007; Beall *et al.*, 2008; Traina *et al.*, 2009; Stelzeneder *et al.*, 2012; Aly *et al.*, 2013), and therefore this confounding factor needs to be considered in future studies.

It was noted that all measurements we completed by a single observer (the candidate), however, extensive training had been undertaken, the segmentation process was assessed for accuracy, and rigorous definitions for completing 2D measurements were used, therefore the risk of measurement error from this was reduced.

7.6.2 *In vitro* Simulation Studies

Initial problems with the design and function of pendulum friction simulator Mk B meant that it could not able to be validated for an extended period of time until all of the modifications had been completed. This reduced the scope of the study meaning that tribological testing was only conducted on what would be considered as “normal” geometry. The main limitation of using pendulum friction simulator Mk B for running the natural hip simulation model is that the equipment can only apply one axis of motion and an axial load. This means that the normal osteokinematics that the hip joint is subjected to *in vivo* (e.g. flexion-extension, abduction-adduction, medial and lateral rotation) cannot be reproduced, which may result in some abnormal stresses being applied to the joint. In addition, the samples being anatomically inverted mean that the axial loading applied to the hip joint *in vitro* is through the femur rather than through the acetabulum of the pelvis, as it is *in vivo*. These factors could reduce the external validity of the study slightly.

7.7 Recommendations for Further Work

Recruitment for future medical imaging studies needs to either target a particular gender, or ideally, recruit larger numbers of participants. Obtaining scans from multiple

centres may facilitate this. The use of radial 3.0 T MRI scans should be investigated for segmenting and reconstructing the complete acetabular labrum and TAL circumferentially. Radial scan sequences have been reported in the literature on less powerful scanners as enabling the labrum to be visualised around the complete acetabular rim more accurately than standard oblique axial or coronal sequences. It may also be possible to visualise the cartilage more accurately with a 3.0 T radial sequence. Additionally, a longitudinal MRI study using the methodology developed in this thesis would enable 3D changes in geometry over time to be investigated, which would be of benefit when looking at risk factors for the development of OA.

The reason for the large difference in sphere size fitted to hips with a mean sphere radius ≥ 25 mm in the study group should be investigated further, as no definitive explanation has been found for this. It may be possible to explore this finding using the complete natural hip joint *in vitro* simulation model, however, the use of computational studies would also be recommended in order to validate any results derived experimentally. Additionally, there appeared to be some geometric differences relating to the superior aspect of the acetabular roof. The aetiology of this was not clear following this study and, as it could have been a natural variation in shape (e.g. acetabular roof dysmorphia) rather than a product of the OA disease process, it warrants further investigation with a larger group size.

Evidence associating acetabular dysplasia, asphericity of the femoral head/neck and acetabulum (i.e. FAI), and other geometric variances with degeneration of the hip joint, have been mainly derived from either clinical or computational studies and the evidence base lacks complete natural joint *in vitro* tribological studies. There is, therefore a need for *In vitro* testing of complete natural hip joints to support this evidence, and this can be explored through the novel simulation model developed in Chapter 6. The fixtures and methodology developed for this thesis will enable simple geometric variances (e.g. FNSA and acetabular version), as well as some of the more complex variations that were observed in the SHIG study, such as deviations in sphericity (Section 3.7.5), to be replicated and explored *in vitro*. It may be possible to simulate some of the variations in hip geometry that are considered to be more complex by mismatching femoral heads and acetabula.

A limitation of this study for future work has been identified as the use of pendulum friction simulator Mk B for running the simulation model, due to only an axial loading

and a single axis of motion (i.e. FE) being applied, and the samples being anatomically inverted. It is therefore suggested that tribological studies using porcine hip joints to investigate complex geometric variations are conducted on a single station hip simulator (SSHS), which is a multi-axis electromechanical hip joint simulator. Any human tissue studies will require the use of the SSHS, as the human hip joint is too large to fit comfortably into pendulum friction simulator Mk B. The complete natural hip model fixtures and methodology developed in this thesis can be easily adapted for use with the SSHS.

7.8 Overall Conclusions

In this thesis, geometric variations in the human natural hip joint in patients with osteoarthritis and asymptomatic participants have been explored with 3.0 T MRI and 3D shape models, and a new pendulum friction simulator (Mk B) has been validated for use with artificial hip bearings and natural tissue. An existing method for creating and analysing shape models of the knee joint was successfully modified for use with the hip joint in the SHIG study, and the results from 2D geometric measurements and 3D surface models were combined enabling a more thorough analysis of the data. Additionally, and a novel *in vitro* simulation model for the tribological testing of complete natural hip joints has been developed and it is envisaged that the knowledge gained from the study of natural hip geometry will be used as geometric parameters in future *in vitro* simulation studies of complete natural hip joints.

To summarise, the main conclusions were:

- An accurate and reliable image processing and segmentation method was developed for the SHIG study using EndPoint software for analysing femoral and pelvic bone on 3.0 T MR images of the hip joint. A small study exploring the use of distortion correction algorithms resulted in 3D distortion correction being applied to all MR images before the analysis. This was performed due to some distortion, caused by slight image intensity inhomogeneity, being detected following standard 2D correction. The accuracy of the osseous segmentation was assessed as being excellent using a porcine tissue substitute model.
- Active shape models created from Imorphics Ltd. algorithms were successfully used for assessing 3D geometric shape variations in human hip joints. The assessment was completed by visually analysing the external surfaces of the femoral and pelvic

models, computationally assessing the shape distributions and discriminative ability of the shape parameters, and by assessing the sphericity of the femoral heads and lunate surfaces. Literature reporting the use of active shape models (ASMs) created using this algorithm is currently limited to research relating to the knee joint.

- The use of 2D morphometric parameters on the distortion corrected MRI scans revealed significantly lower acetabular anteversion angles in the control group, which could be a contributing factor the development of hip OA. Measuring the femoral head extrusion index (FHEI) showed that participants in the study group had greater exposure of the femoral head laterally than the control group. This was confirmed with superolateral migration of the femoral head being observed in a number of the study group participants. Other 2D parameters, although not significantly different (e.g. femoral neck-shaft angle [FNSA]), can be used to inform future *in vitro* simulation testing of complete natural hip joints.
- Flattening of the superior aspect of the femoral head was observed on all study group 3D shape models with varying degrees of severity. Fitting spheres to the femoral heads and viewing the residual errors as 3D vector graphics confirmed this observation. The difference in sphere radii when fitted to the acetabular lunate surfaces and femoral heads was larger for study group participants, with a mean radial sphere size of ≥ 25 mm, which is a novel finding that appears not to have been previously reported. A number of participants in the study group had evidence suggesting osteophytic bone growth on the femoral head, femoral head-neck junction and inferomedially, which is indicative of hypertrophic OA.
- The null hypothesis for the study of hip geometry (SHIG) was that there are no differences in geometry in a group of participants with hip OA when compared with an age-matched asymptomatic group of participants (all ≥ 50 years). The null hypothesis was rejected based on the observations made.
- Pendulum friction simulator Mk B required a number of modifications, the most significant being the replacement of capillary tubing to increase the pressure to float the hydrostatic bearing, before the simulator could be validated. Following the validation process, the null hypothesis stating that the friction factor from testing THR samples and hemiarthroplasties on friction simulator Mk B was equal to the friction factor value gained when repeating the same tests on friction simulator A, was retained for short-duration tests (e.g. two-minutes), and for longer duration tests (e.g. two-hours) providing the results were corrected for measurement drift.

- A novel *in vitro* model for the tribological testing of complete natural hip joints, specifically porcine samples in pendulum friction simulator Mk B, was successfully developed, which can also be adapted for use with larger human tissue samples in the future. The fixtures and methodology will enable complete natural hip joints with different geometric parameters to be tested. The potting method and fixtures designed for the *in vitro* simulation studies (i.e. inclinometer and attachment, femoral head pot and potting rig) are a novel way of controlling the positioning tissue samples in different spatial orientations, and these can be adapted and used for positioning tissue samples other than the hip joint e.g. knee, ankle, spine etc.
- Very few tribological *in vitro* studies of the natural hip joint have been reported in the literature and these have used very heterogeneous methods that would to be unsuitable, or difficult to adapt for studies varying the geometric parameters. Currently, this appears to be the only *in vitro* study comparing the tribology of hip hemiarthroplasty with the complete natural hip joint.
- Friction factor values from the porcine hemiarthroplasty and complete porcine natural hip joint *in vitro* simulation studies displayed a nonlinear time-dependant response over two hours, indicative of the load being transferred from the fluid phase to the solid phase. Mean friction factor was significantly lower in the complete natural hip and did not reach equilibrium during the two-hour test period, unlike the hemiarthroplasty study, which reached equilibrium after ~50 minutes.
- Analysis of the wear scars on the acetabula tested *in vitro* in pendulum friction simulator Mk B showed more evenly distributed chondral damage on the complete joint specimens, which was of a lower Outerbridge classification grade, and had a smaller deformation depth and volume loss, when compared to the hemiarthroplasty specimens.
- It was postulated that in the complete natural joint simulation, the articulating surfaces were more conforming, and therefore the contact area was larger and the contact and shear stresses were less than in the hemiarthroplasty simulation. In addition to the greater conformity of the complete natural joint, the asperities on the two articular cartilage surfaces may also have enhanced fluid film lubrication by reducing the speed of fluid exudation, possibly prolonging the squeeze film phase.

During the past 4 weeks..

✓tick one box for every question.

1. *During the past 4 weeks*.....
How would you describe the pain you usually had from your hip?

None	Very mild	Mild	Moderate	Severe
❑	❑	❑	❑	❑

2. *During the past 4 weeks*.....
Have you had any trouble with washing and drying yourself (all over) because of your hip?

No trouble at all	Very little trouble	Moderate trouble	Extreme difficulty	Impossible to do
❑	❑	❑	❑	❑

3. *During the past 4 weeks*.....
Have you had any trouble getting in and out of a car or using public transport because of your hip? *(whichever you tend to use)*

No trouble at all	Very little trouble	Moderate trouble	Extreme difficulty	Impossible to do
❑	❑	❑	❑	❑

4. *During the past 4 weeks*.....
Have you been able to put on a pair of socks, stockings or tights?

Yes, Easily	With little difficulty	With moderate difficulty	With extreme difficulty	No, Impossible
❑	❑	❑	❑	❑

5. *During the past 4 weeks*.....
Could you do the household shopping on your own?

Yes, Easily	With little difficulty	With moderate difficulty	With extreme difficulty	No, Impossible
❑	❑	❑	❑	❑

6. *During the past 4 weeks*.....
For how long have you been able to walk before pain from your hip becomes severe? *(with or without a stick)*

No pain/ More than 30 minutes	16 to 30 minutes	5 to 15 minutes	Around the house only	Not at all -pain severe on walking
❑	❑	❑	❑	❑

7 *During the past 4 weeks*.....
Have you been able to climb a flight of stairs?

Yes, Easily	With little difficulty	With moderate difficulty	With extreme difficulty	No, Impossible
❑	❑	❑	❑	❑

8 *During the past 4 weeks*.....
After a meal (sat at a table), how painful has it been for you to stand up from a chair because of your hip?

Not at all painful	Slightly painful	Moderately painful	Very painful	Unbearable
❑	❑	❑	❑	❑

9 *During the past 4 weeks*.....
Have you been limping when walking, because of your hip?

Rarely/ never	Sometimes, or just at first	Often, not just at first	Most of the time	All of the time
❑	❑	❑	❑	❑

10 *During the past 4 weeks*.....
Have you had any sudden, severe pain - 'shooting', 'stabbing' or 'spasms' - from the affected hip?

No days	Only 1 or 2 days	Some days	Most days	Every day
❑	❑	❑	❑	❑

11 *During the past 4 weeks*.....
How much has pain from your hip interfered with your usual work *(including housework)*?

Not at all	A little bit	Moderately	Greatly	Totally
❑	❑	❑	❑	❑

12 *During the past 4 weeks*.....
Have you been troubled by pain from your hip in bed at night?

No nights	Only 1 or 2 nights	Some nights	Most nights	Every night
❑	❑	❑	❑	❑

Appendix B: Two-Dimensional Assessment of Femoral Head Sphericity

Participants in the SHIG study were classified as having an aspherical femoral head if the edge of the bone was inside and/or outside a circle of best fit that was fitted to the centre of the femoral head on axial (Figures A and B) or coronal (Figures C and D) MR images.

The bony outline of the femoral head of the study group participant deviates from the circle of best fit in both the anterior-posterior directions (red line on Figure B) and the superior-inferior directions (red line on Figure D). This deviation from sphericity is not observed on the control group participant images (Figures A and C).

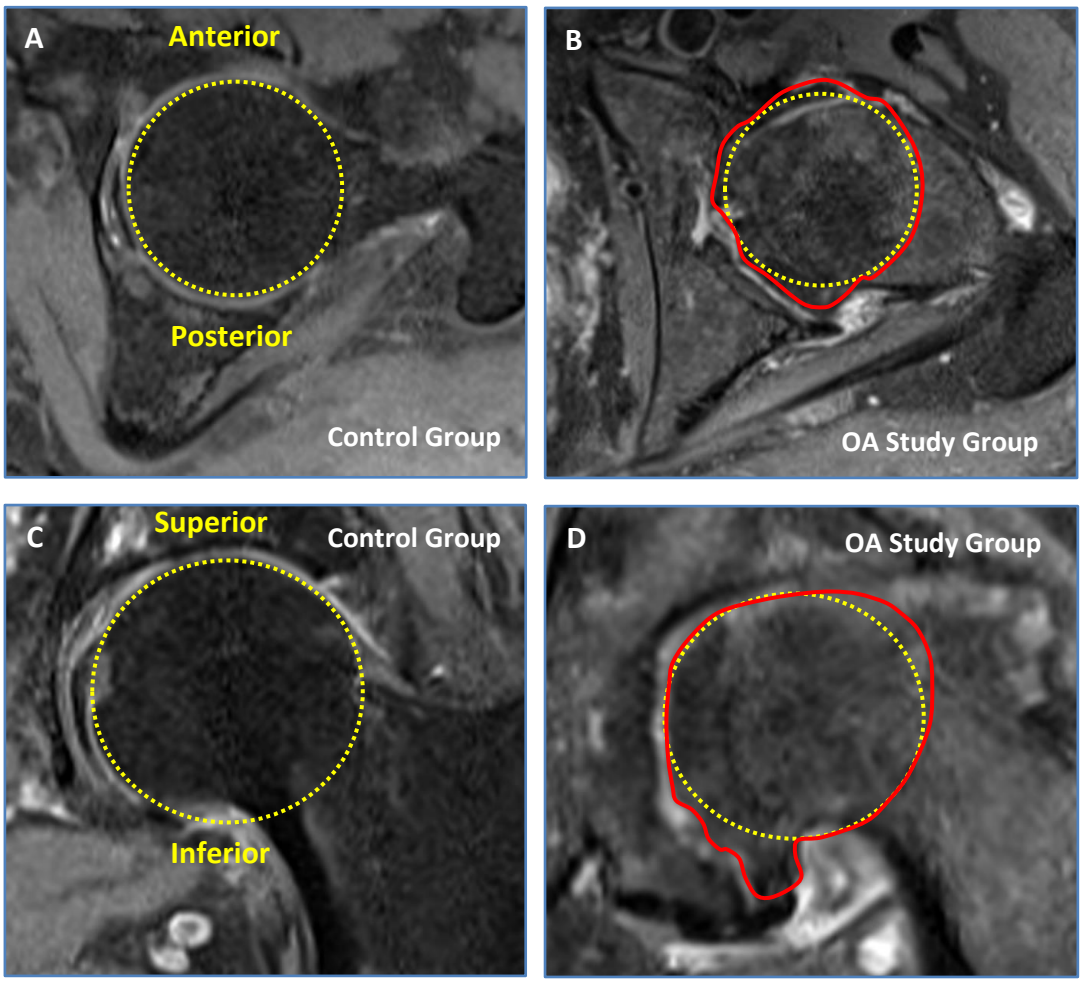

Control group participant	**A: Axial MR image**	**C: Coronal MR image**
Study group participant	**B: Axial MR image**	**D: Coronal MR image**
Yellow dashed circle:	**Circle of best fit fitted to the centre of the femoral head**	
Red line:	**Edge of the bone highlighted in the OA patient**	

<u>Appendix C</u>: Initial Study Plan for Validating Pendulum Friction Simulator Mk B using Total Hip Replacements and Simulator A

Bearings	Test (Load ± FE)	Lubricant	Simulator and Repeat Number
Surface roughness measurements of samples (3 x heads and 3 x cups) – Repeat 1			
28 mm Ø MoP	300 N to 2 kN ± 25°	Water, 25 % & 100 % NBCS	Simulator A – 1
	25N to 800 N ± 15°	Water, 25 % & 100 % NBCS	Simulator A – 1
28 mm Ø MoP	300 N to 2 kN ± 25°	Water, 25 % & 100 % NBCS	Simulator Mk B – 1
	25 N to 800 N ± 15°	Water, 25 % & 100 % NBCS	Simulator Mk B – 1
28 mm Ø CoC and 36 mm Ø CoC	25 N to 2 kN ± 25°	Water, 25 % & 100 % NBCS	Simulator A – 1
	100 N to 2 kN ± 25°	Water, 25 % & 100 % NBCS	Simulator A – 1
	300 N to 2 kN ± 25°	Water, 25 % & 100 % NBCS	Simulator A – 1
	25 N to 800 N ± 15°	Water, 25 % & 100 % NBCS	Simulator A – 1
	300 N Constant ± 25°	Water, 25 % & 100 % NBCS	Simulator A – 1
	1 kN Constant ± 25°	Water, 25 % & 100 % NBCS	Simulator A – 1
28 mm Ø CoC and 36 mm Ø CoC	25 N to 2 kN ± 25°	Water, 25 % & 100 % NBCS	Simulator Mk B – 1
	100 N to 2 kN ± 25°	Water, 25 % & 100 % NBCS	Simulator Mk B – 1
	300 N to 2 kN ± 25°	Water, 25 % & 100 % NBCS	Simulator Mk B – 1
	25 N to 800 N ± 15°	Water, 25 % & 100 % NBCS	Simulator Mk B – 1
	300 N Constant ± 25°	Water, 25 % & 100 % NBCS	Simulator Mk B – 1
	1 kN Constant ± 25°	Water, 25 % & 100 % NBCS	Simulator Mk B – 1
Surface roughness measurements of samples (3 x heads and 3 x cups) – Repeat 2			
28 mm Ø MoP	300N to 2kN ± 25°	Water, 25 % & 100 % NBCS	Simulator A – 2
	25N to 800N ± 15°	Water, 25 % & 100 % NBCS	Simulator A – 2
28 mm Ø MoP	300N to 2kN ± 25°	Water, 25 % & 100 % NBCS	Simulator Mk B – 2
	25N to 800N ± 15°	Water, 25 % & 100 % NBCS	Simulator Mk B – 2
28 mm Ø CoC and 36 mm Ø CoC	25 N to 2 kN ± 25°	Water, 25 % & 100 % NBCS	Simulator A – 2
	100 N to 2 kN ± 25°	Water, 25 % & 100 % NBCS	Simulator A – 2
	300 N to 2 kN ± 25°	Water, 25 % & 100 % NBCS	Simulator A – 2
	25 N to 800 N ± 15°	Water, 25 % & 100 % NBCS	Simulator A – 2
	300 N Constant ± 25°	Water, 25 % & 100 % NBCS	Simulator A – 2
	1 kN Constant ± 25°	Water, 25 % & 100 % NBCS	Simulator A – 2

(Continued)

28 mm Ø CoC and 36 mm Ø CoC	25 N to 2 kN ± 25°	Water, 25 % & 100 % NBCS	Simulator Mk B – 2
	100 N to 2 kN ± 25°	Water, 25 % & 100 % NBCS	Simulator Mk B – 2
	300 N to 2 kN ± 25°	Water, 25 % & 100 % NBCS	Simulator Mk B – 2
	25 N to 800 N ± 15°	Water, 25 % & 100 % NBCS	Simulator Mk B – 2
	300 N Constant ± 25°	Water, 25 % & 100 % NBCS	Simulator Mk B – 2
	1 kN Constant ± 25°	Water, 25 % & 100 % NBCS	Simulator Mk B – 2
Surface roughness measurements of samples (3 x heads and 3 x cups) – Repeat 3			
28 mm Ø MoP	300N to 2kN ± 25°	Water, 25 % & 100 % NBCS	Simulator A – 3
	25N to 800N ± 15°	Water, 25 % & 100 % NBCS	Simulator A – 3
28 mm Ø MoP	300N to 2kN ± 25°	Water, 25 % & 100 % NBCS	Simulator Mk B – 3
	25N to 800N ± 15°	Water, 25 % & 100 % NBCS	Simulator Mk B – 3
28 mm Ø CoC and 36 mm Ø CoC	25 N to 2 kN ± 25°	Water, 25 % & 100 % NBCS	Simulator A – 3
	100 N to 2 kN ± 25°	Water, 25 % & 100 % NBCS	Simulator A – 3
	300 N to 2 kN ± 25°	Water, 25 % & 100 % NBCS	Simulator A – 3
	25 N to 800 N ± 15°	Water, 25 % & 100 % NBCS	Simulator A – 3
	300 N Constant ± 25°	Water, 25 % & 100 % NBCS	Simulator A – 3
	1 kN Constant ± 25°	Water, 25 % & 100 % NBCS	Simulator A – 3
28 mm Ø CoC and 36 mm Ø CoC	25 N to 2 kN ± 25°	Water, 25 % & 100 % NBCS	Simulator Mk B – 3
	100 N to 2 kN ± 25°	Water, 25 % & 100 % NBCS	Simulator Mk B – 3
	300 N to 2 kN ± 25°	Water, 25 % & 100 % NBCS	Simulator Mk B – 3
	25 N to 800 N ± 15°	Water, 25 % & 100 % NBCS	Simulator Mk B – 3
	300 N Constant ± 25°	Water, 25 % & 100 % NBCS	Simulator Mk B – 3
	1 kN Constant ± 25°	Water, 25 % & 100 % NBCS	Simulator Mk B – 3
Surface roughness measurements of samples (3 x heads and 3 x cups) – Repeat 4			

Appendix D: Initial Validation Studies Mean Results

	28 mm Ø MoP – Mean Friction Factor ± SD (n = 3)			
	Friction Simulator A		Friction Simulator Mk B	
	300 N to 2 kN ± 25° FE	25 N to 800 N ± 15° FE	300 N to 2 kN ± 25° FE	25 N to 800 N ± 15° FE
Water	0.031 ± 0.001	0.061 ± 0.007	0.040 ± 0.009	0.058 ± 0.021
25 % NBCS	0.060 ± 0.007	0.070 ± 0.005	0.064 ± 0.005	0.061 ± 0.008
100 % NBCS	0.074 ± 0.005	0.073 ± 0.004	0.072 ± 0.007	0.070 ± 0.004

	28 mm Ø CoC – Mean Friction Factor ± SD (n = 3)			
	Friction Simulator A			
	25 N to 2 kN ± 25° FE	100 N to 2 kN ± 25° FE	300 N to 2 kN ± 25° FE	25 N to 800 N ± 15° FE
Water	0.001 ± 0.001	0.000 ± 0.002	0.000 ± 0.002	0.004 ± 0.001
25 % NBCS	0.041 ± 0.001	0.043 ± 0.003	0.047 ± 0.001	0.063 ± 0.003
100 % NBCS	0.059 ± 0.004	0.060 ± 0.003	0.066 ± 0.004	0.065 ± 0.005
	300 N Constant ± 25° FE	1 kN Constant ± 25° FE		
Water	0.002 ± 0.001	0.002 ± 0.001		
25 % NBCS	0.136 ± 0.008	0.075 ± 0.002		
100 % NBCS	0.125 ± 0.002	0.095 ± 0.002		

	28 mm Ø CoC – Mean Friction Factor ± SD (n = 3)			
	Friction Simulator Mk B			
	25 N to 2 kN ± 25° FE	100 N to 2 kN ± 25° FE	300 N to 2 kN ± 25° FE	25 N to 800 N ± 15° FE
Water	0.001 ± 0.002	0.003 ± 0.002	0.003 ± 0.003	0.002 ± 0.003
25 % NBCS	0.059 ± 0.002	0.067 ± 0.003	0.052 ± 0.004	0.106 ± 0.003
100 % NBCS	0.084 ± 0.002	0.090 ± 0.001	0.073 ± 0.000	0.135 ± 0.005
	300 N Constant ± 25° FE	1 kN Constant ± 25° FE		
Water	0.004 ± 0.002	0.002 ± 0.002		
25 % NBCS	0.151 ± 0.005	0.091 ± 0.001		
100 % NBCS	0.138 ± 0.008	0.111 ± 0.002		

(Continued)

	36 mm Ø CoC – Mean Friction Factor ± SD (n = 3)			
	Friction Simulator A			
	25 N to 2 kN ± 25° FE	100 N to 2 kN ± 25° FE	300 N to 2 kN ± 25° FE	25 N to 800 N ± 15° FE
Water	0.001 ± 0.001	0.000 ± 0.001	0.001 ± 0.001	0.002 ± 0.002
25 % NBCS	0.052 ± 0.002	0.057 ± 0.003	0.060 ± 0.001	0.065 ± 0.001
100 % NBCS	0.063 ± 0.001	0.064 ± 0.001	0.068 ± 0.002	0.068 ± 0.009
	300 N Constant ± 25° FE	1 kN Constant ± 25° FE		
Water	0.003 ± 0.001	0.002 ± 0.001		
25 % NBCS	0.115 ± 0.004	0.085 ± 0.002		
100 % NBCS	0.111 ± 0.003	0.089 ± 0.002		

	36 mm Ø CoC – Mean Friction Factor ± SD (n = 3)			
	Friction Simulator Mk B			
	25 N to 2 kN ± 25° FE	100 N to 2 kN ± 25° FE	300 N to 2 kN ± 25° FE	25 N to 800 N ± 15° FE
Water	0.002 ± 0.001	0.002 ± 0.001	0.002 ± 0.001	0.000 ± 0.002
25 % NBCS	0.057 ± 0.003	0.062 ± 0.002	0.073 ± 0.001	0.106 ± 0.009
100 % NBCS	0.068 ± 0.002	0.064 ± 0.002	0.068 ± 0.001	0.095 ± 0.012
	300 N Constant ± 25° FE	1 kN Constant ± 25° FE		
Water	0.000 ± 0.001	0.001 ± 0.001		
25 % NBCS	0.133 ± 0.020	0.091 ± 0.002		
100 % NBCS	0.109 ± 0.005	0.091 ± 0.003		

Appendix E: Pendulum Friction Simulator A and Mk B Comparison

Feature/Specification	Friction Simulator A	Friction Simulator Mk B
OIL & PUMP		
Oil Type	Shell Tellus 37	Rando HD 32
40°C Kinematic Viscosity	37.0 centistokes (i.e. 0.03 pascal-second)	30.4 centistokes (i.e. 0.03 pascal-second)
Oil Pressure (running with 300N to 2kN load ± 25° FE)	1750 psi Steady state	1150 psi to 1250 psi Fluctuates Pump becomes very hot
HYDROSTATIC BEARING		
Capillary Tube Length	224 mm between the two end nuts	205 mm between the two end nuts
Capillary Tube ID	0.5 mm	0.8 mm
Observation of Oil Flow	Steady and constant	Fast and pulsating
TORQUE SENSOR		
Make & Model	Kistler 9203	Kistler 9217A
Characteristics	Piezoelectric for small tensile & compressive forces	
Transducer Assembly (Floating joint fitted to friction simulator B)	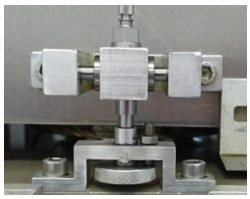	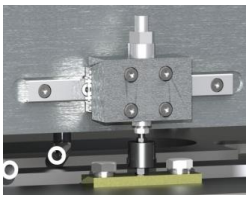
CHARGE AMPLIFIER		
Make & Model	Kistler 5015	Kistler 5073
Position	External	Internal
CONTROL		
Load Axis Control Mode	Force Control (open loop optional)	Open loop with limited PID control
CENTRE OF ROTATION		
Head Height	72.83 mm	99.91 mm (72.83 mm + 27.08 mm spacer)
Cup Height	63.24 mm	63.27 mm

Appendix F: Further Validation Studies Mean Results

	28 mm Ø MoP – Mean Friction Factor ± SD (n = 3)		
	Friction Simulator A		
	300 N to 2 kN ± 25° FE	25 N to 800 N ± 15° FE	800 N Constant ± 15° FE
Water	0.031 ± 0.001	0.035 ± 0.003	0.101 ± 0.010
25 % NBCS	0.055 ± 0.012	0.070 ± 0.005	0.165 ± 0.002
	Friction Simulator Mk B		
	300 N to 2 kN ± 25° FE	25 N to 800 N ± 15° FE	800 N Constant ± 15° FE
Water	0.031 ± 0.003	0.038 ± 0.002	0.104 ± 0.007
25 % NBCS	0.055 ± 0.001	0.062 ± 0.002	0.161 ± 0.004

	36 mm Ø CoC – Mean Friction Factor ± SD (n = 3)		
	Friction Simulator A		
	300 N to 2 kN ± 25° FE	25 N to 800 N ± 15° FE	800 N Constant ± 15° FE
Water	0.001 ± 0.001	0.002 ± 0.003	0.006 ± 0.001
25 % NBCS	0.067 ± 0.002	0.097 ± 0.006	0.071 ± 0.003
	Friction Simulator Mk B		
	300 N to 2 kN ± 25° FE	25 N to 800 N ± 15° FE	800 N Constant ± 15° FE
Water	0.000 ± 0.000	0.005 ± 0.003	0.009 ± 0.001
25 % NBCS	0.072 ± 0.002	0.109 ± 0.006	0.077 ± 0.008

<u>Appendix G</u>: Engineering Drawing of the Acetabulum Pot used for Testing Porcine Tissue in the Pendulum Friction Simulators

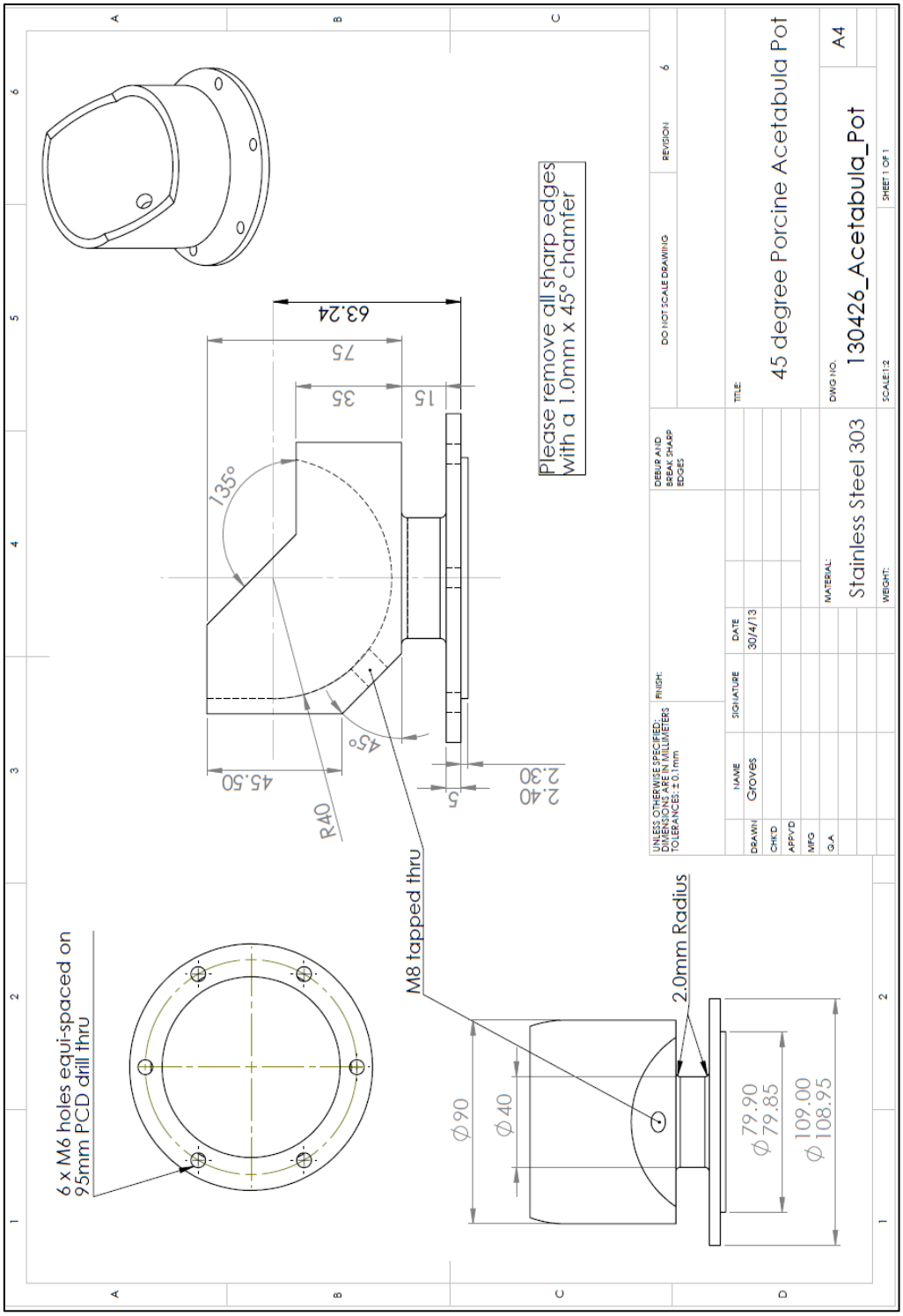

Appendix H: Porcine Femoral Head Test Fixture Concept Drawings

Femoral Head Test Fixture

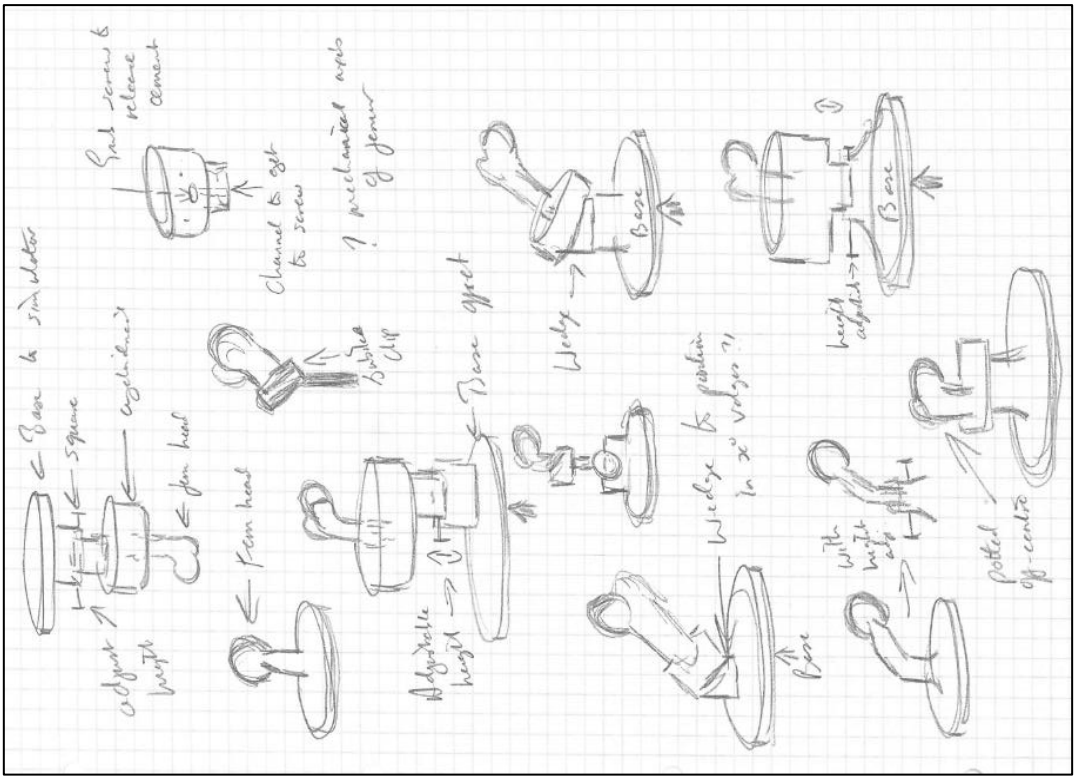

Femoral Head Potting Jig

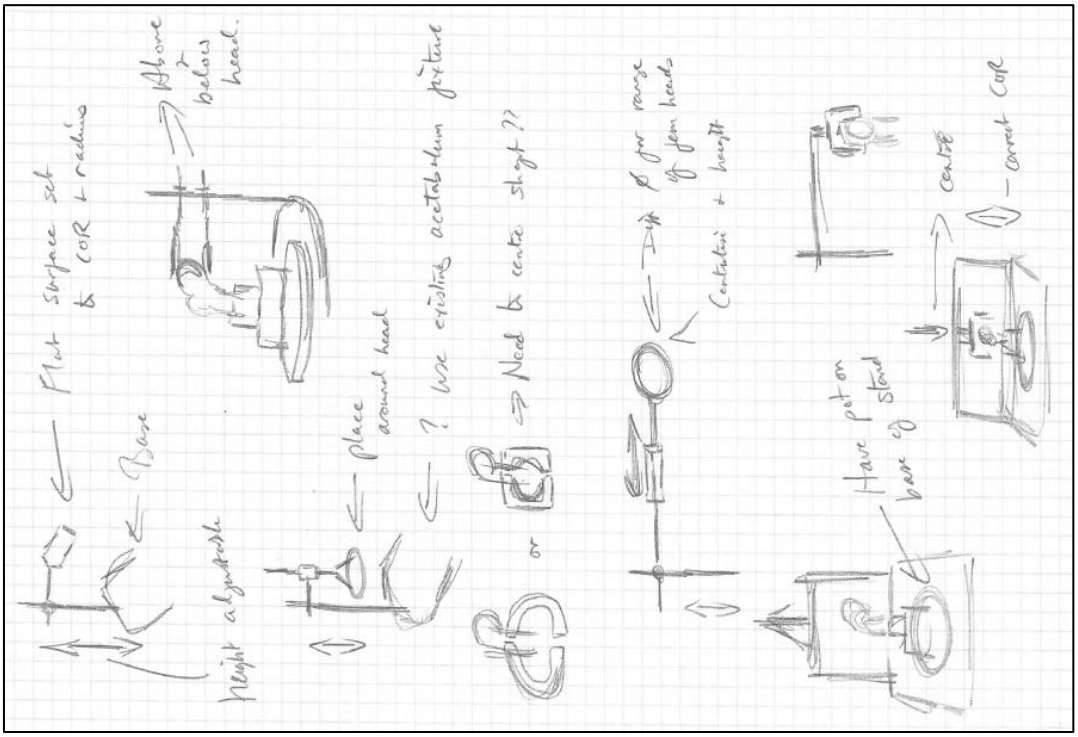

Appendix I: Engineering Drawings of the Test Pot Fixture used for Testing Porcine Femoral Heads in Pendulum Friction Simulator Mk B

Test Pot Fixture Base Plate (Attaches to FE rocker of simulator)

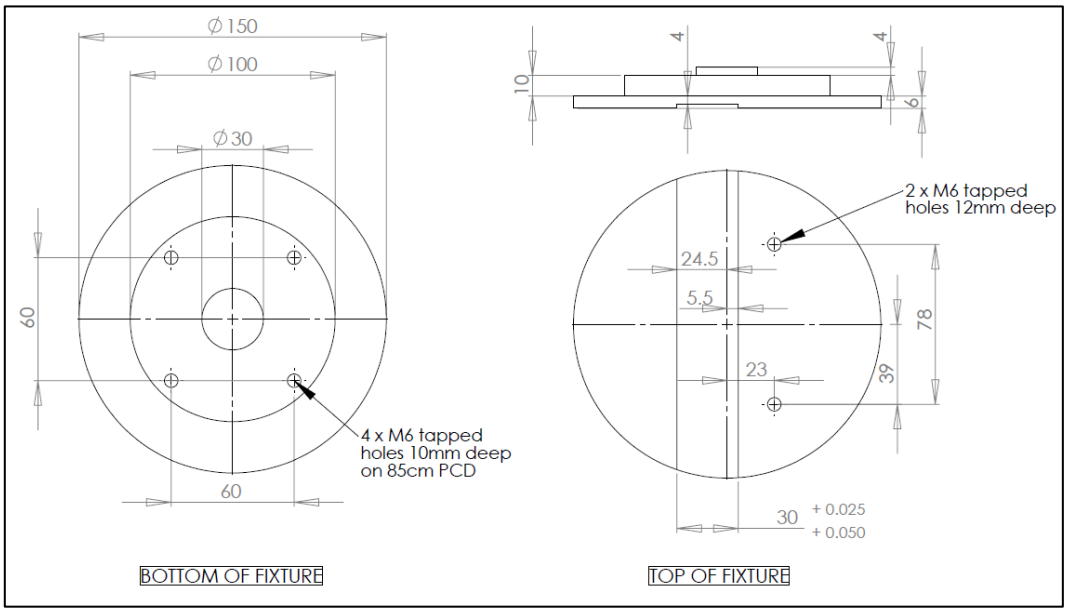

Test Pot Fixture Top Plate

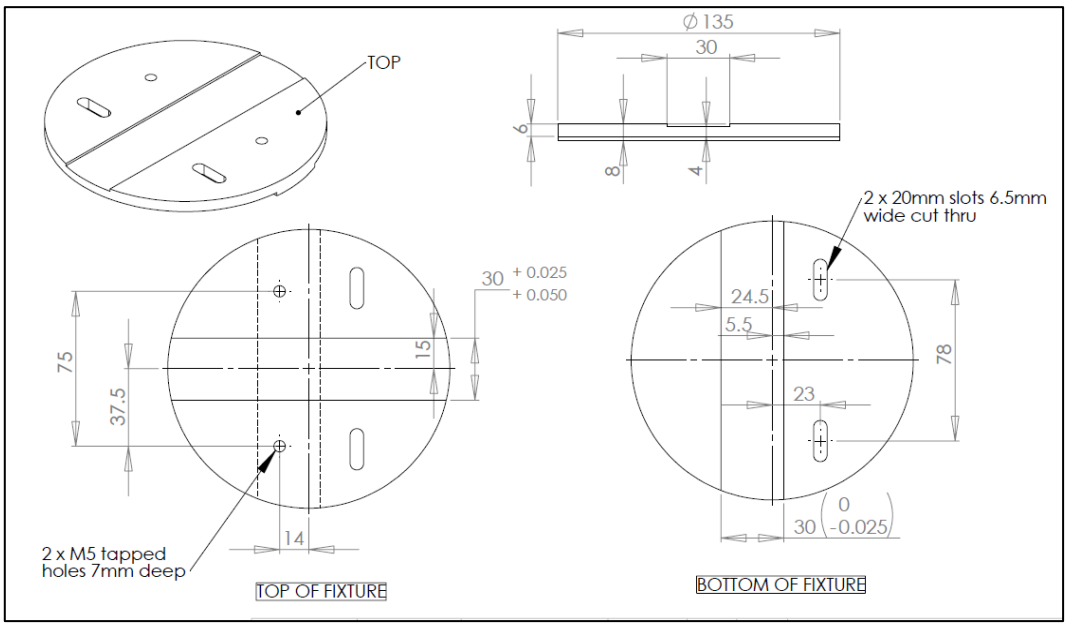

(Continued)

Femoral Head Test Pot

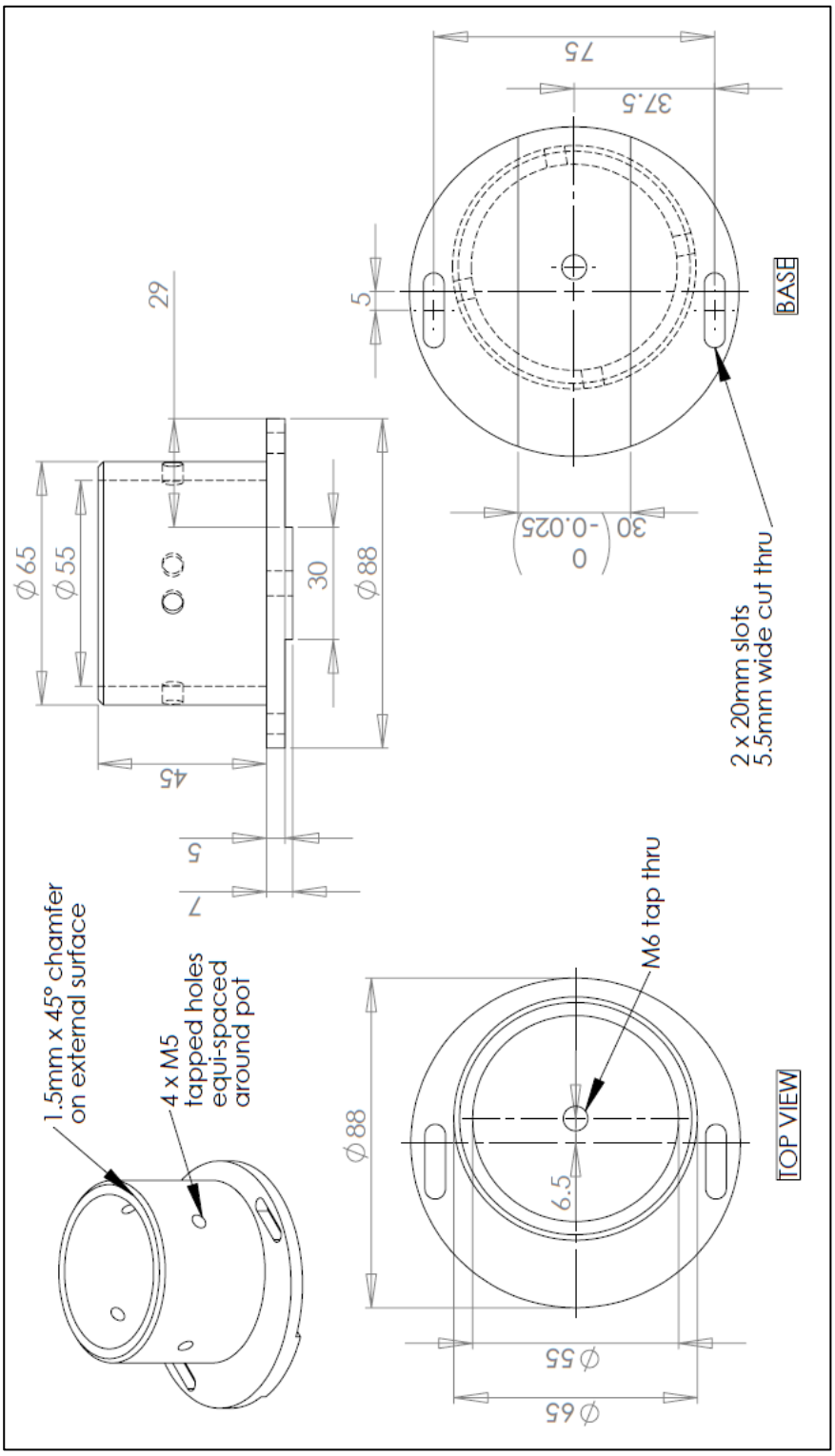

Appendix J: Engineering Drawings for the Femoral Head Potting Jig

Femoral Head Potting Jig Base

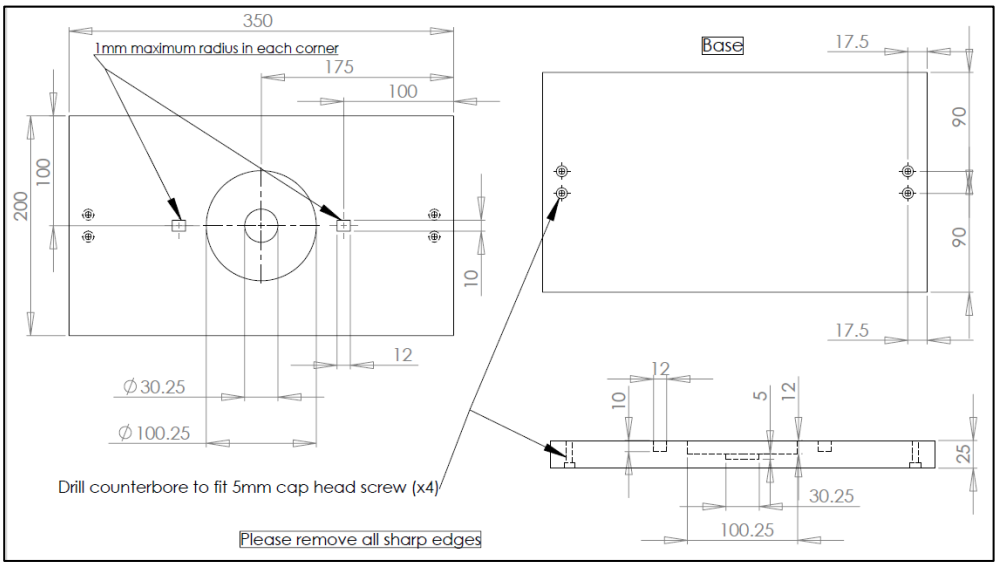

Left Potting Jig Base Post

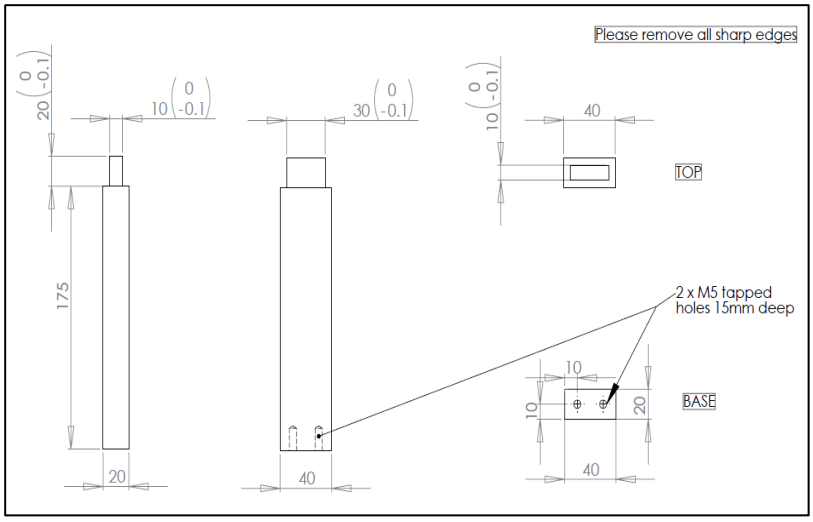

Right Potting Jig Base Post

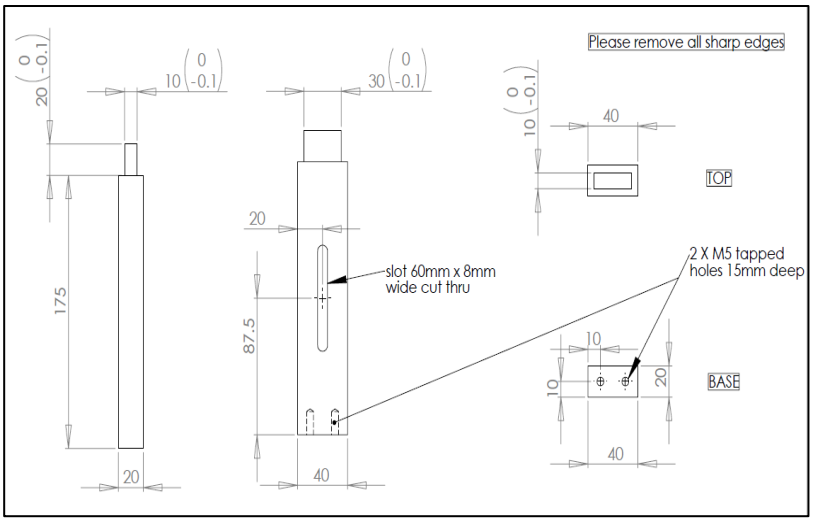

(Continued)

Femoral Head Potting Jig Top Bar

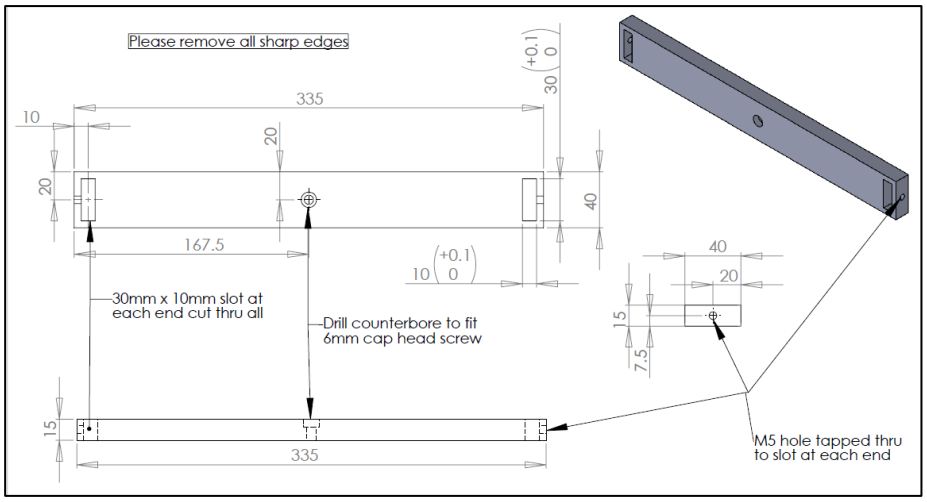

Femoral Head Potting Jig Hemisphere Attachment

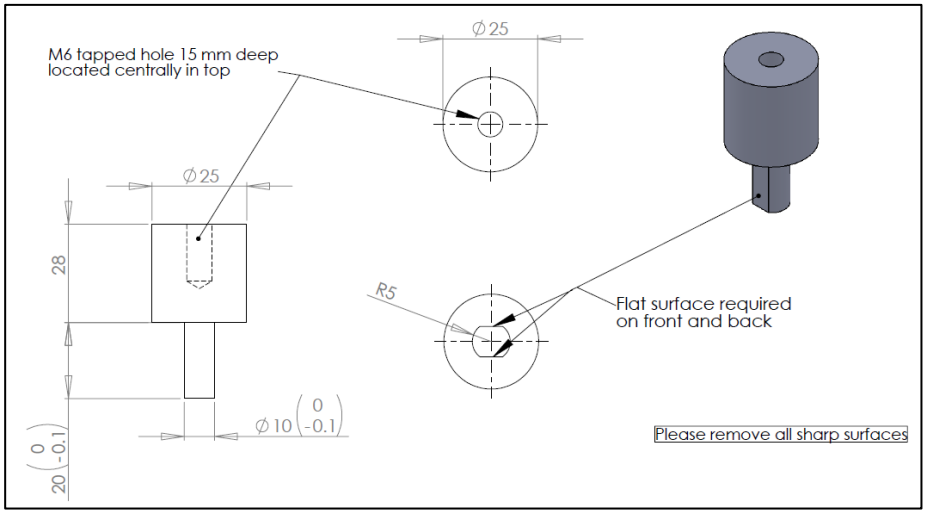

Femoral Head Potting Hemisphere (original design)

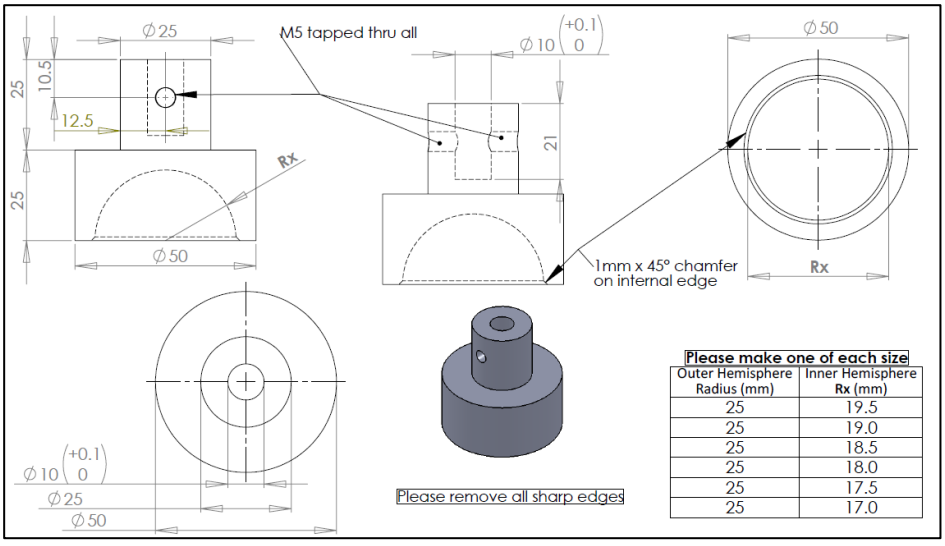

(Continued)

Femoral Head Potting Ring Base Post Attachment

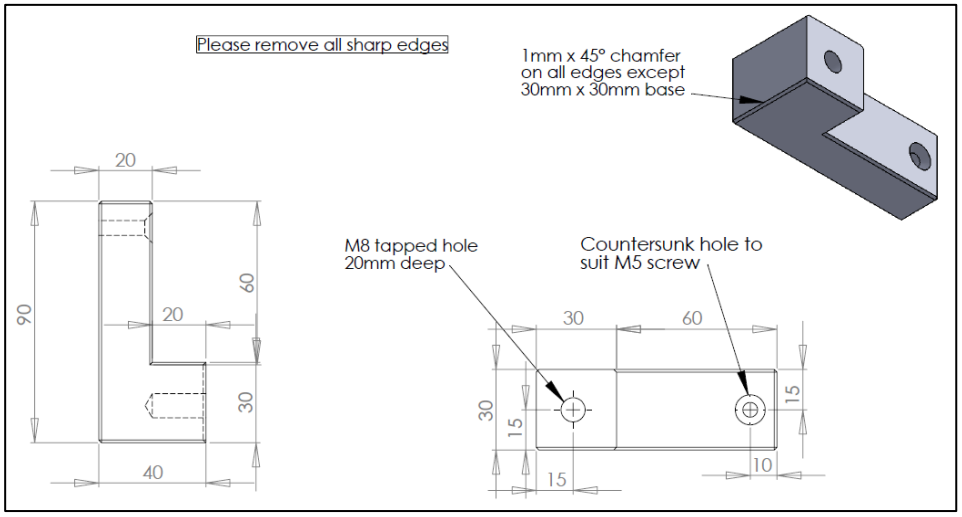

Femoral Head Potting Ring Arm

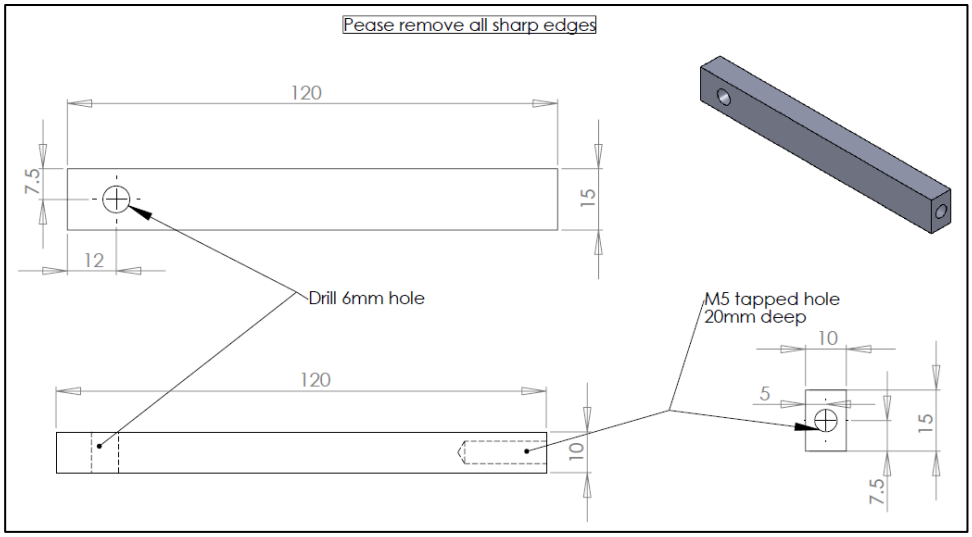

Femoral Head Potting Ring

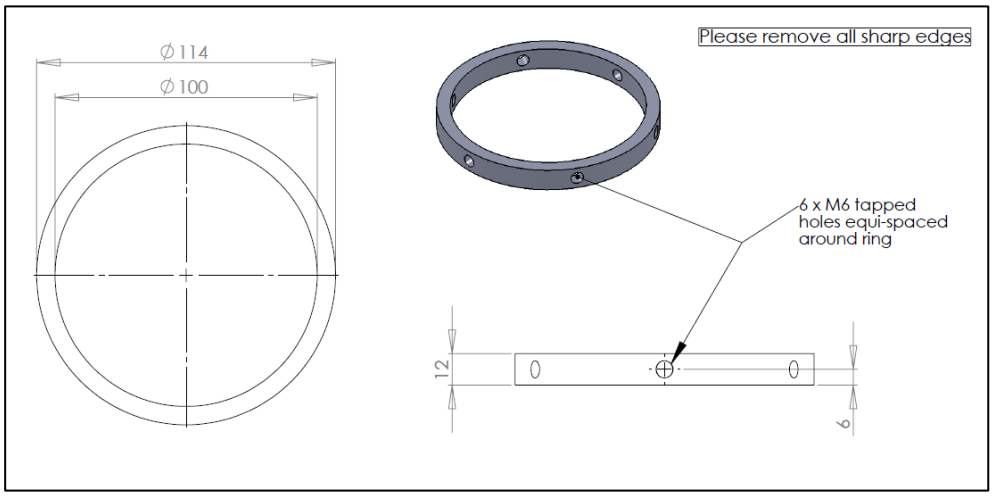

References

Abel, R., Prime, M., Jin, A., Cobb, J. & Bhattacharya, R. 2013. 3D Imaging Bone Quality: Bench to Bedside. Hard Tissue, 10 (2), pp.42-50.

Abraham, E., Gonzalez, M. H., Pratap, S., Amirouche, F., Atluri, P. & Simon, P. 2007. Clinical implications of anatomical wear characteristics in slipped capital femoral epiphysis and primary osteoarthritis. *Journal of Pediatric Orthopedics,* 27 (7)**,** pp.788-795.

Adeeb, S. M., Sayed Ahmed, E. Y., Matyas, J., Hart, D. A., Frank, C. B. & Shrive, N. G. 2004. Congruency effects on load bearing in diarthrodial joints. *Computer Methods in Biomechanics & Biomedical Engineering,* 7 (3)**,** pp.147-157.

Altman, R. D. & Gold, G. E. 2007. Atlas of individual radiographic features in osteoarthritis, revised. *Osteoarthritis and Cartilage,* 15 (Supplement 1)**,** pp.A1-A56.

Aly, A., Rajasekaran, S. & Obaid, H. 2013. MRI morphometric hip comparison analysis of anterior acetabular labral tears. *Skeletal Radiology,* 42 (9)**,** pp.1245-1252.

American College of Radiology 2005. Phantom Test Guidance. Virginia: ACR.

Anderson, A. E., Ellis, B. J., Maas, S. A. & Weiss, J. A. 2010. Effects of idealized joint geometry on finite element predictions of cartilage contact stresses in the hip. *Journal of Biomechanics,* 43 (7)**,** pp.1351-1357.

Anderson, L. A., Peters, C. L., Park, B. B., Stoddard, G. J., Erickson, J. A. & Crim, J. R. 2009. Acetabular Cartilage Delamination in Femoroacetabular Impingement. Risk Factors and Magnetic Resonance Imaging Diagnosis. *Journal of Bone & Joint Surgery - American Volume,* 91 (2)**,** pp.305-313.

Anderson, S. A. & Loeser, R. F. 2010. Why is osteoarthritis an age-related disease? *Best Practice & Research Clinical Rheumatology,* 24 (1)**,** pp.15-26.

Archbold, H., Slomczykowski, M., Cairns, H., Eckman, K., Jaramaz, B. & Beverland, D. 2009. Patient specific cup anteversion in total hip arthroplasty: a computed tomography study investigating the use of the transverse acetabular ligament to control cup placement. *Current Orthopaedic Practice,* 20 (1)**,** pp.73-76.

Archbold, H. A. P., Mockford, B., Molloy, D., McConway, J., Ogonda, L. & Beverland, D. 2006. The transverse acetabular ligament: an aid to orientation of the acetabular component during primary total hip replacement - A preliminary study of 1000 cases investigating postoperative stability. *Journal of Bone and Joint Surgery - British Volume,* 88B (7)**,** pp.883-886.

Arden, N. & Nevitt, M. C. 2006. Osteoarthritis: Epidemiology. *Best Practice & Research Clinical Rheumatology,* 20 (1)**,** pp.3-25.

Aspden, R. M. 2008. Osteoarthritis: a problem of growth not decay? *Rheumatology,* 47 (10)**,** pp.1452-1460.

Ateshian, G. A. 2009. The role of interstitial fluid pressurization in articular cartilage lubrication. *Journal of Biomechanics,* 42 (9)**,** pp.1163-1176.

Ateshian, G. A. & Wang, H. 1995. A theoretical solution for the frictionless rolling contact of cylindrical biphasic articular cartilage layers. *Journal of Biomechanics,* 28 (11)**,** pp.1341-1355.

Athanasiou, K. A., Agarwal, A. & Dzida, F. J. 1994. Comparative study of the intrinsic mechanical properties of the human acetabular and femoral head cartilage. *Journal of Orthopaedic Research,* 12 (3)**,** pp.340-349.

Athapattu, M., Saveh, A. H., Mahmud, J., Alrashidi, M., Wang, B. & Chizari, M. 2013. Accuracy of Measuring Methods on the Femoral Head. *Procedia Engineering,* 68**,** pp.83-87.

Atkinson, H., Johal, K., Willis-Owen, C., Zadow, S. & Oakeshott, R. 2010. Differences in hip morphology between the sexes in patients undergoing hip resurfacing. *Journal of Orthopaedic Surgery and Research,* 5 (1)**,** pp.76-80.

Auger, D. D., Dowson, D., Fisher, J. & Jin, Z. M. 1993. Friction and lubrication in cushion form bearings for artificial hip joints. *Proceedings of the Institution of Mechanical Engineers, Part H: Journal of Engineering in Medicine,* 207 (1)**,** pp.25-33.

Balamoody, S., Williams, T. G., Waterton, J. C., Bowes, M., Hodgson, R., Taylor, C. J. & Hutchinson, C. E. 2010. Comparison of 3T MR scanners in regional cartilage-thickness analysis in osteoarthritis: a cross-sectional multicenter, multivendor study. *Arthritis Research & Therapy,* 12 (5), R202.

Baldwin, L. N., Wachowicz, K., Thomas, S. D., Rivest, R. & Fallone, B. G. 2007. Characterization, prediction, and correction of geometric distortion in 3T MR images. *Medical Physics,* 34 (2)**,** pp.388-399.

Bardakos, N. V. & Villar, R. N. 2009. Predictors of progression of osteoarthritis in femoroacetabular impingement: a radiological study with a minimum of ten years follow-up. *Journal of Bone & Joint Surgery - British Volume,* 91 (2)**,** pp.162-169.

Bargar, W., Jamali, A. & Nejad, A. 2010. Femoral Anteversion in THA and its Lack of Correlation with Native Acetabular Anteversion. *Clinical Orthopaedics and Related Research,* 468 (2)**,** pp.527-532.

Barros, H., Camanho, G., Bernabé, A., Rodrigues, M. & Leme, L. 2010. Femoral Head-neck Junction Deformity is Related to Osteoarthritis of the Hip. *Clinical Orthopaedics and Related Research,* 468 (7), pp.1920-1925.

Beall, D. P., Martin, H. D., Mintz, D. N., Ly, J. Q., Costello, R. F., Braly, B. A. & Yoosefian, F. 2008. Anatomic and structural evaluation of the hip: a cross-sectional imaging technique combining anatomic and biomechanical evaluations. *Clinical Imaging,* 32 (5)**,** pp.372-381.

Beall, D. P., Sweet, C. F., Martin, H. D., Lastine, C. L., Grayson, D. E., Ly, J. Q. & Fish, J. R. 2005. Imaging findings of femoroacetabular impingement syndrome. *Skeletal Radiology,* 34 (11)**,** pp.691-701.

Beaule, P. E., O'Neill, M. & Rakhra, K. 2009. Acetabular Labral Tears. *Journal of Bone & Joint Surgery - American Volume,* 91 (3)**,** pp.701-710.

Beck, M., Kalhor, M., Leunig, M. & Ganz, R. 2005. Hip morphology influences the pattern of damage to the acetabular cartilage: femoroacetabular impingement as a cause of early osteoarthritis of the hip. *Journal of Bone & Joint Surgery - British Volume,* 87 (7)**,** pp.1012-1018.

Beckmann, J., Luring, C., Tingart, M., Anders, S., Grifka, J. & Kock, F. 2009. Cup positioning in THA: current status and pitfalls. A systematic evaluation of the literature. *Archives of Orthopaedic and Trauma Surgery,* 129 (7)**,** pp.863-872.

Bergmann, G., Graichen, F. & Rohlmann, A. 1999. Hip joint forces in sheep. *Journal of Biomechanics,* 32 (8)**,** pp.769-777.

Bergmann, G., Siraky, J., Rohlmann, A. & Koelbel, R. 1984. A comparison of hip joint forces in sheep, dog and man. *Journal of Biomechanics,* 17 (12)**,** pp.907-909, 911-921.

Bhosale, A. M. & Richardson, J. B. 2008. Articular cartilage: structure, injuries and review of management. *British Medical Bulletin,* 87 (1)**,** pp.77-95.

Biewener, A. A. 2003. *Animal Locomotion.* Oxford: Oxford University Press. ISBN: 0198500223.

Bijlsma, J. W. J. & Knahr, K. 2007. Strategies for the prevention and management of osteoarthritis of the hip and knee. *Best Practice & Research Clinical Rheumatology,* 21 (1)**,** pp.59-76.

Bitton, R. 2009. The economic burden of osteoarthritis. *American Journal of Managed Care,* 15 (Supplement 8)**,** pp.S230-S235.

Bland, J. M. & Altman, D. G. 2003. Applying the right statistics: analyses of measurement studies. *Ultrasound in Obstetrics and Gynecology,* 22 (1)**,** pp.85-93.

Bowes, M., DeSouza, K., Neogi, T. & Felson, D. T. 2010. Bone shape is not abnormal prior to OA but changes rapidly tith OA develpment and may be a useful marker of occurrence. *Osteoarthritis and Cartilage,* 18 (Supplement 2)**,** pp.S19-S19.

Bowes, M. A., Vincent, G. R., Wolstenholme, C. B. & Conaghan, P. G. 2015. A novel method for bone area measurement provides new insights into osteoarthritis and its progression. *Annals of the Rheumatic Diseases,* 74 (3)**,** pp.519-525.

Braun, H. J. & Gold, G. E. 2012. Diagnosis of osteoarthritis: Imaging. *Bone,* 51 (2)**,** pp.278-288.

British Stainless Steel Association. 2014. *50 Grades of Stainless Steel - 303* [Online]. [Accessed 28 December 2014]. Available from: http://www.bssa.org.uk/get_campaign.php?id=332

British Standards Institution 1998. BS EN ISO 4288:1998. Geometric Product Specification (GPS) — Surface texture — Profile method: Rules and procedures for the assessment of surface texture. London: BSI.

British Standards Institution 2002. BS ISO 14242-1:2002. Implants for surgery. Wear of total hip joint prostheses *Part 1: Loading and displacement parameters for wear-testing machines and corresponding environmental conditions for test.* London: BSI.

British Standards Institution 2008a. BS 7000-2:2008. Design management systems – Part 2: Guide to managing the design of manufactured products. London: BSI.

British Standards Institution 2008b. BS EN ISO 9001: 2008. Quality management systems. Requirements. London: BSI.

Brittberg, M., Aglietti, P., Gambardella, R., Hangody, L., Hauselmann, H. J., Jakob, R. P., Levine, D., Lohmander, S., Mandelbaum, B. R., Peterson, L. & Staubli, H.-U. 2000. Clinical Cartilage Injury Evaluation System. Göteborg, Sweden: International Cartilage Repair Society (ICRS).

Brockett, C. 2007. *Tribolgy of Large Diameter Metal-on-Metal Hip Resurfacing Replacements.* Ph.D., University of Leeds.

Brockett, C., Williams, S., Jin, Z. M., Isaac, G. & Fisher, J. 2007. Friction of total hip replacements with different bearings and loading conditions. *Journal of Biomedical Materials Research Part B - Applied Biomaterials,* 81B (2)**,** pp.508-515.

Buller, L. T., Rosneck, J., Monaco, F. M., Butler, R., Smith, T. & Barsoum, W. K. 2012. Relationship Between Proximal Femoral and Acetabular Alignment in Normal Hip Joints Using 3-Dimensional Computed Tomography. *The American Journal of Sports Medicine,* 40 (2)**,** pp.367-375.

Bullough, P., Goodfellow, J., Greenwald, A. S. & O'Connor, J. 1968. Incongruent Surfaces in the Human Hip Joint. *Nature,* 217 (5135)**,** pp.1290-1290.

Caligaris, M. & Ateshian, G. A. 2008. Effects of sustained interstitial fluid pressurization under migrating contact area, and boundary lubrication by synovial fluid, on cartilage friction. *Osteoarthritis and Cartilage,* 16 (10)**,** pp.1220-1227.

Cameron, M. L., Briggs, K. K. & Steadman, J. R. 2003. Reproducibility and Reliability of the Outerbridge Classification for Grading Chondral Lesions of the Knee Arthroscopically. *The American Journal of Sports Medicine,* 31 (1)**,** pp.83-86.

Castaño-Betancourt, M. C., Van Meurs, J. B. J., Bierma-Zeinstra, S., Rivadeneira, F., Hofman, A., Weinans, H., Uitterlinden, A. G. & Waarsing, J. H. 2013. The contribution of hip geometry to the prediction of hip osteoarthritis. *Osteoarthritis and Cartilage,* 21 (10)**,** pp.1530-1536.

CeramTec. 2012. *Materials - BIOLOX® Delta* [Online]. [Accessed 5 February 2013]. Available from: http://www.ceramtec.com/ceramic-materials/biolox/delta/

Cereatti, A., Margheritini, F., Donati, M. & Cappozzo, A. 2010. Is the human acetabulofemoral joint spherical? *Journal of Bone & Joint Surgery, British Volume,* 92-B (2)**,** pp.311-314.

Cerveri, P., Manzotti, A. & Baroni, G. 2012. Patient-specific acetabular shape modelling: comparison among sphere, ellipsoid and conchoid parameterisations. *Computer Methods in Biomechanics and Biomedical Engineering,* 17 (5)**,** pp.560-567.

Chang, H. & Fitzpatrick, J. M. 1992. A technique for accurate magnetic resonance imaging in the presence of field inhomogeneities. *Medical Imaging, IEEE Transactions on,* 11 (3)**,** pp.319-329.

Chegini, S., Beck, M. & Ferguson, S. J. 2009. The effects of impingement and dysplasia on stress distributions in the hip joint during sitting and walking: a finite element analysis. *Journal of Orthopaedic Research,* 27 (2)**,** pp.195-201.

Cheng, K. & Rowe, W. B. 1995. A selection strategy for the design of externally pressurized journal bearings. *Tribology International,* 28 (7)**,** pp.465-474.

Cheung, P. P., Gossec, L. & Dougados, M. 2010. What are the best markers for disease progression in osteoarthritis (OA)? *Best Practice & Research Clinical Rheumatology,* 24 (1)**,** pp.81-92.

Clark, J. M., Freeman, M. A. & Witham, D. 1987. The relationship of neck orientation to the shape of the proximal femur. *The Journal of Arthroplasty,* 2 (2)**,** pp.99-109.

Clohisy, J., Schutz, A., St. John, L., Schoenecker, P. & Wright, R. 2009. Periacetabular Osteotomy: A Systematic Literature Review. *Clinical Orthopaedics and Related Research,* 467 (8)**,** pp.2041-2052.

Clohisy, J. C., Carlisle, J. C., Beaule, P. E., Kim, Y.-J., Trousdale, R. T., Sierra, R. J., Leunig, M., Schoenecker, P. L. & Millis, M. B. 2008. A Systematic Approach to the Plain Radiographic Evaluation of the Young Adult Hip. *Journal of Bone & Joint Surgery - American Volume,* 90 (Supplement 4)**,** pp.47-66.

Cobb, S., Merchant, W. R. & Rubin, T. 1957. The relation of symptoms to osteoarthritis. *Journal of Chronic Diseases,* 5 (2)**,** pp.197-204.

Conrozier, T., Jousseaume, C., Mathieu, P., Tron, A., Caton, J., Bejui, J. & Vignon, E. 1998. Quantitative measurement of joint space narrowing progression in hip osteoarthritis: a longitudinal retrospective study of patients treated by total hip arthroplasty. *Rheumatology,* 37 (9)**,** pp.961-968.

Cootes, T. F., Edwards, G. J. & Taylor, C. J. 2001. Active appearance models. *Pattern Analysis and Machine Intelligence, IEEE Transactions on,* 23 (6)**,** pp.681-685.

Cootes, T. F., Taylor, C. J., Cooper, D. H. & Graham, J. 1995. Active Shape Models-Their Training and Application. *Computer Vision and Image Understanding,* 61 (1)**,** pp.38-59.

Croft, P. 2005. The epidemiology of osteoarthritis: Manchester and beyond. *Rheumatology,* 44 (Supplement 4)**,** pp.27-32.

Crowe, J. F., Sculco, T. P. & Kahn, B. 2003. Revision Total Hip Arthroplasty: Hospital Cost and Reimbursement Analysis. *Clinical Orthopaedics and Related Research,* 413**,** pp.175-182.

Curl, W. W., Krome, J., Gordon, E. S., Rushing, J., Smith, B. P. & Poehling, G. G. 1997. Cartilage injuries: A review of 31,516 knee arthroscopies. *Arthroscopy: The Journal of Arthroscopic & Related Surgery,* 13 (4)**,** pp.456-460.

Damen, J., Schiphof, D., Wolde, S. T., Cats, H. A., Bierma-Zeinstra, S. M. A. & Oei, E. H. G. 2014. Inter-observer reliability for radiographic assessment of early osteoarthritis features: the CHECK (cohort hip and cohort knee) study. *Osteoarthritis and Cartilage,* 22 (7)**,** pp.969-974.

Dandachli, W., Islam, S. U., Liu, M., Richards, R., Hall-Craggs, M. & Witt, J. 2009. Three-dimensional CT analysis to determine acetabular retroversion and the implications for the management of femoro-acetabular impingement. *Journal of Bone & Joint Surgery - British Volume,* 91-B (8)**,** pp.1031-1036.

Dandachli, W., Kannan, V., Richards, R., Shah, Z., Hall-Craggs, M. & Witt, J. 2008. Analysis of cover of the femoral head in normal and dysplastic hips: New CT-based technique. *Journal of Bone & Joint Surgery - British Volume,* 90-B (11)**,** pp.1428-1434.

Daniel, M., Iglic, A. & Kralj-Iglic, V. 2008. Hip contact stress during normal and staircase walking: the influence of acetabular anteversion angle and lateral coverage of the acetabulum. *Journal of applied biomechanics,* 24 (1)**,** pp.88-93.

Dawson, J., Fitzpatrick, R., Carr, A. & Murray, D. 1996. Questionnaire on the perceptions of patients about total hip replacement. *Journal of Bone & Joint Surgery - British Volume,* 78-B (2)**,** pp.185-190.

Delfaut, E. M., Beltran, J., Johnson, G., Rousseau, J., Marchandise, X. & Cotten, A. 1999. Fat Suppression in MR Imaging: Techniques and Pitfalls. *Radiographics,* 19 (2)**,** pp.373-382.

DePuy Synthes. 2014. *MARATHON™ Crosslinked Polyethylene* [Online]. [Accessed 20 December 2014]. Available from: https://emea.depuysynthes.com/hcp/hip/products/qs/marathon-crosslinked-polyethylene

Dewey, E. C. 2006. Diseases of the Nervous and Locomoter Systems. *Diseases of the Swine.* 9th ed. Oxford: Blackwell Publishing Ltd. ISBN: 0813817033.

Dezateux, C. & Rosendahl, K. 2007. Developmental dysplasia of the hip. *The Lancet,* 369 (9572)**,** pp.1541-1552.

Doherty, M., Lanyon, P. & Hosie, G. (eds.) 2005. *Osteoarthritis of the Knee and Hip.* Chesterfield: Arthritis Research Campaign.

Dujardin, F. H., Roussignol, X., Mejjad, O., Weber, J. & Thomine, J. M. 1997. Interindividual variations of the hip joint motion in normal gait. *Gait & Posture,* 5 (3)**,** pp.246-250.

Duong, C.-T., Lee, J.-H., Cho, Y., Nam, J.-S., Kim, H.-N., Lee, S.-S. & Park, S. 2012. Effect of protein concentrations of bovine serum albumin and γ-globulin on the frictional response of a cobalt-chromium femoral head. *Journal of Materials Science: Materials in Medicine,* 23 (5)**,** pp.1323-1330.

DuPont Engineering Polymers. 2001. *Delrin® acetal resin - Product and Properties Guide* [Online]. [Accessed 15 January 2012]. Available from: http://plastics.dupont.com/plastics/pdflit/americas/delrin/H76836.pdf

Ecker, T. M., Tannast, M., Puls, M., Siebenrock, K. A. & Murphy, S. B. 2007. Pathomorphologic alterations predict presence or absence of hip osteoarthrosis. *Clinical Orthopaedics and Related Research,* 465**,** pp.46-52.

Eckstein, F., Buck, R. J., Burstein, D., Charles, H. C., Crim, J., Hudelmaier, M., Hunter, D. J., Hutchins, G., Jackson, C., Kraus, V. B., Lane, N. E., Link, T. M., Majumdar, L. S., Mazzuca, S., Prasad, P. V., Schnitzer, T. J., Taljanovic, M. S., Vaz, A., Wyman, B., Le Graverand, M.-P. H. & on behalf of the A9001140 Study Group 2008. Precision of 3.0 Tesla quantitative magnetic resonance imaging of cartilage morphology in a multicentre clinical trial. *Annals of the Rheumatic Diseases,* 67 (12)**,** pp.1683-1688.

Epstein, N., Woolson, S. & Giori, N. 2011. Acetabular Component Positioning Using the Transverse Acetabular Ligament: Can You Find It and Does It Help? *Clinical Orthopaedics and Related Research,* 469 (2)**,** pp.412-416.

Erasmus, L. J., Hurter, D., Naude, M. & Kritzinger, H. G. 2004. A Short Overview of MRI Artefacts. *South African Journal of Radiology,* 8 (4)**,** pp.13-17.

Ezoe, M., Naito, M. & Inoue, T. 2006. The prevalence of acetabular retroversion among various disorders of the hip. *Journal of Bone & Joint Surgery - American Volume,* 88 (2)**,** pp.372-379.

Farjoodi, P., Mesfin, A., Carrino, J. A. & Khanna, A. J. 2010. Magnetic Resonance Imaging of the Musculoskeletal System: Basic Science, Pulse Sequences, and a Systematic Approach to Image Interpretation. *Journal of Bone & Joint Surgery - American Volume,* 92 (Supplement 2)**,** pp.105-116.

Felson, D. T. 2004. Risk factors for osteoarthritis - Understanding joint vulnerability. *Clinical Orthopaedics and Related Research,* 427**,** pp.S16-S21.

Felson, D. T. 2009. Developments in the clinical understanding of osteoarthritis. *Arthritis Research & Therapy,* 11 (1)**,** pp.203-213.

Felson, D. T., Lawrence, R. C., Dieppe, P. A., Hirsch, R., Helmick, C. G., Jordan, J. M., Kington, R. S., Lane, N. E., Nevitt, M. C., Zhang, Y., Sowers, M., McAlindon, T., Spector, T. D., Poole, A. R., Yanovski, S. Z., Ateshian, G., Sharma, L., Buckwalter, J. A., Brandt, K. D. & Fries, J. F. 2000a. Osteoarthritis: new insights. Part 1: the disease and its risk factors. *Annals of Internal Medicine,* 133 (8)**,** pp.635-646.

Felson, D. T., Lawrence, R. C., Hochberg, M. C., McAlindon, T., Dieppe, P. A., Minor, M. A., Blair, S. N., Berman, B. M., Fries, J. F., Weinberger, M., Lorig, K. R., Jacobs, J. J. & Goldberg, V. 2000b. Osteoarthritis: New insights - Part 2: Treatment approaches. *Annals of Internal Medicine,* 133 (9)**,** pp.726-737.

Ferguson, S. J., Bryant, J. T., Ganz, R. & Ito, K. 2003. An in vitro investigation of the acetabular labral seal in hip joint mechanics. *Journal of Biomechanics,* 36 (2)**,** pp.171-178.

Field, A. 2009. *Discovering Statistics using SPSS.* 3rd ed. London, UK: SAGE Publications Ltd. ISBN: 1847879071.

Field, R. E. & Rajakulendran, K. 2011. The Labro-Acetabular Complex. *Journal of Bone & Joint Surgery - American Volume,* 93 (Supplement 2)**,** pp.22-27.

Fisher, R. A. 1936. The use of multiple measurements in taxonomic problems. *Annals of Eugenics,* 7 (2)**,** pp.179-188.

Flanagan, S., Jones, E. & Birkinshaw, C. 2010. In vitro friction and lubrication of large bearing hip prostheses. *Proceedings of the Institution of Mechanical Engineers, Part H: Journal of Engineering in Medicine,* 224 (7)**,** pp.853-864.

Forster, H. & Fisher, J. 1996. The influence of loading time and lubricant on the friction of articular cartilage. *Proceedings of the Institution of Mechanical Engineers, Part H: Journal of Engineering in Medicine,* 210 (28)**,** pp.109-119.

Forster, H. & Fisher, J. 1999. The influence of continuous sliding and subsequent surface wear on the friction of articular cartilage. *Proceedings of the Institution of Mechanical Engineers, Part H: Journal of Engineering in Medicine,* 213 (4)**,** pp.329-345.

Fox, A. J. S., Bedi, A. & Rodeo, S. A. 2009. The Basic Science of Articular Cartilage: Structure, Composition, and Function. *Sports Health: A Multidisciplinary Approach,* 1 (6)**,** pp.461-468.

Fuchs-Winkelmann, S., Peterlein, C. D., Tibesku, C. O. & Weinstein, S. L. 2008. Comparison of pelvic radiographs in weightbearing and supine positions. *Clinical Orthopaedics and Related Research,* 466 (4)**,** pp.809-812.

Fujii, M., Nakashima, Y., Yamamoto, T., Mawatari, T., Motomura, G., Matsushita, A., Matsuda, S., Jingushi, S. & Iwamoto, Y. 2010. Acetabular Retroversion in Developmental Dysplasia of the Hip. *Journal of Bone & Joint Surgery - American Volume,* 92 (4)**,** pp.895-903.

Furey, M. J. & Burkhardt, B. M. 1997. Biotribology: Friction, Wear, and Lubrication of Natural Synovial Joints. *Lubrication Science,* 9 (3)**,** pp.255-271.

Ganz, R., Leunig, M., Leunig-Ganz, K. & Harris, W. H. 2008. The etiology of osteoarthritis of the hip: an integrated mechanical concept. *Clinical Orthopaedics and Related Research,* 466 (2)**,** pp.264-272.

Ganz, R. M. D., Parvizi, J. M. D., Beck, M. M. D., Leunig, M. M. D., Notzli, H. M. D. & Siebenrock, K. A. M. D. 2003. Femoroacetabular Impingement: A Cause for Osteoarthritis of the Hip. *Clinical Orthopaedics and Related Research,* 417**,** pp.112-120.

Garden, R. S. 1961. The Structure and Function of the Proximal End of the Femur. *Journal of Bone & Joint Surgery - British Volume,* 43-B (3)**,** pp.576-589.

Gautschi, G. 2001. *Piezoelectric sensorics : force, strain, pressure, acceleration and acoustic emission sensors, materials and amplifiers.* Berlin: Springer. ISBN: 3540422595.

Getgood, A., Bhullar, T. P. S. & Rushton, N. 2009. Current concepts in articular cartilage repair. *Orthopaedics and Trauma,* 23 (3)**,** pp.189-200.

Ghosh, S., Choudhury, D., Das, N. S. & Pingguan-Murphy, B. 2014. Tribological role of synovial fluid compositions on artificial joints — a systematic review of the last 10 years. *Lubrication Science,* 26 (6)**,** pp.387-410.

Gillard, F. C., Dickinson, A. S., Schneider, U., Taylor, A. C. & Browne, M. 2013. Multi-pelvis characterisation of articular cartilage geometry. *Proceedings of the Institution of Mechanical Engineers, Part H: Journal of Engineering in Medicine,* 227 (12)**,** pp.1255-1264.

Giori, N. J., Trousdale, R. T., Giori, N. J. & Trousdale, R. T. 2003. Acetabular retroversion is associated with osteoarthritis of the hip. *Clinical Orthopaedics and Related Research,* (417)**,** pp.263-269.

Gold, G. E., Han, E., Stainsby, J., Wright, G., Brittain, J. & Beaulieu, C. 2004. Musculoskeletal MRI at 3.0 T: Relaxation Times and Image Contrast. *American Journal of Roentgenology,* 183 (2)**,** pp.343-351.

Gosvig, K. K., Jacobsen, S., Sonne-Holm, S., Palm, H. & Troelsen, A. 2010. Prevalence of Malformations of the Hip Joint and Their Relationship to Sex, Groin Pain, and Risk of Osteoarthritis: A Population-Based Survey. *Journal of Bone & Joint Surgery - American Volume,* 92 (5)**,** pp.1162-1169.

Goudie, S. T., Deakin, A. H. & Deep, K. 2015. Natural acetabular orientation in arthritic hips. *Bone and Joint Research,* 4 (1)**,** pp.6-10.

Govsa, F., Ozer, M. A. & Ozgur, Z. 2005. Morphologic features of the acetabulum. *Archives of Orthopaedic and Trauma Surgery,* 125 (7)**,** pp.453-461.

Gray, H. 2000. Anatomy of the Human Body. *In:* Lewis, W. H. (ed.) 20th ed. Philadelphia: Bartleby.com. ISBN: 1587341026.

Grenier, J.-M. & Wessely, M. A. 2006. Hip and pelvis MRI: Part 1: A basic overview. *Clinical Chiropractic,* 9 (2)**,** pp.92-98.

Groh, M. M. & Herrera, J. 2009. A comprehensive review of hip labral tears. *Current Reviews in Musculoskeletal Medicine,* 2 (2)**,** pp.105-117.

Günther, K. P. & Sun, Y. 1999. Reliability of radiographic assessment in hip and knee osteoarthritis. *Osteoarthritis and Cartilage,* 7 (2)**,** pp.239-246.

Haas, S., Brauer, G. & Dickson, G. 1975. A characterization of polymethylmethacrylate bone cement. *Journal of Bone & Joint Surgery - American Volume,* 57 (3)**,** pp.380-391.

Hamrock, B. J. & Dowson, D. 1978. Elastohydrodynamic Lubrication of Elliptical Contacts for Materials of Low Elastic Modulus I—Fully Flooded Conjunction. Journal of Tribology, 100 (2), pp.236-245.

Harris-Hayes, M. & Royer, N. K. 2011. Relationship of Acetabular Dysplasia and Femoroacetabular Impingement to Hip Osteoarthritis: A Focused Review. *The American Academy of Physical Medicine and Rehabilitation,* 3 (11)**,** pp.1055-1067.

Harris, W. H. 1986. Etiology of Osteoarthritis of the Hip. *Clinical Orthopaedics and Related Research,* 213**,** pp.20-33.

Harrison, M. H. M., Schajowicz, F. & Trueta, J. 1953. Osteoarthritis of the hip: a study of the nature and evolution of the disease. *Journal of Bone & Joint Surgery - British Volume,* 35-B (4)**,** pp.598-626.

Hasegawa, Y., Masui, T., Yamaguchi, J., Kawabe, K. & Suzuki, S. 2007. Factors leading to osteoarthritis after eccentric rotational acetabular osteotomy. *Clinical Orthopaedics and Related Research,* 459**,** pp.207-215.

Hassan, D. M., Johnston, G. H. F., Dust, W. N. C., Watson, G. & Dolovich, A. T. 1998. Accuracy of intraoperative assessment of acetabular prosthesis placement. *The Journal of Arthroplasty,* 13 (1)**,** pp.80-84.

Hayakawa, K., Minoda, Y., Aihara, M., Sakawa, A., Ohzono, K. & Tada, K. 2009. Acetabular component orientation in intra- and postoperative positions in total hip arthroplasty. *Archives of Orthopaedic & Trauma Surgery,* 129 (9)**,** pp.1151-1156.

Heller, M. O., Bergmann, G., Deuretzbacher, G., Dürselen, L., Pohl, M., Claes, L., Haas, N. P. & Duda, G. N. 2001. Musculo-skeletal loading conditions at the hip during walking and stair climbing. *Journal of Biomechanics,* 34 (7)**,** pp.883-893.

Higginson, G. R. 1978. Squeeze films between compliant solids. *Wear,* 46 (2)**,** pp.387-395.

Holroyd, B. & Wedge, J. 2009. (iii) Developmental dysplasia of the hip. *Orthopaedics and Trauma,* 23 (3)**,** pp.162-168.

Hong, R. J., Hughes, T. H., Gentili, A. & Chung, C. B. 2008. Magnetic resonance imaging of the hip. *Journal of Magnetic Resonance Imaging,* 27 (3)**,** pp.435-445.

Hossain, M. & Andrew, J. G. 2008. Current management of femoro-acetabular impingement. *Current Orthopaedics,* 22 (4)**,** pp.300-310.

Hurley, M. V. 2003. Muscle dysfunction and effective rehabilitation of knee osteoarthritis: What we know and what we need to find out. *Arthritis & Rheumatism-Arthritis Care & Research,* 49 (3)**,** pp.444-452.

Hutton, C. W. 1989. Osteoarthritis: the cause not result of joint failure? *Annals of the Rheumatic Diseases,* 48 (11)**,** pp.958-961.

Ilizaliturri, V. M., Byrd, J. W. T., Sampson, T. G., Guanche, C. A., Philippon, M. J., Kelly, B. T., Dienst, M., Mardones, R., Shonnard, P. & Larson, C. M. 2008. A Geographic Zone Method to Describe Intra-articular Pathology in Hip Arthroscopy: Cadaveric Study and Preliminary Report. *Arthroscopy: The Journal of Arthroscopic & Related Surgery,* 24 (5)**,** pp.534-539.

Jackson, E., Bronskill, M., Drost, D., Och, J., Pooley, R., Sobol, W. & Clarke, G. 2010. Acceptance testing and quality assurance procedures for magnetic resonance imaging facilities. College park: American association of physicists in medicine.

Jacobsen, S., Romer, L. & Soballe, K. 2005. Degeneration in dysplastic hips. A computer tomography study. *Skeletal Radiology,* 34 (12)**,** pp.778-784.

Jacobsen, S. & Sonne-Holm, S. 2005. Hip dysplasia: a significant risk factor for the development of hip osteoarthritis. A cross-sectional survey. *Rheumatology,* 44 (2)**,** pp.211-218.

Jang, I. G. & Kim, I. Y. 2008. Computational study of Wolff's law with trabecular architecture in the human proximal femur using topology optimization. *Journal of Biomechanics,* 41 (11)**,** pp.2353-2361.

Jeffery, A. K. 1975. Osteophytes and the osteoarthritic femoral head. *Journal of Bone & Joint Surgery - British Volume,* 57-B (3)**,** pp.314-324.

Jeffery, J. A. & Ong, T. J. 2000. Femoral head measurement in hemiarthroplasty: assessment of interobserver error using 3 measuring systems. *Injury,* 31 (3)**,** pp.135-138.

Jessel, R. H., Zurakowski, D., Zilkens, C., Burstein, D., Gray, M. L. & Kim, Y.-J. 2009. Radiographic and patient factors associated with pre-radiographic osteoarthritis in hip dysplasia. *Journal of Bone & Joint Surgery - American Volume,* 91 (5)**,** pp.1120-1129.

Jin, Z., Dowson, D. & Fisher, J. 1997. Analysis of fluid film lubrication in artificial hip joint replacements with surfaces of high elastic modulus. Proceedings of the Institution of Mechanical Engineers, Part H: Journal of Engineering in Medicine, 211 (3), pp.247-256.

Johnsen, K., Goll, R. & Reikeras, O. 2009. Acetabular dysplasia as an aetiological factor in development of hip osteoarthritis. *International Orthopaedics,* 33 (3)**,** pp.653-657.

Juhakoski, R., Heliovaara, M., Impivaara, O., Kroger, H., Knekt, P., Lauren, H. & Arokoski, J. P. A. 2009. Risk factors for the development of hip osteoarthritis: a population-based prospective study. *Rheumatology,* 48 (1)**,** pp.83-87.

Kalteis, T. A., Handel, M., Herbst, B., Grifka, J. & Renkawitz, T. 2009. In Vitro Investigation of the Influence of Pelvic Tilt on Acetabular Cup Alignment. *The Journal of Arthroplasty,* 24 (1)**,** pp.152-157.

Kang, A. C. L., Gooding, A. J., Coates, M. H., Goh, T. D., Armour, P. & Rietveld, J. 2010. Computed Tomography Assessment of Hip Joints in Asymptomatic Individuals in Relation to Femoroacetabular Impingement. *The American Journal of Sports Medicine* [Online], Published online March 12, 2010. Available: http://ajs.sagepub.com/content/early/2010/03/11/0363546509358320.abstract [Accessed May 14 2010].

Karachalios, T., Karantanas, A. H. & Malizos, K. 2007. Hip osteoarthritis: What the radiologist wants to know. *European Journal of Radiology,* 63 (1)**,** pp.36-48.

Kassarjian, A., Brisson, M. & Palmer, W. E. 2007. Femoroacetabular impingement. *European Journal of Radiology,* 63 (1)**,** pp.29-35.

Katta, J., Jin, Z., Ingham, E. & Fisher, J. 2008. Biotribology of articular cartilage--A review of the recent advances. *Medical Engineering & Physics,* 30 (10)**,** pp.1349-1363.

Katta, J., Jin, Z., Ingham, E. & Fisher, J. 2009. Effect of nominal stress on the long term friction, deformation and wear of native and glycosaminoglycan deficient articular cartilage. *Osteoarthritis and Cartilage,* 17 (5)**,** pp.662-668.

Katta, J., Pawaskar, S., Jin, Z., Ingham, E. & Fisher, J. 2007. Effect of load variation on the friction properties of articular cartilage. *Proceedings of the Institution of Mechanical Engineers, Part J: Journal of Engineering Tribology,* 221 (3)**,** pp.175-181.

Kelley, T. C. & Swank, M. L. 2009. Role of Navigation in Total Hip Arthroplasty. *Journal of Bone & Joint Surgery - American Volume,* 91 (Supplement 1)**,** pp.153-158.

Kellgren, J. H. & Lawrence, J. S. 1957. Radiological Assessment of Osteo-Arthrosis. *Annals of the Rheumatic Diseases,* 16 (4)**,** pp.494-502.

Kennedy, J. G., Rogers, W. B., Soffe, K. E., Sullivan, R. J., Griffen, D. G. & Sheehan, L. J. 1998. Effect of acetabular component orientation on recurrent dislocation, pelvic osteolysis, polyethylene wear, and component migration. *The Journal of Arthroplasty,* 13 (5)**,** pp.530-534.

Kim, W. Y., Hutchinson, C. E., Andrew, J. G. & Allen, P. D. 2006a. The relationship between acetabular retroversion and osteoarthritis of the hip. *Journal of Bone and Joint Surgery - British Volume,* 88B (6)**,** pp.727-729.

Kim, Y.-H., Choi, Y. & Kim, J.-S. 2009. Influence of Patient-, Design-, and Surgery-Related Factors on Rate of Dislocation After Primary Cementless Total Hip Arthroplasty. *The Journal of Arthroplasty,* 24 (8)**,** pp.1258-1263.

Kim, Y.-J., Ganz, R., Murphy, S. B., Buly, R. L. & Millis, M. B. 2006b. Hip joint-preserving surgery: beyond the classic osteotomy. *Instructional Course Lectures,* 55**,** pp.145-158.

Klaue, K., Durnin, C. & Ganz, R. 1991. The acetabular rim syndrome. A clinical presentation of dysplasia of the hip. *Journal of Bone & Joint Surgery - British Volume,* 73-B (3)**,** pp.423-429.

Kohnlein, W., Ganz, R., Impellizzeri, F. M. & Leunig, M. 2009. Acetabular morphology: implications for joint-preserving surgery. *Clinical Orthopaedics and Related Research,* 467 (3)**,** pp.682-691.

Konan, S., Rayan, F., Meermans, G., Witt, J. & Haddad, F. S. 2011. Validation of the classification system for acetabular chondral lesions identified at arthroscopy in patients with femoroacetabular impingement. *Journal of Bone & Joint Surgery - British Volume,* 93-B (3)**,** pp.332-336.

König, H. E. & Liebich, H.-G. 2009. *Veterinary Anatomy of Domestic Mammals: Textbook and Colour Atlas.* Stuttgart: Schattauer. ISBN: 3794526775.

Kosashvili, Y., Backstein, D., Safir, O., Ran, Y., Loebenberg, M. I. & Ziv, Y. B. 2008. Hemiarthroplasty of the hip for fracture—What is the appropriate sized femoral head? *Injury,* 39 (2)**,** pp.232-237.

Krebs, V., Incavo, S. J. & Shields, W. H. 2009. The anatomy of the acetabulum: what is normal? *Clinical Orthopaedics and Related Research,* 467 (4)**,** pp.868-875.

Lane, N. E. 2007. Osteoarthritis of the hip. *New England Journal of Medicine,* 357 (14)**,** pp.1413-1421.

Lane, N. E., Lin, P., Christiansen, L., Gore, L. R., Williams, E. N., Hochberg, M. C. & Nevitt, M. C. 2000. Association of mild acetabular dysplasia with an increased risk of incident hip osteoarthritis in elderly white women: the study of osteoporotic fractures. *Arthritis and Rheumatism,* 43 (2)**,** pp.400-404.

Lane, N. E., Nevitt, M. C., Hochberg, M. C., Hung, Y.-Y. & Palermo, L. 2004. Progression of radiographic hip osteoarthritis over eight years in a community sample of elderly white women.[see comment]. *Arthritis and Rheumatism,* 50 (5)**,** pp.1477-1486.

Lanyon, P., Muir, K., Doherty, S. & Doherty, M. 2003. Age and sex differences in hip joint space among asymptomatic subjects without structural change - Implications for epidemiologic studies. *Arthritis and Rheumatism,* 48 (4)**,** pp.1041-1046.

Lau, E. M., Symmons, D. P. & Croft, P. 1996. The epidemiology of hip osteoarthritis and rheumatoid arthritis in the Orient. *Clinical Orthopaedics and Related Research,* 323**,** pp.81-90.

Lavigne, M., Parvizi, J., Beck, M., Siebenrock, K. A., Ganz, R. & Leunig, M. 2004. Anterior femoroacetabular impingement: part I. Techniques of joint preserving surgery. *Clinical Orthopaedics and Related Research,* 418**,** pp.61-66.

Lavy, C. B. D., Msamati, B. C. & Igbigbi, P. S. 2003. Racial and gender variations in adult hip morphology. *International Orthopaedics,* 27 (6)**,** pp.331-333.

Lecerf, G., Fessy, M. H., Philippot, R., Massin, P., Giraud, F., Flecher, X., Girard, J., Mertl, P., Marchetti, E. & Stindel, E. 2009. Femoral offset: Anatomical concept, definition, assessment, implications for preoperative templating and hip arthroplasty. *Orthopaedics & Traumatology: Surgery & Research,* 95 (3)**,** pp.210-219.

Ledingham, J., Dawson, S., Preston, B., Milligan, G. & Doherty, M. 1992. Radiographic patterns and associations of osteoarthritis of the hip. *Annals of the Rheumatic Diseases,* 51 (10)**,** pp.1111-1116.

Ledingham, J., Dawson, S., Preston, B., Milligan, G. & Doherty, M. 1993. Radiographic progression of hospital referred osteoarthritis of the hip. *Annals of the Rheumatic Diseases,* 52 (4)**,** pp.263-267.

Lee, S.-S., Duong, C.-T., Park, S.-H., Cho, Y., Park, S. & Park, S. 2012. Frictional response of normal and osteoarthritic articular cartilage in human femoral head. *Proceedings of the Institution of Mechanical Engineers, Part H: Journal of Engineering in Medicine*, 227 (2), pp.129-137.

Lee, Y., Seon, J., Shin, V., Kim, G.-H. & Jeon, M. 2008. Anatomical evaluation of CT-MRI combined femoral model. *BioMedical Engineering OnLine,* 7 (1), p.6.

Legaye, J. 2009. Influence of the sagittal balance of the spine on the anterior pelvic plane and on the acetabular orientation. *International Orthopaedics,* 33 (6), pp.1695-1700.

Lembeck, B., Mueller, O., Reize, P. & Wuelker, N. 2005. Pelvic tilt makes acetabular cup navigation inaccurate. *Acta Orthopaedica,* 76 (4), pp.517-523.

Lequesne, M., Malghem, J. & Dion, E. 2004. The normal hip joint space: variations in width, shape, and architecture on 223 pelvic radiographs. *Annals of the Rheumatic Diseases,* 63 (9), pp.1145-1151.

Leunig, M., Beaule, P. E. & Ganz, R. 2009a. The concept of femoroacetabular impingement: current status and future perspectives. *Clinical Orthopaedics and Related Research,* 467 (3), pp.616-622.

Leunig, M., Casillas, M. M., Hamlet, M., Hersche, O., Notzli, H., Slongo, T. & Ganz, R. 2000. Slipped capital femoral epiphysis: early mechanical damage to the acetabular cartilage by a prominent femoral metaphysis. *Acta Orthopaedica Scandinavica,* 71 (4), pp.370-375.

Leunig, M., Nho, S., Turchetto, L. & Ganz, R. 2009b. Protrusio Acetabuli: New Insights and Experience with Joint Preservation. *Clinical Orthopaedics and Related Research,* 467 (9), pp.2241-2250.

Levangie, P. K. & Norkin, C. C. 2001. *Joint Structure and Function: A Comprehensive Analysis.* 3rd ed. Philadelphia: F. A. Davis Company. ISBN: 0803607105.

Lewinnek, G., Lewis, J., Tarr, R., Compere, C. & Zimmerman, J. 1978. Dislocations after total hip-replacement arthroplasties. *Journal of Bone & Joint Surgery - American Volume,* 60 (2), pp.217-220.

Lewis, C. L. & Sahrmann, S. A. 2006. Acetabular labral tears. *Physical Therapy,* 86 (1), pp.110-121.

Lievense, A. M., Bierma-Zeinstra, S. M. A., Verhagen, A. P., Verhaar, J. A. N. & Koes, B. W. 2002. Prognostic factors of progress of hip osteoarthritis: A systematic review. *Arthritis & Rheumatism-Arthritis Care & Research,* 47 (5), pp.556-562.

Life Technologies™ 2013. *Newborn Calf Serum: Certificate of Analysis.* Auckland, New Zealand: Life Technologies Corporation.

Liney, G. 2010. MRI from A to Z: A Definitive Guide for Medical Professionals. 2nd ed. London, UK: Springer-Verlag. ISBN: 1849961349.

Lizhang, J. 2010. *Tribology of Hemiarthroplasty.* Ph.D., University of Leeds.

Lizhang, J., Fisher, J., Jin, Z., Burton, A. & Williams, S. 2011. The effect of contact stress on cartilage friction, deformation and wear. *Proceedings of the Institution of Mechanical Engineers, Part H: Journal of Engineering in Medicine,* 225 (H5), pp.461-475.

Lizhang, J., Taylor, S. D., Jin, Z., Fisher, J. & Williams, S. 2013. Effect of clearance on cartilage tribology in hip hemi-arthroplasty. *Proceedings of the Institution of Mechanical Engineers, Part H: Journal of Engineering in Medicine,* 227 (12)**,** pp.1284-1291.

Llopis, E., Fernandez, E. & Cerezal, L. 2012. MR and CT arthrography of the hip. *Seminars in musculoskeletal radiology*, 16 (1), pp.42-56.

Lorensen, W. E. & Cline, H. E. 1987. Marching cubes: A high resolution 3D surface construction algorithm. *ACM siggraph computer graphics,* 21 (4)**,** pp.163-169.

Lubbeke, A., Katz, J. N., Perneger, T. V. & Hoffmeyer, P. 2007. Primary and revision hip arthroplasty: 5-year outcomes and influence of age and comorbidity. *Journal of Rheumatology,* 34 (2)**,** pp.394-400.

Ludwig, T. E., McAllister, J. R., Lun, V., Wiley, J. P. & Schmidt, T. A. 2012. Diminished cartilage-lubricating ability of human osteoarthritic synovial fluid deficient in proteoglycan 4: Restoration through proteoglycan 4 supplementation. *Arthritis and Rheumatism,* 64 (12)**,** pp.3963-3971.

Macirowski, T., Tepic, S. & Mann, R. W. 1994. Cartilage Stresses in the Human Hip Joint. *Journal of Biomechanical Engineering,* 116 (1)**,** pp.10-18.

Mamisch, T. C., Zilkens, C., Siebenrock, K. A., Bittersohl, B., Kim, Y.-J. & Werlen, S. 2009. Hip MRI and its implications for surgery in osteoarthritis patients. *Rheumatic Diseases Clinics of North America,* 35 (3)**,** pp.591-604.

Martin, J. K. 2004. Measured stiffness and displacement coefficients of a stationary rotor hydrostatic bearing. *Tribology International,* 37 (10)**,** pp.809-816.

Martin, J. K. 2006. Design guidelines for hydrostatic journal bearings. *Industrial Lubrication and Tribology,* 58 (3)**,** pp.135-139.

Maruyama, M. M. D., Feinberg, J. R. P., Capello, W. N. M. D. & D'Antonio, J. A. M. D. 2001. Morphologic Features of the Acetabulum and Femur: Anteversion Angle and Implant Positioning. *Clinical Orthopaedics and Related Research,* 393**,** pp.52-65.

Marx, R. G., Connor, J., Lyman, S., Amendola, A., Andrish, J. T., Kaeding, C., McCarty, E. C., Parker, R. D., Wright, R. W. & Spindler, K. P. 2005. Multirater Agreement of Arthroscopic Grading of Knee Articular Cartilage. *The American Journal of Sports Medicine,* 33 (11)**,** pp.1654-1657.

Matheney, T., Kim, Y.-J., Zurakowski, D., Matero, C. & Millis, M. 2009. Intermediate to long-term results following the Bernese periacetabular osteotomy and predictors of clinical outcome. *Journal of Bone & Joint Surgery - American Volume,* 91 (9)**,** pp.2113-2123.

Mavčič, B., Pompe, B., Antolič, V., Daniel, M., Iglič, A. & Kralj-Iglič, V. 2002. Mathematical estimation of stress distribution in normal and dysplastic human hips. *Journal of Orthopaedic Research,* 20 (5)**,** pp.1025-1030.

Mavčič, B., Slivnik, T., Antolic, V., Iglic, A. & Kralj-Iglic, V. 2004. High contact hip stress is related to the development of hip pathology with increasing age. *Clinical Biomechanics,* 19 (9)**,** pp.939-943.

McCann, L., Ingham, E., Jin, Z. & Fisher, J. 2009a. Influence of the meniscus on friction and degradation of cartilage in the natural knee joint. *Osteoarthritis and Cartilage,* 17 (8)**,** pp.995-1000.

McCann, L., Ingham, E., Jin, Z. & Fisher, J. 2009b. An investigation of the effect of conformity of knee hemiarthroplasty designs on contact stress, friction and degeneration of articular cartilage: A tribological study. *Journal of Biomechanics,* 42 (9)**,** pp.1326-1331.

McCann, L., Udofia, I., Graindorge, S., Ingham, E., Jin, Z. & Fisher, J. 2008. Tribological testing of articular cartilage of the medial compartment of the knee using a friction simulator. *Tribology International,* 41 (11)**,** pp.1126-1133.

McCarthy, J. C., Noble, P. C., Schuck, M. R., Wright, J. & Lee, J. 2001a. The Otto E. Aufranc Award: The role of labral lesions to development of early degenerative hip disease. *Clinical Orthopaedics and Related Research,* 393**,** pp.25-37.

McCarthy, J. C., Noble, P. C., Schuck, M. R., Wright, J. & Lee, J. The role of labral lesions to development of early degenerative hip disease. 7th Open Meeting of the Hip-Society/American-Association-of-Hip-and-Knee-Surgeons, March 3rd 2001b San Francisco, California. Lippincott Williams & Wilkins, pp.25-37.

McKie, S. & Brittenden, J. 2005. (ii) Basic science: magnetic resonance imaging. *Current Orthopaedics,* 19 (1)**,** pp.13-19.

McRobbie, D. W., Moore, E. A., Graves, M. J. & Prince, M. R. 2007. *MRI From Picture to Proton.* 2nd ed. Cambridge, UK: Cambridge University Press. ISBN: 0521683845.

Mechlenburg, I., Nyengaard, J., RÃ¸mer, L. & SÃ¸balle, K. 2004. Changes in load-bearing area after Ganz periacetabular osteotomy evaluated by multislice CT scanning and stereology. *Acta Orthopaedica,* 75 (2)**,** pp.147-153.

Menschik, F. 1997. The hip joint as a conchoid shape. *Journal of Biomechanics,* 30 (9)**,** pp.971-973.

Merriam-Webster Inc. 2006. The Hip Joint. *Encyclopaedia Britannica Online* [Online]. Available: http://www.britannica.com/EBchecked/topic/266529/hip [Accessed 03 April 2010].

Microset Products Ltd. 2014. *MICROSET 101 Thixotropic Replicating Compounds* [Online]. [Accessed 10 December 2014]. Available from: http://www.microset.co.uk/?page_id=5851

Milgram, J. W. M. D. 1983. Morphologic Alterations of the Subchondrall Bone in Advanced Degenerative Arthritis. *Clinical Orthopaedics and Related Research,* 173**,** pp.293-312.

Millis, M. B. & Kim, Y.-J. 2002. Rationale of osteotomy and related procedures for hip preservation: a review. *Clinical Orthopaedics and Related Research,* 405**,** pp.108-121.

Mintz, D. N., Hooper, T., Connell, D., Buly, R., Padgett, D. E. & Potter, H. G. 2005. Magnetic resonance imaging of the hip: Detection of labral and chondral abnormalities using noncontrast imaging. *Arthroscopy: The Journal of Arthroscopic & Related Surgery,* 21 (4)**,** pp.385-393.

Miyoshi, H., Mikami, H., Oba, K. & Amari, R. 2012. Anteversion of the Acetabular Component Aligned With the Transverse Acetabular Ligament in Total Hip Arthroplasty. *The Journal of Arthroplasty,* 27 (6)**,** pp.916-922.

Montgomery, R. J. 2009. (iv) Slipped upper femoral epiphysis. *Orthopaedics and Trauma,* 23 (3)**,** pp.169-174.

Moore, K. L. & Dalley, A. F. 1999. *Clinically Oriented Anatomy.* 4th ed. Philadelphia: Lippincott Williams & Wilkins. ISBN: 0683061410.

Mortensen, E., Morse, B., Barrett, W. & Udupa, J. Adaptive boundary detection using `live-wire' two-dimensional dynamic programming. Computers in Cardiology, 11-14 Oct 1992. pp.635-638.

Mortensen, E. N. & Barrett, W. A. 1998. Interactive Segmentation with Intelligent Scissors. *Graphical Models and Image Processing,* 60 (5)**,** pp.349-384.

Moser, E., Stadlbauer, A., Windischberger, C., Quick, H. H. & Ladd, M. E. 2009. Magnetic resonance imaging methodology. *European Journal of Nuclear Medicine and Molecular Imaging,* 36**,** pp.30-41.

Moskal, J. T. & Capps, S. G. 2010. Improving the Accuracy of Acetabular Component Orientation: Avoiding Malposition. *Journal of the American Academy of Orthopaedic Surgeons,* 18 (5)**,** pp.286-296.

Mow, V. C., Ateshian, G. A. & Spilker, R. L. 1993. Biomechanics of Diarthrodial Joints: A Review of Twenty Years of Progress. *Journal of Biomechanical Engineering,* 115 (4B)**,** pp.460-467.

Mow, V. C. & Huiskes, R. 2005. *Basic Orthopaedic Biomechanics and Mechano-Biology.* 3rd ed. Philadelphia, USA: Lippincott Williams & Wilkins. ISBN: 0781739330.

Mow, V. C., Kuei, S. C., Lai, W. M. & Armstrong, C. G. 1980. Biphasic Creep and Stress Relaxation of Articular Cartilage in Compression: Theory and Experiments. *Journal of Biomechanical Engineering,* 102 (1)**,** pp.73-84.

Mow, V. C. P. & Wang, C. C. B. M. S. 1999. Some Bioengineering Considerations for Tissue Engineering of Articular Cartilage. *Clinical Orthopaedics and Related Research,* 367 (Supplement)**,** pp.S204-S223.

MP Biomedicals LLC. 2014. *Product datasheet for PBS tablets* [Online]. [Accessed 14 October 2014]. Available from: http://www4.mpbio.com/ecom/docs/proddata.nsf/(webtds2)/28103

Muhamad, A. R., Freitas, J. M., Bomar, J. D. & Hosalkar, H. 2012. Acetabular version on magnetic resonance imaging: analysis of two different measuring techniques. *Hip International,* 22 (6)**,** pp.672-676.

Müller, L. P., Degreif, J., Rudig, L., Mehler, D., Hely, H. & Rommens, P. M. 2004. Friction of ceramic and metal hip hemi-endoprostheses against cadaveric acetabula. *Archives of Orthopaedic and Trauma Surgery,* 124 (10)**,** pp.681-687.

Murakami, T., Higaki, H., Sawae, Y., Ohtsuki, N., Moriyama, S. & Nakanishi, Y. 1998. Adaptive multimode lubrication in natural synovial joints and artificial joints. *Proceedings of the Institution of Mechanical Engineers, Part H: Journal of Engineering in Medicine,* 212 (1)**,** pp.23-35.

Murphy, S., Ganz, R. & Muller, M. 1995. The prognosis in untreated dysplasia of the hip. A study of radiographic factors that predict the outcome. *Journal of Bone & Joint Surgery - American Volume,* 77 (7)**,** pp.985-989.

Murray, D. W. 1993. The definition and measurement of acetabular orientation. *Journal of Bone & Joint Surgery - British Volume,* 75 (2)**,** pp.228-232.

Murray, D. W., Fitzpatrick, R., Rogers, K., Pandit, H., Beard, D. J., Carr, A. J. & Dawson, J. 2007. The use of the Oxford hip and knee scores. *Journal of Bone & Joint Surgery - British Volume,* 89-B (8)**,** pp.1010-1014.

Murtha, P. E., Hafez, M. A., Jaramaz, B. & DiGioia, A. M., 3rd 2008. Variations in acetabular anatomy with reference to total hip replacement. *Journal of Bone & Joint Surgery - British Volume,* 90 (3)**,** pp.308-313.

Nakahara, I., Takao, M., Sakai, T., Nishii, T., Yoshikawa, H. & Sugano, N. 2010. Gender differences in 3D morphology and bony impingement of human hips. *Journal of Orthopaedic Research* [Online]. Available: http://dx.doi.org/10.1002/jor.21265 [Accessed November 1st 2010].

Narvani, A. A., Tsiridis, E., Kendall, S., Chaudhuri, R. & Thomas, P. 2003a. A preliminary report on prevalence of acetabular labrum tears in sports patients with groin pain. *Knee Surgery, Sports Traumatology, Arthroscopy,* 11 (6)**,** pp.403-408.

Narvani, A. A., Tsiridis, E., Tai, C. C. & Thomas, P. 2003b. Acetabular labrum and its tears. *British Journal of Sports Medicine,* 37 (3)**,** pp.207-211.

National Electrical Manufacturers Association 2015. The DICOM Standard 2015a. Virginia: NEMA.

Neogi, T., Bowes, M. A., Niu, J., De Souza, K. M., Vincent, G. R., Goggins, J., Zhang, Y. & Felson, D. T. 2013. Magnetic Resonance Imaging–Based Three-Dimensional Bone Shape of the Knee Predicts Onset of Knee Osteoarthritis: Data From the Osteoarthritis Initiative. *Arthritis and Rheumatism,* 65 (8)**,** pp.2048-2058.

Neville, A., Morina, A., Liskiewicz, T. & Yan, Y. 2007. Synovial joint lubrication — does nature teach more effective engineering lubrication strategies? *Proceedings of the Institution of Mechanical Engineers, Part C: Journal of Mechanical Engineering Science,* 221 (10)**,** pp.1223-1230.

Nevitt, M. C. 1996. The Epidemiology of Osteoarthritis in the Peripheral Joints: Session 1: Disease Definition: Definition of hip osteoarthritis for epidemiological studies. *Annals of the Rheumatic Diseases,* 55 (9)**,** pp.652-655.

NHS Scotland 2014. *Scottish Arthroplasty Project - Biennial Report 2014.*

NJR 2014. *National Joint Registry for England, Wales and Northern Ireland 11th Annual Report.* Hertfordshire, UK: Northgate Information Solutions (UK) Ltd.

Nordin, M. & Frankel, V. H. 2012. *Basic Biomechanics of the Musculoskeletal System.* 4th ed. Baltimore, US: Lippincott, Williams & Wilkins. ISBN: 1609133358.

Northwood, E., Fisher, J. & Kowalski, R. 2007. Investigation of the friction and surface degradation of innovative chondroplasty materials against articular cartilage. *Proceedings of the Institution of Mechanical Engineers, Part H: Journal of Engineering in Medicine,* 221 (3)**,** pp.263-279.

Noyes, F. R. & Stabler, C. L. 1989. A system for grading articular cartilage lesions at arthroscopy. *The American Journal of Sports Medicine,* 17 (4)**,** pp.505-513.

Nuki, G. 1999. Osteoarthritis: a problem of joint failure. *Zeitschrift Fur Rheumatologie,* 58 (3)**,** pp.142-147.

Nuki, G. (ed.) 2005. *Osteoarthritis: Risk Factors and Pathogenesis.* Chesterfield: Arthritis Research Campaign.

O'Kelly, J., Unsworth, A., Dowson, D., Hall, D. A. & Wright, V. 1978. A Study of the Role of Synovial Fluid and its Constituents in the Friction and Lubrication of Human Hip Joints. *Engineering in Medicine,* 7 (2)**,** pp.73-83.

Opitz, H. 1967. Paper 8: Pressure Pad Bearings. *Proceedings of the Institution of Mechanical Engineers, Conference Proceedings,* 182 (1)**,** pp.100-115.

Outerbridge, R. E. 1961. The Etiology of Chondromalacia Patellae. *Journal of Bone & Joint Surgery - British Volume,* 43-B (4)**,** pp.752-757.

Palastanga, N., Field, D. & Soames, R. 2002. *Anatomy and Human Movement: Structure and Function.* 4th ed. Oxford: Butterworth Heinemann. ISBN: 0750652411.

Paul, J. P. 1966. Paper 8: Forces Transmitted by Joints in the Human Body. *Proceedings of the Institution of Mechanical Engineers, Conference Proceedings,* 181 (10)**,** pp.8-15.

Pawaskar, S. S., Grosland, N. M., Ingham, E., Fisher, J. & Jin, Z. 2011. Hemiarthroplasty of hip joint: An experimental validation using porcine acetabulum. *Journal of Biomechanics,* 44 (8)**,** pp.1536-1542.

Pearce, C. J., Sexton, S. A., Davies, D. C. & Khaleel, A. 2008. The transverse acetabular ligament may be used to align the acetabular cup in total hip arthroplasty. *Hip International,* 18 (1)**,** pp.7-10.

Postel, M. & Kerboull, M. 1970. Total prosthetic replacement in rapidly destructive arthrosis of the hip joint. *Clinical Orthopaedics and Related Research,* 72**,** pp.138-144.

Potter, H. G. & Schachar, J. 2010. High resolution noncontrast MRI of the hip. *Journal of Magnetic Resonance Imaging,* 31 (2)**,** pp.268-278.

Primal Pictures. 2006a. The Acetabulum. *Anatomy TV* [Online]. Available: http://0-www.anatomy.tv.wam.leeds.ac.uk/new_home.aspx# [Accessed April 16th 2010].

Primal Pictures. 2006b. Proximal Femur. *Anatomy TV* [Online]. Available: http://0-www.anatomy.tv.wam.leeds.ac.uk/new_home.aspx# [Accessed July 26th 2010].

Primal Pictures. 2006c. Three parts of the hip bone viewed from the medial side. *Anatomy TV* [Online]. Available: http://0-www.anatomy.tv.wam.leeds.ac.uk/new_home.aspx# [Accessed January 20th 2010].

Ranawat, A. S. & Kelly, B. T. 2005. Anatomy of the Hip: Open and Arthroscopic Structure and Function. *Operative Techniques in Orthopaedics,* 15 (3)**,** pp.160-174.

Reijman, M., Hazes, J. M. W., Pols, H. A. P., Bernsen, R. M. D., Koes, B. W. & Bierma-Zeinstra, S. M. A. 2004. Validity and reliability of three definitions of hip osteoarthritis: cross sectional and longitudinal approach. *Annals of the Rheumatic Diseases,* 63 (11)**,** pp.1427-1433.

Reijman, M., Hazes, J. M. W., Pols, H. A. P., Bernsen, R. M. D., Koes, B. W. & Bierma-Zeinstra, S. M. A. 2005a. Role of radiography in predicting progression of osteoarthritis of the hip: prospective cohort study. *BMJ,* 330 (7501)**,** pp.1183-1187.

Reijman, M., Hazes, J. M. W., Pols, H. A. P., Koes, B. W. & Bierma-Zeinstra, S. M. A. 2005b. Acetabular dysplasia predicts incident osteoarthritis of the hip: the Rotterdam study. *Arthritis and Rheumatism,* 52 (3)**,** pp.787-793.

Resnick, D. 1975. Patterns of migration of the femoral head in osteoarthritis of the hip: Roentgenographic-pathologic correlation and comparison with rheumatoid arthritis. *American Journal of Roentgenology,* 124 (1)**,** pp.62-74.

Resnick, D. 1983. Osteophytosis of the femoral head and neck. *Arthritis & Rheumatism,* 26 (7)**,** pp.908-913.

Reynolds, D., Lucas, J. & Klaue, K. 1999. Retroversion of the acetabulum: A cause of hip pain. *Journal of Bone & Joint Surgery - British Volume,* 81-B (2)**,** pp.281-288.

Roberts, B. J., Unsworth, A. & Mian, N. 1982. Modes of lubrication in human hip joints. *Annals of the Rheumatic Diseases,* 41 (3)**,** pp.217-224.

Saari, H., Santavirta, S., Nordstrom, D., Paavolainen, P. & Konttinen, Y. T. 1993. Hyaluronate in total hip replacement. *Journal of Rheumatology,* 20 (1)**,** pp.87-90.

Salamon, A., Salamon, T., Sef, D. & Jo-Osvatic, A. 2004. Morphological characteristics of the acetabulum. *Collegium Antropologicum,* 28**,** pp.221-226.

Saleh, K. J., Celebrezze, M., Kassim, R., Dykes, D. C., Gioe, T. J., Callaghan, J. J. & Salvati, E. A. 2003. Functional Outcome After Revision Hip Arthroplasty: A Metaanalysis. *Clinical Orthopaedics and Related Research November,* 416**,** pp.254-264.

Salter, R. B. 1968. Etiology, pathogenesis and possible prevention of congenital dislocation of the hip. *Canadian Medical Association Journal,* 98 (20)**,** pp.933-945.

Sammon, J. W. 1969. A nonlinear mapping for data structure analysis. *IEEE Transactions on computers,* 18 (5)**,** pp.401-409.

Sariali, E., Veysi, V. & Stewart, T. 2008. (i) Biomechanics of the human hip - consequences for total hip replacement. *Current Orthopaedics,* 22 (6)**,** pp.371-375.

Schnitzler, C. M., Mesquita, J. M. & Wane, L. 1992. Bone histomorphometry of the iliac crest, and spinal fracture prevalence in atrophic and hypertrophic osteoarthritis of the hip. *Osteoporosis International,* 2 (4)**,** pp.186-194.

Scholes, S. C. & Joyce, T. J. 2013. In vitro tests of substitute lubricants for wear testing orthopaedic biomaterials. *Proceedings of the Institution of Mechanical Engineers, Part H: Journal of Engineering in Medicine,* 227 (6)**,** pp.693-703.

Scholes, S. C. & Unsworth, A. 2006. The Effects of Proteins on the Friction and Lubrication of Artificial Joints. *Proceedings of the Institution of Mechanical Engineers, Part H: Journal of Engineering in Medicine,* 220 (6)**,** pp.687-693.

Scholes, S. C., Unsworth, A. & Goldsmith, A. A. J. 2000. A frictional study of total hip joint replacements. *Physics in Medicine and Biology,* 45 (12)**,** pp.3721.

Scott, K. T. & Schmeets, S. H. 2005. SPACE: An Innovative Solution to Rapid, Low SAR, T2-Weighted Contrast in 3D Spin Echo Imaging. *TECHNOLOGY - SPACE TECHNICAL* [Online], 2. Available: https://www.healthcare.siemens.co.uk/siemens_hwem-hwem_ssxa_websites-context-root/wcm/idc/groups/public/@global/@imaging/@mri/documents/download/mdaw/mtu3/~edisp/space_innovative_solution_p_92-95-00081897.pdf [Accessed 09 September 2014].

Seldes, R. M., Tan, V., Hunt, J., Katz, M., Winiarsky, R. & Fitzgerald, R. H., Jr. 2001. Anatomy, histologic features, and vascularity of the adult acetabular labrum. *Clinical Orthopaedics and Related Research,* 382**,** pp.232-240.

Setton, L. A., Elliott, D. M. & Mow, V. C. 1999. Altered mechanics of cartilage with osteoarthritis: human osteoarthritis and an experimental model of joint degeneration. *Osteoarthritis and Cartilage,* 7 (1)**,** pp.2-14.

Sharif, K. M. & Parker, M. J. 2002. Austin Moore hemiarthroplasty: technical aspects and their effects on outcome, in patients with fractures of the neck of femur. *Injury,* 33 (5)**,** pp.419-422.

Sharifi, E., Sharifi, H., Morshed, S., Bozic, K. & Diab, M. 2008. Cost-Effectiveness Analysis of Periacetabular Osteotomy. *Journal of Bone & Joint Surgery - American Volume,* 90 (7)**,** pp.1447-1456.

Simulation Solutions Ltd. 2012. *ProSim Friction Simulator III Hardware Manual (Leeds iMBE variant).* 1.7 ed. Stockport, UK: Simulation Solutions Ltd.

Solomon, L. 1976. Patterns of osteoarthritis of the hip. *Journal of Bone & Joint Surgery - British Volume,* 58-B (2)**,** pp.176-183.

Song, Y., Ito, H., Kourtis, L., Safran, M. R., Carter, D. R. & Giori, N. J. 2012. Articular cartilage friction increases in hip joints after the removal of acetabular labrum. *Journal of Biomechanics,* 45 (3)**,** pp.524-530.

Sotereanos, N. G., Miller, M. C., Smith, B., Hube, R., Sewecke, J. J. & Wohlrab, D. 2006. Using Intraoperative Pelvic Landmarks for Acetabular Component Placement in Total Hip Arthroplasty. *The Journal of Arthroplasty,* 21 (6)**,** pp.832-840.

Stelzeneder, D., Hingsammer, A., Bixby, S. & Kim, Y.-J. 2012. Can Radiographic Morphometric Parameters for the Hip Be Assessed on MRI? *Clinical Orthopaedics and Related Research***,** 471 (3), pp.989-999.

Stem, E. S., O'Connor, M. I., Kransdorf, M. J. & Crook, J. 2006. Computed tomography analysis of acetabular anteversion and abduction. *Skeletal Radiology,* 35 (6)**,** pp.385-389.

Steppacher, S. D., Tannast, M., Zheng, G. Y., Zhang, X., Kowal, J., Anderson, S. E., Siebenrock, K. A. & Murphy, S. B. 2009. Validation of a New Method for Determination of Cup Orientation in THA. *Journal of Orthopaedic Research,* 27 (12)**,** pp.1583-1588.

Stewart, T. D. 2010. Tribology of artificial joints. Orthopaedics and Trauma, 24 (6), pp.435-440.

Swann, D., Radin, E., Nazimiec, M., Weisser, P., Curran, N. & Lewinnek, G. 1974. Role of hyaluronic acid in joint lubrication. *Annals of the Rheumatic Diseases,* 33 (4)**,** pp.318-326.

Tannast, M., Goricki, D., Beck, M., Murphy, S. B. & Siebenrock, K. A. 2008. Hip damage occurs at the zone of femoroacetabular impingement. *Clinical Orthopaedics and Related Research,* 466 (2)**,** pp.273-280.

Tannast, M., Langlotz, U., Siebenrock, K.-A., Wiese, M., Bernsmann, K. & Langlotz, F. 2005. Anatomic referencing of cup orientation in total hip arthroplasty. *Clinical Orthopaedics and Related Research,* 436**,** pp.144-150.

Taylor, S. D. 2012. *An In-vitro Medium Term Simulation of Hemiarthroplasty.* Ph.D., The University of Leeds.

Teratani, T., Naito, M., Kiyama, T. & Maeyama, A. 2010. Periacetabular Osteotomy in Patients Fifty Years of Age or Older. *Journal of Bone & Joint Surgery - American Volume,* 92 (1)**,** pp.31-41.

Terjesen, T. & Gunderson, R. B. 2012. Radiographic evaluation of osteoarthritis of the hip: An inter-observer study of 61 hips treated for late-detected developmental hip dislocation. *Acta Orthopaedica,* 83 (2)**,** pp.185-189.

Thompson, M. S., Dawson, T., Kuiper, J. H., Northmore-Ball, M. D. & Tanner, K. E. 2000. Acetabular morphology and resurfacing design. *Journal of Biomechanics,* 33 (12)**,** pp.1645-1653.

Tonnis, D. & Heinecke, A. 1999. Acetabular and femoral anteversion: relationship with osteoarthritis of the hip. *Journal of Bone & Joint Surgery - American Volume,* 81 (12)**,** pp.1747-1770.

Traina, F., De Clerico, M., Biondi, F., Pilla, F., Tassinari, E. & Toni, A. 2009. *Sex Differences in Hip Morphology: Is Stem Modularity Effective for Total Hip Replacement? Journal of Bone & Joint Surgery - American Volume,* 91 (Supplement 6), pp.121-128.

Troelsen, A., Elmengaard, B. & Soballe, K. 2009. Medium-term outcome of periacetabular osteotomy and predictors of conversion to total hip replacement. *Journal of Bone & Joint Surgery - American Volume,* 91 (9)**,** pp.2169-2179.

Unnanuntana, A., Toogood, P., Hart, D., Cooperman, D. & Grant, R. E. 2010. Evaluation of proximal femoral geometry using digital photographs. *Journal of Orthopaedic Research,* 28 (11)**,** pp.1399-1404.

Unsworth, A., Dowson, D. & Wright, V. 1975. The Frictional Behavior of Human Synovial Joints—Part I: Natural Joints. *Journal of Tribology,* 97 (3)**,** pp.369-376.

Usworth, A. 1976. Friction and lubrication of artificial hip joints [proceedings]. *Annals of the Rheumatic Diseases,* 35 (6)**,** pp.539-540.

van der Kraan, P. M. & van den Berg, W. B. 2007. Osteophytes: relevance and biology. *Osteoarthritis and Cartilage,* 15 (3)**,** pp.237-244.

van Ingen Schenau, G. J. & Bobbert, M. F. 1993. The global design of the hindlimb in quadrupeds. *Acta Anatomica,* 46**,** pp.103-108.

Vandenbussche, E., Saffarini, M., Delogé, N., Moctezuma, J.-L. & Nogler, M. 2007. Hemispheric cups do not reproduce acetabular rim morphology. *Acta Orthopaedica,* 78 (3)**,** pp.327-332.

Vandenbussche, E., Saffarini, M., Taillieu, F. & Mutschler, C. 2008. The asymmetric profile of the acetabulum. *Clinical Orthopaedics and Related Research,* 466 (2)**,** pp.417-423.

Viste, A., Chouteau, J., Testa, R., Chèze, L., Fessy, M. H. & Moyen, B. 2011. Is transverse acetabular ligament an anatomical landmark to reliably orient the cup in primary total hip arthroplasty? *Orthopaedics & Traumatology: Surgery & Research,* 97 (3)**,** pp.241-245.

Vossinakis, I. C., Georgiades, G., Kafidas, D. & Hartofilakidis, G. 2008. Unilateral hip osteoarthritis: can we predict the outcome of the other hip? *Skeletal Radiology,* 37 (10)**,** pp.911-916.

Walker, P. S., Dowson, D., Longfield, M. D. & Wright, V. 1968. "Boosted lubrication" in synovial joints by fluid entrapment and enrichment. *Annals of the Rheumatic Diseases,* 27 (6)**,** pp.512-520.

Wang, A., Essner, A., Polineni, V. K., Stark, C. & Dumbleton, J. H. 1998. Lubrication and wear of ultra-high molecular weight polyethylene in total joint replacements. *Tribology International,* 31 (1-3)**,** pp.17-33.

Watanabe, A., Boesch, C., Siebenrock, K., Obata, T. & Anderson, S. E. 2007. T2 mapping of hip articular cartilage in healthy volunteers at 3T: a study of topographic variation. *Journal of Magnetic Resonance Imaging,* 26 (1)**,** pp.165-171.

Wedge, J. H., Wasylenko, M. J. & Houston, C. S. 1991. Minor anatomic abnormalities of the hip-joint persisting from childhood and their possible relationship to idiopathic osteoarthrosis. *Clinical Orthopaedics and Related Research,* (264)**,** pp.122-128.

Wiberg, G. 1953. Shelf Operation in Congenital Dysplasia of the Acetabulum and in Subluxation and Dislocation of the hip. *Journal of Bone & Joint Surgery - American Volume,* 35 (1)**,** pp.65-80.

Williams, S., Jalali-Vahid, D., Brockett, C., Jin, Z., Stone, M. H., Ingham, E. & Fisher, J. 2006. Effect of swing phase load on metal-on-metal hip lubrication, friction and wear. *Journal of Biomechanics,* 39 (12)**,** pp.2274-2281.

Williams, S., Leslie, I., Isaac, G., Jin, Z., Ingham, E. & Fisher, J. 2008. Tribology and wear of metal-on-metal hip prostheses: influence of cup angle and head position. *Journal of Bone & Joint Surgery - American Volume,* 90 (Supplement 3)**,** pp.111-117.

Williams, T. G., Holmes, A. P., Bowes, M., Vincent, G., Hutchinson, C. E., Waterton, J. C., Maciewicz, R. A. & Taylor, C. J. 2010. Measurement and visualisation of focal cartilage thickness change by MRI in a study of knee osteoarthritis using a novel image analysis tool. *British Journal of Radiology,* 83 (995)**,** pp.940-948.

Woodhouse, F. G., Gardiner, B. S. & Smith, D. W. 2015. Short-term consolidation of articular cartilage in the long-term context of osteoarthritis. *Journal of Theoretical Biology,* 368**,** pp.102-112.

Wright, A. A., Cook, C. & Abbott, J. H. 2009. Variables associated with the progression of hip osteoarthritis: a systematic review. *Arthritis and Rheumatism,* 61 (7)**,** pp.925-936.

Wright, D., Whyne, C., Hardisty, M., Kreder, H. & Lubovsky, O. 2011. Functional and Anatomic Orientation of the Femoral Head. *Clinical Orthopaedics and Related Research,* 469 (9), pp.2583-2589.

Yamaguchi, J., Hasegawa, Y., Kanoh, T., Seki, T. & Kawabe, K. 2009. Similar survival of eccentric rotational acetabular osteotomy in patients younger and older than 50 years. *Clinical Orthopaedics and Related Research,* 467 (10)**,** pp.2630-2637.

Yamamoto, T., Schneider, R., Iwamoto, Y. & Bullough, P. 2010. Bilateral rapidly destructive arthrosis of the hip joint resulting from subchondral fracture with superimposed secondary osteonecrosis. *Skeletal Radiology,* 39 (2)**,** pp.189-192.

Yao, J. Q., Laurent, M. P., Johnson, T. S., Blanchard, C. R. & Crowninshield, R. D. 2003. The influences of lubricant and material on polymer/CoCr sliding friction. Wear, 255 (1–6), pp.780-784.

Yoshimura, N., Campbell, L., Hashimoto, T., Kinoshita, H., Okayasu, T., Wilman, C., Coggon, D., Croft, P. & Cooper, C. 1998. Acetabular dysplasia and hip osteoarthritis in Britain and Japan. *Rheumatology,* 37 (11)**,** pp.1193-1197.

Zebala, L. P., Schoenecker, P. L. & Clohisy, J. C. 2007. Anterior femoroacetabular impingement: a diverse disease with evolving treatment options. *Iowa Orthopaedic Journal,* 27**,** pp.71-81.

Zhang, J. L., Fisher, J., Jin, Z., Burton, A. P. & Williams, S. 2010. Effect of clearance on friction and cartilage damage in hip hemi-arthroplasty. *56th Annual Meeting of the Orthopaedic Research Society.* New Orleans:Louisiana.

Zheng, G., Zhang, X., Steppacher, S. D., Murphy, S. B., Siebenrock, K. A. & Tannast, M. 2009. HipMatch: An object-oriented cross-platform program for accurate determination of cup orientation using 2D-3D registration of single standard X-ray radiograph and a CT volume. *Computer Methods and Programs in Biomedicine,* 95 (3)**,** pp.236-248.

Zhu, J., Wan, Z. & Dorr, L. 2010. Quantification of Pelvic Tilt in Total Hip Arthroplasty. *Clinical Orthopaedics and Related Research,* 468 (2)**,** pp.571-575.